The Low-Recycling Lithium Boundary and Implications for Plasma Transport

Erik Michael Granstedt

A Dissertation Presented to the Faculty
of Princeton University
in Candidacy for the Degree
of Doctor of Philosophy

Recommended for Acceptance
by the Program in Plasma Physics
of the Department of
Astrophysical Sciences
Advisers: R. Kaita, and G.W. Hammett

September 2013

© Copyright by Erik Michael Granstedt, 2013.

All rights reserved.

Abstract

Pumping of incident hydrogen and impurity ions by lithium enables control of the particle inventory and fueling profile in magnetic-confined plasmas, and may raise the plasma temperature near the wall. As a result, the density gradient is expected to contribute substantially to the free-energy, affecting particle and thermal transport from micro-turbulence which is typically the dominant transport mechanism in high-temperature fusion experiments.

Transport in gyrokinetic simulations of density-gradient-dominated profiles is characterized by a small linear critical gradient, large particle flux, and preferential diffusion of cold particles. As a result, the heat flux is below 5/2 or even 3/2 times the particle flux, usually assumed to be the minimum for convection. While surprising, this result is consistent with increasing entropy. Coupled TEM-ITG (ion-temperature-gradient) simulations using $\eta_e = \eta_i$ find $\eta = \nabla T/\nabla n \approx 0.8$ maximizes the linear critical pressure gradient, which suggests that experiments operating near marginal ITG stability with larger η would increase the linear critical pressure gradient by transferring free-energy from the temperature gradient to the density gradient.

Simulations were performed with profiles predicted for the Lithium Tokamak Experiment (LTX) if ion thermal transport was neoclassical, while electron thermal transport and particle transport were a fixed ratio above the neoclassical level. A robust TEM instability was found for the outer half radius, while the ITG was found to be driven unstable as well during gas puff fueling. This suggests that TEM transport will be an important transport mechanism in high-temperature low-recycling fusion experiments, and in the absence of stabilizing mechanisms, may dominate over neoclassical transport.

A diagnostic suite has been developed to measure hydrogen and impurity emission in LTX in order to determine the lower bound on recycling that can be achieved in a small tokamak using solid lithium coatings, assess its dependence on the operating condition of the lithium surface, and evaluate its impact on the discharge.

Coatings on the close-fitting stainless-steel substrate produce a significant reduction in recyling, so that the effective particle confinement times are as low as $\lesssim$1 ms. Measurements of particle inventory in the plasma and hydrogen Lyman-α emission indicate that hydrogen recycling at the surface increases as subsequent discharges are performed; nevertheless, strong pumping of hydrogen is observed even after almost double the cumulative fueling is applied that should saturate the lithium coating to the penetration depth of hydrogen ions.

Probe measurements show that when external fueling is terminated, the scrape-off-layer of discharges with fresh coatings decays to lower density and rises to higher electron temperature than for discharges with a partially-passivated surface, consistent with reduced edge cooling from recycled particles. Near the end of the discharge, higher plasma current correlates with reduced τ_p^* and hydrogen emission, suggesting that discharges with fresh coatings achieve higher electron temperature in the core.

A novel approach using neutral modeling was developed for the inverse problem of determining the distribution of recycled particle flux from PFC surfaces given a large number of emission measurements, revealing that extremely low levels of recycling ($R_{\rm core}\sim$0.6 and $R_{\rm plate}\sim$0.8) have been achieved with solid lithium coatings. Together with impurity emission measurements, modeling suggests that during periods of particularly low electron density, influx of impurities from the walls contributes substantially to the global particle balance.

Acknowledgements

First, I would like to thank Bob Kaita, Greg Hammett and Dick Majeski, who have all advised me throughout my thesis endeavor. I also greatly appreciated our scientific discussions, which helped me develop as a scientist and improved the quality of this thesis. Bob, thank you for your encouragement and for reminding me time and time again of the big picture. Thank you also for your model of integrating scientific research with a healthy family life and the Christian faith. Greg, thank you for your patience in explaining physics concepts to me; you are truly an excellent teacher. Dick, thank you for managing the LTX project, and for your creative ideas.

I would also like to thank other staff with whom I worked during my thesis research. In particular, I would like to thank Daren Stotler for use of his well-documented neutral transport code, for his availability to answer questions, and for his encouragement. Daren, thank you also for reading through this thesis on such short notice. I also had the privilege to be able to work closely with Tommy Thomas to develop a digital holography diagnostic. Tommy, thank you for giving me the opportunity to learn about optics, for your persistence, and for the countless hours you spent on the road in order to work with me in Princeton.

I am indebted both to former and current students who have worked on the LTX project. Tim, thank you for your perspective on choosing thesis advisors and for your work which I sought to build upon. Laura, your work configuring the LTX MDSplus system and developing magnetic diagnostics was critical to getting the machine running. Dan, you taught me a lot during our physics discussions. I also appreciated your kindred spirit. Craig, thank you for your sense of humor and for sharing in the challenge of being a father and a graduate student. Dennis, thank you especially for helping me with mundane experimental tasks during this final stretch. Matt, thank you for your work setting up the Langmuir probe, and for your gracious demeanor. Jack, I very much enjoyed working with you during your first-year project. Jono, thank you for laying the groundwork with LRDFIT and edge modeling.

I am also thankful for the technical staff of the LTX project. Tom Kozub, thank you for iterating over numerous mechanical designs with me. Jim Taylor, how you remember where items were stored twenty years ago, I have no idea. Thank you for helping me become at least somewhat competent technically. Dave Moser and Tommy Holomon, thank you for your willingness to help me when I didn't know what I was doing. Enrique Merino, thank you for helping me and the project with whatever tasks needed to get done. Dorian Bohler, thank you for your help with software.

When I first visited the lab, another student mentioned the outstanding graduate program administrator, Barbara Sarfaty, as a reason to choose to come to Princeton. The student was absolutely right. Thank you Barbara for helping me through requirements, processing paperwork on my behalf, and for correcting me when I needed it.

I have also had the opportunity to work with and learn from numerous other research staff. I would like to thank Yevgeny Raitses for being an excellent advisor during my first year. Yevgeny, I greatly enjoyed working alongside you while learning about plasma physics and space propulsion. I also cannot thank you enough for providing contacts and wisdom during my job search. I also appreciated my time working under Leonid Zakharov during my second year. Leonid, I'm impressed by all your talents and your relentless drive. Thank you especially for your encouragement. I would also like to thank Bill Tang, Stephane Ethier, Ernie Valeo, and Gerrit Kramer, who mentored me during a summer practicum. Bill, I still remember watching Olympic swimming at your house.

Several other research staff have assisted me during this thesis. Vlad Soukhanovskii, thank you for giving me a crash-course in spectroscopy and for letting me borrow equipment. Kevin Tritz, thank you for teaching me how to design array instruments and for letting me use your pre-amplifiers. Mike Jaworski, thank you for your encouragement and for sharing with me your expertise in edge plasma physics. Jon Menard, thank you for the time you spent helping me navigate LRDFIT. I would also like to thank Rajesh Maingi and our

ORNL collaborators, Travis Gray and Adam McLean for their help with filterscopes and visible spectrometers.

I could not have asked for better classmates with which to go through the trials and tribulations of graduate school. I'm grateful for the students in years above me, who proved finishing is possible. To each of the students in classes below me, thank you for your eagerness and enthusiasm that help remind us older students of why we came here. I'm especially grateful for the bond with the other students in my class. I enjoyed sharing the party office with you, Luc, during the early days of our time in Princeton. Jessica, thank you for babysitting, baked goods, and other blessings. Eisung, I enjoyed discussing deep questions with you about physics and life. I wish we could have been neighbors longer, and enjoyed many more barbecues together. Jongsoo, it has been a pleasure to know you as a colleague physicist, tennis buddy, and friend.

The technical staff at the lab has served me in numerous ways. John Trafalski, Ted Franckowiak, and Steve Jurczynski, you each helped me conceptualize the mechanical parts I needed, then skillfully constructed them. Ed Lawson and Bob Mozulay, thank you for teaching me enough about circuit design to get me into trouble, and for identifying where I went wrong.

I'm grateful for financial support from the DOE Fusion Energy Sciences Graduate Fellowship and the NSF Graduate Research Fellowship during my graduate years. I also very much appreciate Princeton University for its commitment to students and support for families.

I was blessed to grow up in a cohesive and loving family that nourished my interests and instilled a love for learning. Thank you especially Mom and Dad for teaching me not only about academics, but also about life, and for your prayers on my behalf as well. I have also been blessed by my wife's family who gave of their time to help care for our children while we were both working on our degrees. Caleb and Joel, thank you for giving me a reason to laugh every day.

Finally, I thank my wife Andrea for her tremendous encouragement, especially during my periods of despair. Andrea, you have been a faithful companion and are an outstanding mother to our boys—all while completing a thesis yourself. Thank you for being patient and gracious while also speaking wisdom to me when I needed to hear it. We are finally a "pair-of-docs" (paradox)!

Above all, I thank the Lord Jesus Christ, who invites all those who are weary and burdened to come to Him and receive rest. There were countless times during these past years that I was weary and burdened! Nevertheless, it has been a priviledge to study the patterns You have established to govern the universe with Your wisdom. As the psalmist says, "How many are your works, Lord! In wisdom you made them all."

To Andrea, whose love and encouragement helped me persevere to the end.

Contents

List of Tables

List of Figures

Chapter 1

Introduction: Two Coupled issues for Magnetic Fusion Energy

The goal of magnetic fusion energy (MFE) research can be thought of as developing a magnetic "bottle" to efficiently confine a plasma composed of charged particles (namely electrons and hydrogenic ions) so that it can be heated to temperatures at which thermonuclear fusion reactions occur. In the fusion reaction, some mass of the reactants is converted to the kinetic energy of the fusion products. The kinetic energy of the charged products (generally alpha particles) can then provide additional collisional heating for the plasma, or it could be converted directly to electricity, while any neutrons resulting from the fusion reaction can be thermalized by a blanket material which can be used in a heat cycle to produce electricity.

There are a number of significant hurdles to realizing a viable magnetic-confined fusion reactor including enhanced particle and energy losses due to micro-turbulence in the plasma, the survivability of plasma-facing materials, a build-up of impurities in the confined plasma, embrittlement of the entire device due due neutron damage, gross stability of the plasma, removal of helium ash from the confined plasma, tritium retention in the plasma-facing material, and (not least of all) the economic competitiveness of the energy produced. This work will explore theoretically and computationally how the characteristics of the plasma-

facing materials may modify the turbulent mechanisms in the plasma. Experimentally, this thesis will examine the performance of a particular plasma-facing material in a small magnetic confinement device.

1.1 Turbulent Transport of Particles and Energy: The Problem and Historical Overview

1.1.1 Energy Confinement Requirement

As mentioned earlier, one obstacle to achieving a fusion reactor based on magnetic confinement is the apparently turbulent transport of particles and energy across magnetic field lines–essentially a leaky magnetic "bottle." The gain (Q) of a fusion reactor is defined as the ratio of fusion power output to external heating power input, with "scientific break-even" being $Q = 1$ and "ignition" being $Q \to \infty$. Ignition is achieved if the fusion reaction is maintained by α-particle heating only and external heating can be turned off. Achieving net fusion gain ($Q > 1$) requires sufficient temperature (T) and density (n) for the fusion reactions to occur as well as for energy to be efficiently contained in the system–characterized by the energy confinement time (τ_E). A given fusion gain sets a constraint on the triple product of these quantities[1]:

$$nT\tau_E > \frac{K}{1 + 5/Q} \tag{1.1}$$

For fusion reactions of deuterium and tritium, $K = 3.1 \times 10^{21} \mathrm{m}^{-3} \cdot \mathrm{keV} \cdot \mathrm{s}$. The above expression neglects the effects of impurity ions, helium ash, and radiation, which make the triple product criterion more stringent[1]. When Lyman Spitzer first proposed magnetic confined fusion energy over 60 years ago, he (and others) assumed energy loss would be due to perpendicular diffusion of particles and energy resulting from classical collisions. A random-walk estimate can be used to determine the scaling of thermal diffusivity (χ) for

each plasma species s and hence the energy confinement time from collisional processes:

$$\chi_{cl,s} \propto \frac{\Delta x^2}{\Delta t} \propto \nu_s \rho_s^2 \propto \frac{n Z_s^2 m_s^{1/2}}{T_s^{1/2} B^2} \tag{1.2}$$

$$\tau_{cl,s} \propto \frac{a^2}{\chi_{cl,s}} \rightarrow \quad \tau_{cl,s} \propto \frac{a^2 T_s^{1/2} B^2}{n Z_s^2 m_s^{1/2}} \tag{1.3}$$

Unfortunately, these scalings were not observed in experiments with sufficiently high plasma temperatures. In addition, the measured electron thermal diffusivities were not $\sqrt{m_e/m_i}$ times that of the ions (1/60 for deuterium), but were comparable or even greater. Experiments tended to show "Bohm" scaling:

$$\chi_{B,s} \propto \Omega_s \rho_s^2 \propto \frac{T_s}{Z_s B} \rightarrow \quad \tau_{E,s} \propto \frac{a^2 Z_s B}{T_s} \tag{1.4}$$

This scaling would require prohibitively large devices with very high magnetic fields. Significant fluctuations were measured in the plasma, and thus micro-turbulence became the most likely explanation for the observed electron and ion thermal losses.

1.1.2 Drift Motion and Radial Transport

While a distribution of charged particles can move very quickly along magnetic field lines, their motion in the perpendicular direction is impeded by the magnetic field. For this simple reason, although geometries with relatively straight magnetic field lines that intersect material surfaces (i.e., "mirror machines") have been and continue to be explored as possible fusion concepts, most research is directed towards geometries where the plasma is confined by closed magnetic field lines. Nevertheless, it can be shown that if there are gradients in the magnetic field or if the field lines are curved, particles will drift perpendicular to the field. Therefore magnetic confinement schemes with closed field-lines (which are necessarily curved) must be designed so that their magnetic geometries counteract these drifts. A pressure

gradient results in the local particle distribution having a drift perpendicular to the field because of diamagnetism. This drift, however, is perpendicular to the pressure gradient, so the diamagnetic drift from a radial pressure gradient will not cause radial particle transport.

An electric field (E) or a time-varying electric field will cause particles to drift in the $E \times B$ direction. Therefore, electrostatic potential gradients in the diamagnetic ($\hat{y} \doteq \hat{b} \times \hat{r}$) direction will cause radial particle transport. Charged particles are advected around potential perturbations, and if a background pressure gradient exists, the flux from higher pressure to lower pressure will be greater than the flux in the other direction. If these perturbations were not time-varying, particles would merely continue to orbit around the potential perturbation until experiencing a collision. In this situation, the particle diffusivity would have the same time-step as with collisional diffusion, but with a step-size that may be enhanced by the radial extent of the potential perturbation. Time-varying electrostatic potential fluctuations however, are effectively turbulent eddies which effectively can appear, cause radial particle advection, and decay before particles can drift back to their unperturbed locations. This situation corresponds to micro-turbulence: the plasma may be globally stable, but with enhanced particle diffusivity that (in some parameter regimes) can be related to the radial extent of the eddy and inversely to the eddy decay time. With this picture in mind, measurements of significant fluctuations in the plasma suggested that micro-turbulence could be the primary explanation for why particle and thermal transport losses greatly exceeded collisional estimates. The instability mechanisms causing the observed fluctuations needed to be elucidated.

1.1.3 Instability Mechanisms responsible for Micro-Turbulence

An instability was identified which is driven by the non-adiabatic electron response to drift wave fluctuations due to magnetic trapping, the trapped electron mode (TEM)[2,3,4]. Later, a hydrodynamic instability was found which results from bad curvature on the outside of

the torus, and an ion temperature gradient stronger than the density gradient[5]. The ion temperature gradient (ITG) mode became an entire field of study, and consensus began to build that it may be the dominant instability responsible for ion thermal losses.

Linear gyro-fluid and then gyro-kinetic simulations identified the critical ion temperature gradient, which if exceeded would drive the ITG mode unstable. Subsequent non-linear gyro-kinetic simulations found that in fact toroidally-symmetric (zonal) flows, generated non-linearly by the unstable modes, increased the critical gradient for the instability. Transport models were then developed based on nonlinear gyro-fluid[6,7] and later gyro-kinetic simulations of ITG and TEM turbulence that gave reasonable predictions for core heat transport in many cases. These studies found that once the critical ion temperature gradient was exceeded, the ion thermal transport would increase strongly with increased ion temperature gradient, effectively forcing the temperature profile to the critical gradient[6]. This "stiff" response of the transport to small changes in temperature gradient near the non-linear critical gradient highlights the importance of the edge temperatures in determining the core temperature. If the temperature profile is forced to the critical gradient, the temperature in the core depends exponentially on the temperature at the edge:

$$\frac{a}{T_i}\frac{dT_i}{dr} = -\frac{a}{L_{T_i}^{crit,ITG}} \tag{1.5a}$$

$$T_i(r) = T_i(a)\exp\left[-\int_a^r \frac{dr'}{L_{T_i}^{crit,ITG}(r')}\right]. \tag{1.5b}$$

The role of the TEM has been seen as softening the stiffness of the transport near the critical gradient and increasing the particle transport.

1.1.4 Progress in Turbulence Suppression

In 1982 the ASDEX experiment discovered a sharp transition to a high-confinement regime (H-mode)[8] as the neutral beam heating power was increased during a shot. They found a

more favorable energy confinement scaling termed "Gyro-Bohm":

$$\chi_{gB,s} \propto \frac{\rho_s}{a}\chi_{B,s} \propto \frac{T_s^{3/2} m_s^{1/2}}{Z^2 B^2} \tag{1.6}$$

$$\rightarrow \tau_{gB,s} \propto \frac{a^2 Z^2 B^2}{T^{3/2} m^{1/2}} \tag{1.7}$$

The most widely-held interpretation for the cause of the improved performance is that the higher neutral beam power led to increased shear in the poloidal plasma rotation (due to radial shear in the radial electric field), and this shear was breaking-up turbulent eddies near the edge[9]. Later measurements of temperature fluctuations in a region of high velocity shear near the edge were consistent with this picture[10]. Most current large fusion experiments have been able to access the H-mode regime and in some cases have been able to reduce the ion thermal transport to near the neoclassical prediction, by nature of geometry and beam-driven flow shear[11,12]. Unfortunately, in a reactor with alpha particles providing the dominant heating as opposed to neutral beams, such high velocity shear may not be attainable (though there are some projections that suggest rotation may still be important in an ITER-scale device[13,14]). In addition, the ratio of micro-turbulent to collisional diffusivity scales as $T^{3/2}$ for Bohm scaling, so even if transport losses appear collisional, turbulent losses may dominate at higher temperatures.

1.1.5 Electron Transport

The picture for electron thermal transport is much less clear. Rather than one instability that is usually the driver of enhanced transport, it appears likely that various modes contribute and interact with each other with their relative magnitudes determined by the particularities of the temperature profiles, magnetic shear, and plasma beta. Candidate instability mechanisms include the electron temperature-gradient mode (ETG, which is analogous to ITG but interchanging the electron and ion mass)[15], the TEM, kinetic drift-resistive ballooning turbu-

lence, and micro-tearing modes also driven by the electron temperature gradient. Although initially thought to be too small in scale to drive much energy transport, ETG turbulence can produce radially-elongated streamers, because ETG only weakly drives self-generated zonal flows[15]. Reversed magnetic shear[16,17,18,19] and Shafranov shift[20], due to finite-β compression of flux surfaces on the outboard (bad curvature) side of the torus, have been found to suppress ETG transport and improve performance, though experiments are still studying how to maintain these in a stable way for a long time scale. Good electron thermal confinement may not seem necessary, since after all it is the ion temperature (rather than electron temperature) that is important for fusion reactions. In fact, at high ion temperatures the two can be decoupled because of reduced collisionality. However, in order to approach ignition, energy from fusion alpha particles will need to heat the plasma. Fusion alpha particles primarily transfer their energy to electrons, which in turn heat the ions through electron-ion collisional energy exchange; therefore, electron thermal transport plays a key role in the power balance of a fusion reactor.

1.2 Survivability of Plasma Facing Materials

1.2.1 The Plasma Boundary

A second significant obstacle for a viable fusion reactor is the survivability of the plasma-facing components. Although the magnetic geometry is designed to efficiently trap the high-temperature plasma, reactant ions, fusion products, impurities, and electrons diffuse out of the confined region and strike material surfaces. The "first wall" consists of the ensemble of components that must withstand significant particle, energy, and photon fluxes from the plasma. An intentional, "limiter" structure can be designed to define the last closed-flux-surface of the confined plasma. In this way, the limiter determines the primary region where plasma-material interactions occur and can protect more delicate structures. The scrape-off-

layer (SOL) is the region of open field lines outside the separatrix which intersect a material boundary. An alternative approach to define the last closed-flux-surface is to use vertical field coils to "divert" field lines, creating one or more X-points in the poloidal magnetic field and defining a separatrix that separates the closed field lines inside the confined region from open field lines which intersect material surfaces. An advantage with this approach is that the region where the dominant plasma-material interactions take place can be localized far from the confined plasma.

1.2.2 Material Requirements

In either approach to the geometry of the plasma boundary, the material intersecting the open field lines closest to the separatrix must be capable of handling intense particle and heat loads. For example, although the heat loading on most of the first wall of the ITER experiment is designed to be 0.5 MW/m^2, the divertor target is expected to encounter steady-state heat fluxes of 10–20 MW/m^2 [21]. In addition to high steady-state heat fluxes, the divertor targets must be able to withstand extremely high heat loads from rapid losses of plasma energy. For example, transient edge instabilities (e.g., Edge-Localized Modes or ELMs) are frequently observed in H-mode operation, and can deposit 2–10% of the total plasma thermal energy to the divertor over 0.1–1 ms [21]. Perhaps the worst transient event is the disruption, which rapidly deposits 80–100% of the plasma thermal energy onto the divertor. For ITER, this would imply 10–100 MJ/m^2 over 1–10 ms [21]. Although the frequency of disruptions can be reduced by operating far from stability limits, disruptions still occur occasionally in all operating regimes; therefore, current studies are seeking ways to quickly convert the plasma thermal energy to radiation, which would deposit the plasma stored energy over a larger surface area.

Heat transfer through a material to a coolant is proportional to the thermal conductivity and inversely proportional to the material thickness. By thinning the plasma-facing compo-

nents, heat transfer can be accelerated; for a fixed plasma erosion rate however, the material would have to be replaced more frequently. Therefore, plasma-facing materials need to have high thermal conductivity, but low net erosion.

The dominant processes that cause erosion are physical and chemical sputtering. Between a quasi-neutral plasma and a plasma-facing-material is a plasma sheath which has an electrostatic potential drop that accelerates plasma ions to impact the surface with an energy of about $E \approx 2T + 3ZT$[21], where T is the plasma temperature and Z is the ion charge. Physical sputtering is the process whereby incident ions of sufficient kinetic energy remove substrate atoms from the first few monolayers of material into the plasma. Surface atoms can also be released below the energy threshold for physical sputtering if the incident ions react chemically with the surface atoms, forming volatile compounds. A third erosion process is arcing between a material acting as a cathode, and the plasma which acts as an anode when the sheath potential exceeds the arc voltage threshold. These "unipolar arcs" can be seen in camera images and cause macroscopic damage (tracks, pits) in plasma-facing materials. Their contribution to the overall erosion rate of divertor surfaces may be important, but is not well quantified because of their dependence on surface roughness and their localized and transient nature[21].

Besides needing to handle high heat loads with a low erosion rate, plasma-material interactions need to be controlled in order to minimize the radiated power loss due to impurities in the plasma core. Although the mainstream approach to reducing the heat flux in the divertor is to use impurities in the divertor and outer core plasma to radiate a large portion the thermal exhaust over the area of the vessel wall, impurities in the inner plasma core are detrimental because they dilute the concentration of fuel species (reducing the fusion reactivity) and can negatively affect the power balance via radiative losses. All impurities in the plasma core (whether fully ionized or not) increase the "effective charge" Z_{eff} and therefore increase the bremsstrahlung power loss. Bremsstrahlung radiation is due to free

electrons accelerating near ions and remaining free, and the power loss from this process is[1]:

$$P_{brem} = 5.35 \times 10^{-37} n_e T_e^{1/2} \sum_i n_i Z_i^2 = 5.35 \times 10^{-37} Z_{\text{eff}} n_e^2 T_e^{1/2} \tag{1.8a}$$

$$Z_{\text{eff}} \doteq \frac{\sum_i n_i Z_i^2}{\sum_i n_i Z_i} = \frac{\sum_i n_i Z_i^2}{n_e}. \tag{1.8b}$$

If impurity ions are not fully stripped of their electrons, bound-bound electron transitions contribute to power loss from line radiation. Line radiation from low-Z impurities in the scrape-off-layer could be used to distribute exhaust power over a larger area, but line radiation from high-Z impurities in the plasma core must be minimized because this removes power from the regions in which fusion reactions occur.

Finally, it is essential that the accumulation of tritium in the plasma-facing materials be minimized in order to keep the radioactivity of the fusion reactor within safe limits[21].

1.2.3 Solid Material Candidates

Carbon has been used extensively in current fusion experiments because of its ability to tolerate high heat fluxes, maintain its form despite large temperature swings and not melt. Carbon also has a low atomic number, so although it sputters easily it is fully ionized in the core plasma and hence does not lead to a large radiated power loss. However, carbon is most likely incompatible with a D-T reactor, because it undergoes chemical sputtering which would lead to co-deposition of tritium with eroded carbon. If carbon is used in the ITER divertor, modeling estimates the tritium co-deposition rate to be 2–20 g per plasma pulse[21]. The tritium inventory operating limit for ITER is about 350 g, so at the estimated tritium co-deposition rate, plasma operations might have to be interrupted weekly in order to remove tritium from the machine[21].Even if this maintenance schedule is acceptable for ITER, it certainly will not be tolerable for a reactor. Worse, tritium removal techniques require either

exposure to oxygen at elevated plasma temperatures or oxygen plasma discharges, which are deleterious to vacuum performance, or extremely high temperature vacuum bake-out ($>$ 900 K) which is technically very challenging[21].

With carbon removed from consideration, tungsten is currently the only solid material candidate for the divertor region of a fusion reactor. Tungsten does not suffer from the same tritium retention issue as carbon and discrete tungsten structures (rods, brushes) mounted on water-cooled copper back-plates have performed favorably in high heat flux tests, however questions remain about degradation from reactor-relevant fusion neutron fluences[22]. Tungsten alloys are brittle below 700 °C , so they will have to be kept hot (700—1000 °C) so that they are self-annealing[23]. Tungsten has a low physical sputtering yield[24], however because of its high atomic number, it is not fully ionized at D-T fusion ($\approx$ 20 keV) temperatures. A concentration of 0.01% would radiate about 10% of the total thermonuclear power (in a D-T reactor at T_e = 10 keV)[1], therefore if tungsten is used as a plasma-facing material it is necessary to minimize sputtering using an operating scenario with a low-temperature ($\lesssim$ 10 eV) divertor and edge plasma.

However, post-mortem analysis of tungsten surfaces on both Alcator C-MOD and linear devices have shown significant surface damage. Tungsten nano-tendrils (or "fuzz") can grow on the surface if the tungsten temperature is between 1000 K and 2000 K, and is bombarded by He ions with energies above 20 eV[25]—for example, high fluxes of alpha particles generated in a fusion reactor. Although these structures reduce physical sputtering and cracking from thermal stress, they reduce the thermal conductivity, and may lead to significant tungsten dust formation because of their mechanical fragility. In a reactor, this tungsten dust would be neutron activated and tritiated and therefore may be a safety concern. Finally, tendrils may release large quantities of impurities into the plasma when they break.[25,26].

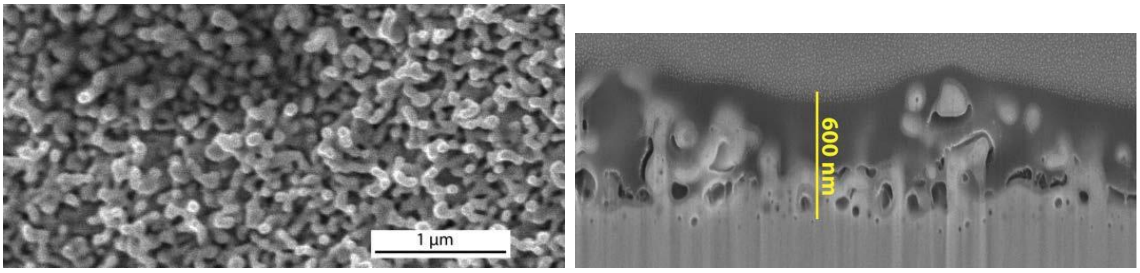

Figure 1.1: Example tokamak plasma damage to tungsten surfaces. Helium plasmas in Alcator C-Mod were operated with reduced flux expansion in the divertor and the strike point moved to contact a tungsten Langmuir probe. The probe was exposed to 30—40MW heat flux for about 22 s[25].

1.3 Coupling between Transport and Material Survivability

At first glance the issues of turbulent transport and material survivability appear unrelated; one is a plasma physics issue, the other a plasma-materials interaction issue. Nevertheless, the two issues are coupled. On the one hand, plasma-material interactions with the first wall set the boundary condition for the plasma. Moreover, transport due to core ITG turbulence increases quickly once the nonlinear critical gradient in ion temperature has been exceeded. As a result of this transport stiffness, the edge ion temperature practically dictates the maximum attainable core temperature. Recent studies of ETG suggest similar profile stiffness in some parameter regimes. Although stabilizing mechanisms such as $\mathbf{E} \times \mathbf{B}$ shear and negative magnetic shear can increase the nonlinear critical gradient, for ITG and ETG respectively, once exceeded the transport remains stiff.

Experiments and theory have consistently demonstrated that increased edge temperature leads to improved energy confinement. Similarly, experiments have shown the importance of controlling plasma-material interactions in order to obtain good plasma performance. Conditioning the wall is necessary in order to prevent plasma-wall interactions from releasing hydrogenic ions or impurities and thereby polluting the plasma. High-temperature bake-out and glow-discharge cleaning are used in order to remove hydrogen and impurities from

the wall and pump them out[21]. On TFTR, the high-performance super-shot regime was accessible only after conditioning to remove deuterium from the limiter[27], and plasma performance was further improved by reducing the carbon influx[28]. TFTR experiments also demonstrated that deposition of a few mg of lithium on the limiter resulted in steep density profiles[29], and a substantial reduction in the ion thermal diffusivity leading to longer energy confinement times and up to a factor of 64× increase in the fusion triple product[29]. Many other experiments have achieved improved performance after coating plasma-facing surfaces with boron[21]. Finally, even the discovery of the high-confinement mode (H-mode) was directly related to a divertor geometry which isolated the plasma core from the wall, and the regime could not be accessed when run in a limiter configuration[8]. TFTR, a limited machine, was able to transition to H-mode, but only with much more neutral beam heating: 11 MW of neutral beam heating for each MA of plasma current[30]. In contrast, the diverted ASDEX machine was able to transition to H-mode using 6.3 MW of neutral beam heating for each MA of plasma current (1.9 MW heating, 0.3 MA plasma current)[8].

At the same time, the core transport is directly related to the problem of material survivability. To maintain a confined plasma in steady-state with a total stored energy W and energy confinement time τ_E, the following heating power (whether supplied externally from Joule heating, neutral beams, or RF waves, or internally from fusion alpha particles) is needed:

$$P = \frac{W}{\tau_E}. \tag{1.9}$$

This power must be exhausted onto a material surface. If a diverted configuration is used, the area will be $A \approx 2\pi R_0 L_q$, where R_0 (a) is the plasma major (minor) radius and L_q is the heat-flux scale length. Using $\tau_E = a^2/\chi_{\text{eff}}$, the heat flux to the plasma-facing material is

$$q = \frac{W\chi_{\text{eff}}}{2\pi R_0 a^2 L_q}. \tag{1.10}$$

This power is exhausted to the first wall either via plasma particle flux, charge exchange, or optical radiation. Therefore, for a given stored energy and plasma size, the heat flux to the PFC scales as the core thermal diffusivity. Therefore improvement in the core confinement (reduced χ_{eff}) will reduce the steady-state heat flux in the divertor. Alternatively, the size of the reactor could be reduced. It is also interesting to note the inverse dependence on the heat-flux scale length. Enhanced perpendicular diffusion in the scrape-off-layer is desirable therefore, in order to broaden the heat-flux profile.

1.3.1 Wall Recycling as a Powerful Control Knob

In typical MFE experiments, when a hydrogen ion diffuses out of the plasma and strikes a material surface, it is neutralized and re-enters the main plasma. Despite experimental evidence for the performance benefit of reduced hydrogenic and impurity fluxes from the plasma-facing materials, most fusion experiments remain dominated by fueling from cold neutrals sourced from the wall. Particles in the core diffuse to the wall, deposit their energy to the wall, and are "recycled" back into the core. The plate recycling coefficient is defined as the ratio of the flux out of the PFC to the flux into the PFC:

$$R_p \doteq \frac{\Gamma_{wall-SOL}}{\Gamma_{SOL-wall}}. \tag{1.11}$$

With this definition, the recycled flux includes back-scattering and reflection of particles that retain a significant fraction of their incident energy as well as particles which are desorbed at low energies. In general, the plate recycling can vary spatially across the plasma-facing-surfaces due to differences in materials, non-uniform surface conditioning, and non-uniform interaction with the plasma. Surfaces in a steady-state sorption equilibrium will have $R_p \approx 1$ resulting in a large, uncontrolled recycled flux from the wall. In this light, an optimal plasma-facing material must not only be able to withstand high temperature fluxes, but should also be able to reduce particle recycling by retaining incident plasma ions. In order to maintain

pumping capability over many discharges (or in steady-state) and to keep tritium retention to safe levels, efficient methods must also exist to desorb entrained hydrogen.

To further elucidate the relationship between recycling, the effective particle confinement time, and the plasma temperature near the wall, a 0-D model can be used. For simplicity, R_p is taken to be the surface average plate recycling. First, consider expressions for the total particle and energy balance, neglecting radiation:

$$\frac{dN_{total}}{dt} = \Gamma_g + \Gamma_{wall-SOL} - \Gamma_{SOL-wall} \tag{1.12a}$$

$$= \Gamma_g + \Gamma_{wall-SOL}\left(1 - \frac{1}{R_p}\right) \tag{1.12b}$$

$$\frac{dU_{total}}{dt} = P - q_a \tag{1.12c}$$

$$q_a \doteq \gamma_{wall}\Gamma_{SOL-wall}T_{wall}. \tag{1.12d}$$

Here, Γ_g is the (controllable) external fueling (from gas puffs, neutral beams, pellets) P is the total heating (external and fusion), q_a is the heat flux to the wall, T_{wall} is the temperature of the plasma in contact with the wall, and γ_{wall} is the total heat transmission factor from the SOL plasma to the wall. The expressions have been summed over all plasma species, and integrated over the entire plasma volume. Note that the heat flux to the wall (eq. 1.12d) is the same boundary condition used in refs.[31,32,33]. Now consider the particle and energy balance in the confined (core) plasma:

$$\frac{dN_{core}}{dt} = \eta_g\Gamma_g + \Gamma^R_{SOL-core} - \Gamma_{core-SOL} \tag{1.13a}$$

$$= \eta_g\Gamma_g + \eta_R\Gamma_{wall-SOL} - \Gamma_{core-SOL} \tag{1.13b}$$

$$\frac{dU_{core}}{dt} = \eta_P P - q_{LCFS} \tag{1.13c}$$

$$q_{LCFS} \doteq \gamma_{LCFS}\Gamma_{core-SOL}T_{LCFS} \tag{1.13d}$$

Here η_g is the efficiency of external fueling at supplying neutrals to the core. All injected neutrals are assumed to be ionized, with fraction η_g ionized in the core, while η_R is the corresponding (surface-averaged) efficiency of recycled neutrals to be ionized in the core. γ_{LCFS} is the total heat transmission coefficient $\gamma = \gamma_e + \gamma_i$ from the confined plasma to the SOL and is dependent on the cross-field transport processes in the edge plasma; typically γ ~6–8[34]. By analogy with the plate recycling coefficient (eq. 1.10), the core recycling coefficient is defined as:

$$R_{core} \doteq \frac{\Gamma^R_{SOL-core}}{\Gamma_{core-SOL}} = \frac{\eta_R R_p \Gamma_{SOL-wall}}{\Gamma_{core-SOL}}. \tag{1.14}$$

Lastly, particle and energy balance in the SOL can be modeled as:

$$\frac{dN_{SOL}}{dt} = (1-\eta_g)\,\Gamma_g + (1-\eta_R)\,\Gamma_{wall-SOL} + \Gamma_{core-SOL} - \Gamma_{SOL-wall} \tag{1.15a}$$

$$\frac{dU_{SOL}}{dt} = (1-\eta_P)\,P + q_{LCFS} - q_a \tag{1.15b}$$

Particle Confinement and Density Decay Times

The flux of particles out of the core and into the SOL can be expressed as:

$$\Gamma_{core-SOL} = \frac{N_{core}}{\tau_p}. \tag{1.16}$$

where τ_p is the confinement time of particles in the confined region and is determined by the micro-turbulent and collisional transport physics in the core. Using the definition of R_{core} (1.14), the core particle balance can be re-written:

$$\frac{dN_{core}}{dt} = \eta_g \Gamma_g - \frac{N_{core}}{\tau_p}\,(1 - R_{core})\,. \tag{1.17}$$

If all external fueling is removed, the core density will decay exponentially with an e-folding time of:

$$\tau_p^* \doteq -\frac{N_{core}}{dN_{core}/dt} = \frac{\tau_p}{1 - R_{core}}. \tag{1.18}$$

It is important to realize that τ_p is determined by particle transport in the plasma core. In contrast, R_{core} is determined by the plasma-material interactions (which determine R_p directly), and the parameters of the SOL which determine the average efficiency η_R of fueling by recycling.

Implications for Steady-State

Steady-state solutions to the expressions derived previously illustrate the relationship between the temperature of the plasma near the wall and at the last closed-flux-surface, and recycling, fueling efficiency, and scrape-off-layer transport. A steady-state condition for the total energy and number of particles requires:

$$\Gamma_{SOL-wall} = \frac{\Gamma_g}{1 - R_p} \tag{1.19a}$$

$$T_{wall} = \frac{P\,(1 - R_p)}{\gamma_{wall}\Gamma_g}. \tag{1.19b}$$

To satisfy steady-state in the core:

$$\Gamma_g = \frac{\Gamma_{core-SOL}}{\eta_g}\left[\frac{1 - R_p}{1 - R_p\,(1 - \eta_R/\eta_g)}\right] \tag{1.20a}$$

$$T_{LCFS} = \frac{\eta_P P}{\gamma_{LCFS}\Gamma_{core-SOL}}. \tag{1.20b}$$

Using eq. 1.16, gives final expressions for the required external fueling, and the plasma temperatures at the wall and LCFS:

$$\Gamma_g = \frac{N_{core}}{\tau_p \eta_g} \left[\frac{1 - R_p}{1 - R_p \left(1 - \eta_R / \eta_g\right)} \right] \tag{1.21}$$

$$T_{wall} = \frac{P \tau_p \eta_g (1 - R_p)}{\gamma_{wall} N_{core}} \left[1 - R_p \left(1 - \frac{\eta_R}{\eta_g} \right) \right] \tag{1.22}$$

$$T_{LCFS} = \frac{\eta_P P \tau_p}{\gamma_{LCFS} N_{core}}. \tag{1.23}$$

Plots of required external fueling (eq. 1.21) and plasma temperature near the wall vs. R_p (eq. 1.22) are shown in fig. 1.2a and fig. 1.2b, respectively. The first plot illustrates the increased external fueling requirement with reduced recycling. It also illustrates that the fueling required to maintain a constant core particle content N_{core} can be a test of the recycling, with increased sensitivity for lower external fueling efficiency. Fig. 1.2b illustrates that to maximize the plasma temperature at the wall for a given external power input, the external fueling efficiency should be maximized and the average plate recycling minimized, the SOL-wall heat transmission factor be minimized, and the core particle confinement time be maximized the SOL minimized. Only the latter is determined by core transport physics. Maximizing the plasma temperature at the LCFS (i.e., near the outboard mid-plane) requires in addition that the heating efficiency be maximized and the heat transmission factor for the core-SOL plasma be minimized.

The very simple model above illustrates that recycling suppresses the edge temperature by diluting the edge plasma with low-temperature particles recycled from the wall. Therefore, if a hot plasma core is achieved by strong heating, a large temperature gradient exists across the plasma. Unfortunately, temperature gradients provide a free energy source to drive numerous instabilities including those mentioned in 1.1. Also, if recycling is the dominant fueling mechanism, then the density profile becomes difficult (or impossible) to control; as

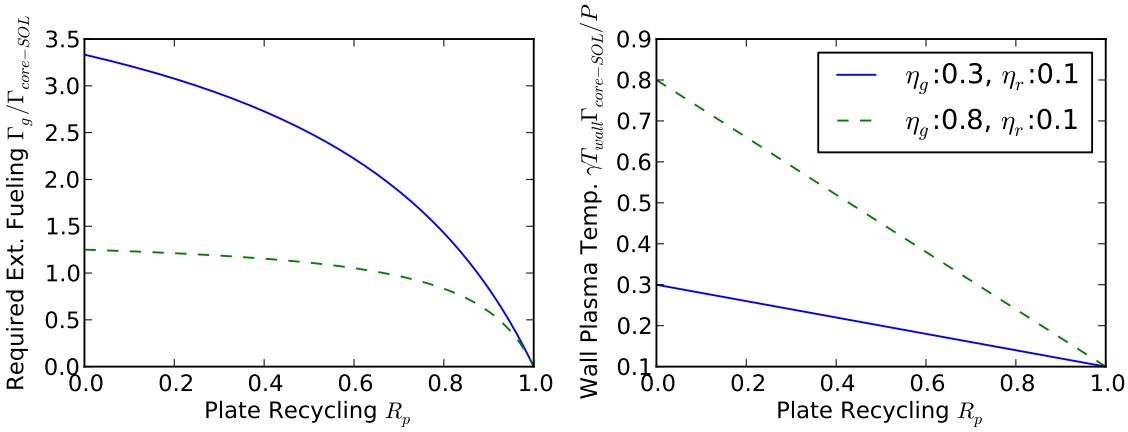

(a) (b)

Figure 1.2: Plots of the dependence of (a) required external fueling (eq. 1.21) and (b) plasma temperature near the wall (eq. 1.22) on plate recycling for both high $\eta_g = 0.8$ and moderate $\eta_g = 0.3$ external fueling efficiencies.

a case in point, NSTX discharges without lithium wall conditioning are characterized by an uncontrollable density rise throughout the discharge[35]. In order to attain some density control, strong cryo-pumping can be employed as on DIII-D[36,37]; however, recycling typically remains close to unity[37]. Alternatively, an optimal plasma-facing material can be selected which can not only withstand high heat fluxes, but can also reduce particle recycling by binding incident plasma ions. Note, however, that in order to maintain pumping capability over many discharges (or in steady-state) and to minimize tritium retention to safe levels, efficient methods must be used to desorb entrained plasma particles.

1.4 A Potential Solution to the Plasma-Material and Transport Problems

An alternative approach to overcome the issues with solid plasma-facing materials discussed in 1.2.3 would be to employ a liquid first wall. A constantly renewed liquid PFC would have the intrinsic advantages of being self-healing, having the potential to distribute localized head loads through convection, and allowing the flow rate to be chosen to limit material loss

from evaporation or sputtering. Slow-flowing films would protect the underlying material from plasma damage allowing thinner layers of underlying material and faster heat transfer to a coolant. Alternatively, fast flows could remove heat with the liquid itself. By protecting substrate materials from plasma-material interactions, liquid PFCs allow the substrate materials to be optimized for resilience to neutron damage, thermoconduction, structural integrity, and other bulk material requirements.

Potential liquid PFCs include lithium, tin, gallium, and a 80/20 tin/lithium eutectic. Of these, lithium has a relatively high vapor pressure (10^{-7} torr at 400 °C) and therefore a higher evaporation rate; however, its much lower atomic number permits a higher concentration to accumulate in the plasma before radiation losses become significant. Being liquid metals and electrically conductive, these liquids are subject to magneto-hydrodynamic (MHD) forces which could be used to create fast-flowing jets[38], but can also lead to significant ingestion and disruption of the plasma if not properly controlled[39]. Although recent work with slow flowing capillary-pore systems shows good adhesion of the lithium to the substrate even during a disruption[40], present usage of liquid metals in plasma devices tend to focus on thin static coatings since the short discharges of present experiments (compared with a reactor) is compatible with between shot replenishment of the liquid.

Liquid lithium has also shown its ability to rapidly distribute intense localized heat loads of about 60 MW/m^2 through temperature-gradient-driven convection[41,42]. This capability would reduce the possibility that an ELM or other localized transient event would cause evaporation of a small spot and damage the underlying material. As an interesting and related aside, experiments on NSTX have shown that evaporative lithium deposition between shots reduces the occurrence of large ELMs in the first place[35]. At modest flow rates generated perhaps by thermo-capillary or thermo-electric MHD[43], liquid lithium could remove large steady-state heat fluxes from a reactor.

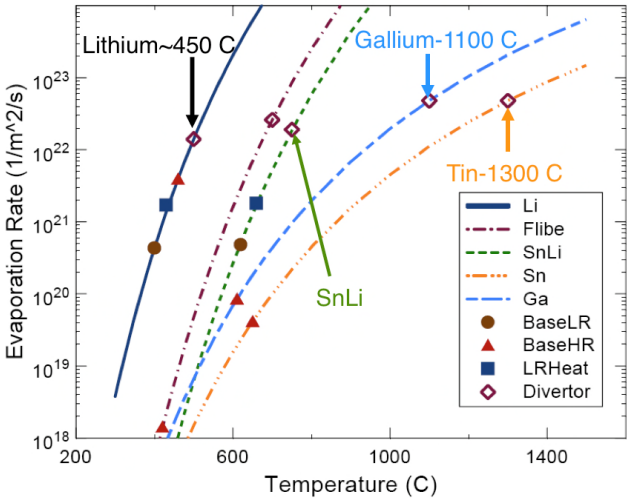

Figure 1.3: Evaporation rates for candidate liquid metal PFCs. Higher fluxes are permissible from the divertor because the divertor plasma can be more isolated from the core. For wall PFCs, temperature limits also differ depending on whether a high-recycling ($T \lesssim 20$ eV, high density) or low-recycling (higher temperature, lower density) scrape-off-layer is desired because of the dependence of sputtering yield on the energy of incident ions. Figure taken from ref. 23.

1.4.1 Lithium can Provide a Low-Recycling Boundary

Chemical compatibility with each of the liquid metals mentioned previously constrains the choice of substrate materials and, in practice, all materials within the vacuum vessel; however, chemical activity can be beneficial. As a plasma-facing material, liquid lithium has the advantageous property of absorbing nearly all incident hydrogenic species, and retaining the hydride formed in solution[44] via the following reactions:

$$\mathrm{Li} + \mathrm{H}^+ + \mathrm{e}^- \rightarrow \mathrm{LiH} \tag{1.24a}$$

$$\mathrm{Li} + \mathrm{H} \rightarrow \mathrm{LiH} \tag{1.24b}$$

$$2\mathrm{Li} + \mathrm{H}_2 \rightarrow 2\mathrm{LiH}. \tag{1.24c}$$

Note that the last reaction is substantially slower. Surface science experiments have shown that deuterium is retained in solution until nearly all the bulk liquid has been converted to

lithium deuteride[44]. Therefore, lithium can provide a low-recycling boundary and therefore reduced plasma densities and perhaps higher plasma temperatures in the scrape-off-layer. Particles entrained in the liquid lithium can be desorbed by heating to about 400 °C [44],

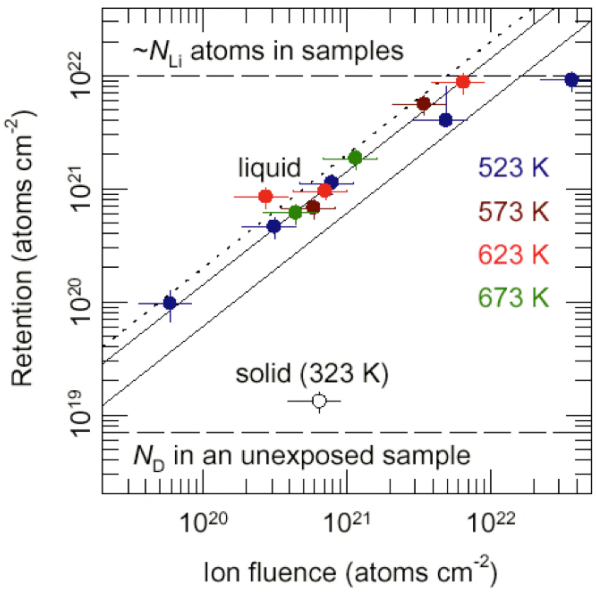

Figure 1.4: Deterium retention vs. plasma ion fluence, with the solid line indicating full retention of ions, the dotted line an estimate of the total ion + atom fluence. Figure from ref. 44, 23.

providing a mechanism for tritium removal. Thin coatings of solid Li have also been found to retain hydrogen ions up to a 1:1 ratio as well[45]; however, figure 1.4 shows thicker coatings of solid Li to be much less effective, suggesting only the top few monolayers to be important[44]. Note however, that calculation of the lithium thickness must account for intercalation with the substrate, which is significant on graphite and sprayed coatings of refractory metals[46]. Liquid gallium and tin do not appear to retain hydrogen to nearly the same degree[47], but the pumping capability of lithium-tin is not fully known[47,46].

1.4.2 Hydrogen Reflection from Lithium

In the absence of hydrogen desorption, hard-sphere (direct) reflection places a lower limit on the recycling coefficient. Figure 1.5 shows plots of the particle reflection coefficient and energy reflection coefficients at normal incidence for D^+ on Li, C, O, Mo, and W using equations 1 and 2 and parameters from Table 1 of ref. 48. Note that because of the mass dependence, the particle reflection coefficient for H on Li is substantially greater than that for D on Li at the lowest energies (Li 40% vs. 30%). These calculations are for normal incidence only. For oblique incidence, measurements of D^+ incident at 45° show more than a doubling in the reflection coefficient (at 100 eV, to 20%)[49]. In either case, the reflected D can retain 20–30% of its incident energy.

1.4.3 Impurity Reactions with Lithium

The preceding discussion of hydrogenic recycling and reflection from lithium surfaces has tacitly assumed a pure lithium surface, which can be obtained in UHV conditions of controlled surface science experiments having a base pressure and partial pressure of water $< 10^{-9}$ torr. Vacuum conditions in fusion experiments are typically an order of magnitude (or more) higher. The high chemical activity of lithium (and especially liquid lithium) binds to residual gasses in the vacuum vessel and oxide layers on substrate materials, improving vacuum conditions for plasma operations. Important reactions of lithium with background gasses include[50]:

$$4\mathrm{Li} + \mathrm{O_2} \rightarrow 2\mathrm{LiO_2} \tag{1.25a}$$

$$2\mathrm{Li} + \mathrm{O_2} \rightarrow \mathrm{Li_2O_2} \tag{1.25b}$$

$$6\mathrm{Li} + \mathrm{N_2} \rightarrow 2\mathrm{Li_3N} \tag{1.25c}$$

$$2\mathrm{Li} + 2\mathrm{H_2O} \rightarrow 2\mathrm{LiOH} + \mathrm{H_2}. \tag{1.25d}$$

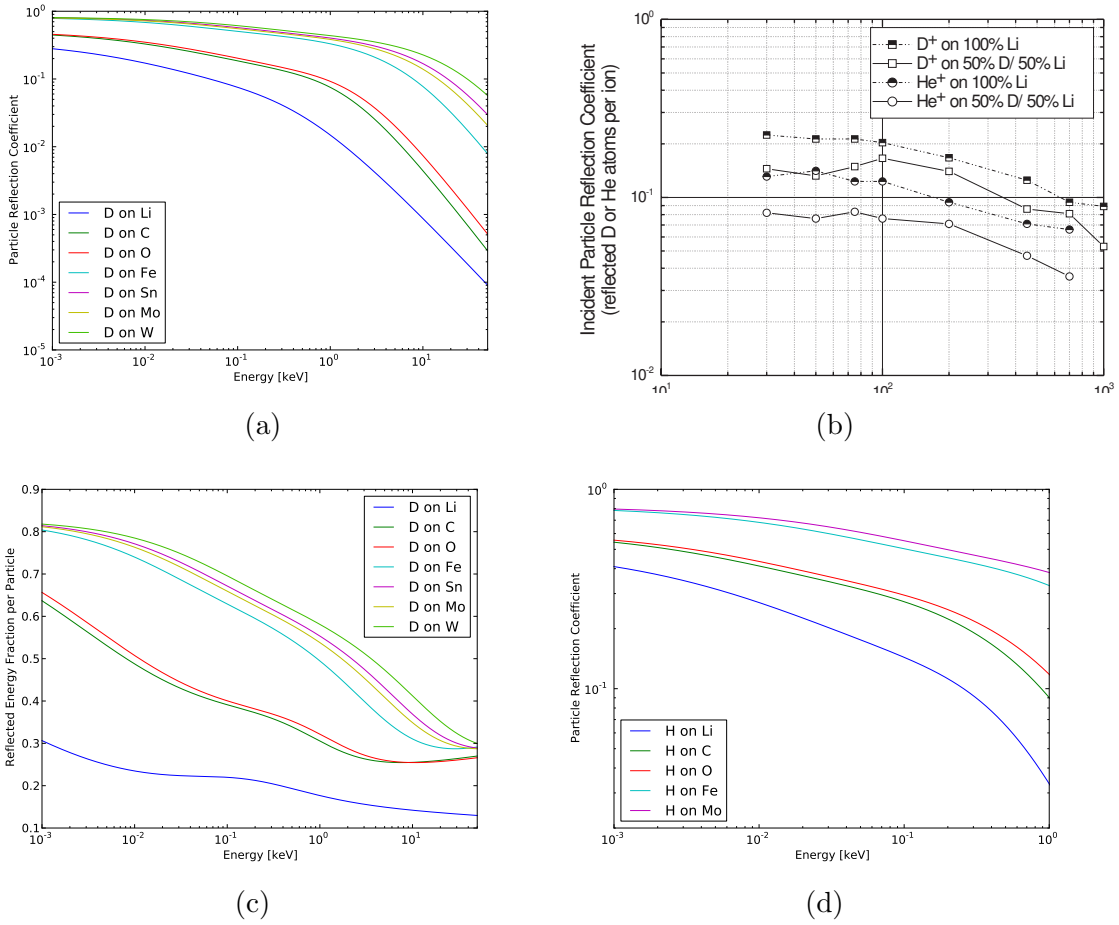

Figure 1.5: Particle and energy reflection coefficients for incident D^+ a reactor, and for LTX which is currently operating with hydrogen rather than deuterium. Figs. a, c, and d are computed from equations 1-2 and parameters from table 1 of ref. 48, while fig. b is from ref. 49.

Since water vapor is often the largest residual gas in a fusion experiments, the last reaction is particularly noticeable when comparing residual gas analyzer traces before and after lithium is introduced into the vacuum environment. Surface science experiments have shown that lithium is an excellent pump for oxygen (fig. 1.6, consistent with eq. 1.24a.

On the other hand, these interactions will likely create a dynamically evolving mixed material surface state which will likely show different hydrogen retention and reflection properties than discussed in the previous sections. The chemical composition over the deuteron penetration distance (10s of nm) will have the greatest effect. Interestingly, recent simulations[51] and laboratory experiments[46]of lithium on graphite have shown that in fact oxygen is primarily responsible for binding hydrogen, and hydrogen is retained efficiently in lithium because lithium acts as a catalyst to bring sufficient oxygen to the surface during irradiation with hydrogen atoms[46]. Alternatively, experiments with lithium on stainless-steel have shown that an electron beam can be used both to liquefy and stir the lithium, providing a fresh, low-recycling lithium surface[41,52].

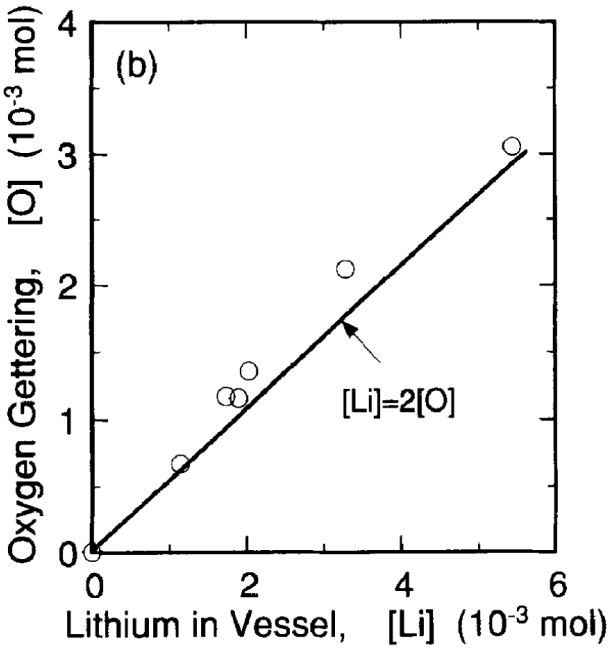

Figure 1.6: Lithium acts as a strong pump for oxygen, consistent with the formation of lithium oxide (Li_2O). Figure from[45].

1.4.4 Lithium Impurity Injection Mechanisms

Macroscopic injection of lithium due to MHD forces was discussed briefly in sec. 1.4. The interested reader is encouraged to consult refs.[39,38,40] and[53]. The principal microscopic mechanisms for lithium injection into the plasma are evaporation, sputtering from incident hydrogenic ions, and lithium-lithium self-sputtering. The lithium evaporation rate is given by[45]:

$$\Gamma_{evap} = 4.37 \times 10^{-3} p_{sat} \sqrt{M/T} \tag{1.26}$$

$$\log_{10}(p_{sat}) = 9.7641 - 5802.7/T - 1.174 \log_{10} T \tag{1.27}$$

with $M = 6.941$ amu and temperature is in Kelvin.

Contamination of the plasma from sputtered lithium is expected to be minimal, because about 2/3 of of the sputtered lithium flux is ionized[49,54] and would therefore be accelerated back to the surface by an electron sheath. Secondly, sputtered or evaporated neutral lithium also has a low first ionization energy (5.4 eV), so neutral lithium cannot diffuse far into the plasma before being ionized, its cross-field diffusion impeded by the magnetic field, and its parallel diffusion impeded by friction with the scrape-off-layer plasma flowing towards the limiting material surface. Finally, lithium has a low ionization energy for full ionization (122 eV) so would not contribute significantly to line radiation power loss in the core of a fusion reactor.

The sputtering yield of D^+ incident on non-deuterium-saturated solid lithium is about 0.6–0.7[49]. Unexpectedly, the erosion yield of liquid lithium from a variety of incident ions was found to exceed the combination of physical sputtering and evaporation and depends linearly on the incident ion flux[55,56]. A model was developed to explain this effect and predict the energy and angular dependence of sputtered particles as a function of lithium temperature[57]. A characteristic feature of the temperature-dependent erosion measurements

is a shift in the sputtered particle distributions to lower energies.[57]. Total (neutral + ion) sputtering yields can exceed unity at sufficient temperature and incident particle energy; however the net yield can be approximately half this value[58] because of prompt re-deposition of sputtered ions. Fusion experiments employing solid evaporative coatings typically have minimal lithium concentration in the core. In NSTX, 0.1% is a typical value[59], while even with a keV-temperature edge plasma, the core lithium concentration in TFTR was only 0.5%[60].

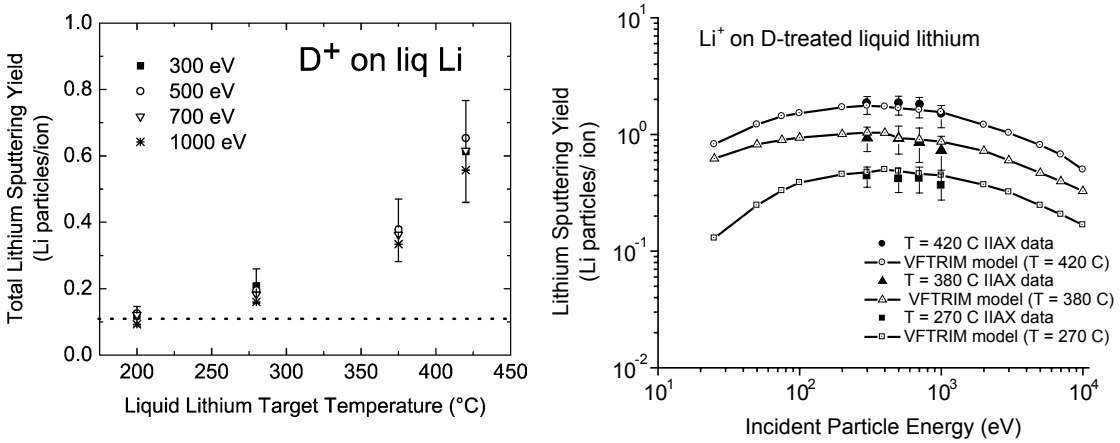

(a) (b)

Figure 1.7: Measurements of liquid lithium sputtering yields for (a) deuterium and (b) lithium ions incident at 45deg. Figures are from ref. 54 and 58.

1.4.5 Electron Emission from a Lithium Surface

In some way analogous to recycling of fuel ions and sputtering from PFCs, secondary electron emission from PFCs provides a "recycled" electron flux from the PFC. Secondary electron emission comes in two forms, electron induced and ion induced, and the latter has two processes, kinetic and potential emission. Kinetic emission occurs via the transfer of kinetic energy from an incident particle to bound electrons in a target. This process only occurs above an energy threshold because of the energy necessary for collisional excitation of the electron, transport to the surface, and penetration through the surface potential barrier[61].

Potential emission occurs when an incident ion approaches a target and a bound electron is accelerated by the potential well of the incident ion, filling a vacancy. As in the Auger process, the released energy may be transferred to another bound electron in the target and escape from the target surface[61]. For this process to occur, the energy released by neutralizing the incident ion must be at least twice the work function of the target surface[62]. All of these processes are sensitive to surface non-uniformities and impurities, so measurements on flat, clean, and pure materials under UHV conditions may differ significantly from performance in fusion experiments[61].

Pure lithium has the lowest electron-induced secondary electron emission coefficient of any material, having a maximum value of 0.5 at 85 eV for normal incidence (fig. 1.8a)[63,64]. Oblique incidence primarily shifts the peak to higher primary energies, while the effect of a magnetic field is unknown[23]. Liquid targets are expected to behave similarly to flat materials[23], although as mentioned previously, the surface composition is likely very important.

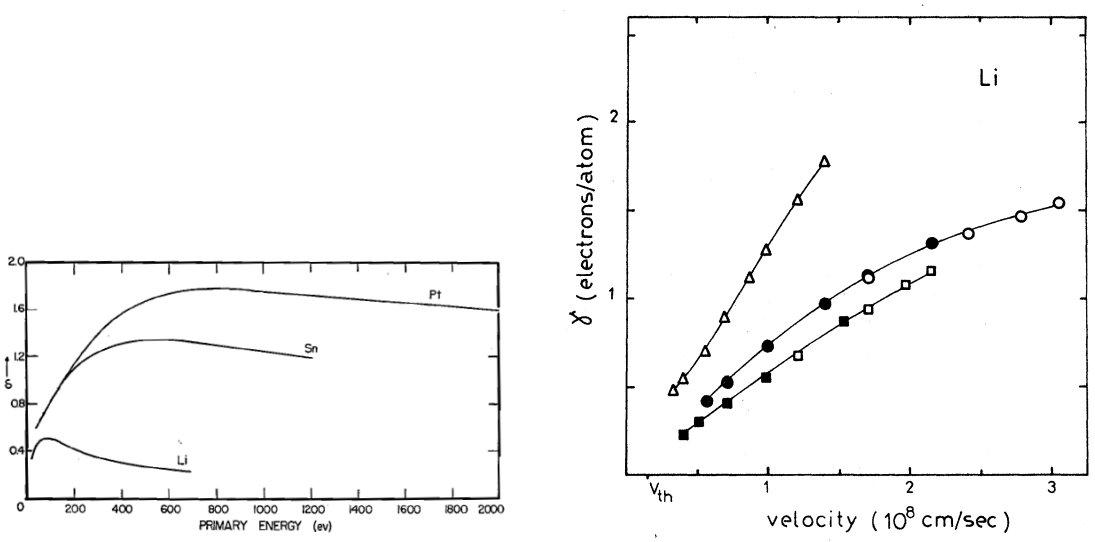

(a) (b)

Figure 1.8: (a) Electron-induced and (b) ion-induced secondary-electron-emission coefficient for (a) various metals and (b) lithium. In fig. b, empty (filled) circles correspond to $H^+(D^+)$, empty(filled) squares to $H_2^+(D_2^+)$, and triangles to He^+. The threshold velocity $v_{th} = 1.7 \times 10^7$ cm/s (150 eV for H^+). Fig. a is from ref. 63, 64, and (b) is from ref. 62.

Electron emission from hydrogenic ions, molecular hydrogenic ions and He^+ incident on Li was examined in ref. 62, but only at high velocities of the incident ion (> 2.5 keV for H^2). Eq. 2 from ref. 62 provides an expression for the threshold velocity for kinetic emission:

$$v_{thr} = \frac{1}{2} v_F \left[\sqrt{1 + 2\frac{\phi_w}{m_e v_F^2}} - 1 \right]. \tag{1.28}$$

For lithium, the work function $\phi_w = 2.9$ eV and the Fermi energy and velocities are $E_F = 4.74$ eV and $v_F = 1.29 \times 10^8$ cm/s[65], giving a threshold velocity of 1.7×10^7 cm/s (150 eV for H^+). Kinetic emission increases for incident velocities and is fit by a semi-empirical expression for the total ion-induced secondary electron emission[61]:

$$\gamma = \gamma_p + \gamma_k = \gamma_p + \Lambda S_e(E) g\,(E_{th}/E) \tag{1.29}$$

$$\gamma \approx \gamma_p + C\sqrt{E}\,(1 - E_{th}/E)^2\,\Theta(E - E_{th}). \tag{1.30}$$

In the above expression Θ is the Heaviside step function ($\Theta(x) = 0$ for $x < 0$, $\Theta(x) = 1$ for $x > 0$). The fit coefficient for lithium was not evaluated in this work. Since lithium has the lowest work function of any element, the potential emission process is significant. Eq. 17 in ref. 66 gives an estimate for the potential emission coefficient:

$$\gamma_p \approx \frac{0.2}{E_F}\,(0.8E_i - 2\phi_w)\,. \tag{1.31}$$

Here, E_i corresponds to the ionization energy for the incident particle and is claimed to be valid in the range $3\phi_w < E_i < 2(E_F + \phi_w)$, which includes hydrogenic ions. The computed value using this expression $\gamma_p = 0.2$ is consistent with the measurements near v_{th} in ref. 62. Note that for tungsten, this expression gives $\gamma_p = 0.079$, a value about 2.5× lower.

Assuming equal fluxes of ions and electrons to a surface with incident energy $\lesssim 140$ eV, the sum of the electron-induced and ion-induced secondary electron emission coefficients

should be $\lesssim$0.8, which is still low relative to other elements. The photoelectric effect may be another important source of electron emission from lithium[67], especially since visible photons with energy above ϕ_w=2.9 eV (430 nm) may contribute. Finally, it is important to emphasize that the strong dependence on surface composition and topology for each of these effects makes it difficult to accurately predict electron emission from lithium in a fusion environment.

1.4.6 Residual Transport in the Low-Recycling Regime

In the theoretical limit of zero recycling from the wall, information (in the form of fuel particles, impurity particles and electrons) does not propagate from the wall to the edge plasma. Without these boundary cooling channels, the edge plasma is completely decoupled from the wall and could have a temperature equal to (or even greater than) the plasma core. Assuming a fixed plasma temperature near the wall is therefore an inaccurate boundary condition; rather, a heat flux boundary condition should be used.

The boundary condition in eq. 1.12d was employed by ref. 31, along with a model of neoclassical and temperature-gradient-driven turbulent thermal transport in the core, to examine the effect of zero wall recycling on the performance of magnetic fusion devices. They found low recycling led to many improvements, including an elevated plasma temperature at the wall, minimal transport from temperature-gradient-driven instabilities, and the full plasma volume contributing to fusion power. In addition, a flattened current profile enabled access to higher plasma β[31,32,33]. Finally, a low-recycling wall material would allow placement of conductive structures near the plasma last closed-flux-surface, eliminating free-boundary MHD instabilities due to conductive wall stabilization[32,33].

In another work, a perfectly isothermal tokamak was examined, and an exact solution for the equilibrium was found containing rigid-body toroidal rotation, a density profile depending exponentially on the poloidal flux, and very low thermal transport[68]. Without temperature-

gradient-driven instabilities (ITG, ETG, micro-tearing modes), remaining transport mechanisms include TEM drift-wave turbulence driven by the density gradient, parallel transport along wandering field lines or around magnetic islands, and neoclassical collisional transport. Of course the idealized zero-recycling limit with complete decoupling of the wall is impossible to achieve because of finite reflection, sputtering, and electron emission; nevertheless simple models of these cooling channels (such as described in sec. 1.3.1) motivates more detailed study of transport mechanisms that may dominate in the very low-recycling regime.

Few investigations exist of micro-turbulent transport relevant for plasmas with low-recycling and core fueling. While much numerical simulation of plasma micro-instabilities has been done for situations where the electron or ion temperature gradient provides the dominant source of free energy, relatively little attention has been paid to systems with weak temperature gradients and a stronger density gradient. One work used a nonlinear gyro-kinetic code to examine the destabilization of TEMs inside internal transport barriers (ITB) in Alcator C-mod experiments[69,70]. Peaked density and relatively flat temperature profiles were developed within the ITB over the course of the discharge, and on-axis ion cyclotron heating was used to terminate density buildup in the core and prevent radiative collapse. This work found toroidal ITG modes were suppressed inside the barrier, while the crossing of the TEM linear stability boundary was nearly coincident with the density gradient reaching steady-state. The authors found a nonlinear up-shift of the critical density gradient (analogous to the nonlinear critical temperature gradient up-shift seen with the toroidal ITG instability[71]) and a simulated turbulent particle diffusivity which matched experimental values inferred from particle balance within experimental uncertainty. The simulated turbulent diffusivity increased with temperature, explaining how on-axis heating could function as a control mechanism. Subsequent work on Alcator C-Mod found excellent agreement between wavelength spectra from nonlinear gyro-kinetic simulations and spectra measured by vertical phase contrast imaging[72].

More recent work has further explored the parametric dependence of transport and zonal flows on the electron density and temperature gradients[73], and on the ratio of ion to electron temperatures[74,75,76]. A study of a low-recycling ignited spherical tokamak predicted an absolute minimum magnetic well could be established in the plasma[33] configuration. If achieved, the trapped particle precession would reverse direction, potentially eliminating the resonant drive for certain trapped electron modes[77,2]. To evaluate the performance of magnetic fusion devices which combine low-recycling walls with core fueling, it is essential to determine the role of micro-instabilities in enhancing the particle and electron thermal transport. This is particularly crucial in order to extrapolate the performance of small devices (with low to moderate T) to reactor-scale devices with much higher T. Since $\chi_{gB} \propto T^{3/2}$ while $\chi_{neo} \propto T^{-1/2}$, a small component of turbulent in a $T_e \sim 1$ keV plasma may be amplified $400\times$ over the neoclassical prediction in a $T_e \sim 20$ keV reactor.

1.5 Thesis Overview

The objectives of this thesis are two-fold. The first goal is to explore computationally and theoretically the physics of core particle and thermal transport for profiles that would be expected if core fueling dominates over wall recycling. In this regime, an elevated edge temperature leads to a flattened temperature profile. Meanwhile, particle pumping at the wall leads to a stronger density gradient. Although other studies have explored some aspects of TEM particle and thermal transport, this thesis addresses several specific questions for how the micro-turbulent transport might change. How does the linear critical gradient vary with the ratio of temperature gradient to density gradient? If $\eta \lesssim 1$, and the critical pressure gradient is exceeded, is the transport stiff? Is thermal transport dominated by convection or conduction in this situation? How does impurity transport change? These questions are the focus of chapter 3.

The second goal of this thesis is to measure the limit of low-recycling that can be achieved in a small tokamak using evaporatively-deposited solid lithium coatings. The experimental device, diagnostics, fueling systems, and lithium application are discussed in chapter 2. Several diagnostics were developed, substantially improved, or calibrated as part of this work. Measurements of effective particle confinement time, cumulative recycling, hydrogen line emission, and impurity emission are presented for plasmas with evaporatively-deposited solid lithium coatings in chapter 4. These measurements indicate that different recycling conditions can exist even among discharges that achieve comparably high plasma currents. In addition, measurements of impurity emission indicate differences in impurity content between discharges with different recycling conditions.

Chapter 5 builds on the measurement results by applying a neutral particle modeling code in order to quantify the plate recycling, core recycling, and recycling fueling efficiency for a subset of these plasmas. In this chapter, an inverse approach to determine the desorbed particle fluxes from the walls is described and applied to study the particle balance in a number of discharges.

Finally, chapter 6 summarizes the key results and suggests research avenues for future work.

Chapter 2

The Lithium Tokamak Experiment

The Lithium Tokamak Experiment (LTX) is a small spherical torus designed to generate tokamak plasmas characterized by the limit of very low wall recycling and to explore stability and transport in this regime. Although the LTX uses the same vacuum vessel and toroidal field coils as its predecessor, the Current Drive Experiment—Upgrade (CDX-U) device, other aspects have been substantially modified: the OH system and several vertical field coils have been upgraded; however, the most notable change is the addition of conducting shell structures inside the vacuum vessel and in close contact with the plasma. When the shells are fully covered with lithium coatings, lithium covers about 85% of the plasma-facing surfaces. Additional details of the LTX design and construction are covered in published papers (refs. 78, 79, 80) and theses (refs. 81, 82).

An overview of the motivation behind the LTX is given in section 2.1.1, followed by a brief description of the design (sec. 2.1.2) and predicted performance (sec. 2.1.3). A description of the diagnostics and fueling systems used in this thesis follow in sec. 2.2. Diagnostics which were developed or substantially enhanced over the course of this work include filterscopes (sec. 2.2.1 and sec. 2.2.5), fast visible cameras (sec. 2.2.3), visible survey spectrometers (sec. 2.2.2), Lyman-α diagnostics (sec. 2.2.4), and a bolometer array (sec. 2.2.6). These

instruments will be described in detail, while others will be described briefly and references will direct the interested reader as to where to find additional information.

2.1 Motivation for the LTX, its Design, and Predicted Performance

2.1.1 LTX Design Motivation

Several experiments have used lithium coatings in order to substantially improve plasma performance. As mentioned briefly in sec. 1.3, the highest high-performance TFTR supershot discharges were obtained after discharge cleaning and coating of the graphite limiter with lithium, in order to reduce carbon influx and hydrogenic recycling. Coatings were applied by injecting lithium pellets into conditioning discharges or during the Ohmic phase of supershot discharges[29]. Particle transport modeling of a lithium conditioned supershot matched the measured D_α emission when a plate recycling coefficient of 0.85 was used, resulting in a core recycling of 0.71[83]. Perturbative lithium pellets or helium gas puffs highlighted the connection between recycling, edge T_i, and energy confinement[84]. These discharges were characterized by strongly peaked density profiles ($2.2 < n_e(0)/\langle n_e \rangle < 3.8$)[29], an energy confinement time that increased linearly with density peakedness[29], and $T_e \gtrsim 1$ keV out to the edge[29]. This last result is consistent with at least partial decoupling of the edge plasma parameters from the wall, as a result of reduced recycling and core fueling described by equation 1.22.

Analysis of well-conditioned (but pre-lithium) supershots found that beam fueling (as opposed to recycling) was the dominant particle source in over half the plasma core[85], and that for $r < a/3$, thermal transport was dominated by convection: $q_i/(\Gamma_i T_i) \sim 3/2$ and $q_e/(\Gamma_e T_e)$ ~2—2.5. Experimental ion thermal transport agreed with the neoclassical prediction for the central core $r/a \lesssim 0.2$, but outside could exceed the neoclassical prediction

by up to 40×[85]. Perturbative transport experiments confirmed the convection dominance in the core for both ion and electron thermal transport[86]. In later D-T experiments, the region where ion thermal transport was dominated by convection extended to $r < a/3$[87]. These experiments suggest that in the region dominated by core fueling (from neutral beams) rather than wall recycling, the resulting plasma profiles were not dominated by transport from temperature-gradient-driven turbulence.

More recently, several other magnetic fusion experiments have used lithium coatings in order to substantially improve plasma performance including T-11M[40], FTU[88], and NSTX[59,89]. The CDX-U fielded a large-area, liquid lithium toroidal limiter as the primary tokamak PFC in combination with full-wall lithium coatings up to 100 Å on the stainless steel vacuum vessel wall[41]. The coatings were applied between shots by liquefying and stirring the lithium with an electron beam so that the lithium temperature was uniformly raised until evaporation readily occurred. Under these conditions, the core recycling was reduced to 70–80%[52]. Reduced recycling yielded a six-fold improvement in the energy confinement time and a 2× enhancement over the ITER98P(y,1) confinement scaling[90] which would otherwise be expected to match the performance of a small spherical tokamak reasonably well.

A reference transport model (RTM), based on the hypothesis that all transport was taking place at the ion neoclassical rate[1], was implemented in the ASTRA-ESC[91] transport-equilibrium and stability codes. Assuming zero energy loss due to recycling from the walls, and varying the external fueling to match the measured plasma β, this model was able to approximately reproduce several measured global parameters in the experiment: the internal inductance, the loop voltage, the global energy confinement time, the central plasma density, and the central electron temperature inferred from Spitzer resistivity[78]. The RTM did not

[1]Note that this model assumes that electron thermal transport and particle diffusion are still anomalous (increased by the square root of the ion/electron mass ratio), but scale with neoclassical rather than drift-wave transport.

approximate well the measured ion temperature, however, which it underestimated by a factor of two.

Unfortunately, CDX-U was not sufficiently diagnosed during its lithium operation to measure core thermal transport profiles and for rigorous comparison to transport models. The experiment lacked direct electron and ion temperature profile measurements, adequate magnetic diagnostics for reliable equilibrium reconstructions, and fluctuation diagnostics to rigorously evaluate the particle and thermal transport. Nevertheless, the tremendous improvement in energy confinement time measured in the CDX-U device with only about 5% (0.2 m^2) of the plasma-facing area covered by liquid lithium[79] raised the question of the performance that can be achieved if nearly all of the plasma-facing surfaces consist of an extremely low-recycling material. The LTX was conceived in order to test this limit while fielding improved profile diagnostics to compare to transport models and improved magnetics diagnostics to study MHD stability.

2.1.2 LTX Device Description

A cutaway of the Pro/Engineer solid model representation of LTX is shown in fig. 2.1. LTX inherits its vacuum vessel from CDX-U. The outer cylinder is 3/8" thick stainless steel, with an outer radius of 70.2 cm. The top and bottom flanges are sealed with vulcanized Viton O-rings to enable high-temperature bake-out or high-temperature operation of the shells. The center-stack contains the OH solenoid and inner legs for the toroidal field coils. The typical toroidal field at a major radius (R) of 40 cm is 1.8 kG, while future connection of water cooling lines will allow 3.5 kG to be achieved.

Four shell quadrants are mounted inside the vacuum vessel to provide a conducting wall conformal to the last closed flux surface of an idealized spherical torus (I_p ~300 kA) equilibrium with major radius (R_0) 40 cm, minor radius (a) 26 cm, elongation (κ) 1.6, and triangularity (δ) 0.4. The motivation for placing a conducting structure in close contact

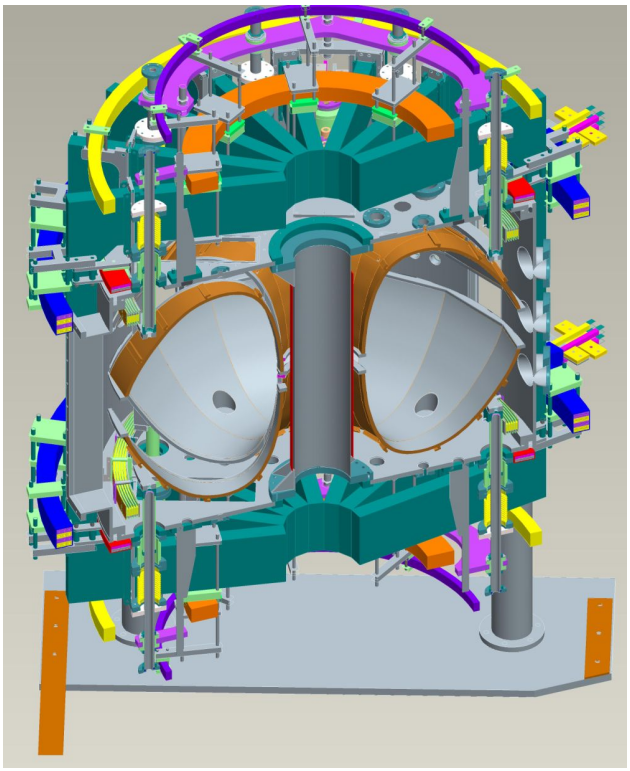

Figure 2.1: Isometric cutaway view of the Pro/Engineer solid model representation of LTX. Lithium coatings are applied to the plasma-facing, stainless steel surface of the four in-vessel shell segments. The copper backing of each segment is fitted with resistive heaters for high-temperature bake-out or to liquefy the deposited lithium coating. Note also the two vertical field coils which are internal to the vacuum vessel to provide fast time response.

with the plasma is to make optimal use of conductive stabilization of MHD instabilities (by minimizing the vacuum gap) in order to access higher plasma β. Two toroidal and two poloidal breaks in the shells prohibit axissymmetric currents from flowing in the shells and enable penetration of the externally applied magnetic fields.

The plasma-facing surface of the shells consists of 1/16" thick 304 stainless-steel explosively-bonded to 3/8" copper backing which can be heated by resistive heaters to $\gtrsim$400 °C [78]. For reference, the chemical composition of the stainless steel plasma-facing surface is shown in table 2.1. The high thermal conductivity of the copper backing enables nearly uniform heating of the each shell, while the stainless steel face protects the copper from exposure to hot lithium. Although close-fitting conducting walls were common during the early days of magnetic fusion research, these discharges tended to suffer from high radiated power losses from high-Z metallic impurities. LTX intends to avoid contamination by metallic impurities and achieve low recycling by applying lithium coatings to the stainless steel shell substrate. When fully coated, lithium coatings constitute 85% of the plasma-facing surfaces. Finally, a set of molybdenum limiters are installed in each of the lower shells near the toroidal gaps in order to define the limiter contact point. Each limiter is composed of two parallel plates spaced to wick liquid lithium to the upper surface which is (nominally) in contact with the plasma. Additional details of the LTX design and construction are covered in published papers[78,79,80] and theses[81,82].

Grade		C	Mn	Si	P	S	Cr	Ni	N
304L	max	0.08	2.0	0.75	0.045	0.030	20.0	10.5	0.10
ER308L/H	min	—	1.0	0.30	0.03	0.03	19.5	9.0	—
	max	0.03/0.08	2.5	0.65	0.03	0.03	22.0	11.0	—

Table 2.1: Chemical composition of the shell plasma-facing surface. The shell plasma-facing surface is 304L stainless-steel, and weld wire was used to fuse each plate together to form the shell quadrants. All values are percentages by mass with iron constituting the remainder. Note that the chromium reacts with oxygen to form a passivation layer or chromium oxide (Cr_2O_3). This is the "ideal" substrate onto which lithium coatings are applied.

Thin lithium coatings are deposited onto the shells via evaporation. When heated above the the melting point of lithium 180 °C , LTX can examine the performances of discharges with liquefied thin film coatings. Alternatively, lip structures at the toroidal breaks allow filling the lower shells with a several mm-thick lithium pool. An electron beam has been installed in a port in the top vessel flange to allow direct heating of the lithium surface in conjunction with (or instead of) resistive heating of the shells.

The toroidal and vertical field coil power supply connections and programming for the shots studied in this work is the same as that in ref. 82. The coil current waveforms during plasma operation (440—460 ms) are shown in fig. 2.2. Note that the toroidal field coil current is essentially flat during the discharge, while the current in other vertical field coils is being ramped as the plasma current increases. The internal coils show significant current oscillations due to a poor impedance match with the driving power supplies. For these shots, the OH supply delivers a loop voltage which decreases linearly with time. Since these shots were taken, additional impedance has been added to the OH circuit in order to utilize the capacitor stored energy more efficiently and obtain longer discharges with decreased initial loop voltage.

2.1.3 Predicted LTX Performance

The reference transport model (RTM) used to match the global parameters of low-recycling discharges in CDX-U was applied to predict the performance of the LTX. For reference, the

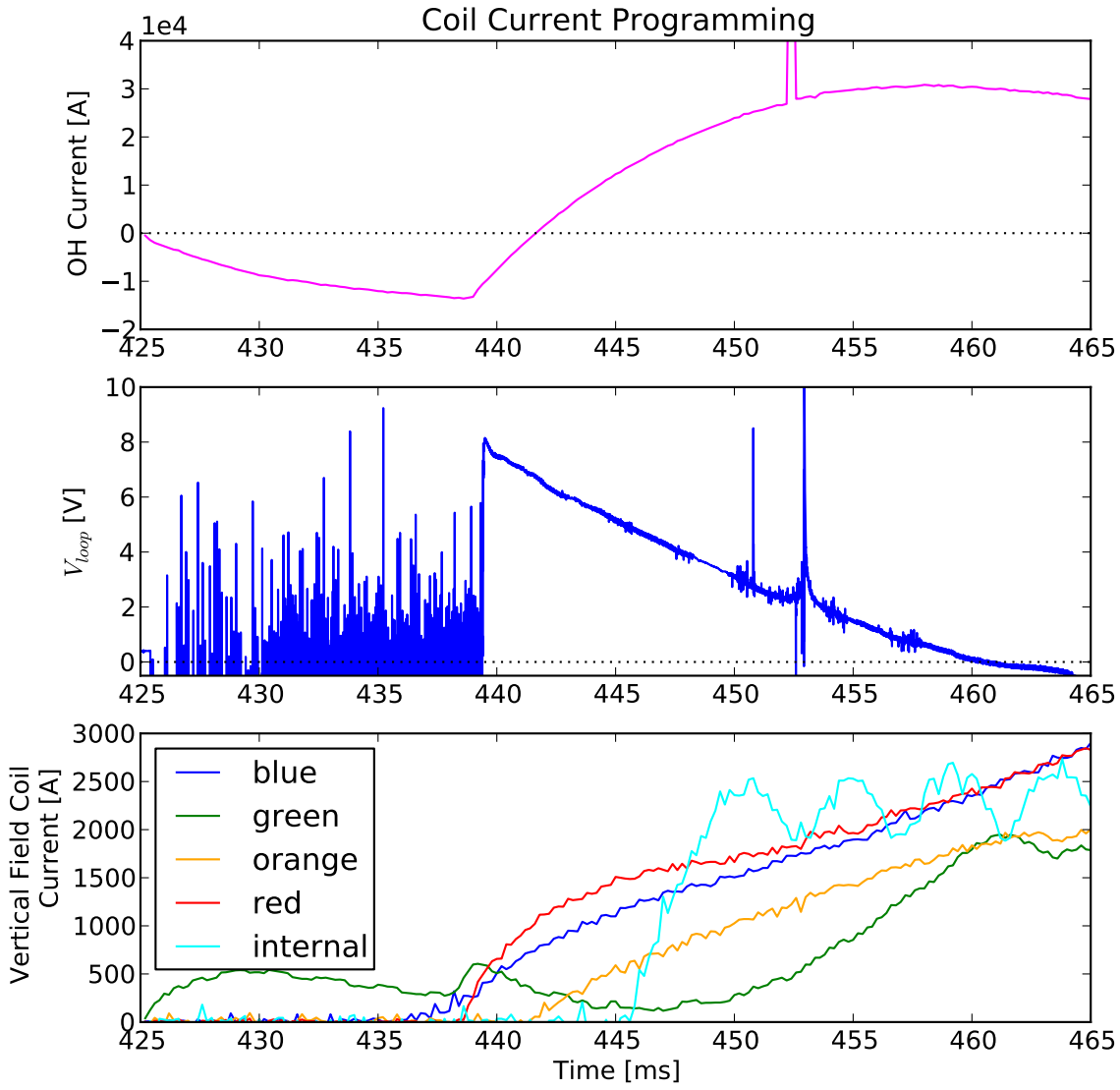

Figure 2.2: Standard coil current programming used in this work. The yellow coils were not used. Note the large oscillations in the internal field coils (cyan) are due to a poor impedance match with the power supplies. The large spike in the OH current and toroidal loop voltage is due to the disruption that terminated this discharge.

governing equations for the RTM are:

$$D = 0.1[\mathrm{m}^2/\mathrm{s}] + \chi_{i,neo} \tag{2.1}$$

$$V_r = V_{Ware} \tag{2.2}$$

$$\chi_i = 0.1[\mathrm{m}^2/\mathrm{s}] + \chi_{i,neo} \tag{2.3}$$

$$\chi_e = 0.1[\mathrm{m}^2/\mathrm{s}] + \chi_{i,neo} \approx 0.1[\mathrm{m}^2/\mathrm{s}] + \sqrt{m_i/m_e}\chi_{e,neo}. \tag{2.4}$$

To repeat, the assumption is that all cross-field transport is taking place at the ion neoclassical rate. Electron thermal transport and diffusion are therefore substantially above the neoclassical value by the square root of the mass ratio, but are assumed to have neoclassical transport scaling (i.e., decreasing with temperature) rather than a turbulent scaling. A spherical torus equilibrium with 300 kA plasma current was assumed in the transport analysis. Note that although the maximum achieved plasma current to date is ~70 kA, the LTX OH system is operating with only about one quarter its designed stored energy. In addition, without water cooling on the toroidal field coils, the TF field is limited to 1.9 kG rather than 3.5 kG used in the modeling. The following boundary conditions were used:

$$n(a) = 0.05[10^{19}\mathrm{m}^{-3}\ ] \tag{2.5}$$

$$q_i(a) = \gamma_i T_i \Gamma \tag{2.6}$$

$$q_e(a) = \gamma_e T_e \Gamma. \tag{2.7}$$

In the above expressions, $\gamma_i = \gamma_e = 5/2$. In order to maintain a steady-state density, a 2 eV neutral source (gas puff) and parabolic (i.e., core-localized) fueling source were used. The model gave a 25 ms energy confinement time with central $T_e(0)$ =1.4 keV and boundary $T_e(a)$ =0.72 keV[78]. Transiently pulsing off the external neutral sources raised the boundary electron temperature above the central value and increased the energy confinement time to

over 30 ms[78]. The model was also applied to neutral beam heated LTX discharges which are planned for the future. The results of this model applied to Ohmic LTX discharges have been duplicated in this thesis work and are presented in figure 3.17 in section 3.7.

2.2 Diagnostics

LTX is instrumented with a suite of diagnostics to measure plasma properties and constrain interpretive modeling. A major part of this thesis was a significant development effort to equip LTX with a comprehensive suite of visible and VUV spectroscopy diagnostics, therefore those instruments will be described in detail here. Other instruments including microwave interferometers, Thomson scattering, and magnetics were used as well; these diagnostics will be described more briefly and the interested reader is encouraged to explore the references cited herein.

2.2.1 Filterscopes

LTX is fitted with an extensive suite of visible spectroscopic instruments to measure radiation from bound electron transitions in plasma atoms and ions. A filterscope[92] consists of a lens which focuses collimated light onto a set of optical fibers. Each fiber runs to the data acquisition room where a second lens collimates the light exiting the fiber so that it passes through a band-pass interference filter to a photon detector. Compact photo-multiplier tubes with integrated high-voltage power supplies are used as detectors because they provide low-noise (current) amplification of small photon fluxes and have fast time response. Despite having a lower quantum efficiency relative to photodiodes or avalanche photodiodes, the lower noise of the electron avalanche used for amplification of the (cathode) photo-current provides a higher signal-to-noise ratio for small photon fluxes. Trans-impedance amplifiers convert the detector current to a voltage which is then digitized and stored in the LTX data

system. The center wavelength of each interference filter is chosen to measure light from a specific hydrogen or impurity transition line.

Three filterscope assemblies have been constructed for LTX using electronics and detectors provided by a collaboration with the Oak Ridge National Laboratory (ORNL). The first, "head A", is fitted with 5 fibers and is mounted on a midplane port to examine emission from the inner lip of the upper shell. The second, "head B" is fitted with 6 fibers and is mounted on an angled port to examine emission from the lower shell. The third, "head C" is fitted with 8 fibers and is mounted on another angled port to examine emission from one of the small molybdenum mirrors located near the shell gap at the Thomson entrance. The toroidal locations of the filterscopes are shown in figure 2.3a. Figure 2.3b shows the view of each filterscope collapsed onto a single poloidal plane.

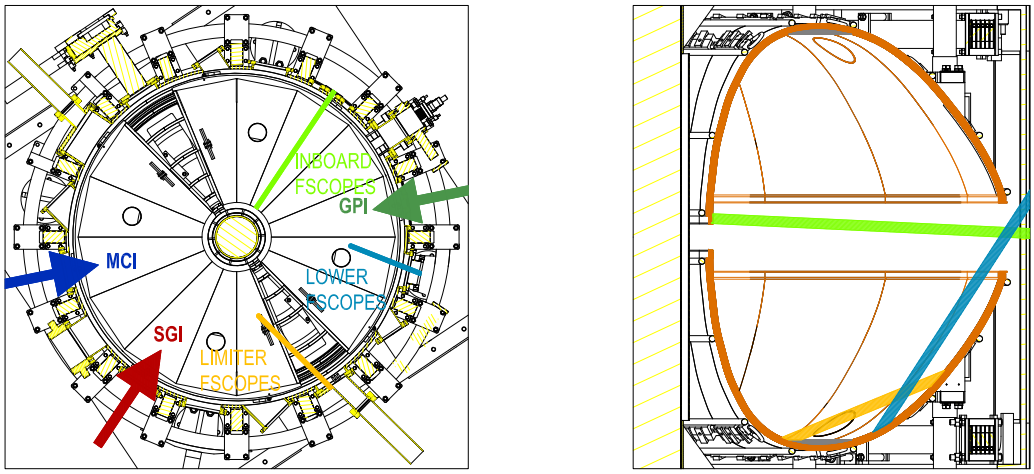

(a) (b)

Figure 2.3: (a) midplane view of filterscope sightlines as well as gas fueling locations. (b) Filterscope views collapsed into a single poloidal plane. The inboard-viewing filterscope is shown in light green, the lower-shell filterscope is shown in blue, and the limiter-viewing filterscope is shown in orange. In view (b), all filterscope instruments are located on the right of the figure.

LTX has been equipped with filters to measure emission from neutral hydrogen (H_α, H_β, H_γ), lithium (neutral, singly-ionized, and doubly-ionized), carbon (singly-ionized and

doubly-ionized), and singly-ionized oxygen. Each channel is photometrically calibrated using a broad-band calibrated illumination source. Additional technical details for the fibers, filters, detectors, pre-amplifiers, data acquisition, and calibration procedure are located in appendix A.2.

Using equation A.8 from appendix A, the line emission intensity is simply proportional to the measured voltage:

$$I_{\lambda_0}^{line}\left[\frac{\text{photons}}{\text{s}-\text{m}^2-\text{sr}}\right] = C_{\lambda_0} V^{line}[\text{V}] \tag{2.8}$$

The measured emission intensity is the integral of all emission along the sightline. In an ionizing plasma, atoms, ions, and molecules released from a surface (due to reflection, recycling, sputtering, evaporation, or thermal desorption) will persist in the plasma with a finite lifetime before being brought to a higher ionization state by either collisional excitation with plasma electrons and ions, or by charge-exchange collisions. During this time, the particle released from the surface will have its excited states populated due to collisional excitation processes. Non-metastable excited states have short lifetimes (given by the Einstein "A" coefficient), so they can be assumed to be in a quasi-static equilibrium with the ground (or meta-stable) state. Collisional-radiative modeling can determine the population of the ground and metastable states for each ionization state. As a result, measurement of the emission rate (photons/s $-$ m^3) or line-integrated emission rate (photons/s $-$ m^2 $-$ sr) allows the density of each ionization state or the ionization flux from the surface to be determined.

If the plasma electron density and temperature can be assumed to be reasonably homogeneous during the lifetime of the particular ionization state for the ion of interest, the collisional-radiative model described above can be performed for various values of n_e and T_e, generating a set of "effective emissivities" and ionization per photon coefficients. The latter are also referred to as S/XB coefficients, where S and X are the ionization and excitation rates, respectively, and B is the the branching ratio (ratio of the radiative decay probabilities)

for the spectral line of interest. In fact, the Atomic Data and Analysis Structure (ADAS) database has tabulated this data for many ions of interest to magnetic fusion plasmas[93]. This thesis makes use of the S/XB coefficients computed by ADAS in order to relate measured line-integrated emission to a flux from a surface for various ions (i) and wavelengths (λ)[94]:

$$\Gamma_i^{wall-plasma} = 4\pi(S/XB)_{i,\lambda} I_{i,\lambda}, \quad (S/XB)_{i,\lambda} = f(n_e, T_e) \tag{2.9}$$

For completeness, the density and temperature dependence of the S/XB coefficients for atomic transition lines of interest are shown in appendix A.5.

2.2.2 Visible Survey Spectrometers

Through a collaboration with the ORNL, LTX has been able to use three Ocean Optics HR2000+ Spectrometers as instruments to survey hydrogen and impurity emission from about 390—590 nm. Each spectrometer has a linear detector array with 2048 pixels and 14-bit A/D conversion. The spectrometers are powered and communicate with a Windows computer via a USB interface. They are triggered externally by a WGM-201 waveform generator, which is also controlled by the host PC over a USB interface to output a burst square-waveform. The burst output is triggered by the LTX timing system. Typically the spectrometers are triggered to acquire 600 spectra per second. One spectrometer is associated with each of the filterscopes; therefore, the spectrometers and filterscopes provide complementary measurements of emission over approximately the same plasma volume. Photometric and wavelength calibrations have been performed and are described in appendix A.4. A custom C++ interface for the spectrometers was developed by a summer student[95] and completed with this thesis work. The interface controls the spectrometer parameters, automates high-speed data acquisition, and stores data directly into the LTX MDSPlus tree.

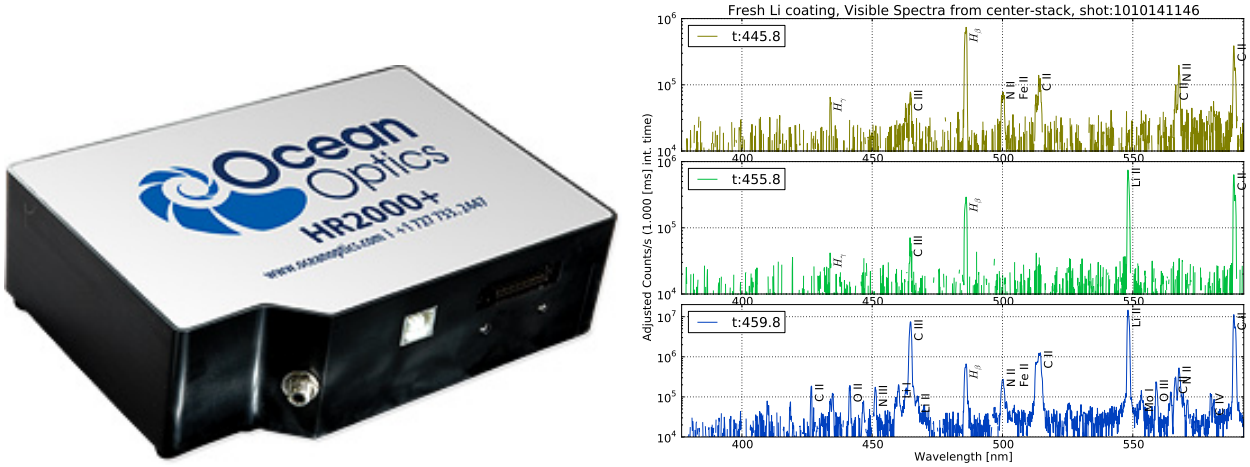

(a) (b)

Figure 2.4: (a) Image of one of the visible survey spectrometers. (b) Sample spectra at the beginning, middle, and end of a plasma discharge with a fresh Li wall coating. Significant emission from O, N and potentially high-Z impurities (Fe, Mo) is seen when the discharge terminates; however, during the middle of the discharge, the only noticeable impurity emission is from Li and C.

2.2.3 Fast Visible Cameras

High-speed cameras can be equipped with a narrow-band interference filter to provide 1-D profiles (in the case of a line-scan camera) or 2-D images of atomic line emission. LTX has a 2-D monochrome Phantom V210 with Cannon Ultrasonic Zoom lens (EF 24-105mm, 1:4 L IS USM) which is typically fitted with a 2" diameter, H_α interference filter (657.1 nm wavelength center, 5.25 nm FWHM, $\sim$ 0.6 transmission) and configured at a tangential midplane port to image emission during high-efficiency (SGI or MCI) fueling[82] and changes in shell recycling. The Phantom V210 has a 1280 x 800 CMOS sensor and can acquire just over 2000 full frames per second. Typical LTX operation uses a reduced window (512 x 384) at 10,000 frames per second with 10-100 μs exposure time. The photometric calibration is described in appendix A.1 and A.3.1.

LTX also has two Dalsa Spyder3 GigE linescan monochrome cameras which can provide high-resolution 1-D profiles of atomic line emission. One camera has 1024 pixels and a

maximum line rate of 68 kHz, while the other has 2048 pixels and a maximum line rate of 185 kHz.

2.2.4 Lyman-α Diagnostics

Motivation for Lyman-α Measurements

Measurements of H_α emission from magnetic fusion devices are routinely used to monitor the ionization source rate; however, measured signals can be contaminated by light sources outside the field-of-view of the detector which are reflected from structures inside the vacuum vessel. Even the relatively low reflectivity of H_α from the graphite tiles of many fusion devices is sufficient to contribute significantly to measurements of main chamber recycling[96]. An examination of the normal-incidence reflectivity for various wall materials (table 2.2) suggests that measurement "contamination" from reflected light is likely to be substantially higher for devices with metal walls. Although models have been developed to account for reflections in fusion devices[96,97,52], lithium coatings further complicate the analysis because of the dynamic nature of the lithium surface. Elemental solid lithium is silvery-white, and when clean, can have a mirror-like surface with high specular reflectivity. In contrast lithium passivated as lithium hydroxide or lithium carbonate is a nearly white surface, leading to diffuse reflections.

Material	H_α $R(\theta = 0)$	Ly_α $R(\theta = 0)$	Ref.
Iron	0.564	0.210	98
Molybdenum	0.576	0.217	98
Tungsten	0.518	0.274	98
Lithium (solid)	0.915	0.028	98
Beryllium	0.43-0.56	0.56-0.63	99
Graphite	0.10-0.18	0.04-0.06	100

Table 2.2: Comparison of normal-incidence reflectivity for clean samples of fusion device wall materials.

In order to circumvent analysis difficulties with reflections from clean lithium surfaces in particular, this work has chosen instead to take advantage of the negligible reflectivity of lithium in the VUV (and lower reflectivity of stainless steel in the VUV as well) and use the hydrogen Lyman-α line at 121.6 nm (corresponding to the n=2—1 transition) for quantitative recycling measurements. As a consequence, more diagnostic development effort is required since VUV detectors (as opposed to commercial visible cameras) and specialty filters are needed in order to isolate and measure the Lyman-α emission line.At the Lyman-α wavelength, the complex index of refraction of lithium is $n_{Li} = 0.732 + 0.106i$, Reflections off the substrate material can thus be ignored if the lithium layer is greater than about 200 nm thick, which is easily satisfied by the evaporatively-deposited shell coatings.

Lyman-α Arrays

Two filtered pinhole instruments with a 1-D detector have been developed to measure Lyman-α emission. One is mounted on a tangential port to measure recycling from the outboard side of the shell, while the other is mounted on a radial port to primarily measure recycling from the inboard side of the shell. The outboard-viewing array mounts to a 4.5" conflat flange which contains a 25-pin D-sub electrical feedthrough. This flange then mates to a custom-designed 6" conflat to 4.5" conflat adapter assembly. The inboard-viewing array is mounted in a 4.5" conflat flange which contains two 25-pin feedthroughs and contains two diode arrays. The first is mounted with a Lyman-α filter, while the second is currently configured without any filter to provide a proxy measurement for total radiated power. The 4.5" conflat flange mates to a 6" conflat to 4.5" conflat reducer which then mates to a 6" conflat gate valve. The reducer flange provides enough space for the aperture assembly to clear the gate valve knife edge and also provides a pump-out port. Photos of the outboard and inboard arrays are presented in figures 2.6 and 2.5 respectively.

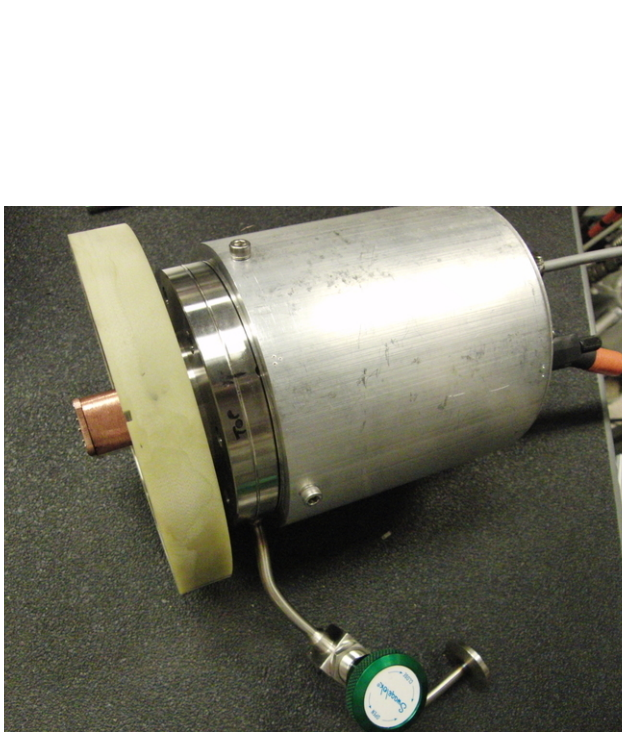

(a)

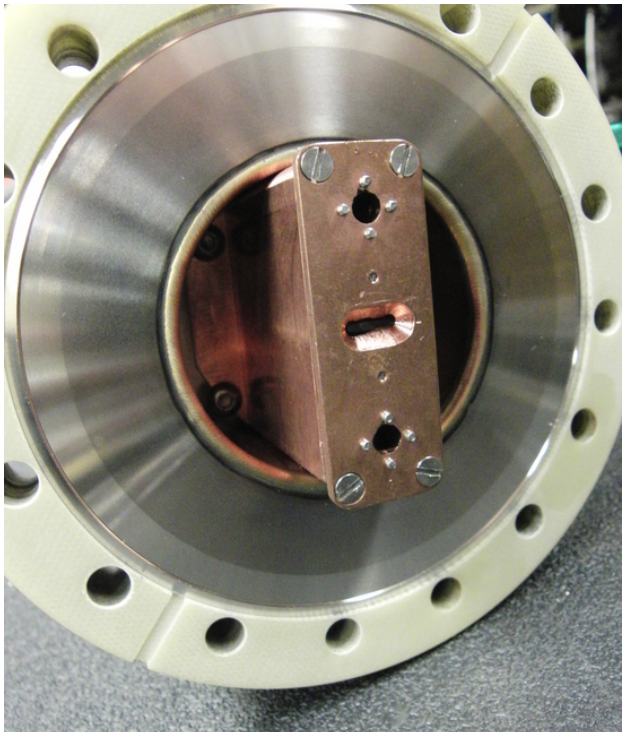

(b)

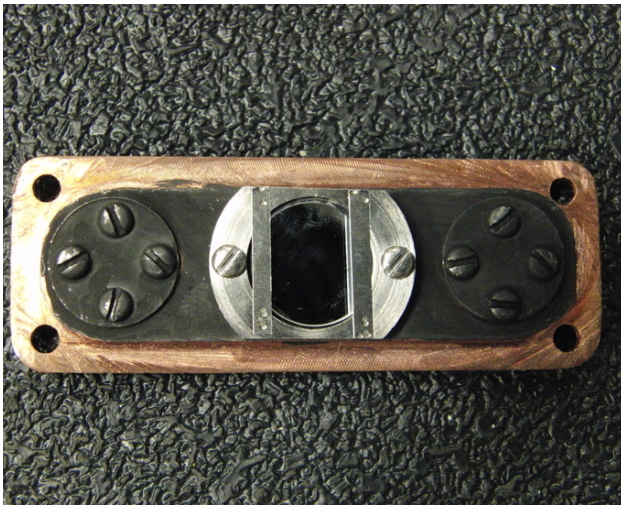

(c)

Figure 2.5: Photographs of the outboard-viewing array. The aperture assembly mounts to a 4.5" conflat flange fitted with a DB-25 vacuum electrical feedthrough connector. The 4.5" conflat flange is connected to a custom-designed 6" to 4.5" reducer assembly. A PEEK gasket G10 bolt-circle are used for electrical isolation. The assembly is then mated to a gate valve and the aperture sits about 1/4" from the gate valve knife edge. Image (a) shows the full assembly including pre-amplifier housing on the air-side. The center hole is the aperture, while the top and bottom circular vent holes are covered on the back of the aperture plate to prevent stray light from reaching the detector. Image (b) on the left shows the full vacuum-side aperture assembly. The back side of the aperture mounting plate is shown in (c).

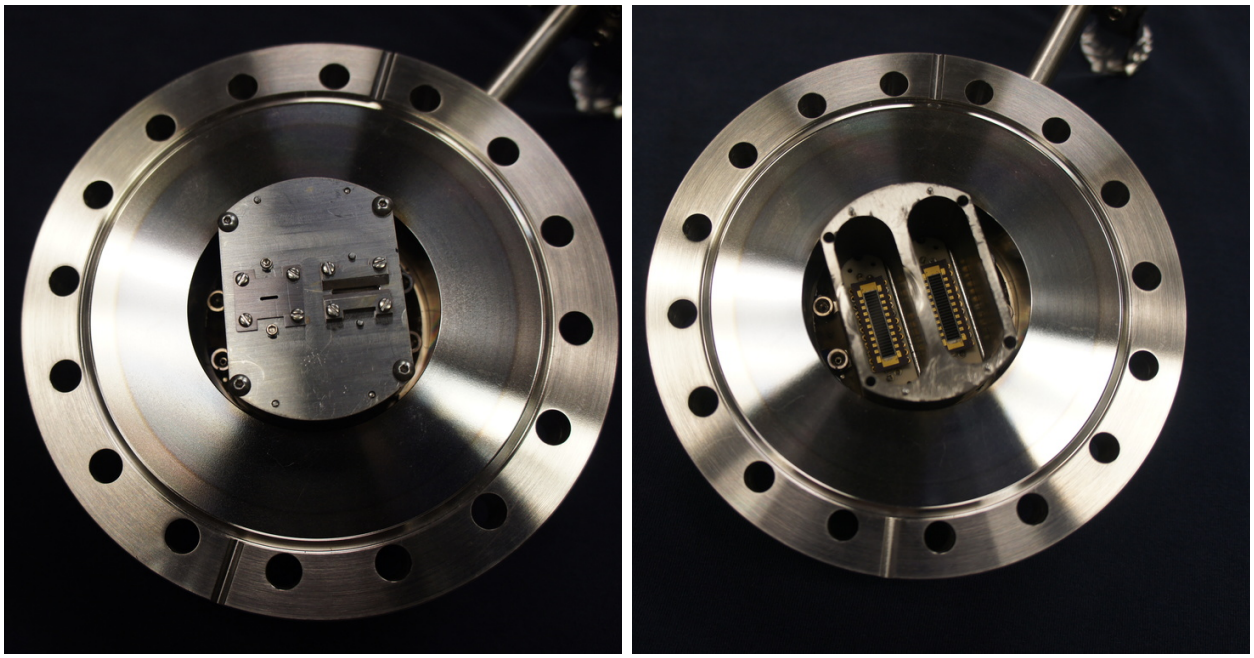

(a) (b)

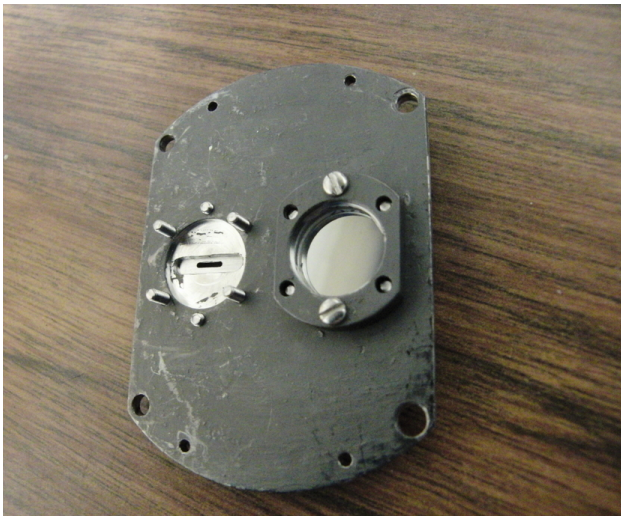

(c)

Figure 2.6: Photographs of the vacuum-side of the inboard-viewing array. The aperture assembly mounts to a 4.5" conflat flange fitted with 2x DB-25 vacuum electrical feedthrough connectors. The 4.5" conflat flange is connected to a 6" to 4.5" conflat reducer flange using a PEEK gasket and sleeved bolts for electrical isolation. The assembly is then mated to a gate valve and the conflat reducer flange provides enough depth for the aperture assembly to clear the gate valve knife edge. Image (a) shows the full assembly including the unfiltered (left) aperture and aperture fitted with a Lyman-α filter (right). The top aperture holder plate has been removed in (b) to show the AXUV20-ELM diode arrays and adapter PCBs. The back side of the aperture mounting plate is shown in fitted with the Lyman-α filter in (c). Vent grooves have been cut into the base of the aperture assembly to facilitate pump-out of both aperture cavities.

The detectors consist of a 20-channel AXUV20-ELM diode array from International Radiation Detectors (now part of Opto Diode Corp./ITW Photonics Group), which have a responsivity of 0.11 A/W for incident photons with λ=121.6 nm. The diodes are reverse-biased to 15V in order to decrease the capacitance and permit higher gain-bandwidth trans-impedance amplification. Refs.[101,102,103,104,105,106,107,108,109,110] describe a sampling of diagnostics applied to magnetic fusion experiments which utilize AXUV diodes. The arrays are fitted with a 0.5" diameter Acton Research Corp. filter model FN-122-XN which is deposited on a MgF_2 substrate. The particular filters mounted on the inboard and outboard arrays have a measured peak transmission of 0.056 at 121.6 nm.The diode arrays mount into an in-vacuum PCB adapter board which then mounts into a 25-pin D-sub vacuum electrical feedthrough. The two-stage pre-amplifiers were designed by K. Tritz as part of the work in ref. 111. The first stage trans-impedance amplifier is built around the MAZeT MTI04 4-channel programmable gain trans-impedance amplifier. The second stage adds a voltage gain of 5$\times$ and provides a low output impedance to drive the analog voltage signals over SCSI III (individually-shielded twisted-pair) cables into the data acquisition room where signals are digitized at 500 kHz by a D-TACQ ACQ196CPCI digitizer.

By taking into account the etendue of each channel, filter transmission, diode response, and pre-amplifier gain, the absolute emission intensity can be determined. The voltage signal measured by the digitizer is:

$$V_{sig} = eA\Omega G \int_0^\infty d\lambda \eta_{QE}(\lambda)\eta_f(\lambda)I_{emis}(\lambda). \tag{2.10}$$

Here e is the electron charge [C], $A\Omega$ is the etendue of the system [m^2-ster], G is the pre-amplifier gain [V/A], η_{QE} is the quantum efficiency of the detector [electrons/photon], η_f is the filter efficiency and I_{emis} is the wavelength-dependent plasma photon emission rate [photons/s-m^2-ster-λ]. If a single emission wavelength is filtered out, this can be inverted to

yield:

$$I_{emis,\lambda} = \frac{V_{sig}}{eA\Omega G\eta_{QE,\lambda}\eta_{filter,\lambda}}. \tag{2.11}$$

Additional information about the diagnostic hardware, bandwidth for each gain setting, and etendue for each channel can be found in appendix B. Vertical and poloidal views of the Lyman-α measurement sightlines are shown in fig. 2.7.

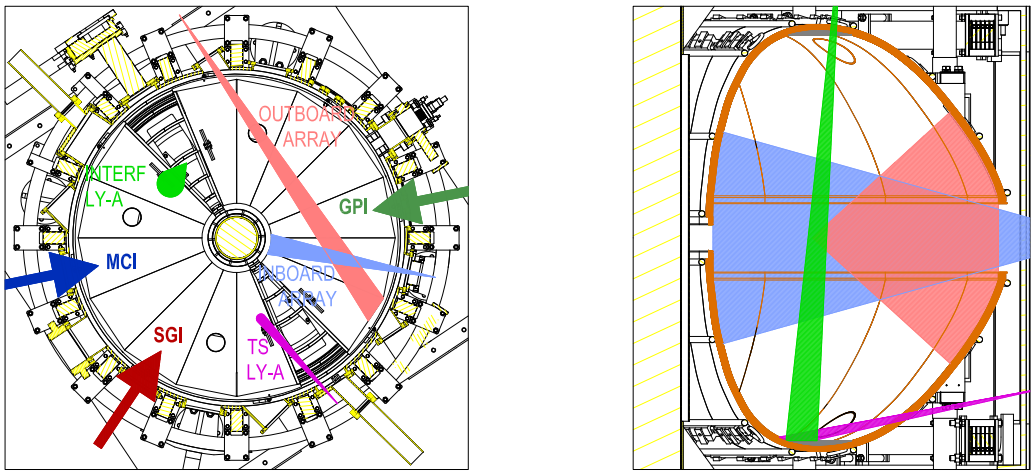

(a) (b)

Figure 2.7: (a) Midplane view of Lyman-α sightlines as well as gas fueling locations. (b) Lyman-α sightlines collapsed into a single poloidal plane.

Single Lyman Alpha Detectors

In addition to the Lyman-α arrays, two single-detector instruments were developed. Rather than using a bare AXUV diode with separate filter, these detectors use a 10 mm x 10 mm AXUV100GLA diode with a Lyman-α filter directly-deposited onto the diode surface. Visible light blocking was measured to be 1.2×10^{-3} for the diode viewing the limiter near the Thomson entrance port, and 9.3×10^{-4} for the diode viewing the limiter near the interferometer flange; in both cases, substantially less than the 10^{-4} blocking claimed by the manufacturer.

The diode is mounted directly into a custom-designed UHV trans-impedance pre-amplifier (fig. 2.8). By placing the pre-amplifier in vacuum it was hoped that the signal-to-noise ratio could be improved. A second-stage pre-amplifier sits on the air-side of the 9-pin electrical feedthrough in order to drive the output signal through about 40 ft. of cabling to the digitizer. The diode array and feedthrough flange mount to a welded bellows. A laser was used to align the bellows on each instrument so that the detector viewed one of the small molybdenum limiters in the lower shell on each side of the machine. The aperture sits at the front end of the bellows. A PEEK gasket and sleeved bolts are used to electrically isolate the entire assembly and pre-amplifiers from the vessel.

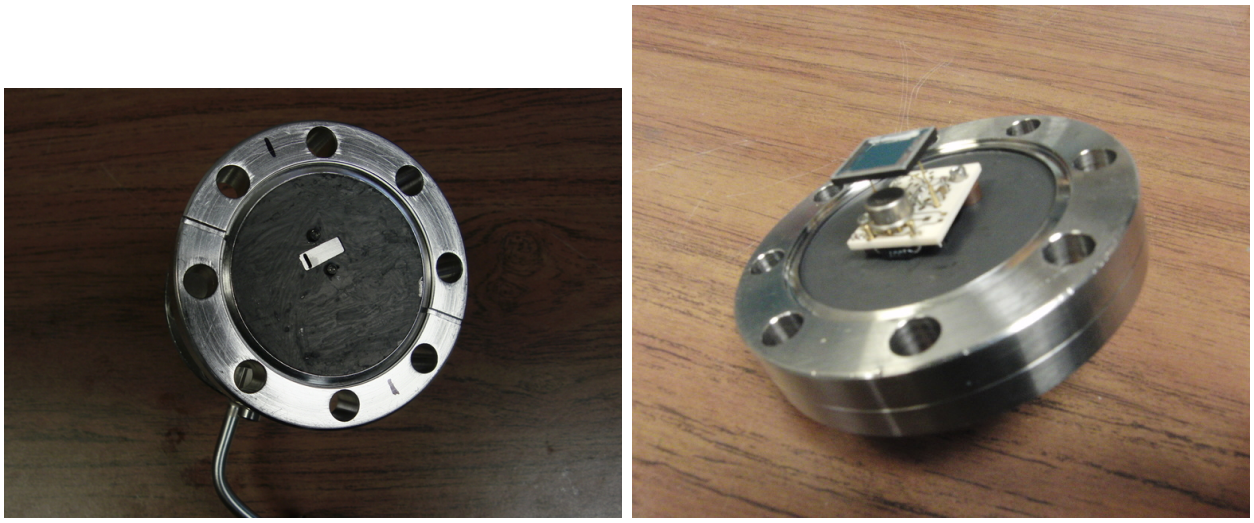

(a) (b)

Figure 2.8: Photographs of one of the single-detector Lyman-α instruments. (a) Vacuum-side of the bellows assembly showing the aperture. (b) View of the UHV trans-impedance pre-amplifier mounted to the electrical feedthrough flange with the AXUV100GLA diode in place.

2.2.5 Visible Bremsstrahlung

One of the filterscopes is equipped with a filter centered at λ=527.0 nm with a full-width at half-maximum of 4.5 nm. Visible survey spectrometers (e.g., fig. 2.4b) show this region

to be relatively free of line radiation, therefore the signal corresponds to continuum emission. Neglecting recombination since $\hbar\omega \ll R_y$ for this wavelength, the continuum emission consists of bremsstrahlung only[112]:

$$j(\omega) = K\frac{\bar{g}_{ff} n_e^2 Z_{\text{eff}}}{\sqrt{T_e}} \tag{2.12}$$

where $K = 8.0 \times 10^{-55}$ W/m^3-sr if n_e is in [m^{-3}] and T_e is in [eV]. The measured signal is the emission integrated along a midplane chord:

$$V = 2w\eta_\lambda K \bar{g}_{ff} \int_0^a dr \frac{n_e(r)^2 Z_{\text{eff}}(r)}{\sqrt{T_e(r)}}. \tag{2.13}$$

Absent additional measurements, if Z_{eff} is assumed to be constant with radius it can be pulled out of the integral:

$$Z_{\text{eff}} = \frac{V}{2w\eta_\lambda K \bar{g}_{ff}} \left[\int_0^a dr \frac{n_e(r)^2}{\sqrt{T_e(r)}}\right]^{-1}. \tag{2.14}$$

2.2.6 Total Radiated Power

The bolometer array sits in the inboard-viewing array described in 2.2.4 and is configured without a filter to accept all light and provide a total radiated power measurement. The aperture and etendue of the bolometer array are the same as for the inboard Lyman-α array. Converting the measured signal into total radiated power is complicated by the nonlinear response of the AXUV diodes at energies below about x. (see plot)

Since the power per unit wavelength is $P(\lambda) = hcI_{emis}(\lambda)/\lambda$, if one defines the diode power efficiency as

$$\eta_P(\lambda) \doteq \frac{e\lambda}{hc}\eta_{QE}(\lambda) \tag{2.15}$$

the total detected signal can be written as:

$$V_{sig} = A\Omega G \left(e \sum_{n=1}^{N_{line}} \eta_{QE}(\lambda_n) I_{emis,\lambda_n} + \int_0^\infty d\lambda \eta_P(\lambda) P_{cont}(\lambda) \right) \tag{2.16}$$

where $P_{cont}(\lambda)$ is the continuum emission and I_{emis,λ_n} is the line emission at discrete wavelengths. From the standpoint of calculating the total radiated power, it is the emission in the nonlinear region which complicates the situation:

$$P_{tot} = P_{line} + P_{cont} = P_{tot,lin} + P_{tot,NL} = P_{tot,lin} + P_{line,NL} + P_{cont,NL} \tag{2.17}$$

$$V_{sig} = A\Omega G \left(\eta_{P,lin} P_{tot,lin} + \sum_{n=1}^{N_{line,NL}} \eta_{P,\lambda_n} P_{\lambda_n} + \int_{\lambda_{NL}}^\infty d\lambda \eta_P(\lambda) P_{cont}(\lambda) \right) \tag{2.18}$$

At high electron temperatures, the total radiated power could be estimated by assuming the power radiated in the nonlinear region is small:

$$P_{tot,approx} \doteq \frac{V_{sig}}{A\Omega G \eta_{P,lin}} \approx P_{tot,lin} \tag{2.19}$$

This estimate can be improved with knowledge of the line emission. Substituting $P_{tot,approx}$ into equation (2.18) and assuming the power from continuum radiation in the nonlinear region to be negligible:

$$P_{tot} = P_{tot,approx} + \sum_{n=1}^{N_{line,NL}} \left(1 - \frac{\eta_{P,\lambda_n}}{\eta_{P,lin}} \right) P_{\lambda_n} \tag{2.20}$$

Since the bolometer array is integrated with the inboard Lyman-α array, a direct measurement of the Lyman-α emission along each chord is available. Therefore the detector response to Lyman-α emission can be correctly accounted for in the radiated power measurement, which is the dominant source of hydrogen line emission for the plasmas of inter-

est. Impurity line emission and continuum emission in the nonlinear region has not been accounted for; therefore this calculation of total radiated power is only an estimate.

2.2.7 Microwave Interferometers

Measurement Principle

Interferometry measures changes in the plasma refractive index, allowing the line-averaged density to be determined. For frequencies much larger than the electron cyclotron frequency, the plasma permittivity tensor is nearly diagonal, and the dispersion relation for the ordinary mode (O-mode) in CGS units is:

$$\omega^2 = \omega_p^2 + c^2 k^2, \quad \omega_{pe}^2 = \frac{4\pi n_e e^2}{m_e}. \tag{2.21}$$

For frequencies far above the O-mode cutoff ($\omega \gg \omega_p$) the relative phase difference can be simplified:

$$\Delta\phi = (k - k_{vac})L = \frac{\omega}{c}\left(\sqrt{1 - \frac{4\pi \bar{n_e} e^2}{\omega^2 m_e}} - 1\right) L \approx \frac{\omega_{pe}^2 \lambda_{vac} L}{4\pi c^2} = \frac{e^2 \lambda_{vac} \bar{n_e} L}{m_e c^2}. \tag{2.22}$$

In the above expressions, $k_{vac} \doteq \omega/c$ and $\lambda_{vac} \doteq 2\pi c/\omega$ are the vacuum wavenumber and wavelengths, $\bar{n_e}L$ is the line-integrated electron density. Therefore changes in the relative phase are linearly proportional to changes in the density.

$$\bar{n_e} L = K \Delta\phi, \quad K \doteq \frac{m_e c^2}{e^2 \lambda_{vac}} \tag{2.23}$$

2mm Interferometer

The primary interferometer for the work presented here is a 140 GHz (2mm) interferometer[113] which can be moved vertically between shots to view different horizontal chords, allowing the

density profile to be determined via Abel inversion of multiple shots. The 2mm system uses a superheterodyne technique[112] to remove ambiguity in the direction of the phase shifts, and the relative phase of the 30 Mhz IF reference and signal are compared to determine the line-integrated electron density. Additional details regarding the operation of this instrument for the shots presented here can be found in ref. 82. The phase shift of the signal relative to the reference can either be determined by a hardware phase comparator or the 30 MHz signal and reference can be digitized and the phase calculated via a post-processing algorithm. The hardware phase comparator used here has a full span of 4π, meaning phase jumps occur at $\pm 2\pi$ which correspond to ± 1.9 V[82]. This instrument ceased functioning in the spring of 2012.

Phase Difference Algorithm

In addition to digitized phase from hardware phase comparators, direct digitization of the signal and reference allows the phase to be computed via post-processing. The particular algorithm used on LTX is based on the method described in ref. 114. For completeness, steps in the approach are as follows:

1. Calculate the frequency of the oscillator by finding the peak of the power spectrum of the reference time-series.

2. Apply a short-time-FFT filter to the reference time-series. This keeps only data within a particular frequency range (currently $\pm 0.1 f_n$ where f_n is the Nyquist frequency, and $f_n = f_{sampling}/2$). The data can then be down-sampled. The result is a 2-D array of complex Fourier frequency amplitudes vs. time.

3. Compute the complex reference time-series by zeroing out Fourier amplitudes of negative frequencies and taking the inverse short-time-FFT. This can be thought of as equivalent to retaining the positive side-band in a heterodyne system.

4. Apply the same short-time-FFT filter to the signal time-series, keeping only data within the chosen frequency range, down-sampling the data if desired, and computing the complex signal time-series.

5. Compute the (complex) product of the complex reference time-series and complex conjugate of the signal time-series. The time-series of the angle in the complex plane (i.e., $\phi(t) = \mathrm{Arg}(x(t) + iy(t))$) is the phase difference between the plasma and reference beams.

2.2.8 Langmuir Probe

One swept, single-tip Langmuir probe was installed at the outboard midplane during the 2011-2012 LTX run campaign. The probe was mounted on a bellows drive to allow placement at different major radii in between shots. Typically the probe was positioned to be at the same radius as the inner wall of the outboard shell, R=66 cm. The probe material was 1.0 mm diameter tungsten with 5.0 mm exposed tip length. At this major radius, for T_e=T_i=5–20 eV, ρ_e=0.05–0.1 mm and ρ_i=2–4 mm for a hydrogen ion (assuming a toroidal field at the nominal magnetic axis of B_0 =1.8 kG at R_0=40 cm). Since ions can be treated as unmagnetized, the appropriate collection area is $A = \pi r_p(2L + r_p)$ when converting the measured ion saturation current to current density. Although electrons are magnetized, the electron temperature derived from the I-V curve is not affected. The probe tip was swept ±35 V using a Kepco bipolar power supply which was driven by a 500 Hz triangle wave. The current and voltage waveforms were transmitted to the DAQ room using analog voltage-to-frequency converters with optical fibers in order to reduce electrical noise and isolate the digitizer from any possible voltage spikes.

Custom software was developed in order to quickly and accurately process I-V traces. To analyze the data, first the current and voltage waveforms are calibrated using the known resistances of the circuit model. Next, the power spectrum of the bias voltage was used

to find the actual driving frequency. Then the start and end points of each sweep were identified by finding the maxima and minima of the sine wave produced by using a filter in frequency space to select only the fundamental of the bias waveform. The voltage and current waveforms are then smoothed using a convolution filter. At this point, each sweep was analyzed using a semi-automated routine which does the following:

1. processes the characteristic by removing voltages above a given maximum voltage to eliminate the oscillations at the high probe currents approaching electron saturation

2. solves for the I_{sat}, T_e, V_f which minimizes the χ^2 using the L-BFGS-B algorithm

3. loops over the solver trying different values for the initial guesses of the solution parameters and the fraction of the characteristic to use in fitting

4. the solution with the minimum χ^2 is taken as the best fit ($\bar{x}$)

5. uncertainty in the fit parameters is determined by examining the distribution of converged solutions:

$$w_i \doteq (\chi^2)^{-4} \tag{2.24}$$

$$\hat{\sigma_x^2} \doteq \frac{\sum_i (\bar{x} - x_i)^2 w_i^2}{\sum_i w_i^2} \tag{2.25}$$

$$\sigma_x^2 = \hat{\sigma_x^2} + \sigma_{\mathrm{I_{max}}}^2 q^2 \tag{2.26}$$

In the above expression, $\hat{\sigma_x}$ is the uncertainty in the fit parameter $x = [I_{sat}, T_e, V_f]$ due to the distribution of solutions only, while σ_x is the uncertainty in the parameter x including a noise estimate of the signal. This estimate is calculated by taking the uncertainty in the maximum probe current (approximately I_{sat} and multiplying by the parameter $q = [1, T_e/I_{sat}, T_e/I_{sat}]$ for $x = [I_{sat}, T_e, V_f]$, respectively. The user can then examine the I-V trace and fit results,

and either accept the fit or re-do the analysis with modified control parameters. A sample analyzed I-V trace using this analysis procedure is shown in fig. 2.9.

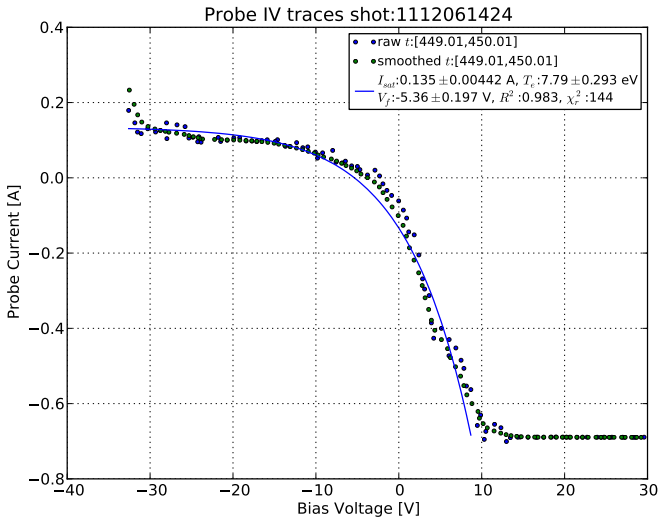

Figure 2.9: Sample Langmuir probe IV trace. Raw data points are shown in blue, smoothed points in green, and the result of the fit is the blue line.

2.2.9 Magnetic Diagnostics

External magnetic diagnostics provide measurements of poloidal flux, poloidal magnetic fields outside the plasma, total plasma current, and plasma diamagnetism in order to constrain a reconstruction of the magnetic equilibrium, measure the total energy stored in the plasma, and determine the energy confinement time. The existing suite of magnetic diagnostics is described in detail elsewhere[115,116,81]. Despite toroidal and poloidal breaks, higher-order currents eddy currents are induced by the vertical field coils and Ohmic solenoid in the vacuum vessel. These non-axissymmetric eddy currents complicate reconstruction of the magnetic equilibrium.

The current model for calculating eddy currents and magnetic equilibria is a 2-D axis-symmetric model incorporated in LRDFIT[117]. The shell resistivity in this model has been

modified with a poloidal distribution in order to best match signals from the flux loops and Mirnov coils. The induced eddy currents are considered to be axissymmetric, but then their sum is canceled by a current flowing through the whole shell[81]. Some recent work using this model has shown reasonable flux surface shapes using a singular value decomposition to match the measurements[118]. Nevertheless, this is clearly an ad-hoc model in its treatment of the inherently non-axissymmetric eddy currents, although perhaps at later times in high plasma current discharges the axissymmetric plasma current will dominate. Without a true 3D model to compare with, equilibrium reconstructions should be treated as uncertain; nevertheless, numerous errors in the previous LRDFIT model have been fixed over the course of this work. The limiter geometry used in LRDFIT now corresponds to the most-limiting surfaces of the shells (edges on the inboard side and flats on the outboard side) and integrator drift correction works accurately even if the discharge ends in a disruption.

Unfortunately, during the 2010 and especially 2011 LTX run campaigns, the magnetic suite was severely compromised. During the 2010 run, eddy currents caused the shells to move substantially, moving several flux loops from their original positions. Improvements to the shell supports eliminated this problem in 2011; however, saturation of the digitizer inputs and high-voltage transients due to the disruption at the end of the discharge became issues. This problem was solved by installing transient voltage suppression diodes to clamp the magnitude of the voltage going into the integrators and therefore prevent arcing. Lastly, over time many of the Mirnov coils shorted to the shells, detached from their original locations, or became otherwise unusable. Therefore, the primary magnetic diagnostics used in this work are flux loops, Mirnov coils from the CDX-U poloidal array, and the plasma current Rogowski coil.

2.2.10 Thomson Scattering

LTX is currently equipped with a multi-point "TV" Thomson scattering system to measure electron temperature and density at 11 simultaneous points between R =40–64 cm (nominally r =0–23 cm) at a single time during the discharge[119]. The illumination source is a high-power Ruby laser, and a diffraction grating and CCD are used to measure the spectral distribution of scattered light. An additional edge Thomson system is being developed to provide high-spatial-resolution measurements of the plasma edge. Edge electron density is anticipated to be low during operation with low-recycling lithium surfaces; therefore, the edge diagnostic requires a higher product of quantum efficiency (QE) and transmissivity in order to maintain an adequate signal-to-noise ratio. The higher QE is achieved by using polychromators and discrete APD detectors, similar to the type employed on NSTX[120] except with filters tuned for scattered Ruby laser light

2.2.11 Charge Exchange Recombination Spectroscopy

Through a collaboration with ORNL, LTX has been fitted with a charge-exchange recombination spectroscopy (CHERS) instrument. For the shots presented here, the instrument consisted of a Kaiser Holospec F/1.8 spectrometer imaged onto a Princeton Instruments ProEM 512x512 pixel CCD. A high dispersion holographic transmission grating and prism with a central wavelength of 5175 Å was used in order to measure the Li III line at 5166.89 Å. Commercial 85 mm lenses are used at the entrance and exit resulting in a 0.9 Å instrument function, corresponding to 35 eV. This configuration captures light from 11 fibers simultaneously, with 6 typically oriented toroidally and 5 oriented vertically. Tangency radii of these fibers span R ∼37—53 cm corresponding to $0 < |r/a| < 0.5$. Spectra with adequate signal-to-noise can be acquired every 1.5 ms. Interestingly, the brightest lines measured by the instrument are from C II. The intensity of the Li III line is typically larger or comparable

to the nearby C_2 Swan bands from 5150–5165.25 Å and a line at 5168.9 Åwhich is attributed to Fe I.

2.3 Fueling Systems

Three gas fueling systems are installed on LTX: a gas puff injector (GPI), a supersonic gas injector (SGI), and a high-pressure supersonic gas injector. The latter can be cryogenically cooled using liquid nitrogen. When cooled, clusters of H_2 molecules are expected to form in the outflow; thus it is typically referred to as the molecular cluster injector (MCI) whether operated at room-temperature or with cryogenic cooling. The response time for flow from each of the fueling systems to terminate is less than one millisecond. A previous thesis on LTX examined the fueling efficiency of each of these systems[82], and the following discussion borrows from that work. The particle flux as a function of backing pressure and fueling efficiencies are summarized in table 2.3.

For the shots studied in this work, the gas puffer was mounted on a side vessel port. Flow from the Maxtek MV-112 piezo-electric valve was directed radially inward (towards the plasma) with a 1/2" ID, 2.25" long guide tube which extends to the outboard edge of the shell lip. The SGI was inherited from CDX-U[52,121,122], but was configured with a Mach 5.5 stainless-steel converging-diverging nozzle. The nozzle is mounted directly to a PV-10 piezoelectric valve, and has a 0.02" diameter throat. The valve assembly is mounted to a bellows and is typically pushed inside the LTX vacuum vessel so that the nozzle exit is flush with the outer shell lip at $R \approx 68$ cm. The MCI uses a Parker Series 99 fast solenoid valve surrounded by a copper cooling jacket. Liquid nitrogen flows through copper tubing brazed to the jacket, which cools the gas in the valve body. A diverging nozzle is attached to the valve exit identical to the diverging section of the SGI nozzle. A 1" diameter skimmer is typically installed to keep uncollimated gas from entering the plasma. This allows higher

backing pressures to be used, which promotes particle clustering, without the total gas throughput becoming unacceptably high.

Fueling System	$\Gamma(P_0)$ [H-atoms/s-psia]	η_f	Note
GPI	3.7×10^{20}	24/22	P_0=23/31 psia
SGI	2.8×10^{20}	31–32	R=66–70 cm
MCI (warm)	6.2×10^{19}	28–30	1" skimmer, P_0=50–250 psia
MCI (cold)	1.8×10^{20}	30/26	1" skimmer, P_0=50/100 psia

Table 2.3: Gas throughput and fueling efficiencies for the LTX fueling systems. Table composed from data in a previous work[82].

2.4 Pre-Lithium Wall Preparation and Discharges

After pumping down the LTX vacuum vessel and before evaporating lithium onto the stainless-steel shell surfaces, the vessel is "baked-out" over several days in order to volatize and pump-out gasses which have been adsorbed onto material surfaces. Vessel bake-out is performed by driving currents through the resistive heaters affixed to the copper surface of the shells. Thermal radiation from the shells then heats other materials inside the vacuum vessel. The shells are typically heated up to about 350 °C , while the vacuum vessel will stay below about 80 °C . The maximum temperature is limited by the OH solenoid insulation.

Before applying lithium coatings onto the shells, the maximum plasma current achieved during tokamak operation was less than 10 kA, and discharges were limited to $\lesssim$5 ms in duration (fig. 2.10). In order for the peak plasma current to exceed a few kA, only a small amount ($\lesssim 4 \times 10^{18}$ H atoms or a vessel pressure of about 3×10^{-5} torr) of hydrogen gas prefill could be used[82]. Line emission from hydrogen as well as oxygen and carbon impurities increases slightly over the course of the discharge. Although uncertainty in the edge electron temperature prevents calculation of the relative fluxes, it is clear that plasma-wall interactions result in the release of both hydrogen and impurities. A probable explanation for the discharge behavior is that electrons accelerated by the toroidal electric field (from the OH solenoid) are slowed by friction with neutral hydrogen and impurities. As a result, power from Ohmic heating is most likely being transferred to line radiation rather than electron heating. The significant oxygen emission is consistent with substantial water on the surface of the stainless-steel shells, which is released as a result of plasma bombardment. Residual gas analyzer (RGA) traces (fig. 2.11a, blue) indicate that water is a dominant residual gas.

In addition to baking, a glow discharge has occasionally been used to help desorb gasses from the shell surfaces. In this process, a glow discharge is generated between the grounded shells and a glow probe which is biased by 480V AC. During glows, the vessel is filled with 5–100 mtorr of either He, Ne, or Ar. RGA traces (fig. 2.11) indicate that He glow discharge

cleaning is effective at reducing the water peak by about a factor of 3. He glow discharge cleaning also volatizes other compounds, reducing the other peaks gas well. Interestingly, hydrocarbons are also released by the He glow discharge. The carbon within the stainless-steel shells ($\lesssim$0.08% carbon by mass) seems too small to account for the observed hydrocarbon spectra.

After conditioning, but before introducing lithium, the typical base pressure inside the LTX vacuum vessel was $\sim$1–5 $\times$ 10^{-7} torr for the 2010 and 2011 run campaigns.

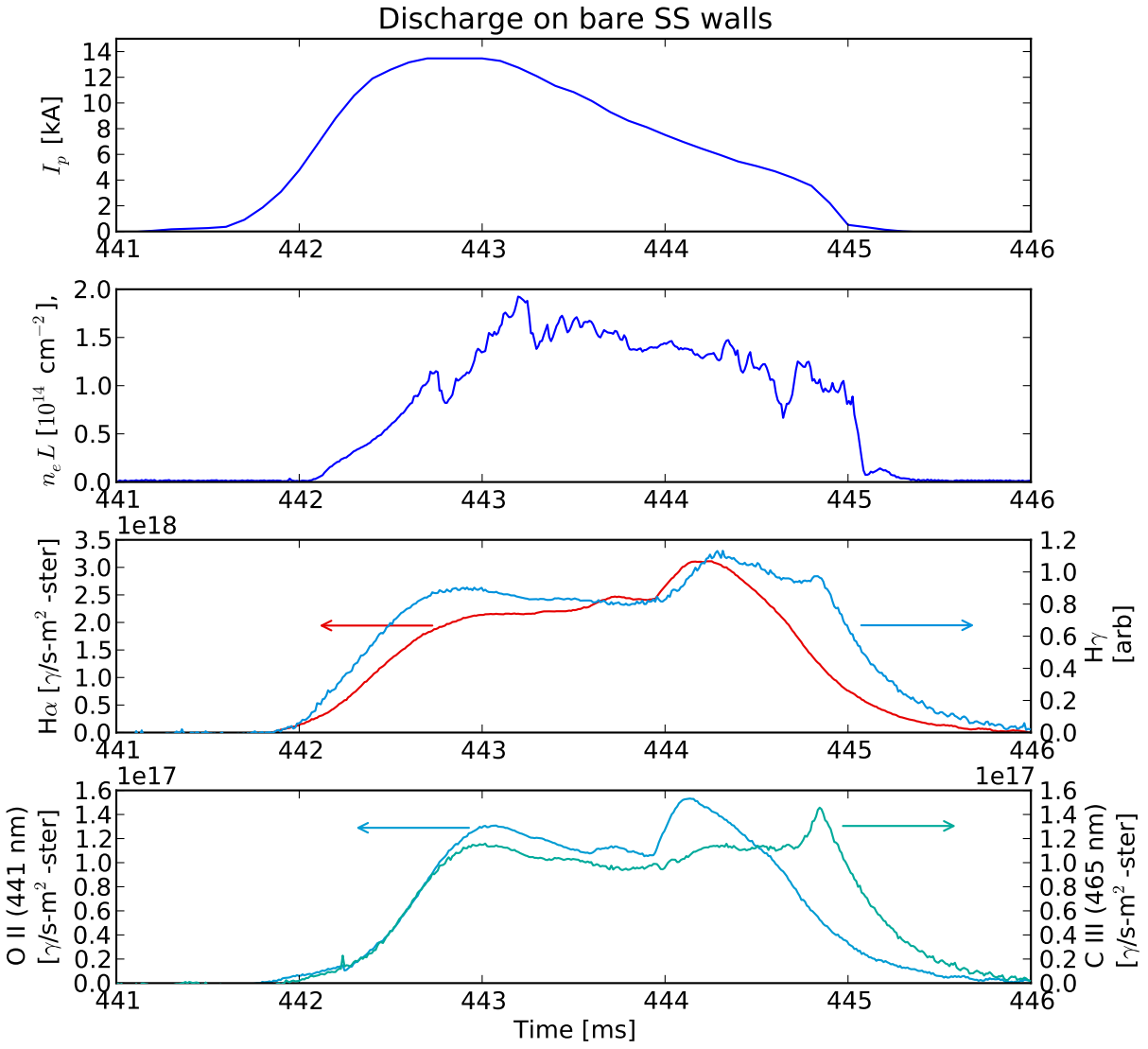

Figure 2.10: Plasma discharge on bare stainless-steel walls before lithium evaporation. These discharges typically last $\lesssim 5$ ms with peak plasma currents limited to $\lesssim 15$ kA. Line emission from hydrogen as well as oxygen and carbon rise over the course of the discharge. The neutral particle inventory (not shown) after this shot is more than double the value before the shot, indicating that the wall is a net particle source[82]. The plasma termination is consistent with a radiative collapse. This is LTX shot 1009031457.

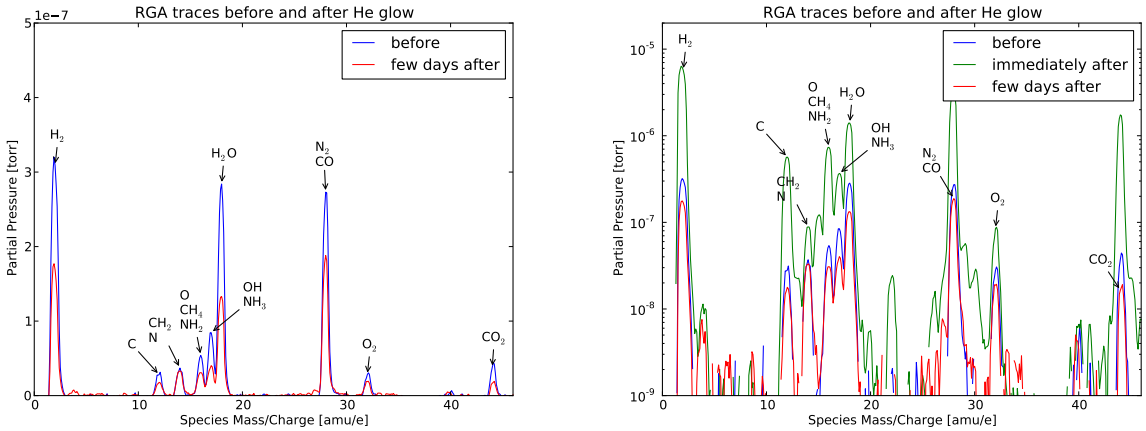

(a) (b)

Figure 2.11: (a) RGA traces before (blue) and a few days after (red) 10 hours of He glow discharge cleaning of cold shells. LTX had been under vacuum for almost a year, and the vessel and shells had been baked out by heating the shells up to 300 °C ; despite being under vacuum for so long and several bake-outs, the water peak remained high. He fill pressure was varied during the glow from 6–50 mtorr. (b) Shows the same traces and also the RGA trace immediately after (green) the He glow discharge cleaning on a log scale. The He glow discharge was effective at volatizing gasses desorbed onto the shell surfaces. Interestingly, despite all-metal PFCs, hydrocarbons were volatized during the He glow discharge cleaning. The carbon source is unknown. These traces were taken during Fall 2010.

2.5 Lithium Application and Subsequent Discharges

Lithium coatings are evaporatively deposited onto the shell surfaces by two lithium evaporator systems that can be attached to the LTX vessel. The evaporators consist of crucible ovens mounted on a long bellows and sealed by a gate valve. The crucible oven is composed of a ceramic (yttria) cup surrounded by a tantalum heater and mounted on a stainless-steel holder (fig. 2.12). Solid lithium is loaded into the crucibles in an argon atmosphere; then the gate valve is closed to transport the assembly to LTX to minimize passivation of the surface of the lithium. The evaporator is then attached to the machine and pumped down, at which point the gate valves are opened and the crucible oven is translated into the machine near the geometric center of the shells.

The tantalum heaters in each crucible are resistively heated by high-current power supplies in order to achieve oven temperatures of 575–600 °C , as measured by thermocouples that are immersed in the lithium. Maintaining the lithium at this temperature for about an hour is sufficient to evaporate about 1 gram of lithium from each evaporator, which is adequate to achieve significant wall pumping and high-performance discharges.

Two methods were used to help distribute the evaporated lithium more evenly over the shell surfaces. The first evaporations in October 2010 were performed into a ∼65 mtorr helium glow discharge; however, this method required disconnecting diagnostics in order to prevent the potentially high voltages in the glow discharge from damaging the digitizers. Electronic interference from the AC glow also prevented reading the temperature from the thermocouples. Due to these issues, evaporations beginning in November 2010 were performed into ∼5 mtorr He, which appeared to produce a reasonably uniform coating by visual inspection. This experimental finding is consistent with DEGAS 2 modeling of the distribution of evaporated lithium[123], which found 1–10 mtorr He was the optimum pressure range to distribute the lithium over the shell surface.

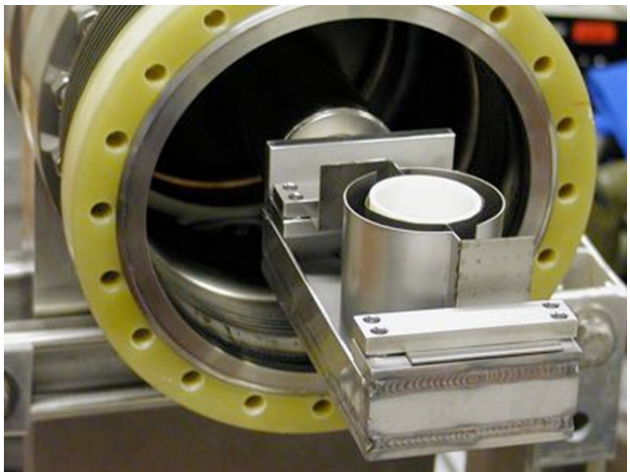

Figure 2.12: Photo one of the two LTX evaporators which can be mounted on a vacuum vessel port and inserted into the vessel through the outboard midplane shell gap. Solid lithium in the yttria crucible is heated to ∼450 °C in to deposit evaporated coatings onto the shells. Evaporation is performed in the presence of about 5 mtorr He so that collisions with He atoms help to spread out the lithium coatings over the shell surfaces. (Image courtesy of M. Lucia.)

While evaporating lithium from the crucible heaters, the He glow also volatized hydrocarbons and other gases which were adsorbed onto the PFCs (fig. 2.13a, green), just as when a He glow discharge was used to clean the bare stainless-steel shells. The lithium evaporation further reduced the water peak on the RGA by about 60% (fig. 2.13a, red) and essentially eliminated the oxygen peaks at 16 and 32 amu. The large H_2 peak is consistent with the formation of LiOH. After plasma operations and allowing the cold lithium coating to passivate with the residual vessel gases, the water peak returned to its pre-lithium value (fig. 2.13b, cyan).

In contrast, when evaporating lithium into He gas, hydrocarbons are not released (fig. 2.14a, green). However, hydrocarbons are present after tokamak plasma operations (fig. 2.14b, red).

Plasma discharges on fresh evaporatively-deposited solid lithium coatings (fig. 2.15) show substantially improved performance compared to operation on a bare stainless-steel surface.

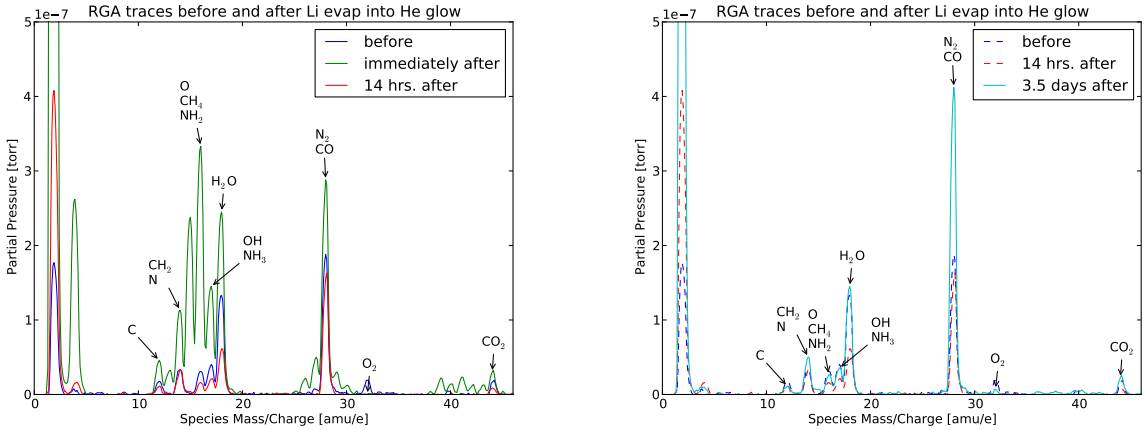

(a) (b)

Figure 2.13: (a) RGA traces before (blue) and after evaporating 1.2 g Li into He glow. Once again, RGA traces immediately following the He glow (green) indicate show molecules containing carbon. After 14 hours (red), the RGA shows the H_2O peak has been reduced by half, while the H_2 peak has doubled from the pre-lithium value. Plasma operations on at this time resulted in high-performance discharges. (b) The final RGA trace (cyan) was taken after allowing the vessel to passivate an additional 2 days, for a total of 3.5 days after the lithium evaporation. Notice that the H_2O peak has returned to its pre-lithium value. These traces were taken during Fall 2010.

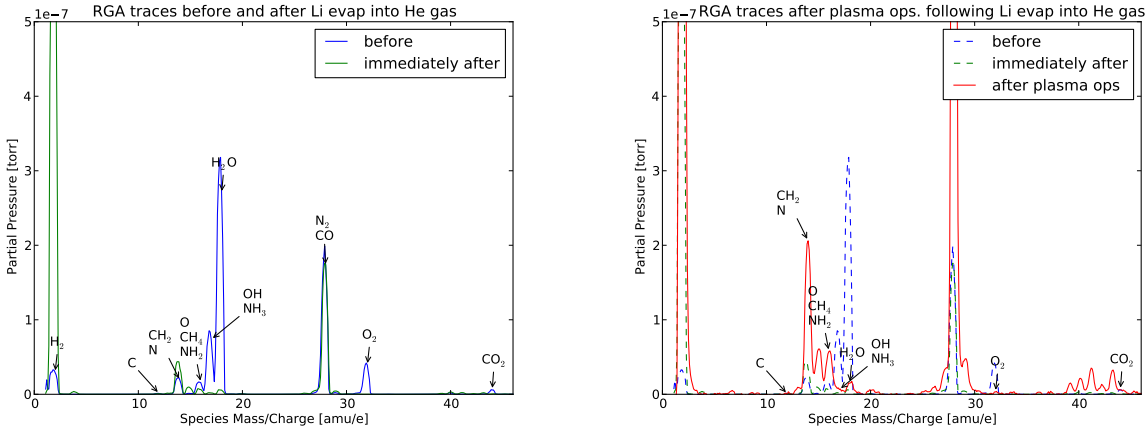

(a) (b)

Figure 2.14: (a) RGA traces before (blue) and after (green) Li evaporation into He gas. The Li evaporation was effective in virtually eliminating the H_2O and O_2 peaks. In contrast to Li evaporation in a He glow (fig. 2.13), there is no evidence of hydrocarbons volatized by the Li application. Plasma operations at this time resulted in high-performance discharges. (b) After plasma operations (red), the RGA shows a very high 28 peak, as well as smaller peaks typically associated with hydrocarbons.

This discharge was taken about 17.5 hours after evaporating ∼4 g from each evaporator. The external fueling for this discharge was a large pre-fill and a short pulse from the MCI at 444 ms. The slow decrease in electron density indicates sub-unity recycling. Note that before the plasma instability and current crash at 445 ms, the peak Hα emission was about a factor of 3 lower than the pre-Li discharge (fig. 2.15), and was decreasing (rather than constant) over the course of the discharge. The oxygen emission has the same temporal behavior as the Hα emission, again a factor of 4 lower than the pre-Li discharge, consistent with the reduced water and oxygen peaks on the RGA (fig. 2.14). In contrast, the carbon emission is substantially higher than the pre-Li discharge. The difference between the temporal trends of the Hα and Hγ emission is consistent with a reduced ratio of neutral molecular hydrogen to neutral atomic hydrogen and decreasing electron density over the course of the discharge.

After allowing the lithium surface to passivate with residual gases for an additional 3 days, plasma discharges are substantially degraded (fig. 2.16), although performance is still improved compared to shots on bare stainless steel. The Hα emission drops only slightly over the course of the discharge, while Hγ emission and impurity emission from oxygen and carbon increase substantially over the same time period. Despite the much smaller external fueling compared to the discharge on a fresh lithium surface, the plasma density is actually higher, consistent with increased recycling and impurity influx. Comparing the neutral pressure before and after the discharge (not shown in the figure) indicates that the wall is acting as a very small particle source[82] and therefore recycling is near unity.

A significant range of recycling conditions have been achieved on LTX. Plasma discharges on fresh evaporatively-deposited solid lithium wall coatings show optimal performance and sub-unity recycling. These discharges also show substantially reduced oxygen emission consistent with the lithium reacting with water adsorbed onto the shell surface. With this wall condition, plasma current and discharge duration are limited by the OH system. Over time,

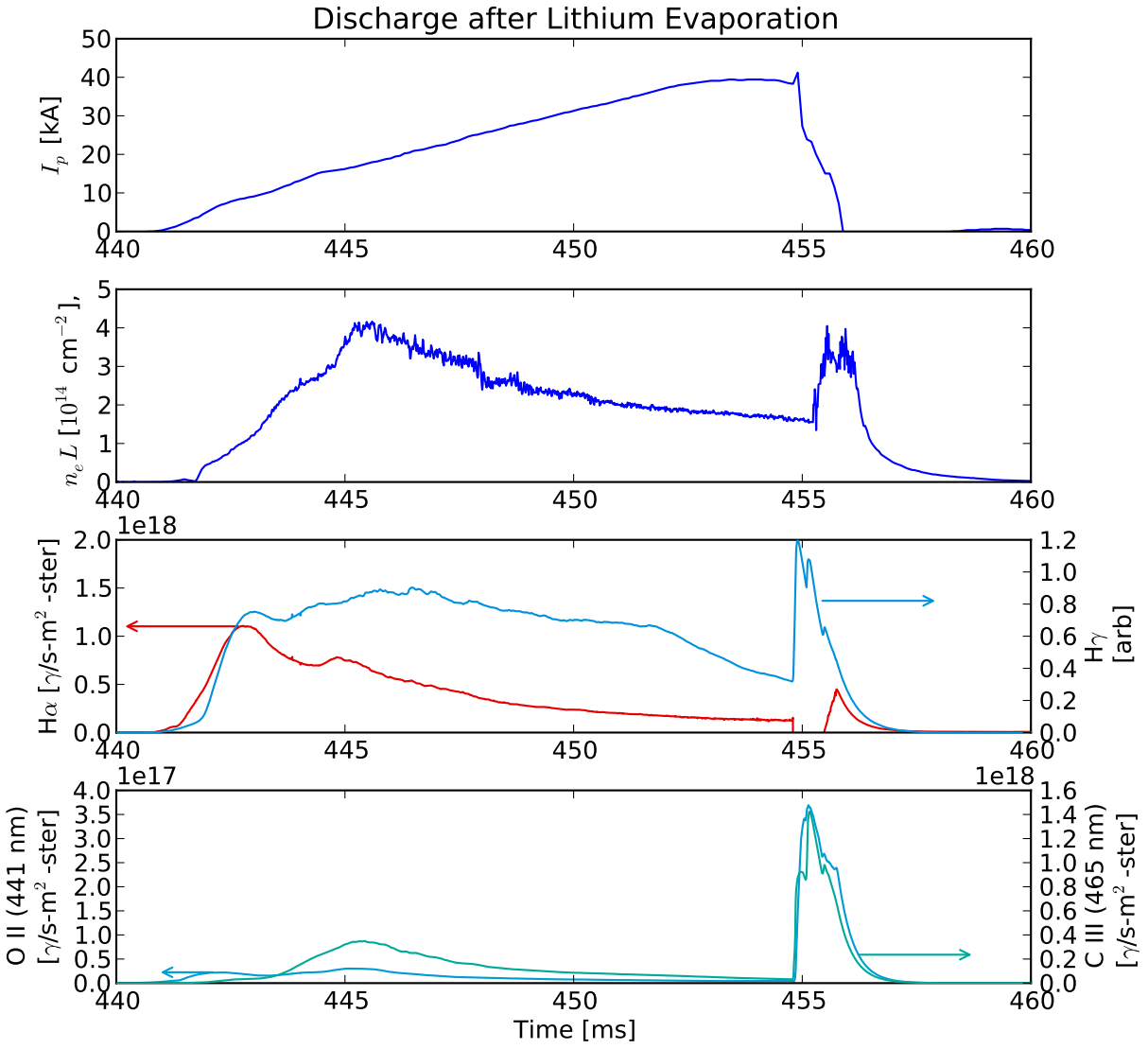

Figure 2.15: Plasma discharge on fresh lithium surface. A prefill of 5.5×10^{19} H atoms is used, followed a small amount of additional fueling from the MCI at 444 ms. The peak plasma current is about 40 kA. After the fueling is terminated, the density decreases slowly, consistent with sub-unity recycling. At 445 ms, the plasma becomes unstable and hits a material surface, resulting in a current crash and ingestion of hydrogen and other impurities from the wall. This is LTX shot 1010141157.

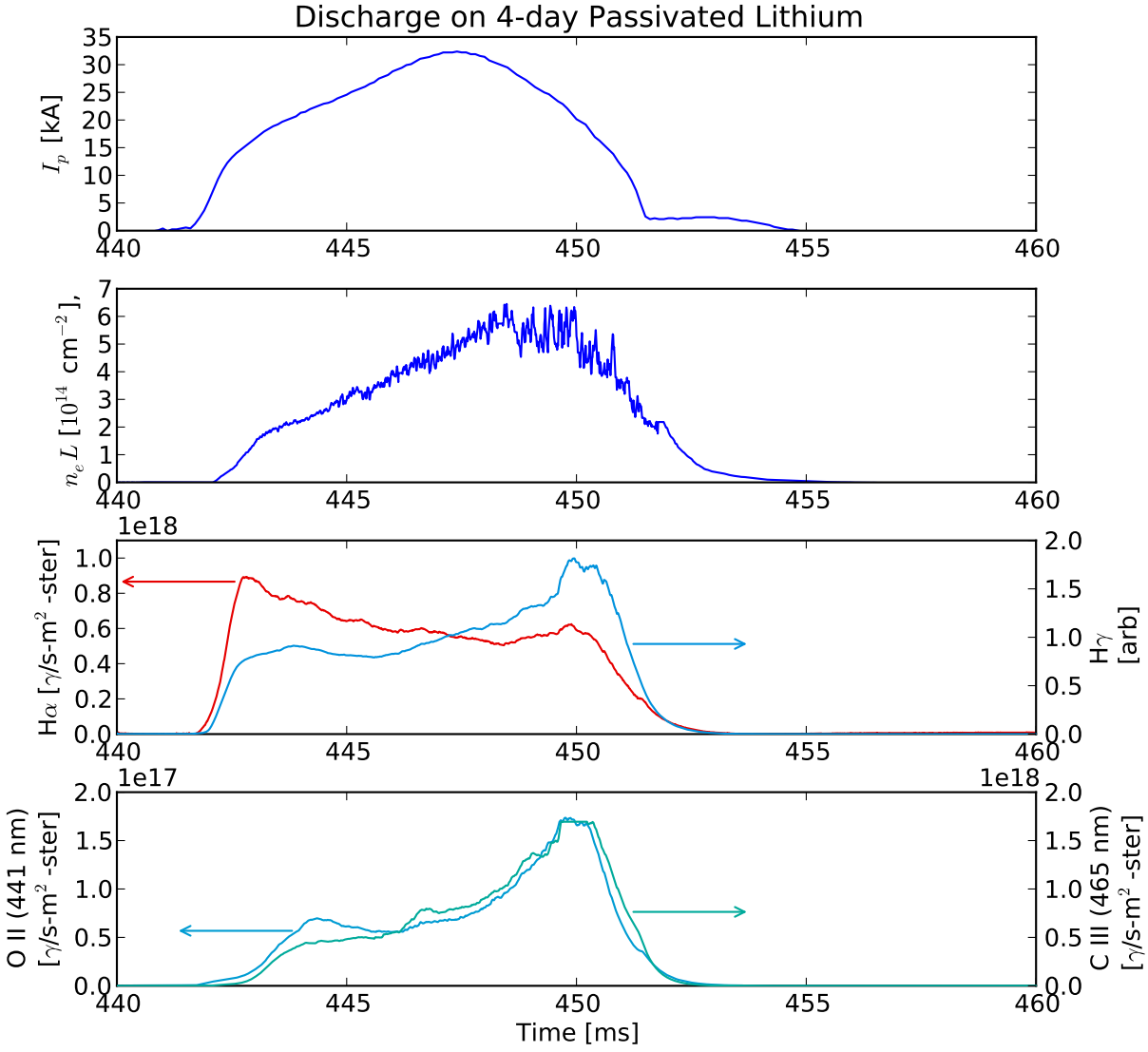

Figure 2.16: Plasma discharge on 4-day passivated lithium. A prefill of 5.3×10^{18} H atoms was used[82]. The plasma current and duration are substantially lower than the discharge on a fresh lithium surface. Although the Hα emission decreases slightly over the course of the discharge, Hγ emission and impurity emission from oxygen and carbon show the opposite trend. The peak electron density is higher than in the discharge on a fresh lithium surface despite a factor of 10 less external fueling. This is LTX shot 1010181122.

plasma operations and reactions with residual gases passivate the lithium surface producing near unity recycling and degraded plasma performance. This thesis will focus detailed analysis on high-performance discharges with cold evaporatively-deposited lithium coatings in order to quantify the achievable recycling on LTX.

Chapter 3

Core Transport Modeling

The goal of this work was to explore the characteristics of plasma micro-turbulence for the types of profiles that might be expected with a low-recycling boundary and core fueling. In particular, linear and non-linear simulations were performed using GYRO. First, local (flux-tube) simulations were performed in order to study the basic physics of plasma micro-turbulence in density-gradient-dominated regimes. In order to compare with other work, plasma parameters from a common community benchmark (the Cyclone base-case[71]) were used. Since other work has explored the effect of flux-surface shaping, a simple circular flux-surface geometry was assumed here. Several cases have been considered:

1. $\nabla T_e = \nabla T_i = 0$ and varying $\nabla P = \nabla n$ in order to examine micro-turbulence driven by only a density gradient.

2. $\nabla T_i = 0$ and varying ∇P and $\eta_e \doteq \nabla T_e / \nabla n$ in order to examine only TEM transport as the free-energy gradient is distributed between density and temperature.

3. $\nabla T_i = \nabla T_e = \nabla T$ and varying ∇P and $\eta \doteq \nabla T / \nabla n$ in order to examine coupled ITG and TEM transport.

What distinguishes this work is the focus on the regime where $\eta \lesssim 1$.Over 10,000 linear simulations have been performed, each using 8 processor cores and 5 minutes to 24 hours of

wall-clock time. Over 50 nonlinear flux-tube simulations have been performed, each using 128–256 processor cores and 36–96 hours of wall-clock time. In order to analyze output from the simulations, a suite of object-oriented visualization tools have been developed in Python using the NumPy, SciPy, and Matplotlib libraries. All of the analysis presented here used these post-processing utilities.

In addition, an analytic model has also been derived which captures important features of the nonlinear simulations. To complement this, a thermodynamic constraint on the energy flux has been derived as a function of the ratio of the temperature gradient to density gradient.

In addition to studying the basic physics of plasma micro-turbulence in regimes dominated by a density gradient, simulations were also performed using profiles predicted for a specific high-temperature device with a low-recycling boundary under the assumption that transport obeys a neoclassical scaling. The goal with this work was to evaluate potential enhancement to the transport as a result of micro-turbulence. First, a tool was developed to convert output from the ASTRA-ESC equilibrium and transport code into a form suitable to initialize a GYRO simulation. Next, linear simulations were carried out in order to examine the gyrokinetic stability of the predicted profiles.

3.1 Introduction to Kinetic Plasma Modeling and Gyrokinetics

3.1.1 Kinetic Plasma Models

As discussed in the introduction, collisional processes and turbulence can both cause particle and thermal transport across the magnetic field. To model both processes, for a plasma composed of N particles, one could begin with an equation of motion for each plasma particle

(ion or electron) which is affected by the fields from the other $N-1$ point-charges.

$$\frac{\partial \mathbf{x}_i}{\partial t} = \mathbf{v}_i(t) \tag{3.1}$$

$$\frac{\partial \mathbf{v}_i}{\partial t} = \frac{q_i}{m_i} \sum_{j \neq i} \left(\mathbf{E}_j(\mathbf{x}_i(t), t) + \frac{\mathbf{v}_i}{c} \times \mathbf{B}_j(\mathbf{x}_i(t), t) \right) \tag{3.2}$$

Alternatively, this problem could be cast in 7 dimensions (3 in physical space, 3 in velocity space, and time) by defining a microscopic distribution function containing each individual particle:

$$N(\mathbf{x}, \mathbf{v}, t) = \sum_i \delta(\mathbf{x} - \mathbf{x}_i(t)) \delta(\mathbf{v} - \mathbf{v}_i(t)) \tag{3.3}$$

$$\frac{\partial N}{\partial t} + \mathbf{v} \cdot \frac{\partial N}{\partial \mathbf{x}} + \frac{q}{m} \left(\mathbf{E}^m(\mathbf{x}, t) + \frac{\mathbf{v}}{c} \times \mathbf{B}^m(\mathbf{x}, t) \right) \cdot \frac{\partial N}{\partial \mathbf{v}} = 0. \tag{3.4}$$

The expression above is called the Klimontovich equation. An N-body description such as this captures all the physics, but is intractable for the problem at hand because of the large ($\gtrsim 10^{20}$) numbers of particles involved. Consider instead smoothed functions of the microscopic quantities:

$$\delta N(\mathbf{x}, \mathbf{v}, t) \doteq N(\mathbf{x}, \mathbf{v}, t) - \langle N(\mathbf{x}, \mathbf{v}, t) \rangle, \quad f(\mathbf{x}, \mathbf{v}, t) \doteq \langle N(\mathbf{x}, \mathbf{v}, t) \rangle \tag{3.5}$$

$$\delta \mathbf{E}(\mathbf{x}, t) \doteq \mathbf{E}^m(\mathbf{x}, t) - \langle \mathbf{E}^m(\mathbf{x}, t) \rangle, \quad \mathbf{E}(\mathbf{x}, t) \doteq \langle \mathbf{E}^m(\mathbf{x}, t) \rangle \tag{3.6}$$

$$\delta \mathbf{B}(\mathbf{x}, t) \doteq \mathbf{B}^m(\mathbf{x}, t) - \langle \mathbf{B}^m(\mathbf{x}, t) \rangle, \quad \mathbf{B}(\mathbf{x}, t) \doteq \langle \mathbf{B}^m(\mathbf{x}, t) \rangle \tag{3.7}$$

$$\frac{\partial f}{\partial t} + \mathbf{v} \cdot \frac{\partial f}{\partial \mathbf{x}} + \frac{q}{m} \left(\mathbf{E}(\mathbf{x}, t) + \frac{\mathbf{v}}{c} \times \mathbf{B}(\mathbf{x}, t) \right) \cdot \frac{\partial f}{\partial \mathbf{v}} = C[f(\mathbf{x}, \mathbf{v}, t)] \tag{3.8}$$

$$C[f(\mathbf{x}, \mathbf{v}, t)] \doteq \frac{q}{m} \left\langle \left(\delta \mathbf{E}(\mathbf{x}, t) + \frac{\mathbf{v}}{c} \times \delta \mathbf{B}(\mathbf{x}, t) \right) \cdot \frac{\partial f}{\partial \mathbf{v}} + \left(\mathbf{E}(\mathbf{x}, t) + \frac{\mathbf{v}}{c} \times \mathbf{B}(\mathbf{x}, t) \right) \cdot \frac{\partial \delta N(\mathbf{x}, \mathbf{v}, t)}{\partial \mathbf{v}} \right\rangle \tag{3.9}$$

$$\frac{\partial \delta N}{\partial t} + \mathbf{v} \cdot \frac{\partial \delta N}{\partial \mathbf{x}} + \frac{q}{m} \left(\delta \mathbf{E}(\mathbf{x}, t) + \frac{\mathbf{v}}{c} \times \delta \mathbf{B}(\mathbf{x}, t) \right) \cdot \frac{\partial \delta N}{\partial \mathbf{v}} = 0 \tag{3.10}$$

The complete system now also includes Maxwell's equations, which describe how the macroscopic fields are coupled to the particle distribution function and to each other. So far, no physics has been lost in going from the microscopic picture of eqs. 3.1–3.4 to the macroscopic picture of eqs. 3.8–3.10; however, even if only the evolution of the distribution function $f(\mathbf{x}, \mathbf{v}, t)$ is of interest, it cannot be computed without also evolving the full microscopic system. The term on the right-hand-side of eq. 3.8 contains the physics of how the microscopic system couples to the macroscopic system. The dimensionless quantity that characterizes the importance of thermal effects to microscopic coupling is the number of particles in a Debye sphere, also known as the plasma parameter (in CGS units):

$$\Lambda \doteq \frac{4\pi}{3} n \lambda_D^3, \quad \lambda_D^2 \doteq \frac{T}{4\pi n e^2} \tag{3.11}$$

In some systems, such as cold ion traps, this term is small and inter-particle correlations dominate over thermal effects. In plasmas such as those of interest in this work, $\Lambda \gg 1$ and thermal effects dominate. This allows the term on the right-hand-side of eq. 3.8 to be greatly simplified by only considering 2-particle correlations. The effect of this "collision operator" is to maximize entropy under the constraints of conservation of density, momentum, and energy of the sum of all particles at a particular point in space.

3.1.2 The Gyrokinetic Model

In magnetized plasmas, if the phenomena of interest occur on a long time-scale relative to the frequency of gyration around the magnetic field (cyclotron motion), then eq. 3.8 can be further simplified by averaging over this motion. One approach would be to perform a coordinate transform from the instantaneous particle position in physical and velocity space to the position of the gyro-center, the velocity parallel to the magnetic field, the velocity perpendicular to the magnetic field (or the magnetic moment), and the gyro-

phase. The reader interested in the derivation of the gyrokinetic equation can examine references[124,125,126,127,128,129,130,131,132,133,134]. The Fokker-Planck equation (eq. 3.8) can be further simplified if the equilibrium is assumed to be slowly-varying, while perturbations are small but can vary rapidly:

$$\frac{\omega}{\Omega_i} \sim \frac{k_\parallel v_{ti}}{\Omega_i} \sim \frac{\rho_i}{L_\perp} \sim \frac{e\varphi}{T_e} \sim \frac{\delta f}{f_0} \sim O(\epsilon) \ll 1 \tag{3.12}$$

The first ratio limits applicability to frequencies below the cyclotron frequency. The second ratio considers phenomena with wavelengths along the magnetic field much larger than the gyro-radius. The third ratio limits applicability to regions where the length scale of radial gradients in equilibrium quantities (eg. density, temperature) are long relative to the ion gyro-radius. The last two ratios limit consideration of small perturbations in the fields and distribution functions. The idea is to separate eq. 3.8 into ensemble-averaged and fluctuating components, then expand in powers of the gyrokinetic parameter, $\rho_* \doteq \rho_s/a$. $\rho_s = c_s/\Omega_i$ is the ion sound radius, while a is an equilibrium length scale, for example the minor radius of the torus. The lowest-order, ensemble-averaged equation gives a Maxwellian distribution in a rotating frame. The first-order ensemble-averaged equation is the drift-kinetic equation which is used to solve for the neo-classical (i.e., collisional) transport. The first-order equation for the fluctuating quantities gives the gyro-kinetic equation.

3.2 A Simplified Analytic Model

Although the coupled gyrokinetic-Maxwell system is too complex to solve analytically, examination of the linearized system can give useful insights. The following treatment loosely follows chapters 2 and 3 of ref. 128 with some modification.

3.2.1 Ion Treatment

Linearizing the gyro-kinetic equation for the ions gives the perturbed ion gyro-center distribution function:

$$f_i = \frac{f_{i,0} J_0 e\phi}{T_{i,0}} \left(\frac{k_\parallel v_\parallel + \omega_{dv,i} - \omega^T_{*,i}}{\omega - k_\parallel v_\parallel - \omega_{dv,i}} \right) = \frac{f_{i,0} J_0 e\phi}{T_{i,0}} \left(-1 + \frac{\omega - \omega^T_{*,i}}{\omega - k_\parallel v_\parallel - \omega_{dv,i}} \right) \tag{3.13}$$

where $J_0 \doteq J_0(k_\perp v_\perp / \Omega_i)$ is the gyro-average operator. A low-β plasma equilibrium has been assumed in order to treat the grad-B and curvature drifts together. This combined drift and the diamagnetic drift are:

$$\omega_{dv,\sigma} = \omega_{d,\sigma}(v_\parallel^2 + \mu B)/v_{t\sigma}^2, \quad \omega^T_{*,\sigma} = \omega_{*,\sigma} \left[1 + \eta_\sigma \left(\frac{v_\parallel^2}{2 v_{t\sigma}} + \frac{\mu B}{v_{t\sigma}} - \frac{3}{2} \right) \right] \tag{3.14}$$

For simplicity, the poloidal dependence of the drifts is neglected and the values at the outboard midplane are used:

$$\omega_{d,\sigma} = -\sigma \frac{k_\theta \rho_\sigma v_{t\sigma}}{R}, \quad \omega_{*,\sigma} = -\sigma \frac{k_\theta \rho_\sigma v_{t_\sigma}}{L_n} \tag{3.15}$$

where σ is 1 (-1) for ions (electrons). The total perturbed ion density is the sum of the polarization density and the density of ion gyro-centers. The ion polarization density is:

$$\frac{n_{i,pol}}{n_0 e\phi / T_{i,0}} = -\left(1 - \Gamma_0\right) \approx -\frac{b_i}{1 + b_i} \tag{3.16}$$

where $\Gamma_n \doteq I_n(b_i) e^{-b_i}$ and $b_i \doteq k_\perp^2 \rho_i^2$. To calculate the ion density, we will treat the ions as a fluid by expanding the resonant denominator with the "cold plasma" or "fast wave" approximation ($\omega \gg \omega_{dv,i}, k_\parallel v_{ti}$) keeping terms to second order. We will also assume $\omega, \omega_{dv,i}, \omega_{*,i} \gg k_\parallel v_{ti}$ and drop the $k_\parallel v_{ti}$ terms entirely. The ion gyrocenter density is found by integrating the perturbed distribution function for ion gyro-centers, weighted by another power of J_o to take full account of finite Larmor radius (FLR) effects:

$$\frac{n_{i,gc}}{n_0 e\phi/T_{i,0}} = -\frac{\omega_{*,i}}{\omega}\left[\Gamma_0 + \eta_i b_i \delta\Gamma_{1,0}\right] + \frac{\omega_{di}}{\omega}\left(1 - \frac{\omega_{*,i}}{\omega}\right)\left[2\Gamma_0 + b_i\delta\Gamma_{1,0}\right]$$
$$- \frac{\omega_{*,i}\omega_{di}\eta_i}{\omega^2}\left[(2-b_i)\Gamma_0 + b_i(3-2b_i)\delta\Gamma_{1,0}\right] + \frac{\omega_{di}^2}{\omega^2}\left[(7-b_i)\Gamma_0 + b_i(5-2b_i)\delta\Gamma_{1,0}\right] \quad (3.17)$$

where $\delta\Gamma_{1,0} \doteq \Gamma_1 - \Gamma_0$. The above expression is similar to eq. 18 in ref. 135 and eq. 1 in ref. 136 but contains additional terms. The total perturbed ion density, normalized to an electron adiabatic response is:

$$\frac{n_i}{n_0 e\phi/T_{e,0}} = -\frac{1}{\tau} + \frac{\Gamma_0}{\tau} + \frac{\omega_{*,e}}{\omega}\left[\Gamma_0 + \eta_i b_i \delta\Gamma_{1,0}\right] - \frac{\omega_{de}}{\omega}\left(1 + \frac{\omega_{*,e}\tau}{\omega}\right)\left[2\Gamma_0 + b_i\delta\Gamma_{1,0}\right]$$
$$- \frac{\omega_{*,e}\omega_{de}\tau\eta_i}{\omega^2}\left[(2-b_i)\Gamma_0 + b_i(3-2b_i)\delta\Gamma_{1,0}\right] + \frac{\omega_{de}^2\tau}{\omega^2}\left[(7-b_i)\Gamma_0 + b_i(5-2b_i)\delta\Gamma_{1,0}\right]. \quad (3.18)$$

3.2.2 Electron Treatment

Electrons are treated much differently from ions for two reasons. First, as a result of their small mass, at the same temperature, their gyro-radius is much less than that of the ions; therefore, when considering perturbations on the ion-scale and larger, the electron position and gyro-center can be assumed equal. Secondly, the fast motion of electrons along magnetic field lines allows passing electrons to respond adiabatically to potential perturbations. Electrons which have a larger ratio of magnetic moment to energy are trapped in the magnetic well of the outboard side of the torus, and bounce back and forth between the turning points. The frequency of this bounce motion is much faster than that of the perturbations of interest, so they "bounce-average" the perturbation. The total perturbed electron distribution function can be written as:

$$f_e = f_{e,0}\frac{e\phi}{T_e} + \left[\langle f_e\rangle_b - f_{e,0}\frac{e\,\langle\phi\rangle_b}{T_e}\right]_t \quad (3.19)$$

where the subscript t indicates this is evaluated only for trapped electrons. Passing electrons are treated as adiabatic. The response of the bounce-averaged trapped particles is found by linearizing the bounce-averaged electron drift-kinetic equation:

$$\langle f_e \rangle_b = -f_{e,0} \frac{e \langle \phi \rangle_b}{T_{e,0}} \left(\frac{\langle \omega_{dv,e} \rangle_b - \omega^T_{*,e}}{\omega - \langle \omega_{dv,e} \rangle_b} \right) = f_{e,0} \frac{e \langle \phi \rangle_b}{T_{e,0}} \left(1 - \frac{\omega - \omega^T_{*,e}}{\omega - \langle \omega_{dv,e} \rangle_b} \right) \tag{3.20}$$

The bounce-averaged drift is the toroidal precession frequency, which for small ϵ is:

$$\langle \omega_{dv,e} \rangle_b = \omega_{d,e} \frac{v^2}{2v_{te}^2} G(\hat{s}, \kappa), \quad G(\hat{s}, \kappa) \doteq \left(2\frac{E(\kappa^2)}{K(\kappa^2)} - 1 \right) + 4\hat{s} \left(\frac{E(\kappa^2)}{K(\kappa^2)} - 1 + \kappa^2 \right). \tag{3.21}$$

E and K are the complete elliptic integrals of the first and second kind, $\hat{s}$ is the shear in the q-profile, and κ is related to the turning points for trapped particles:

$$\kappa^2 \doteq \frac{1 - \mu B_{min}/E}{2\epsilon_B} = \sin^2(\theta_t). \tag{3.22}$$

To get the perturbed electron density, an integration is performed over energies and the trapped particle pitch-angles. Define

$$X_n(a) \doteq \frac{2^n}{(2n+1)!!} \frac{2}{\sqrt{\pi}} \int_0^\infty \frac{E^{n+1/2} e^{-E} dE}{1 - E/a} \tag{3.23}$$

$$a \doteq \frac{\omega}{\omega_{d,e}} \frac{1}{G(\hat{s}, \kappa)}. \tag{3.24}$$

Note that X_n, for $n > 0$, can be written in terms of X_0; for example,

$$X_1(a) = \frac{2}{3} a (X_0(a) - 1), \quad X_2(a) = \frac{4}{15} a^2 (X_0(a) - 1) - \frac{2}{5} a \tag{3.25}$$

Then the perturbed density and energy can be written as:

$$\frac{n_e}{n_0} = \phi - \langle\langle\phi\rangle_b\rangle_\kappa + \frac{\omega_{*,e}}{\omega}\left(1-\frac{3}{2}\eta_e\right)\langle X_0(a)\langle\phi\rangle_b\rangle_\kappa - \frac{3}{2}\frac{\omega_{d,e}}{\omega}\left\langle\left(G(\hat{s},\kappa)-\frac{R}{L_n}\eta_e\right)X_1(a)\langle\phi\rangle_b\right\rangle_\kappa \tag{3.26a}$$

$$\frac{E_e}{\frac{3}{2}n_0T_{e,0}} = \phi - \langle\langle\phi\rangle_b\rangle_\kappa + \frac{\omega_{*,e}}{\omega}\left(1-\frac{3}{2}\eta_e\right)\langle X_1(a)\langle\phi\rangle_b\rangle_\kappa - \frac{5}{2}\frac{\omega_{d,e}}{\omega}\left\langle\left(G(\hat{s},\kappa)-\frac{R}{L_n}\eta_e\right)X_2(a)\langle\phi\rangle_b\right\rangle_\kappa \tag{3.26b}$$

where following ref. 20,

$$\hat{B}(\theta) \doteq B(\theta)/B_{min}, \quad \epsilon_B \doteq (1-B_{min}/B_{max})/2 \tag{3.27a}$$

$$\langle g(\kappa)\rangle_\kappa \doteq \int_{\sin(\theta/2)}^1 \frac{2\epsilon_B\hat{B}(\theta)\kappa g(\kappa)d\kappa}{\sqrt{1-\hat{B}(\theta)(1-2\epsilon_B\kappa^2)}} \tag{3.27b}$$

$$\langle\phi(\theta)\rangle_b \doteq \left[\int_{-\theta_t}^{\theta_t}\frac{\phi(\theta)d\theta}{\sqrt{1-\hat{B}(\theta)(1-2\epsilon_B\kappa^2)}}\right] / \left[\int_{-\theta_t}^{\theta_t}\frac{d\theta}{\sqrt{1-\hat{B}(\theta)(1-2\epsilon_B\kappa^2)}}\right] \tag{3.27c}$$

$X_0(a)$ can be written in terms of the complex error function, or for $\mathrm{Im}(a) > 0$, the plasma dispersion function ($Z(\zeta)$.

$$X_0(a) = -2a\left[1-\sqrt{\pi}\sqrt{-a}e^{-a} - i\sqrt{\pi}\sqrt{a}e^{-a}\,\mathrm{erf}(i\sqrt{a})\right] = -2a\left[1+\sqrt{a}Z(\sqrt{a})\right] = a\frac{dZ(\zeta)}{d\zeta},\ \zeta\to\sqrt{a} \tag{3.28}$$

At this point, quasineutrality is enforced in order to set up the dispersion relation. This is the approach taken by ref. 3, except in their case, they set $G(\hat{s},\kappa)\to 1$, $\langle\langle\phi\rangle_b\rangle_\kappa \to \phi$. They also neglect the last three terms in the equation for the perturbed ion density (eq. 3.18). Instead, the "fast wave" approximation $\omega \gg \omega_{dv,e}$ is used to expand the X_n integrals. Note that this expansion of the resonant denominator is not valid near marginal stability, where

this approximation breaks down. To second order:

$$X_0(a) \approx 1 + \frac{3}{2a} + \frac{15}{4a^2} + ... \tag{3.29a}$$

$$X_1(a) \approx 1 + \frac{5}{2a} + \frac{35}{4a^2} + ... \tag{3.29b}$$

$$X_2(a) \approx 1 + \frac{7}{2a} + \frac{63}{4a^2} + ... \tag{3.29c}$$

Next let

$$\langle \langle \phi \rangle_b \rangle_\kappa = A_0 f_T \phi \tag{3.30a}$$

$$\left\langle \frac{\langle \phi \rangle_b}{a^n} \right\rangle_\kappa = \frac{\omega_{d,e}^n}{\omega^n} \langle G(\hat{s}, \kappa)^n \langle \phi \rangle_b \rangle_\kappa = \frac{\omega_{d,e}^n}{\omega^n} A_n f_T \phi \tag{3.30b}$$

where $f_T = \sqrt{2\epsilon_B}$ is the fraction of trapped particles at the outboard midplane ($\theta = 0$). With this expansion, the total perturbed electron density becomes:

$$\begin{aligned} \frac{n_e}{n_0 e\phi/T_{e,0}} = 1 - A_0 f_T + f_T \frac{R}{L_n} \frac{\omega_{d,e}}{\omega} \left(1 - \frac{3}{2}\eta_e\right) \left(A_0 + \frac{3}{2}\frac{\omega_{d,e}}{\omega} A_1 + \frac{15}{4}\frac{\omega_{d,e}^2}{\omega^2} A_2\right) \\ + \frac{3}{2}\frac{R}{L_n}\frac{\omega_{d,e}}{\omega}\eta_e f_T \left(A_0 + \frac{5}{2}\frac{\omega_{d,e}}{\omega} A_1 + \frac{35}{4}\frac{\omega_{d,e}^2}{\omega^2} A_2\right) - \frac{3}{2}\frac{\omega_{d,e}}{\omega} f_T \left(A_1 + \frac{5}{2}\frac{\omega_{d,e}}{\omega} A_2 + \frac{35}{4}\frac{\omega_{d,e}^2}{\omega^2} A_3\right) \end{aligned} \tag{3.31a}$$

Eq. 3.31a can then be re-expressed as:

$$\frac{n_e}{n_0 e\phi/T_{e,0}} = [1 - A_0 f_T] + f_T \left[A_0 \frac{R}{L_n} - \frac{3}{2} A_1\right] \frac{\omega_{d,e}}{\omega} + f_T \frac{3}{2} \left[A_1 \frac{R}{L_n} (1 + \eta_e) - \frac{5}{2} A_2\right] \left(\frac{\omega_{d,e}}{\omega}\right)^2 \tag{3.32}$$

3.2.3 Linear Frequencies

The linear dispersion relation is obtained from the quasineutrality condition $n_e = n_i$ and the equations for the perturbed ion and electron densities (eq. 3.18 and eq. 3.32).

$$\begin{aligned} 0 = &\left[1 - A_0 f_T + \frac{1-\Gamma_0}{\tau}\right] \\ &+ \frac{\omega_{d,e}}{\omega}\left[f_T\left(A_0\frac{R}{L_n} - \frac{3}{2}A_1\right) - \frac{R}{L_n}\left[\Gamma_0 + \eta_i b_i \delta\Gamma_{1,0}\right] + \left[2\Gamma_0 + b_i\delta\Gamma_{1,0}\right]\right] \\ &+ \frac{\omega_{d,e}^2}{\omega^2}\left\{\frac{3}{2}f_T\left[A_1\frac{R}{L_n}(1+\eta_e) - \frac{5}{2}A_2\right] + \tau\frac{R}{L_n}\left[2\Gamma_0 + b_i\delta\Gamma_{1,0} + \eta_i\left[(2-b_i)\Gamma_0 + b_i(3-2b_i)\delta\Gamma_{1,0}\right]\right]\right. \\ &\left. -\tau\left[(7-b_i)\Gamma_0 + b_i(5-2b_i)\delta\Gamma_{1,0}\right]\right\} \end{aligned} \tag{3.33}$$

This quadratic expression can be numerically evaluated very quickly to get an approximate solution for the growth rate. Due to the fast-wave approximation (among others), solutions are most accurate when strongly unstable.

3.2.4 Quasilinear Fluxes

Since the (outward) radial $\mathbf{E}\times\mathbf{B}$ velocity is $\mathbf{v}_{E\times B}\cdot\mathbf{r} = -ick_y\phi/B$, electrostatic potential perturbations that vary in the diamagnetic direction give rise to cross-field particle and thermal transport. The quasilinear particle and electron energy fluxes are due to a particular wavenumber are:

$$\Gamma \doteq \Re\left\langle \int_T d^3v f_e \mathbf{v}^*_{E\times B}\right\rangle = \Im\left\langle k_y\rho_s c_s \int_T 4\pi v^2 dv \left\langle f_{e,0}\left(\frac{\omega-\omega^T_{*,e}}{\omega - \langle\omega_{dv,e}\rangle_b}\right)\frac{|\langle\phi\rangle_b|^2}{T^2_{e,0}}\right\rangle_\kappa\right\rangle \tag{3.34a}$$

$$q_e \doteq \Re\left\langle \int_T d^3v \frac{m_e v^2}{2} f_e \mathbf{v}^*_{E\times B}\right\rangle = \Im\left\langle k_y\rho_s c_s \int_T 4\pi v^2 dv \frac{m_e v^2}{2}\left\langle f_{e,0}\left(\frac{\omega-\omega^T_{*,e}}{\omega - \langle\omega_{dv,e}\rangle_b}\right)\frac{|\langle\phi\rangle_b|^2}{T^2_{e,0}}\right\rangle_\kappa\right\rangle. \tag{3.34b}$$

The T subscripts in the preceding expressions indicate the velocity-space integrals are over the trapped region of velocity space only. The outer angle brackets represent an integral over the flux-surface. Note that passing electrons are assumed to respond adiabatically to the potential perturbation; therefore, the real part of f_e and $\mathbf{v}^*_{E\times B}$ are 90° out-of-phase for passing particles. As a result, passing electrons do not contribute to cross-field fluxes.

3.3 The GYRO Code

The GYRO code[137] solves the gyrokinetic-Maxwell system of equations in a toroidally-symmetric geometry. It was developed by R. Waltz and J. Candy at General Atomics Corp. and has a large non-developer user base throughout the world. The initial motivation for the code was to generalize a previous δf flux-tube gyrokinetic-Maxwell code (GS2) by allowing profile variation. A local approximation or flux-tube limit is the limit of $\rho_* \to 0$, in which the micro-turbulence on a particular flux-tube depends only on the local plasma properties and their gradients. The resulting transport in this limit necessarily has gyro-Bohm scaling. Actual experiments, however, often show non gyro-Bohm transport, and GYRO is able to capture both[138]. Since GYRO can treat global profiles, it can simulate large regions of the torus where fluctuations are small relative to equilibrium quantities and hence the δf formalism is valid. GYRO can also perform flux-tube simulations by taking $\rho_* \to 0$. First results using the code were obtained in 2002, and new features are being added routinely. Small, linear flux-tube simulations can be performed on a laptop, while large non-linear runs can run efficiently on over 100,000 processors at national high-performance computing systems. A complete description of the GYRO code and the specific equations it solves can be found in refs. 137 and 139.

Numerically, the code discretizes the gyro-center distribution function on a fixed (Eulerian) grid using field-following coordinates. GYRO uses energy and pitch-angle (at the outboard midplane) as its velocity-space coordinates. The pitch-angle integration is done

separately for trapped and passing particles, since there may be a discontinuity at the trapped-passing boundary. Gauss-Legendre integration is used to determine the optimal locations of the grid points and the weights when computing fluid moments[137].

In physical space, GYRO uses a spectral decomposition in the diamagnetic direction. As a result, the gyro-average becomes simply a multiplication. Efficient fast Fourier transforms are used for the nonlinear terms. GYRO uses finite differences in the remaining directions, with upwinding in the direction along the magnetic field. The nonlinear Poisson bracket term is treated with the Arakawa method[140]. In addition, in the direction along the magnetic field, GYRO uses an evenly-spaced grid in orbit time rather than in physical space. This eliminates the integrable singularities at the trapped-particle turning points and solves the Ampere cancellation problem[137]. Since the positions of the grid points along the magnetic field varies depending on pitch angle, a simple finite-difference treatment of Maxwell's equations does not work. Instead, the fields are represented with a blending function expansion.

Temporally, GYRO uses a 2nd-order implicit-explicit Runge-Kutta strong-stability-preserving (IMEX-RK-SSP) integrator. Electron advection along the magnetic field is the "stiff" term which is treated implicitly. Treating this term implicitly overcomes the parallel electron Courant limit and the even more troublesome electrostatic-Alfven wave Courant limit[137]. All terms are "non-stiff" and treated explicitly.

3.3.1 A Note on Units

Results of all the simulations presented in this chapter are in normalized units. For linear simulations, growth rates and real frequencies are normalized to $\bar{c}_s/a$ where $\bar{c}_s = \sqrt{\bar{T}_e/m_i}$ and a is the outer midplane minor radius of the last closed-flux surface of the toroidal device. The overbar indicates that T_e is to be evaluated at the center of the simulation domain. Nonlinear fluxes are in gyro-Bohm units. Recall from eq. 1.4 that $D_{gB} = (\rho_s/a)D_B$, where the Bohm diffusion coefficient $D_B \doteq \Omega_i \rho_s^2 = T_e c/(eB)$. The gyro-Bohm particle and energy

fluxes are[139]:

$$\Gamma_{gB} \doteq \bar{n_e}\bar{c_s}\left(\frac{\bar{\rho}_{s,\text{unit}}}{a}\right)^2 \tag{3.35}$$

$$q_{gB} \doteq \bar{n_e}\bar{c_s}\bar{T_e}\left(\frac{\bar{\rho}_{s,\text{unit}}}{a}\right)^2. \tag{3.36}$$

Once again, the overbar indicates that T_e and n_e are to be evaluated at the center of the computational domain. Also, in evaluating $\bar{\rho}_{s,\text{unit}}$, the "unit" subscript indicates that the magnetic field to be used is[139,141]:

$$B_{\text{unit}} \doteq \frac{1}{r}\frac{d\chi_t}{dr} = \frac{q}{r}\frac{d\psi}{dr}, \tag{3.37}$$

where χ_t is the toroidal flux, q is the safety factor, and ψ is the poloidal flux. The effective field strength B_{unit} corresponds to the field strength if the arbitrarily-shaped flux-surface were deformed into a circle with the enclosed flux held fixed. To convert the fluxes from the simulations described in sections 3.4– to diffusion coefficients:

$$D = \frac{\Gamma}{\Gamma_{gB}}\frac{R\bar{c_s}}{R/L_n}\left(\bar{\rho}_{s,\text{unit}}/a\right)^2 \tag{3.38}$$

$$\chi_{tot} = \frac{q}{q_{gB}}\frac{R\bar{c_s}}{R/L_T}\left(\bar{\rho}_{s,\text{unit}}/a\right)^2, \tag{3.39}$$

where the "tot" subscript indicates that the total energy flux is used and not merely the conductive contribution, and R is the major radius of the magnetic axis of the toroidal device. Finally, collisionalities in this work are reported in units of $\nu a/\bar{c_s}$. This is related to $\nu_* \doteq \nu_e q R_0/(\epsilon^{3/2} v_{te})$ by:

$$\nu_* = q\left(1 + Z_{\text{eff}}\right)\frac{\nu_{ei}a}{\bar{c_s}}\left(\frac{R_0}{a}\right)^{5/2}\left(\frac{a}{r}\right)^{3/2}\sqrt{\frac{m_e}{m_i}} \tag{3.40}$$

3.4 Purely Density-Gradient-Driven Simulations

The first case considered in this thesis was that of purely density-gradient-driven transport. The particular question of interest is if all the free-energy is transferred to the density without modifying the equilibrium in other respects, what level of turbulent transport can be expected? How does this level of transport compare to ITG transport? To compare with other work, the benchmark "Cyclone base case" [71] (with kinetic electrons) was used, with the temperature gradients set to zero. The density gradient was varied to examine the onset of instability and the stiffness of the transport relative to the ITG case.

Parameter	EQU Model	R_0/a	r/a	q	$\hat{s}$	R/L_n	R/L_{T_e}	R/L_{T_i}	T_i/T_e	$\nu_{ei}a/c_s$
Cyclone	$\hat{s}-\alpha$	2.778	0.5	1.4	0.786	0.8	6.9	6.9	1.0	0.0
∇n	$\hat{s}-\alpha$	2.778	0.5	1.4	0.786	varied	0.0	0.0	1.0	0.0
	$\hat{s}-\alpha$	2.778	0.5	1.4	0.786	varied	0.0	0.0	1.0	0.01
	$\hat{s}-\alpha$	2.778	0.5	1.4	0.786	varied	0.0	0.0	0.2	0.0
	Miller-circle	2.778	0.5	1.4	0.786	varied	0.0	0.0	1.0	0.0
	Miller-circle	2.778	0.5	1.4	0.786	varied	0.0	0.0	1.0	0.01
$\eta_i = 0, \eta_e$ scan	Miller-circle	2.778	0.5	1.4	0.786	varied	$\eta_e R/L_n$	0.0	1.0	0.01
$\eta_i = \eta_e = \eta$ scan	Miller-circle	2.778	0.5	1.4	0.786	varied	$\eta R/L_n$	$\eta R/L_n$	1.0	0.01

Table 3.1: Simulation parameters used in the Cyclone base case as well as this work.

3.4.1 Linear Simulations show a Robust Instability

Linear simulations show a robust instability with a linear critical density gradient $R/L_n^{crit} = 1.35$. This result is similar to previous studies using the GS2 code [142,143]. They find a linear critical density gradient of $R/L_n^{crit} = 1.44$, but include small electron and ion collisions. The effects of geometry models, small collisions, and the T_i/T_e ratio were examined next. Growth rates are consistently higher when using a Miller circle rather than $s-\alpha$ geometry. This is most likely due to the difference between how the $s-\alpha$ and Miller circle models treat the $1/R$ term in the expression for the drifts (eq. 3.15). For a circular flux-surface, $R = R_0 + r\cos\theta$, which is the expression used by the Miller circle geometry. The $\hat{s}-\alpha$

geometry, however, merely uses the center, $R \to R_0$. Since the outboard side of the torus is where particles experience "bad curvature" (and are most unstable), and the linear critical gradient can be expressed in terms of R_{local}/L_n, the Miller circle model with $(R_0+r)/L_n$ will be more unstable. For the parameters in these simulations, the instability drive R_{local}/L_n is 18% higher in the simulations using a Miller circle than in those with $s-\alpha$ geometry. A tiny collisionality (comparable to what might be expected in a reactor) is shown to substantially reduce the growth rate for these modes. Cold ions are also stabilizing.

3.4.2 Nonlinear Simulations show Significant Thermal Transport

Nonlinear simulations show substantial particle and energy fluxes (fig. 3.3a). Plots of the particle flux versus simulation time (fig. 3.3b) show that the simulations are temporally well converged. Although the linear growth rates are substantial beyond the range of $k_y\rho_s$ included in the simulations, examination of the particle flux versus mode (fig. 3.3c) shows that sufficiently high wavenumbers are retained in the simulations. The flux peaks for $k_y\rho_s = 0.2 - 0.3$ and is dominated by modes with $k_y\rho_s < 0.5$.

These simulations also reproduce the nonlinear up-shift found in previous work[142,143]. In addition to providing a helpful cross-code validation, it is interesting to compare the nonlinear critical gradient and fluxes with the ITG Cyclone case. With zero collisions, the density-gradient-driven TEM is shown to have a lower critical pressure gradient relative to the ITG case. Once nonlinearly unstable, the electron energy flux increases with pressure gradient about as sharply as for the Cyclone ITG case (with kinetic electrons), while the ion energy flux increases much slower than in the ITG case. Most notably, the TEM drives a substantial outward particle flux, in contrast to the ITG case which actually generates a particle pinch. The outward particle flux in the TEM case is so large in fact relative to the energy flux that $q_{e,i} < 3\Gamma T/2$, well below the $q_{e,i} = 5\Gamma T/2$ typically assumed for pure

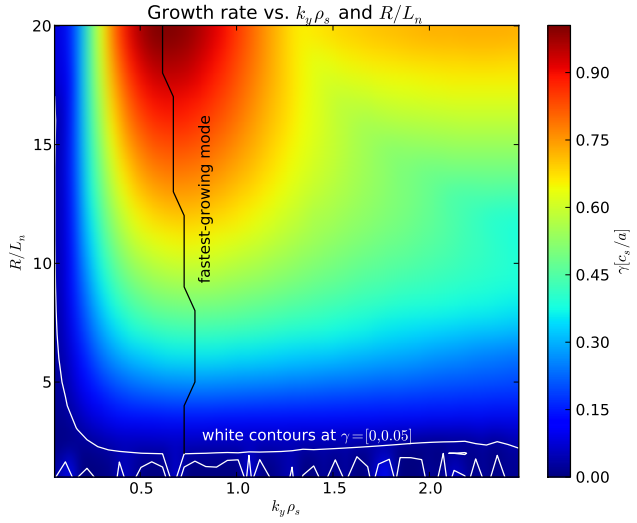

(a)

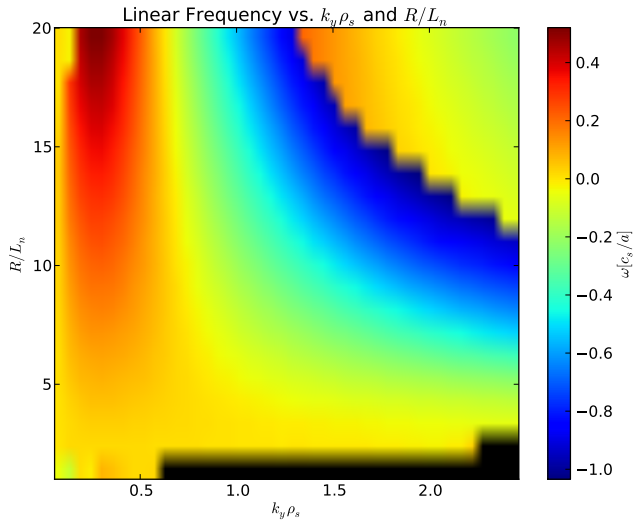

(b)

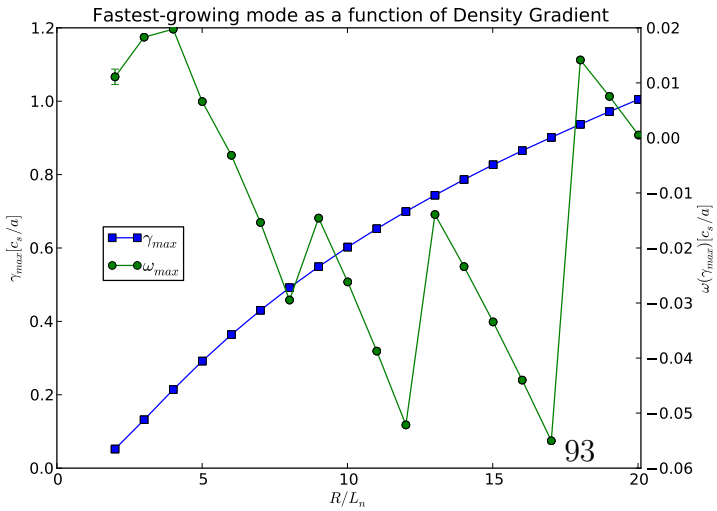

(c)

Figure 3.1: Growth rates (a) and real frequencies (b) for purely ∇n-driven modes as a function of binormal wavenumber ($k_y\rho_s$) and density gradient (R/L_n). Examining the fastest-growing mode as a function of driving gradient (c) shows a linear critical gradient of $R/L_n|_{crit} \approx 1.35$.

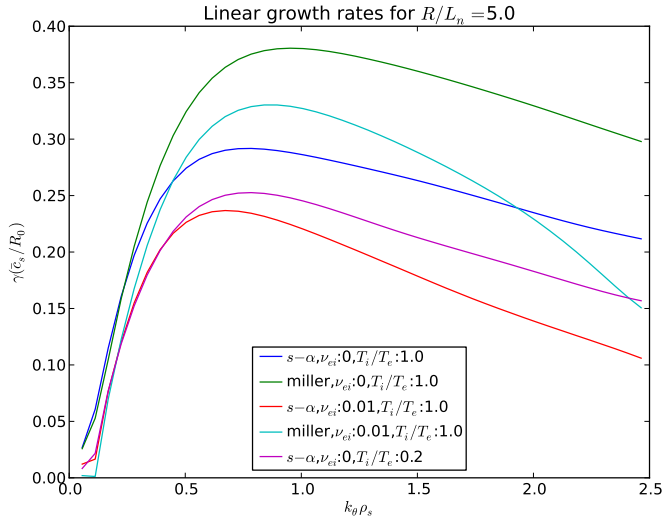

(a)

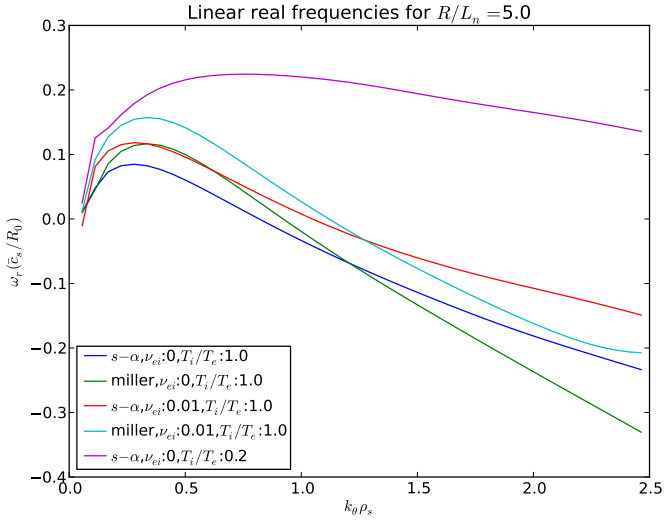

(b)

Figure 3.2: Growth rates (a) and real frequencies (b) for purely ∇n-driven modes as a function of binormal wavenumber ($k_y\rho_s$). A Miller-circle geometry produces substantially higher growth rates relative to the $s-\alpha$ geometry case. Addition of even a small collisionality is stabilizing. Likewise cold ions are also stabilizing.

convection. The ratio of energy flux to particle flux is shown to increase with density gradient (fig. 3.4) but is always less than 3/2.

Examination of the electron particle flux in velocity space (fig. 3.5) shows that only low-energy trapped particles are contributing to the flux. Passing particles virtually contribute nothing to the particle flux, which is consistent with passing electrons responding adiabatically to the potential perturbations. For the ions, low-energy trapped particles contribute dominantly to the flux, but low-energy passing particles also are involved. Note that the units for the vertical axis in the velocity-space flux figures are defined as,

$$\lambda \doteq \frac{v_\perp^2 B_{\text{unit}}(r)}{v^2 B(r,\theta)} = \frac{\mu}{E}. \tag{3.41}$$

In the equation above, μ has dimensions of E, since the magnetic field has been normalized out. λ is a constant-of-motion and ranges from 0 to $\lambda_{max} = B_{\text{unit}}(r)/B(r,\theta=0)$. The pitch angle at a given poloidal angle, is:

$$\xi \doteq \frac{v_\parallel}{v} = \sqrt{1 - \frac{\mu B(r,\theta)}{E B_{\text{unit}}(r)}}. \tag{3.42}$$

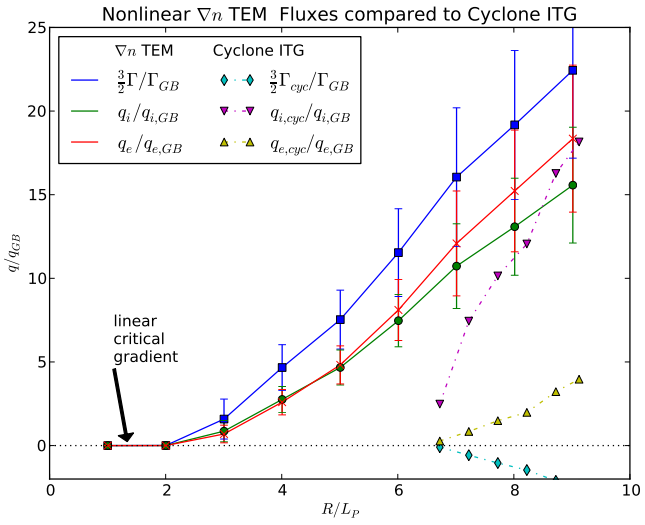

(a)

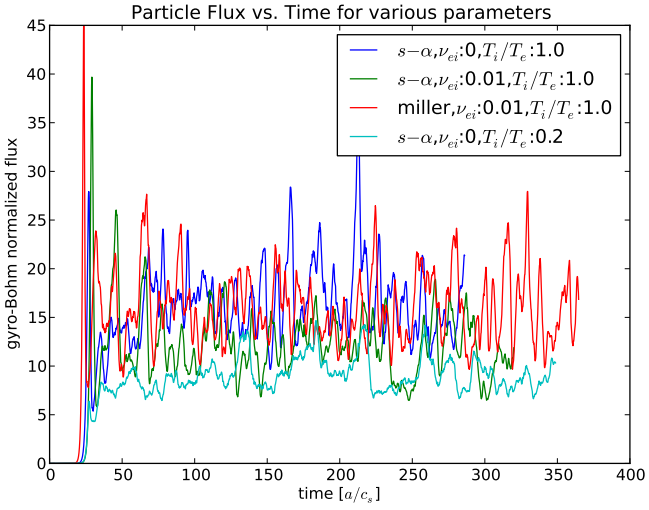

(b)

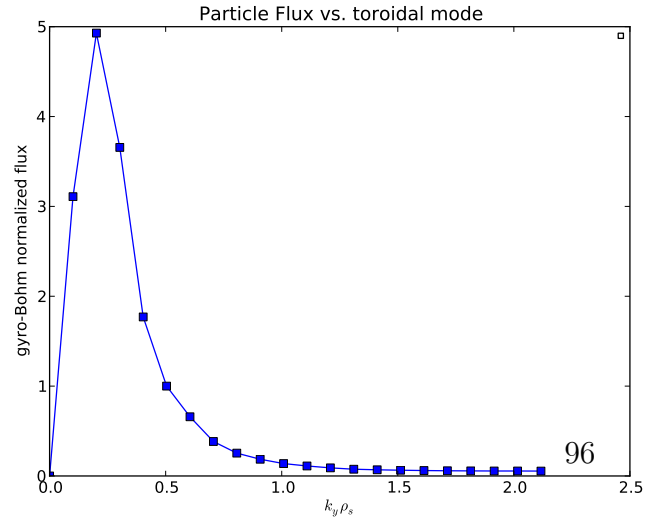

(c)

Figure 3.3: Nonlinear simulations of purely ∇n driven transport. (a) Particle and energy fluxes versus pressure gradient scale length, compared to the Cyclone ITG with drift-kinetic electrons[144]. As in previous work, a nonlinear up-shift is found for the purely ∇n-driven TEM[142]. The TEM becomes unstable at a much lower pressure gradient than the ITG; however, at large pressure gradients, the ion energy flux is larger in the ITG case. The electron energy flux is much higher than in the ITG case. Interestingly, the particle flux is very large as well, such that $q_{e,i} < 3\Gamma T/2$. (b) Particle flux versus simulation time for the $R/L_P = 10$ case using various geometry models, finite electron and ion collisions, and a reduced T_i/T_e. The biggest effect is seen with the reduced T_i/T_e, which decrease the flux by about 30%. Finite collisions are slightly stabilizing, while a Miller circle geometry model is less stable relative to the $s-\alpha$ case. (c) Particle flux versus toroidal mode for the $R/L_P = 10$. Although the linear growth rate spectrum shows modes with $k_y\rho_s > 1.5$ to be unstable, they contribute insignificantly to the transport as might be expected from a mixing-length argument.

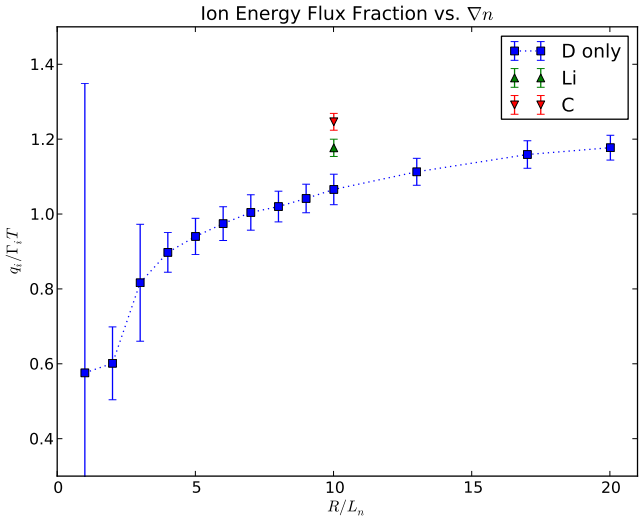

(a)

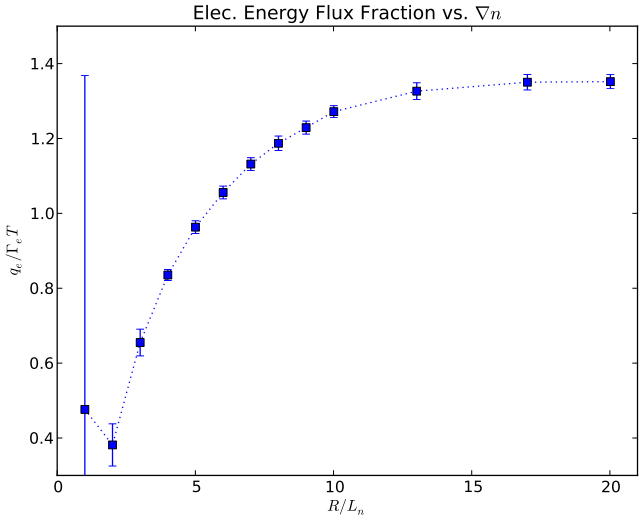

(b)

Figure 3.4: Ratio of energy flux to particle flux for (a) ions and (b) electrons versus density gradient. As the TEM goes from marginally stable to strongly unstable, the average energy flux per particle increases but is always less than $3T/2$. Interestingly, the average energy of lost impurity ions is higher than that of deuterium.

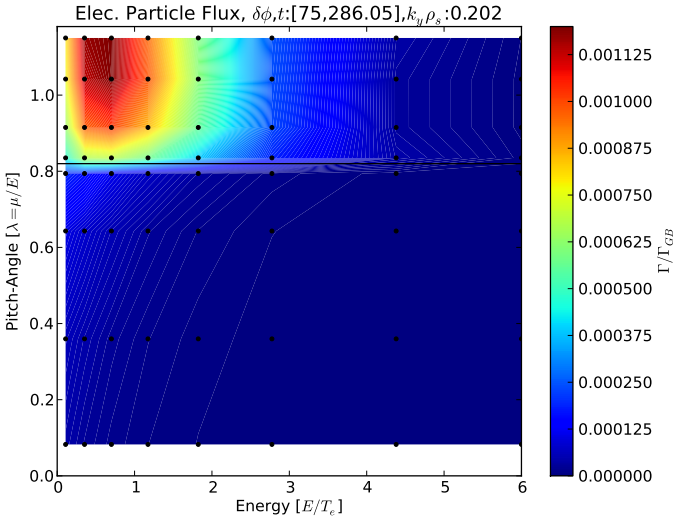

(a)

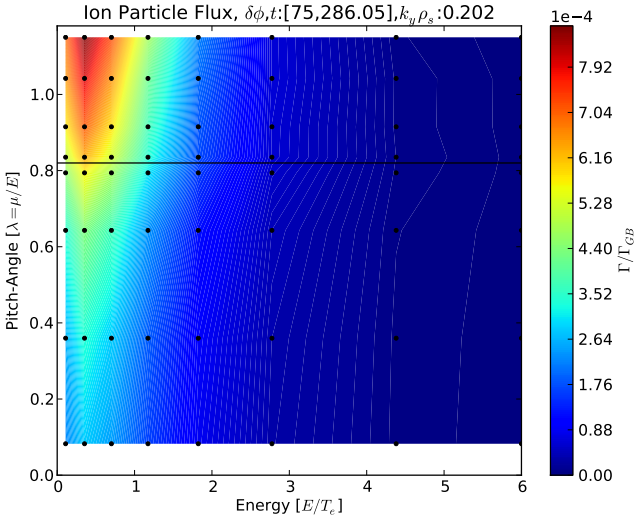

(b)

Figure 3.5: Velocity-space fluxes for (a) electrons and (b) ions for the case of purely ∇n-driven TEM transport. Passing electrons are almost completely adiabatic, so they do not contribute to the outward particle flux; in fact, only *low-energy* trapped electrons are diffusing outward. Low-energy trapped ions also constitute most of the ion particle flux, although low-energy passing ions are also involved.

3.4.3 Preferential Expulsion of Impurity Ions by Transport

Next, the effect of impurity ions was investigated. Quasineutrality sets a constraint on the ratios of deuteron density to electron density (f_D) and impurity density to electron density (f_i):

$$n_e = \sum_\sigma n_\sigma Z_\sigma = n_D + Z_i n_i = n_e(f_D + Z_i f_i). \tag{3.43}$$

Note that the ratio of impurity density to deuteron density is:

$$n_D/n_i = \frac{f_i}{1 - Z_i f_i}. \tag{3.44}$$

For these simulations, the density gradient is distributed evenly between the ions, so that f_D and f_i are independent of minor radius. Simulations were performed at $R/Ł_n = 10$ using $f_D = 0.85$ with fully-ionized Li ($Z = 3$) and C ($Z = 6$) as impurities.

Nonlinear simulations show a reduction in the electron density flux of 11% (13%) in the case with Li (C). More interestingly, re-scaling the particle flux by the ratio of the species density to the electron density shows that impurity ions are lost at a higher rate than deuterium ions. For Li, the normalized particle fluxes $n_D/n_{Li}\Gamma_{Li}/\Gamma_D = 1.30$, while for C, $n_D/n_C\Gamma_C/\Gamma_D = 1.44$. Another interesting result is that average energy of lost impurities is higher than the average energy of lost deuterons, shown in fig. 3.4a.

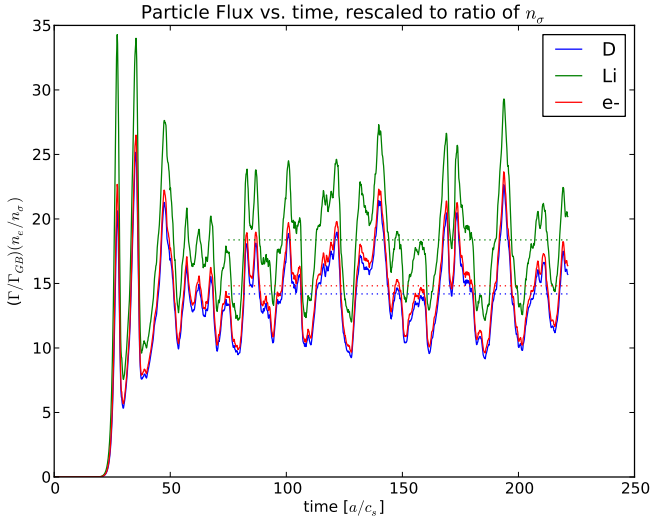

(a)

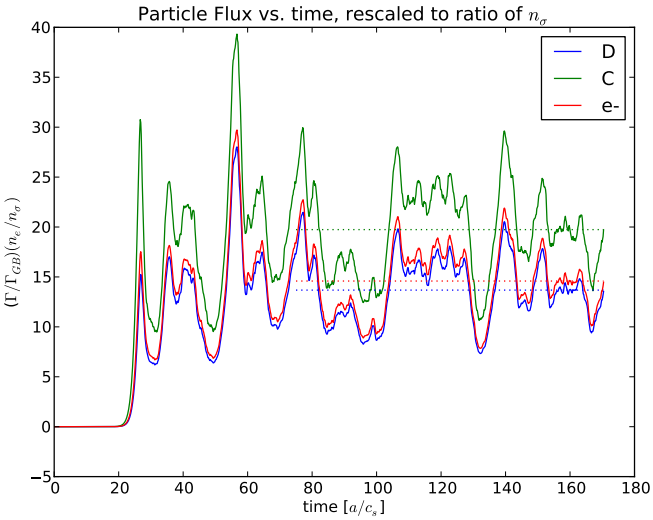

(b)

Figure 3.6: Particle flux versus simulation time for pure ∇n-driven transport including (a) fully-ionized lithium impurity and (b) fully-ionized carbon impurity. In both cases, n_D/n_e=0.85, so in (a) n_{Li}/n_e=0.05 and in (b) n_C/n_e=0.025. Particle fluxes are normalized to the ratio of n_σ/n_e. In (a), lithium is expelled at a 30% higher rate than deuterium. The effect is even stronger in carbon (b), which is expelled at a 44% higher rate than deuterium.

3.5 Simulations with Density and Electron Temperature Gradients

After examining the limiting case of a purely density-gradient drive on drift-wave stability and transport, the effect of distributing the free-energy gradient between density and electron temperature was explored. In order to scan $\eta_e \doteq \nabla T_e/\nabla n_e$ while keeping R/L_P fixed, the density gradient scale length is set to:

$$R/L_n = R/L_p \frac{1+\tau}{1+\eta_e+\tau(1+\eta_i)}. \tag{3.45}$$

In the preceding expression, $\tau = T_i/T_e$ and $\eta_e \doteq \nabla T_i/\nabla n_i$. For equal electron and ion temperatures, but zero ion temperature gradient:

$$R/L_n = R/L_p \frac{2}{2+\eta_e} \tag{3.46}$$

3.5.1 Linear Results

Linear simulations were carried out scanning R/L_P from 2 to 30, and η_e from 0 to 2 for modes with $k_y\rho_s$ from 0.112 to 2.0. Simulations used $s-\alpha$ geometry, including a small amount of electron pitch-angle scattering ($\nu_{ei}a/c_s$ =0.01) collisions and corresponding ion collisions.

The linear critical pressure gradient (fig. 3.7d is found to be smallest in the purely density-gradient-driven $\eta_e = 0$ case. The stabilizing effect of finite collisions increased the linear critical gradient from $R/L_P = 1.35$ in sec. 3.4.1 to $R/L_P = 1.6$. The linear critical pressure gradient has a maximum of R/L_P=3.8 at $\eta_e = 1$ before falling to about R/L_P=3.4 at $\eta_e = 2$. Although at low R/L_P, the value of η_e with the smallest growth rate is at $\eta_e \approx 1$, the least unstable η_e moves to $\eta_e = 0$ as R/L_P is increased (fig. 3.7a).

Figure 3.7b shows that for $\eta_e < 1$ real frequencies are near zero, but slightly in the electron diamagnetic direction (positive). The most unstable modes are within $0.4 < k_y\rho_s < 1$. At $\eta_e \approx 1$ there is a sharp transition to large wavenumbers. For strong drive, mode frequencies move into the ion diamagnetic direction, while for weak drive mode frequencies move more deeply in the electron diamagnetic direction. Very close to marginal stability ($R/L_P < 5$), modes behave differently. In this region, the most unstable modes are at $k_y\rho_s < 1$ and have small positive real frequencies, similar to modes with $\eta_e < 1$.

Figure 3.8a shows that the quasilinear electron energy flux per particle increases with η_e. Values of $q_e/(\Gamma T)$ are found near marginal stability for $\eta_e \approx 0$. The electron quasilinear energy flux per particle increases gradually with η_e until $\eta_e \approx 1$, beyond which it increases very quickly. At $\eta_e = 1$, $q_e \approx 5\Gamma T/2$. The quasilinear ion energy flux does not have an obvious dependence on η_e and remains < 1 throughout the domain.

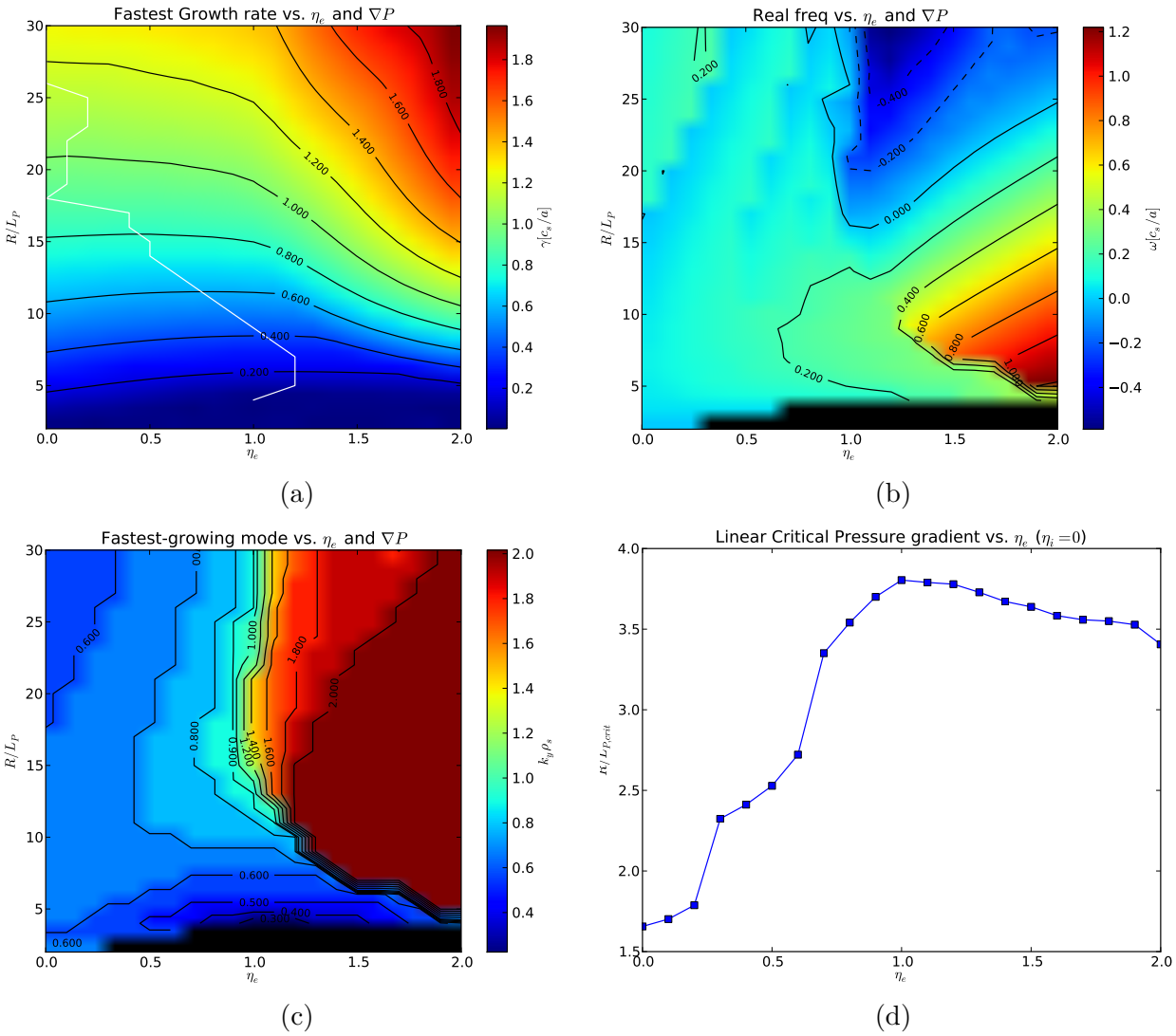

Figure 3.7: Real linear growth rates (a) and real frequencies (b) for the fastest-growing $k_y\rho_s$ mode (c) computed by GYRO at the for various density and temperature-gradient scale lengths. The white line in (a) traces the least unstable η_e for each R/L_P. For $\eta_e < 1$ real frequencies are near small and in the electron diamagnetic direction (positive). The most unstable modes are within $0.4 < k_y\rho_s < 1$. At $\eta_e \approx 1$ there is a sharp transition; for large (small) R/L_P, modes move into the ion (electron) diamagnetic direction. In either case, modes move to $k_y\rho_s > 1$. The exception is near marginal stability, $R/L_P < 5$; in this region, the most unstable modes are at $k_y\rho_s < 1$ and have small positive real frequencies. (d) Linear critical pressure gradient versus η_e. The largest pressure gradient that can be sustained before becoming linearly unstable is about $R/L_P = 3.8$ at $\eta_e = 1$.

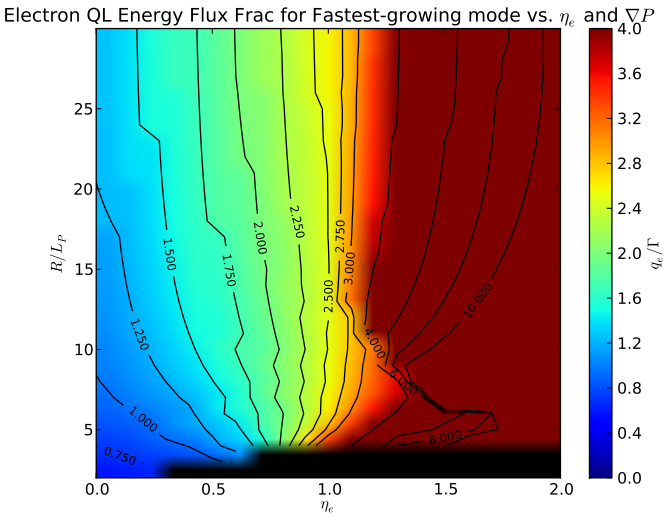

(a)

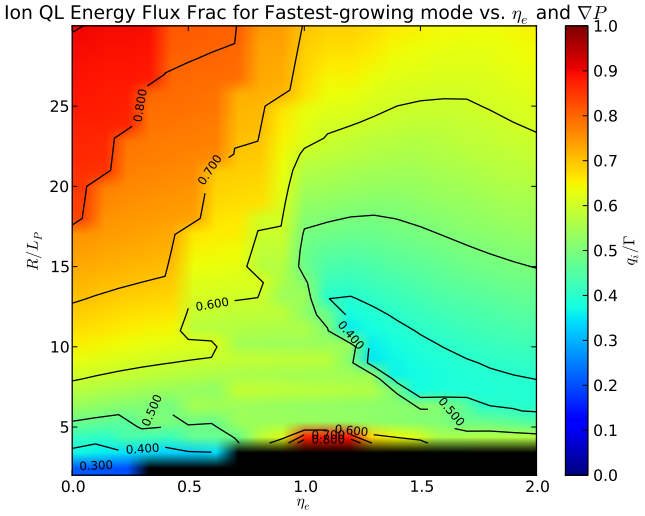

(b)

Figure 3.8: Quasilinear energy flux per particle for (a) the electrons and (b) the ions for the fastest growing mode. The electron energy flux per particle increases with η_e. The energy flux per particle increases slowly for $\eta_e < 1$. At $\eta_e = 1$ $q_e \approx 5\Gamma T/2$ and there is a sharp transition such that the energy flux per particle increases much faster with η_e for $\eta_e > 1$. The ion energy flux per particle remains small $q_i < \Gamma T$ throughout.

3.5.2 Quasilinear Model

At this point, it is worthwhile to consider what causes the quasilinear electron energy flux per particle (fig. 3.8a) to have such a clear dependence on η_e. From equation 3.34a and the form of the toroidal precession drift $\langle \omega_{dv,e} \rangle_b$, it can be seen that the electrons in resonance with the wave have energy

$$E_{\text{resonance}} = \frac{\omega}{c_s/R} \frac{1}{k_y \rho_s G(\hat{s}, \kappa)}. \tag{3.47}$$

Here the function $G(\hat{s}, \kappa)$ depends on the shear of the q-profile for the magnetic equilibrium ($\hat{s}$) and a pitch-angle variable κ. Might electrons satisfying this resonance condition be responsible for the observed trend in the quasilinear energy flux per particle? It would appear not. Since for positive shear nearly all trapped particles (except barely trapped particles) have $G > 0$, the resonance condition can only be satisfied for $\omega > 0$, i.e., the wave phase velocity is in the electron diamagnetic direction. Solution of the linear dispersion relation (using either eq. 3.33 or using the GYRO code in the next section) shows that the phase velocity is in the electron diamagnetic direction for small $k_y \rho_s$, but then moves in the ion diamagnetic direction for larger $k_y \rho_s$. The fastest-growing wave tends to be near where $\omega \approx 0$ or is only slightly negative, and does not move considerably for $\eta_e \lesssim 0.7$. Therefore, the condition for resonance is not strongly dependent on η_e, so the resonance condition cannot account for an increase in the average energy of lost particles with η_e.

Instead, examining equation 3.34a once again, the term in parentheses can be expanded for $\omega \gg \omega_{*,e}^T, \langle \omega_{dv}, e \rangle_b$, which one would expect to be valid far from marginal stability:

$$\left(\frac{\omega - \omega_{*,e}^T}{\omega - \langle \omega_{dv,e} \rangle_b} \right) \approx 1 - \frac{1}{w} \left(\omega_{*,e}^T - \langle \omega_{dv,e} \rangle_b \right) + O\left(\frac{\omega_{*,e}^T \langle \omega_{dv,e} \rangle_b}{\omega^2} \right). \tag{3.48}$$

Recognizing that only the imaginary part of this expression contributes to particle and thermal transport, the leading-order term will be directed outward if:

$$\frac{\gamma}{|w|^2}\left(\omega_{*,e}^T - \langle\omega_{dv,e}\rangle_b\right) > 0. \tag{3.49}$$

For growing modes, plugging in the definitions of the diamagnetic frequency and toroidal precession frequency gives constraints on the energy of electrons contributing to outward particle flux. Assuming $R/L_n > 3G(\hat{s},\kappa)/2$, which is almost certainly true if there is any instability at all gives three different regimes of η_e:

$$\frac{E}{T_e}\begin{cases} < \frac{1-3\eta_e/2}{G(\hat{s},\kappa)L_n/R-\eta_e} & \text{if } \eta_e < G(\hat{s},\kappa)L_n/R \\ > 0 & \text{if } G(\hat{s},\kappa)L_n/R < \eta_e < 2/3, \\ \geq \frac{3}{2}\frac{\eta_e-2/3}{\eta_e-G(\hat{s},\kappa)L_n/R} & \text{if } \eta_e \geq 2/3 \end{cases} \tag{3.50}$$

For small η_e there is a constraint on the maximum energy of electrons diffusing radially outward, while for large η_e there is a constraint on the minimum energy of electrons diffusing outward. Taking the ratio of the particle and energy fluxes (eq. 3.34a and eq. 3.34b) gives the average energy flux per particle. A fluid treatment of these equations is considered by expanding the resonant denominator and keeping only terms to first order in $\omega_{d,e}/\omega$,$\omega_{*,e}/\omega$, which gives:

$$\frac{q_e}{\Gamma T} = \left\langle\frac{E}{T_e}\right\rangle = \frac{3}{2}\left[(1+\eta_e) - \frac{A_1}{A_0}\frac{L_n}{R}\left(1-\frac{3}{2}\eta_e\right)\right] \tag{3.51}$$

The coefficients A_0 and A_1 are both of order unity and are defined in eq. 3.30a and eq. 3.30b. They describe the relationship between the potential perturbation and the average effective potential felt by all trapped electrons over their bounce motion. Therefore for small η_e, the outward radial flux is composed of trapped electrons with an energy near $3/2T_e$. Toroidal curvature effects (smaller R/L_n) reduce the average energy of lost electrons and can even

make the convective multiplier smaller than $3T_e/2$ if η_e is small. The average energy of lost electrons increases with η_e, and larger values of R/L_n decrease the average energy of lost electrons. Finally for $\eta_e > 2/3$, from eq. 3.50 it is seen that low-energy electrons move radially inward. Although expressions for the linear ion response to electrostatic perturbations and the bounce-averaged electron response have been known for some time, to the author's knowledge, an expression for the quasilinear energy flux per electron (eq. 3.51) does not appear in the literature.

3.5.3 Thermodynamic Constraints on the energy flux per particle

Often in fluid systems the total energy flux is separated into convective and conductive components:

$$\mathbf{q} = \mathbf{q}_{conv} + \mathbf{q}_{cond} = \gamma T \mathbf{\Gamma} - n\chi \nabla T \tag{3.52}$$

$$\mathbf{\Gamma} = -D\nabla n \tag{3.53}$$

The coefficient γ is taken to be 5/2 from consideration of adiabatic expansion. The previous linear simulations found that for $\eta_e \lesssim 1$, $q_e/(\Gamma T)$ was less than 5/2. From eq. 3.52, this would indicate that $\chi_e < 0$, which seems un-physical. In kinetic (and therefore gyrokinetic) systems, however, these linear relationships do not hold. Rather it is best to consider both q and Γ to be general nonlinear functions of fields (e.g., n, T) and gradients (e.g., ∇n, ∇T). Thermodynamics requires that the total change in entropy in the system be non-decreasing. The total entropy is:

$$S = -k_B \sum_a \int d^3x \int d^3v f \ln f \tag{3.54}$$

Assuming that f is a Maxwellian, and using particle conservation for a closed system while ignoring boundary terms, the total derivative of global entropy becomes:

$$\frac{dS}{dt} = -k_B \sum_a \int d^3x \left[\ln(n_a) \frac{\partial n_a}{\partial t} - \frac{3}{2} \ln T_a \frac{\partial n_a}{\partial t} - \frac{3}{2T_a} \frac{\partial n_a T_a}{\partial t} \right] \geq 0 \tag{3.55}$$

Particle and energy transport equations similar to the ones used by GYRO (eq. 55 and 56 of ref. 130) can be written as:

$$\frac{\partial n_a}{\partial t} + \frac{1}{V'} \frac{\partial}{\partial \Psi} (V' \Gamma_a) = \int d^3v I_a = S_a \tag{3.56a}$$

$$\frac{3}{2} \frac{\partial}{\partial t} n_a T_a + \frac{1}{V'} \frac{\partial}{\partial \Psi} (V' q_a) = \int d^3v \frac{m_e v^2}{2} (C_a + D_a + I_a) = Q_a \tag{3.56b}$$

For simplicity, the case of zero toroidal rotation and mean radial electric field has been considered and a flux-surface average of all quantities is assumed. The energy-weighted integrals of C_a, D_a, and I_a represent the collisional and turbulent energy transfers and the auxiliary injected power. Also, a slightly different expression for the energy flux is used here than ref. 130. The radial particle and energy fluxes are defined as:

$$\begin{pmatrix} \Gamma \\ q_e \end{pmatrix} \doteq \int d^3v f_a \begin{pmatrix} 1 \\ m_e v^2/2 \end{pmatrix} \mathbf{v} \cdot \nabla \boldsymbol{\Psi} \tag{3.57}$$

When run in a local (flux-tube) mode, the local entropy must be non-decreasing. Using the expressions above, the local entropy change for species a can be written as:

$$\frac{1}{k_B} \frac{dS_{loc}}{dt} = \sum_a \left\{ \frac{1}{T_a L_{n_a}} \left[q_a \eta_a - \frac{3}{2} \Gamma_a T_a \left(\eta_a - \frac{2}{3} \right) \right] + \frac{Q_a}{T_a} \right\} \geq 0 \tag{3.58}$$

In deriving the above expression, it is assumed that the sources on the right-hand-sides of eq. 3.56a and eq. 3.56b are zero, so that Q_a only contains the collisional and turbulent energy

exchange between species. Since $\sum_a Q_a = 0$, the Q_a/T_a term vanishes with the sum over species for the case of $T_i/T_e = 1$. Constraints for the energy flux are derived for two cases:

$$\eta_i = 0 \;\Rightarrow\; q_e \geq \Gamma T \left(\frac{3}{2} - \frac{2}{\eta_e}\right) \tag{3.59}$$

$$\eta_i = \eta_e = \eta \;\Rightarrow\; q_e + q_i \geq \Gamma T \left(3 - \frac{2}{\eta}\right) \tag{3.60}$$

Equation 3.59 shows that the energy flux per particle found in the linear simulations in sec. 3.5.1 and predicted by equation 3.51 are thermodynamically permitted. In the limit that $\eta \to \infty$, eq. 3.60 shows that the average energy flux $\bar{q} \doteq q_e + q_i \to 3/2\Gamma T$. Although the expression for the change in total entropy (eq. 3.55), is well-known in the literature (see for example ref. 130, 139), the author is not aware of a reference that specifically illustrates the thermodynamic constraints on the energy flux (eq. 3.59 and 3.60) as a function of η.

3.5.4 Temperature Profile Steepening

Having settled the question as to whether preferential diffusion of low-energy particles is thermodynamically permitted, the question arises as to how the transport would modify the profiles. If diffusion of hot particles causes the temperature profile to relax, what is the maximum average energy of outwardly-diffusing particles for the temperature profile to steepen? Going back to the energy transport equation (eq. 3.56b), and taking the flux-surface average of n_a and T_a separately (consistent with the low-transport ordering), the continuity equation can be used to remove the density from the time derivative:

$$\frac{3}{2} n_a \frac{\partial T_a}{\partial t} + \frac{1}{V'} \frac{\partial}{\partial \Psi} \left[V' \left(q_a - \frac{3}{2} \Gamma_a T_a \right) \right] + \frac{3}{2} \Gamma_a \frac{\partial}{\partial \Psi} (T_a) = Q_a - \frac{3}{2} T_a S_a \tag{3.61}$$

Ignoring for the moment the sources on the right-hand-side, this expression indicates that if the second term on the left-hand-side is less than zero and $\nabla T_a = 0$, the flux-surface average

temperature of species a will increase. Therefore, since $q_{e,i} < 3\Gamma T/2$ for the simulations with $\nabla T = 0$, transport would act to steepen the temperature profile. In the usual case, $\nabla T_a < 0$ (points inward) and relaxes the condition on the second term. By summing over all species and invoking quasi-neutrality, the collisional and turbulent energy exchange terms in Q_a can be eliminated, leaving only external sources in Q_a and S_a. In order to take into account profile variation, consider the mean density and nT product inside a given minor radius:

$$\langle n \rangle_r \doteq \frac{1}{V(r)} \int_0^r \frac{dV}{dr'} n(r') dr', \quad \langle nT \rangle_r \doteq \frac{1}{V(r)} \int_0^r \frac{dV}{dr'} n(r') T(r') dr' \tag{3.62}$$

Since temperature is not a conserved quantity in the same sense as density or energy, the volume-average temperature within minor radius r is defined here as:

$$\langle T \rangle_r \doteq \frac{\langle nT \rangle_r}{\langle n \rangle_r} \tag{3.63}$$

The volume-average temperature changes with time according to:

$$\frac{\partial}{\partial t} \langle T \rangle_r = -\frac{\langle nT \rangle_r}{\langle n \rangle_r^2} \frac{\partial \langle n_a \rangle}{\partial t} + \frac{1}{\langle n \rangle_r} \frac{\partial}{\partial t} \langle n_a T_a \rangle = \frac{2}{3 \langle n \rangle_r} \left[\langle Q \rangle_r - \frac{3}{2} \langle T \rangle_r \langle S \rangle_r - \frac{1}{V_r} \left(q_r - \frac{3}{2} \langle T \rangle_r \Gamma_r \right) \right] \tag{3.64}$$

In the absence of external sources, the average temperature will increase inside radius r if $q_r < 3/2 \langle T \rangle_r \Gamma_r$. It is important to understand that this requirement is not in terms of the temperature at radius r where the fluxes are evaluated (i.e., $T(r)$), but rather the volume-averaged temperature inside r, which is generally higher. For parabolic density and temperature profiles ($n/n_0 = 1 - (1 - n_a/n_0)(r/a)^2$, where n_0 and n_a correspond to the density at the magnetic axis and $r = a$ boundary, respectively), fig. 3.9 shows the resulting ratio between these two temperatures for various values of n_a/n_0 and T_a/T_0. This figure demonstrates first that the condition for the average temperature to rise inside a finite volume may be substantially relaxed, and is generally much easier to achieve at larger

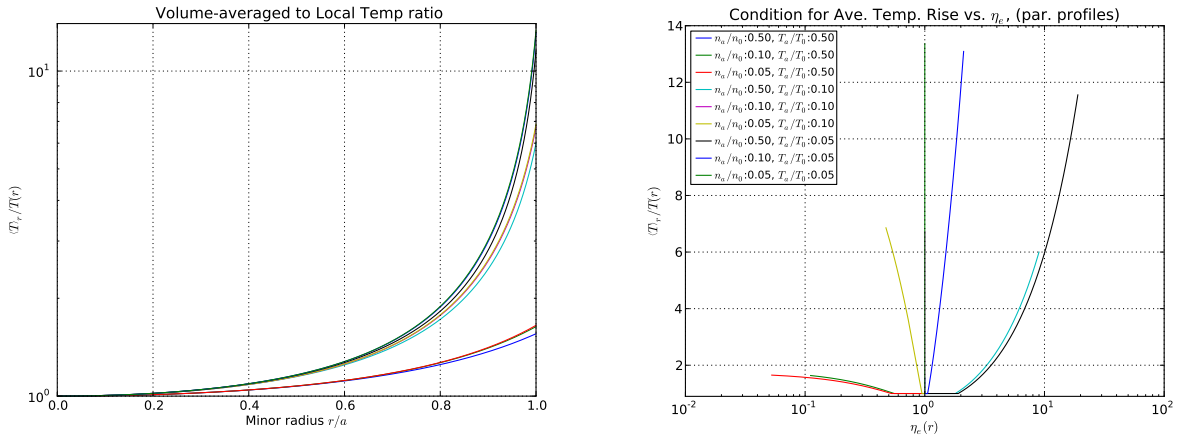

(a) (b)

Figure 3.9: Volume-averaged temperature to boundary temperature ratio ($\langle T \rangle_r / T(r)$) as a function of (a) r/a and (b) η_e for parabolic density and temperature profiles.

minor radii. Second, profiles with $\eta_e \approx 1$ can achieve high values of $\langle T \rangle_r / T(r)$ near the boundary. For example, for $n_a/n_0 = 0.1$, $T_a/T_0 = 0.1$ ($\eta_e = 1$ throughout), and at $r = a$, $\langle T \rangle_a / T(a) = 3.7$, indicating that $q(a) \leq 5.5\Gamma(a)T(a)$ for the average temperature to rise and hence temperature profile steepening to occur. This condition is referred to here as a "temperature pinch". Of course, if external particle sources are turned off, the density is decaying and so the temperature steepening is a transient effect. If the temperature profile steepens faster than the decaying density profile, equation 3.51 suggests that the average energy of diffusing particles will rise until the temperature pinch shuts itself off. If on the other hand, the system is maintained in steady-state with external sources of particles and energy, the temperature pinch effect is hidden in the balance equations for density and energy: the average temperature is simply higher than would be the case with a higher average energy of outwardly diffusing particles.

3.5.5 Nonlinear Results

Local, nonlinear simulations were carried out for several pressure gradients while scanning η_e frm 0 to 2. Simulations were performed with $s-\alpha$ geometry and no collisions, a Miller circle geometry with no collisions, and a Miller circle geometry with a small amount of electron and ion pitch-angle scattering ($\nu_{ei}a/c_s = 0.01$). Particle and energy fluxes from the latter case are shown in figure 3.10. These simulations used 128 velocity-space grid-points (8 energies, 8 pitch angles, and 2 signs of parallel velocity) and 22 toroidal modes spanning $k_y\rho_s$ from 0 to 2.1. In real space, the simulation domain spanned $[L_x/\rho_s,L_y/\rho_s]$=[63,62] with 96 radial grid-points and used ρ_s/a=4×10^{-4}. A nonlinear up-shift of the critical gradient appears for all η_e. For all pressure gradients, the particle flux and ion energy flux decrease with η_e, while the electron energy flux increases with η_e. The electron energy flux is many times higher than in the Cyclone ITG case for all the relevant pressure gradients. Although the critical pressure gradient is lower than the ITG case (even for $\eta_e = 1.5$), the ion energy flux increases less steeply with R/L_P than the ITG case. At moderate pressure gradients, the ITG drives more ion energy transport.

The saturated energy flux per particle is shown in figure 3.11 as a function of η_e for various choices of the total pressure gradient R/L_P. The solid line corresponds to the analytic estimate for q_e/Γ given by eq. 3.51, which does an excellent job of matching the nonlinear values for the cases of moderate and strong instability drive. The analytic estimate doesn't capture the weakly-driven case as well, consistent with a break-down of the "fast-wave" approximation used in its derivation. Nevertheless, the nonlinear simulations confirm that for relatively low η_e, decreasing R/L_P results in a lower energy flux per particle. Better agreement between the simple scaling and the nonlinear result can be obtained by using the ratio of A_1/A_0 and the coefficient in front of η_e as adjustable parameters. The cases with moderate and strong drive cross $q_e = 3\Gamma T/2$ at $\eta_e \approx 0.1$, while the case with weak drive crosses this point near $\eta_e \approx 0.35$. All cases cross $q_e = 5\Gamma T/2$ around $\eta_e \approx$0.7–0.8. Collision-

less simulations are very similar, since collisions primarily damp modes with $k_y\rho_s > 1$ which already contribute only a small amount to the total flux.

Velocity-space plots of the electron particle flux (fig. 3.12) also show that as the average energy of lost electrons increases with η_e. In addition, these plots show that above a threshold η_e there is a minimum energy below which electrons move inward. Nevertheless, for small values of η_e, low-energy electrons clearly dominate the total flux.

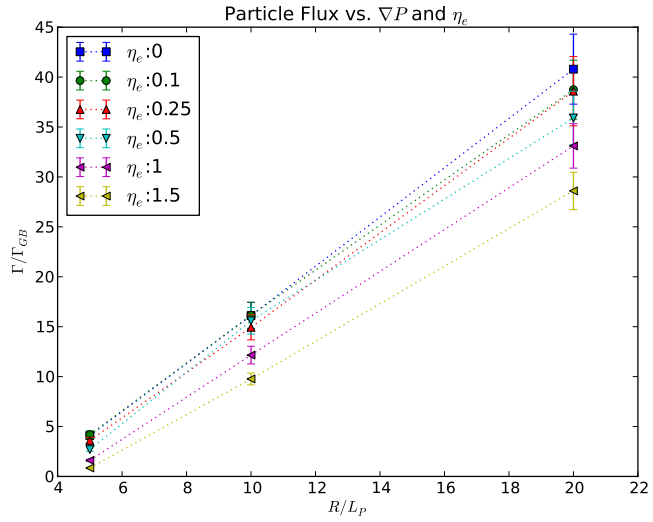

(a)

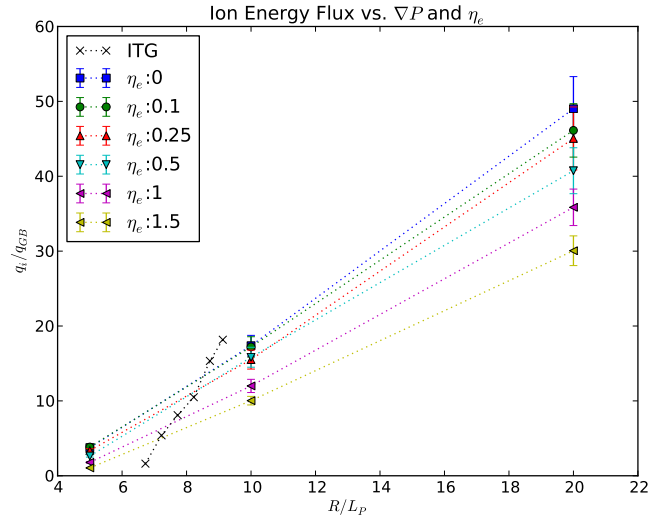

(b)

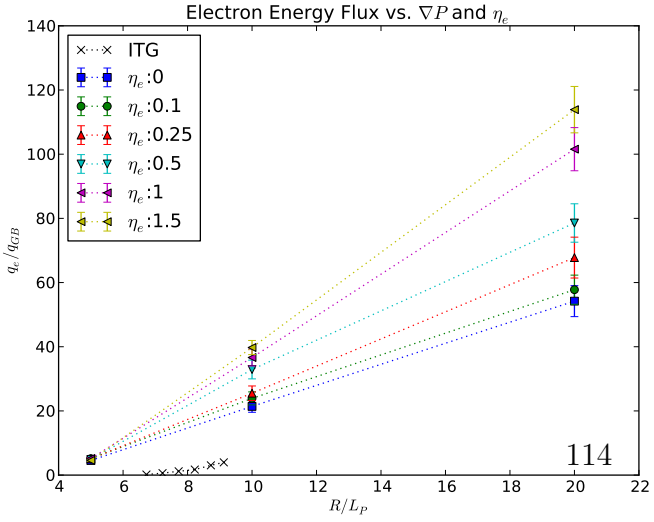

(c)

Figure 3.10: Nonlinear (a) particle flux, (b) ion energy flux, and (c) electron energy flux. The ion and electron energy fluxes are compared to ITG energy fluxes for the same pressure gradients; the particle flux in the ITG case is not shown because it is negative (inward). The ITG cases all have a fixed density gradient, $R/L_n = 2.2$, and increasing ion and electron temperature gradient from R/L_T=4.5 to 6.9. Note that the ITG energy fluxes were taken from ref. 144, which used $s-\alpha$ geometry and different numerical parameters. As a result, the ITG energy fluxes may be somewhat lower than if the same geometry and numerical parameters were used as in the other cases. Nevertheless, the electron energy fluxes are substantially higher than the ITG case for all η_e shown. Even the ion energy flux is unstable at lower pressure gradients; however, as R/L_P is increased beyond where the ITG case is unstable, the ion energy flux in the $\eta_i = 0$ cases do not increase as quickly with R/L_P.

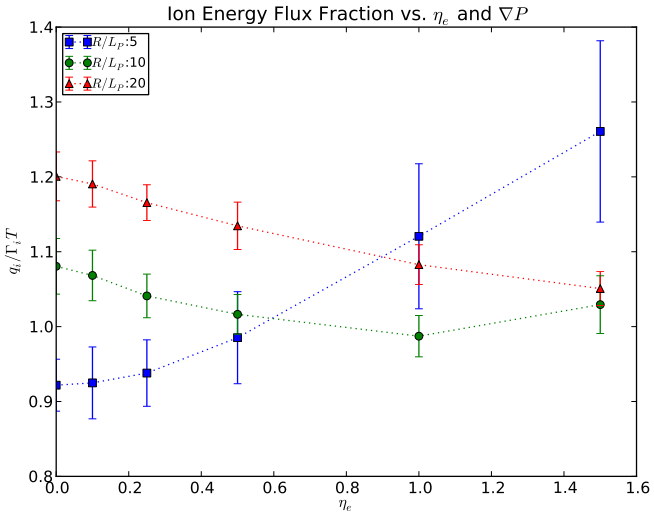

(a)

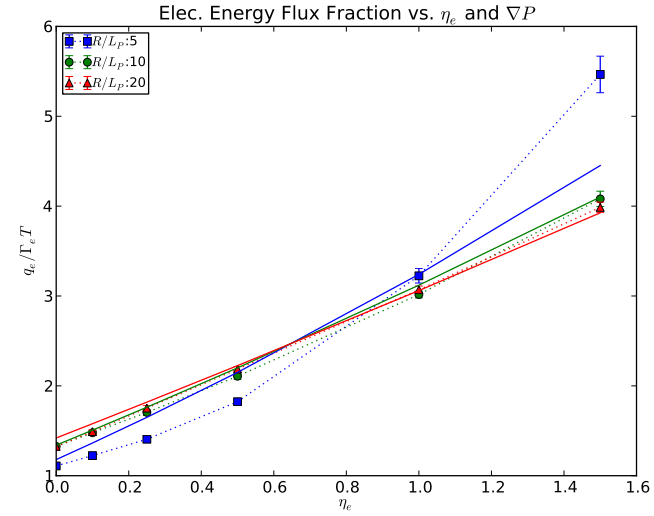

(b)

Figure 3.11: Nonlinear Energy flux per particle for (a) ions and (b) electrons, with the solid lines in (b) corresponding to the simple scaling of eq. (3.51). Note the different scales for ions and electrons.

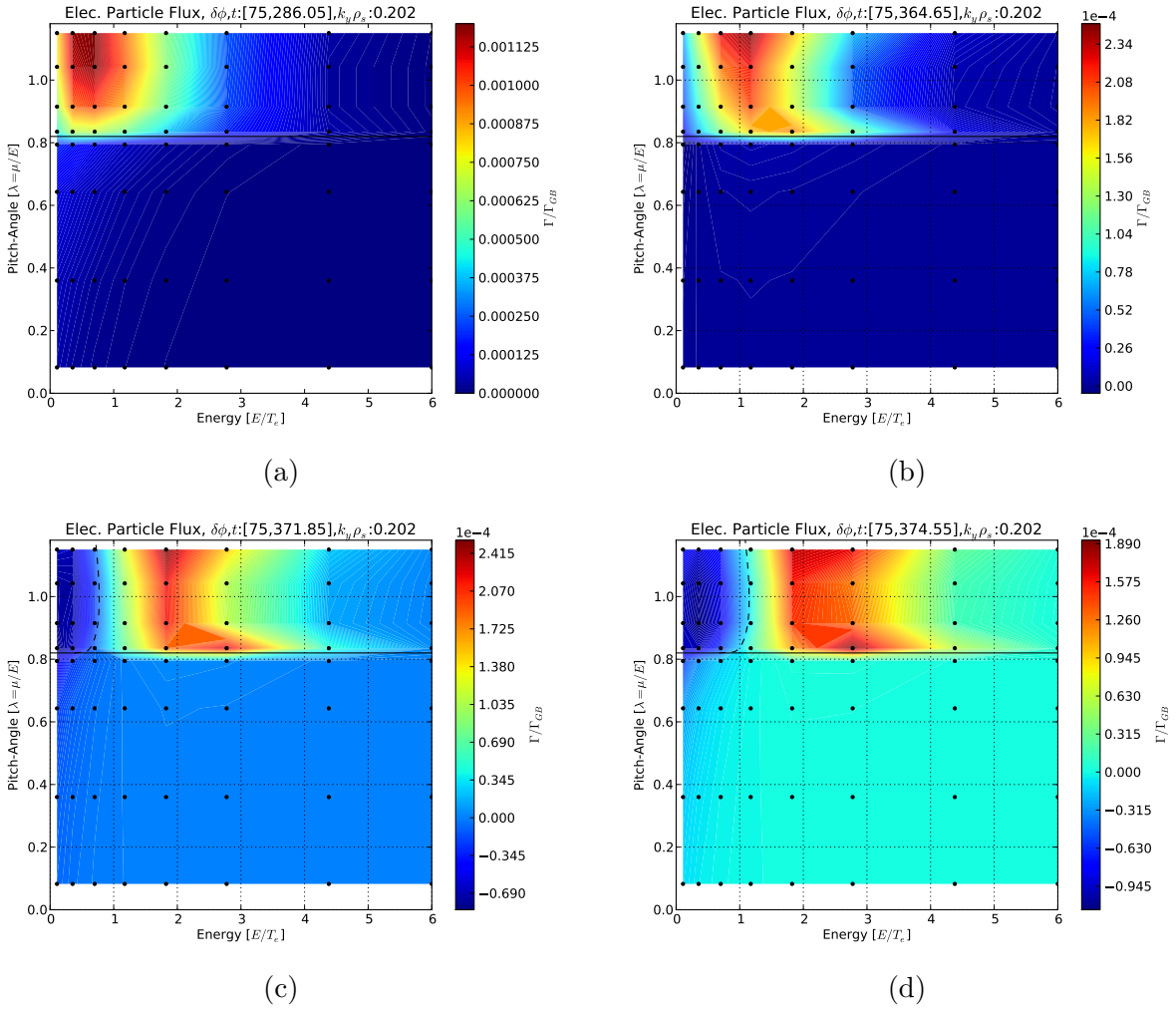

Figure 3.12: Velocity-space plots of the electron particle flux for $\eta_e = 0$ (a), $\eta_e = 0.5$ (b), $\eta_e = 1$ (c), $\eta_e = 1.5$ (d). The vertical axis λ is a pitch-angle variable that is a constant of the motion ranging from 0–$\lambda_{tp} = B_{\rm unit}(r)/B(r)_{max}$ for passing particles and λ_{tp}–$B_{\rm unit}(r)/B(r)_{min}$ for trapped particles. Trapped particles are located above the trapped-passing boundary (solid black horizontal line) and passing particles below. $E_{min}(\lambda)$ calculated from eq. 3.47 for particles contributing to the outward flux is shown by the black dashed line.

3.6 Coupled Trapped-Electron and Ion-Temperature-Gradient Simulations

Finally, the effect of distributing the free-energy gradient between density and both electron and ion temperature was examined. These simulations scanned $\eta_e = \eta_i = \eta$ and R/L_P. For a given R/L_P, $R/L_{T_{e,i}} = \eta R/L_n$. Using eq. 3.58,

$$R/L_n = R/L_p \frac{1}{1+\eta} \tag{3.65}$$

3.6.1 Linear Simulations scanning $\eta_e = \eta_i$ and R/L_P

Linear simulations were carried out scanning R/L_P from 2 to 30, and η_e from 0 to 2 for modes with $k_y\rho_s$ from 0.112 to 2.0. Simulations used a Miller circle geometry including a small amount of electron pitch-angle scattering ($\nu_{ei}a/c_s$ =0.01) collisions and corresponding ion collisions.

Once again, the linear critical pressure gradient (fig. 3.13d) is found to be smallest in the purely density-gradient-driven case. The linear critical pressure gradient increases with η and is a maximum at $\eta = 0.8$, where $R/L_{P,crit} = 4.8$. Interestingly, $\eta = 0.8$ is one edge of the stability boundary for the ITG[145] mode if electrons are assumed to be adiabatic, although at this pressure gradient the ion temperature gradient is still in the region that should be stable to the adiabatic-electron ITG mode. Figure 3.13a shows that the least unstable η for a given R/L_P moves from $\eta \approx 1$ to $\eta \geq 2$ for larger R/L_P, which corresponds to inside the region where the adiabatic ITG is unstable. Real frequencies (fig. 3.13b) are also in the ion diamagnetic direction for $\eta > 0.8$, consistent with the ITG mode being dominant.

Figure 3.14 shows that the quasilinear energy flux per particle increases with η for both the electrons and ions. As in the $\eta_i = 0$ case, the energy flux per particle increases slowly with η for $\eta < 1$, reaching $q_{e,i} = 5\Gamma T/2$ at $\eta \approx 1$. The quasilinear energy flux per particle

increases quickly with η for $\eta > 1$, especially for the ions. This behavior is consistent with the dominant mode moving from a TEM to ITG mode.

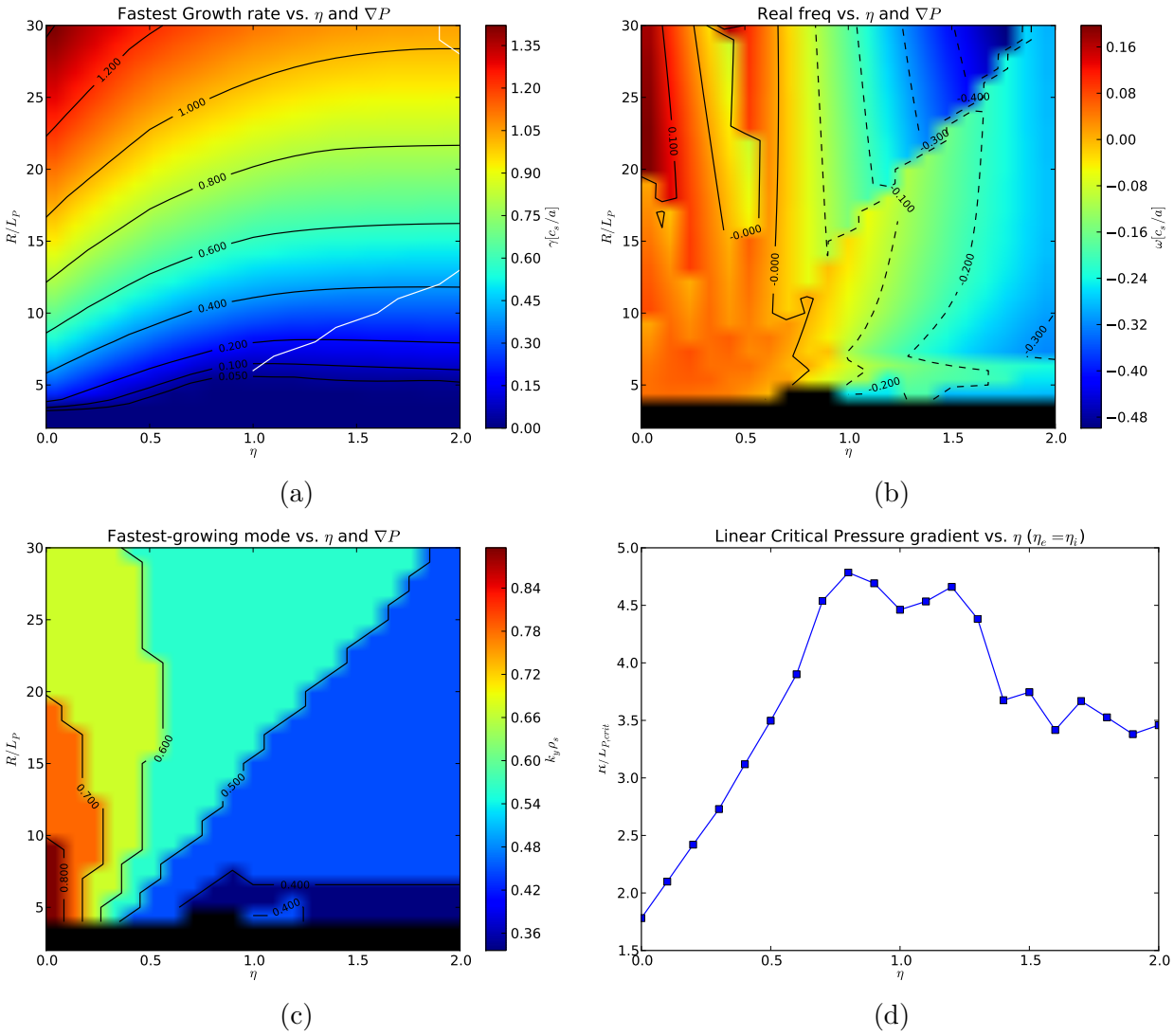

Figure 3.13: Linear growth rates (a) and real frequencies (b) for the fastest-growing $k_y\rho_s$ mode (c) for various density and temperature-gradient scale lengths. The white line in (a) traces the least unstable η for each R/L_P. Real frequencies move from the electron diamagnetic direction to the ion diamagnetic direction as η increases. The most unstable $k_y\rho_s$ mode also moves to lower wavenumber with η. (d) Linear critical pressure gradient versus η. The highest linear critical pressure gradient ($R/L_P = 4.8$) is found at $\eta = 0.8$.

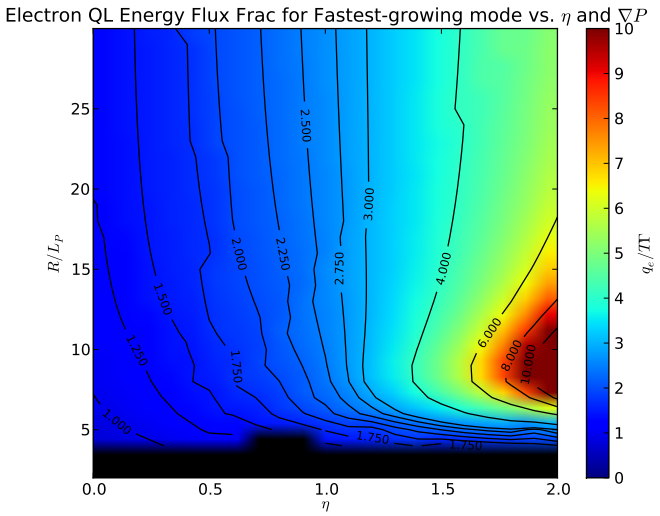

(a)

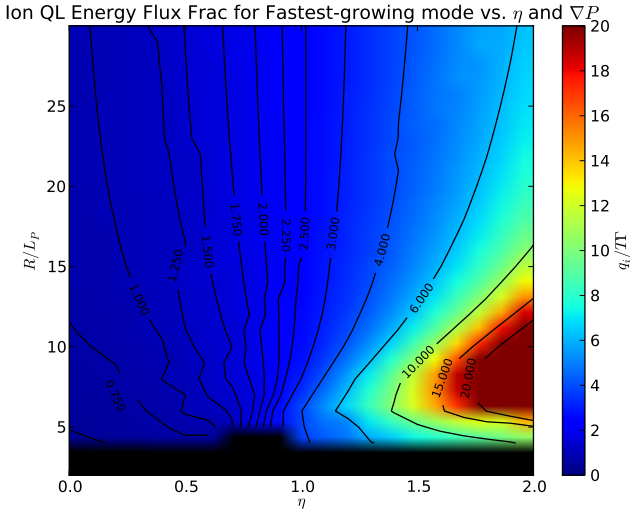

(b)

Figure 3.14: Quasilinear energy flux per particle for (a) the electrons and (b) the ions for the fastest growing mode. The electron energy flux per particle increases with η. Once again, the energy flux per particle increases slowly for $\eta < 1$. At $\eta = 1$ $q \approx 5\Gamma T/2$ for both the ions and the electrons and there is a sharp transition such that the energy flux per particle increases much faster with η for $\eta > 1$.

3.6.2 Nonlinear Simulations scanning $\eta_e = \eta_i$ and R/L_P show transition from TEM to ITG

Local, nonlinear simulations were carried out for several pressure gradients while scanning η from 0 to 2. Simulations were performed with a Miller circle geometry and a small amount of electron and ion pitch-angle scattering ($\nu_{ei}a/c_s = 0.01$). Particle and energy fluxes versus driving pressure gradient are shown in figure 3.15. These simulations used 128 velocity-space grid-points (8 energies, 8 pitch angles, and 2 signs of parallel velocity) and 32 toroidal modes spanning $k_y\rho_s$ from 0 to 2.0. In real space, the simulation domain spanned $[L_x/\rho_s, L_y/\rho_s]$=[97,96] with 128 radial grid-points and used ρ_s/a=4.5 $\times$ 10^{-4}. A nonlinear up-shift of the critical pressure gradient is most pronounced for the $\eta \geq 1$ cases. For all cases, particle flux decreases as η is increased, which corresponds to reduced R/L_n at fixed R/L_P. As in the $\eta_i = 0$ case examined in sec. 3.5.5, the electron energy flux is always higher than the Cyclone ITG reference, while for strong drive the ion energy flux can be comparable to or less than the Cyclone ITG reference. The simulations with $\eta > 1$ drive more ion thermal transport than electron thermal transport, consistent with the ITG being the dominant instability for these cases.

The saturated energy flux per particle is shown in figure 3.16 as a function of η for various R/L_P. The solid line corresponds to the analytic estimate for $q_e/(\Gamma T)$ given by eq. 3.51, which captures the general trend with η, but does not fit the data from the nonlinear simulations nearly as well than in the $\eta_i = 0$ case. Although this discrepancy is partly due to the fact that these simulations were carried out closer to marginal stability than in the $\eta_i = 0$ case, even the most strongly-driven case does not fit well with the analytic estimate. Interestingly, the effect of reduced R/L_P at decreasing the average electron energy flux per particle is much more pronounced than in the $\eta_i = 0$ case. In fact, $q_e < 3\Gamma T/2$ up to $\eta \approx 0.6$ for the most weakly-driven case, and $q_e < 5\Gamma T/2$ at $\eta = 1$ for the two most weakly-driven

cases. For the ions, $q_i \leq 3\Gamma T/2$ for all cases with $\eta \leq 0.5$. Above $\eta = 0.5$ the energy flux per particle increases quickly as the ITG becomes the dominant driver of the transport.

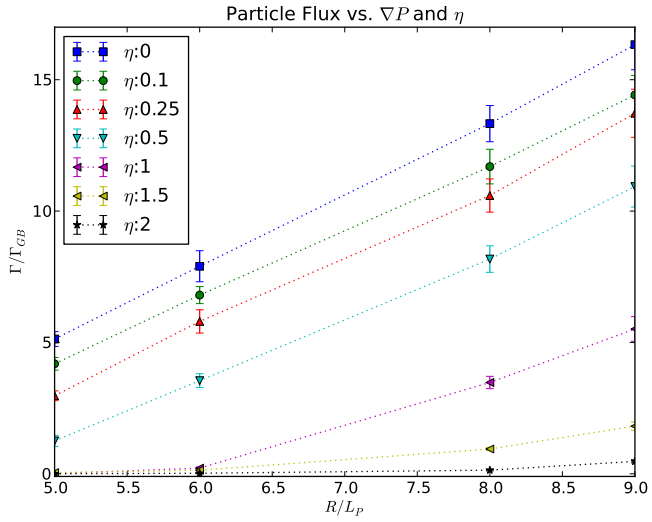

(a)

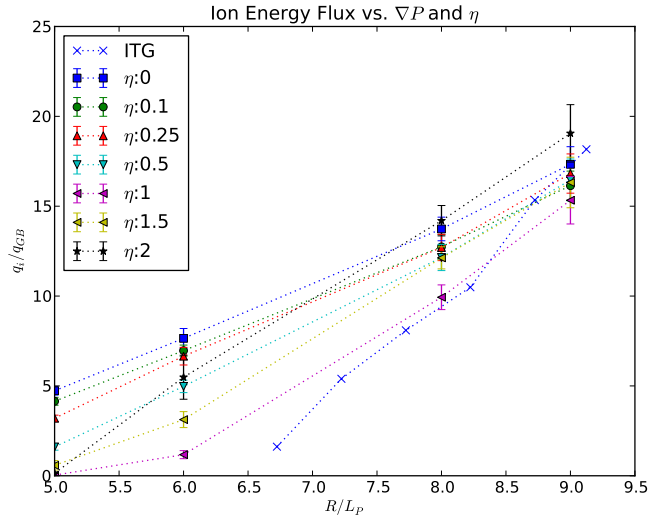

(b)

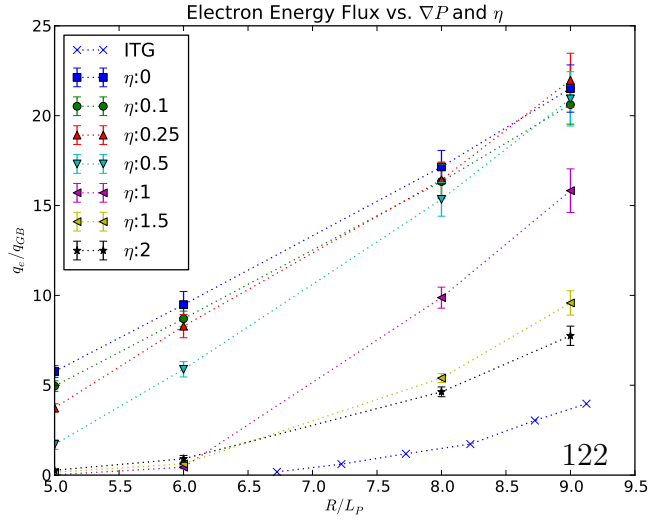

(c)

Figure 3.15: Nonlinear (a) particle flux, (b) ion energy flux, and (c) electron energy flux. The ion and electron energy fluxes are compared to energy fluxes from a reference ITG case[144] for the same pressure gradients; the particle flux in the ITG case is not shown because it is negative (inward). The ITG cases all have a fixed density gradient, $R/L_n = 2.2$, and increasing ion and electron temperature gradient from R/L_T=4.5 to 6.9. Note that the reference ITG simulations used $s-\alpha$ geometry and different numerical parameters. As a result, the ITG energy fluxes are likely lower than if the same geometry and numerical parameters were used as in the other cases. The electron energy fluxes are substantially higher than the ITG case for all η shown. Even the ion energy flux is greater at lower pressure gradients; however, as R/L_P is increased beyond where the ITG case is unstable, the ion energy flux in the $\eta_i = 0$ cases do not increase as quickly with R/L_P.

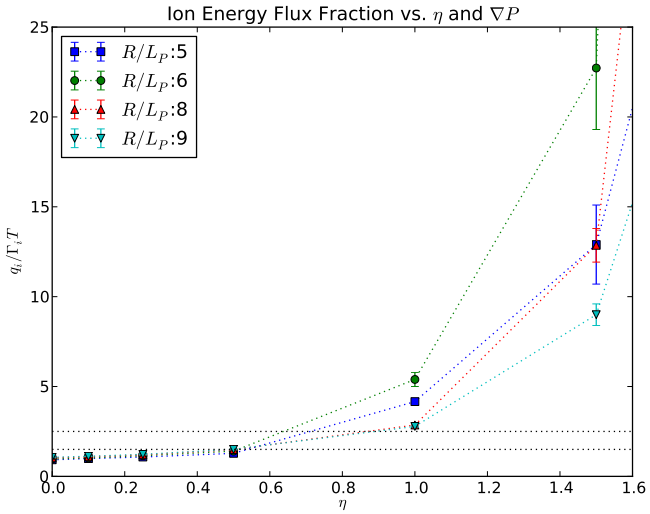

(a)

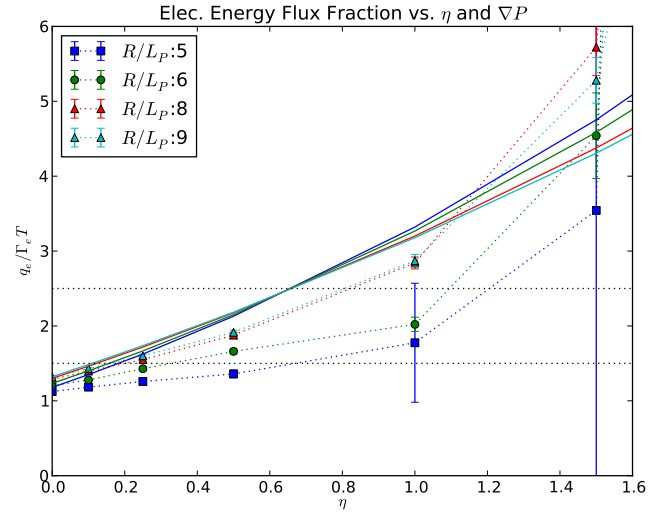

(b)

Figure 3.16: Nonlinear Energy flux per particle for (a) ions and (b) electrons, with the solid lines in (b) corresponding to the simple scaling of eq. (3.51). Black dotted lines mark where $q/(\Gamma T)$=3/2 and 5/2. Note the different scales for ions and electrons.

3.7 Comparison with a Reference Neoclassical Transport Model

As mentioned in sec. 2.1.1 and sec. 2.1.3, the reference transport model was used to predict the performance of low-recycling devices including LTX[78], under the assumption that ion thermal transport is neoclassical, while particle transport and electron thermal transport are also at the ion neoclassical thermal transport rate. The purpose of this section is to assess whether these profiles are susceptible to drift-wave instabilities and the potential contribution of micro-turbulence to the total transport. Figure 3.17 shows the predicted profiles for a low-$\beta(4\%)$, Ohmic LTX discharge[78] with 3.5 kG toroidal field and 300 kA plasma current. A 2 eV edge neutral source (gas puff) and a small cold, parabolic (i.e., core-localized) fueling source were used. Particle and energy confinement times are 23 ms and 25 ms respectively. Figure 3.18 shows the predicted profiles after the edge neutral source has been turned off. While the density has decayed about 30%, the average electron temperature has increased about 50%. Particle and energy confinement times of 46 ms and 31 ms are predicted.

3.7.1 Linear, flux-tube simulations of RTM profiles show TEM and ITG instabilities

An interface was developed in Python to convert the ASTRA output into a format suitable to initialize a GYRO simulation. Linear GYRO simulations have been conducted in order to examine the stability of these profiles to drift-wave micro-turbulence. Figure 3.19 shows the linear growth rates and real frequencies for the equilibrium during edge gas fueling at $r/a = 0.7$. Linear simulations indicate that during active gas-puffing, both the ITG and TEM modes are unstable at this minor radius. The TEM mode peaks at $k_y\rho_s = 0.5$, while the ITG peak is near $k_y\rho_s = 1.25$. Note that because $T_i/T_e = 0.126$, the ITG peak corresponds

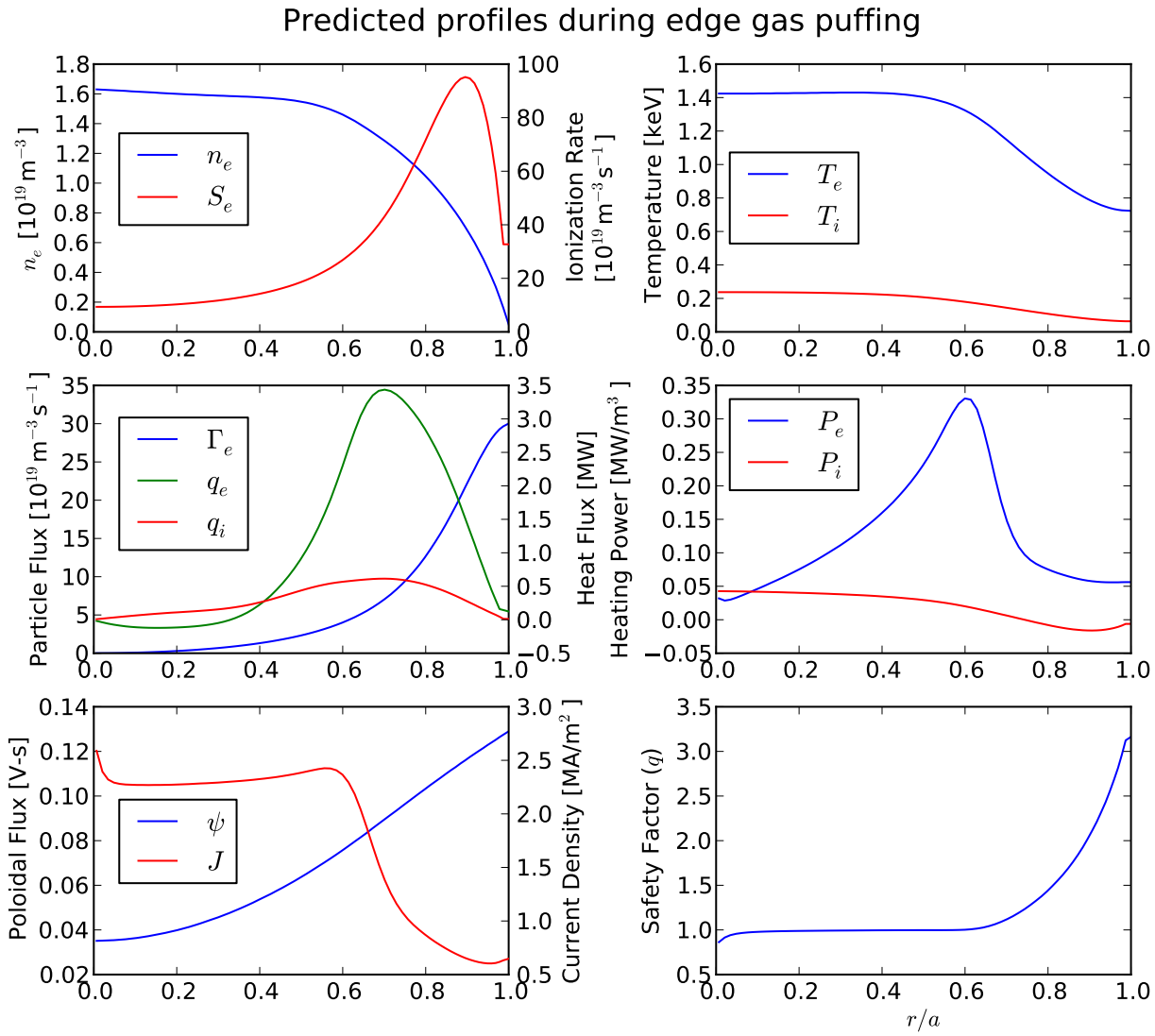

Figure 3.17: Predicted LTX profiles during gas fueling for a sample low-β (4%) equilibrium[78] with 3.5 kG toroidal field and 300 kA plasma current. Fueling sources consist of a cold, parabolic (i.e., core-localized) source as well as a 2 eV edge neutral source such as a gas puff. There is a strong temperature gradient for $r/a > 0.6$ due to the dominant edge fueling source. For $r/a \lesssim 0.5$, the temperature profile is flat, resulting in flat current and q-profiles in this region.

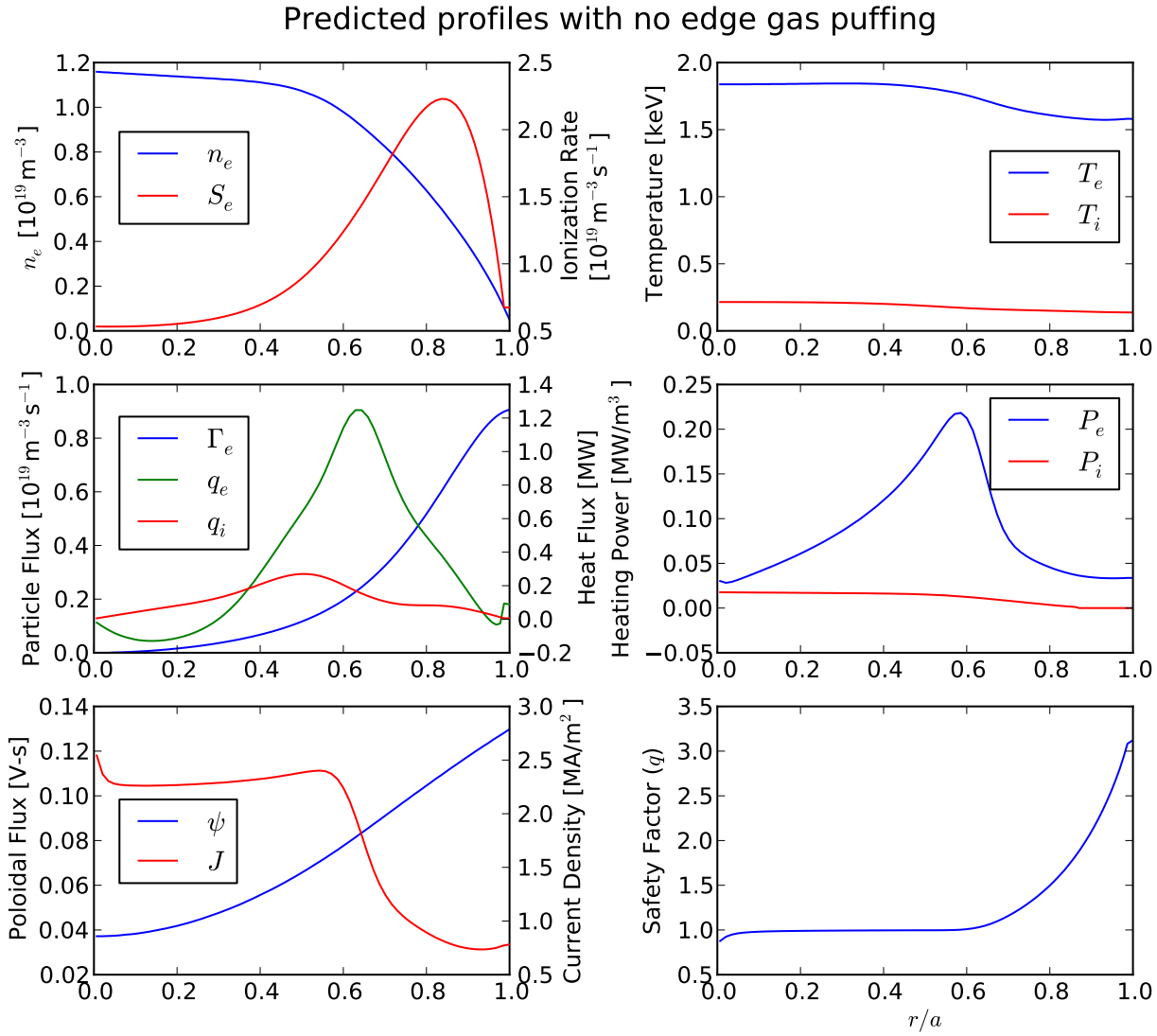

Figure 3.18: Predicted LTX profiles after transiently turning off the edge gas fueling. For this equilibrium, the β=3.6%. The ion and electron temperature profiles are nearly flat while the density profile is peaked in the core. The current and q-profiles are similar to the case with edge gas fueling. Note again that this simulation was for 3.5 kG toroidal field and 300 kA plasma current.

to $k_y\rho_i = 0.44$. At $r/a = 0.8$ (fig. 3.20), the much steeper density gradient drives the TEM very strongly. The ITG is still unstable, but has been shifted to even higher $k_y\rho_s$. These linear simulations show that even with low-recycling walls, charge-exchange losses with gas puff neutrals and weak electron-ion coupling suppress the edge T_i, resulting in a steep ion temperature gradient during gas puffing and low T_i/T_e which drive the ITG mode unstable. Nevertheless, the TEM is most likely to be the dominant source of micro-turbulent particle and thermal transport. Not only are the TEM growth rates substantial, but it also peaks at relatively low wavenumber. A mixing length estimate for the diffusion coefficients $D \sim \gamma/k_y^2$ using the most unstable modes would suggest $D \sim 1.2 D_{GB}$ at both $r/a = 0.7$ and $r/a = 0.8$, corresponding to $D \sim$87 m^2/s and 52 m^2/s respectively for the predicted LTX parameters.

How does this picture change when edge gas puffing is turned off? Figure 3.21 shows the linear growth rates and real frequencies at $r/a = 0.7$ for the equilibrium after edge gas sources have been turned off and the profile has been allowed to relax. The ITG mode appears stable, since linear simulations with adiabatic electrons show no hint of instability. In contrast, the TEM is actually more unstable than in the case with edge gas fueling, driven by a stronger density gradient. A mixing-length estimate for the diffusion coefficient using the most unstable mode would suggest $D \sim 0.66 D_{GB}$, corresponding to $D \sim$82 m^2/s, which is very close to the case during a gas puff. This simulation illustrates that even though temperature-gradient modes can be stabilized when edge fueling sources are removed, density-gradient-driven modes may remain unstable and can possibly drive substantial particle and thermal transport. However, since the temperature gradient is reduced, the quasilinear energy flux per electron (not shown) is also reduced substantially: $q_e/(\Gamma T)$=1.1 compared to 3.6 for the case during a gas puff, suggesting the energy flux may be reduced substantially.

r/a	0.7
R_0/a	1.66
Δ	-0.11
κ	1.32
s_κ	0.018
δ	0.16
s_δ	0.20
q	1.12
s	1.38
ρ_*	0.035
ν_{ei}	0.022
ν_{ii}	0.008
a/L_n	1.56
a/L_{T_e}	1.78
a/L_{T_i}	2.57
T_i/T_e	0.126
β_e	1.9%

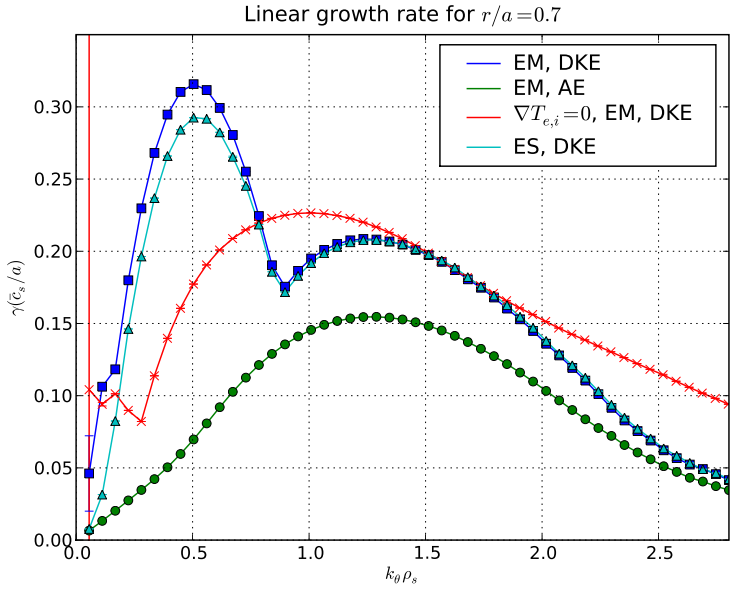

(a)

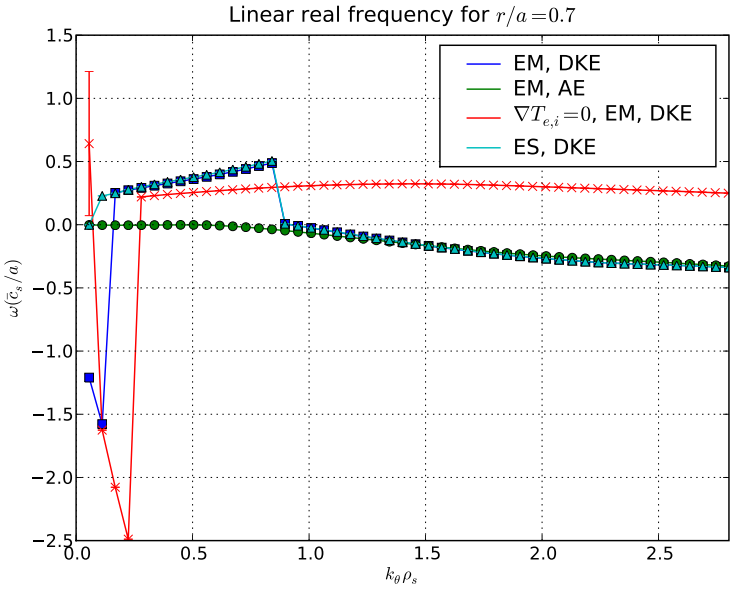

(b)

Figure 3.19: GYRO linear (a) growth rates and (b) real frequencies at $r/a = 0.7$ during gas puffing. Electromagnetic effects are weak due to the low β (2.1%). For $k_y\rho_s < 1.0$, the TEM dominates and the drift is in the electron diamagnetic direction. For $k_y\rho_s > 1.0$, the ITG mode dominates and the drift is in the ion direction.

r/a	0.8
R_0/a	1.65
Δ	-0.17
κ	1.33
s_κ	0.11
δ	0.20
s_δ	0.38
q	1.44
s	2.48
ρ_*	0.029
ν_{ei}	0.026
ν_{ii}	0.011
a/L_n	2.80
a/L_{T_e}	1.98
a/L_{T_i}	3.24
T_i/T_e	0.111
β_e	1.0%

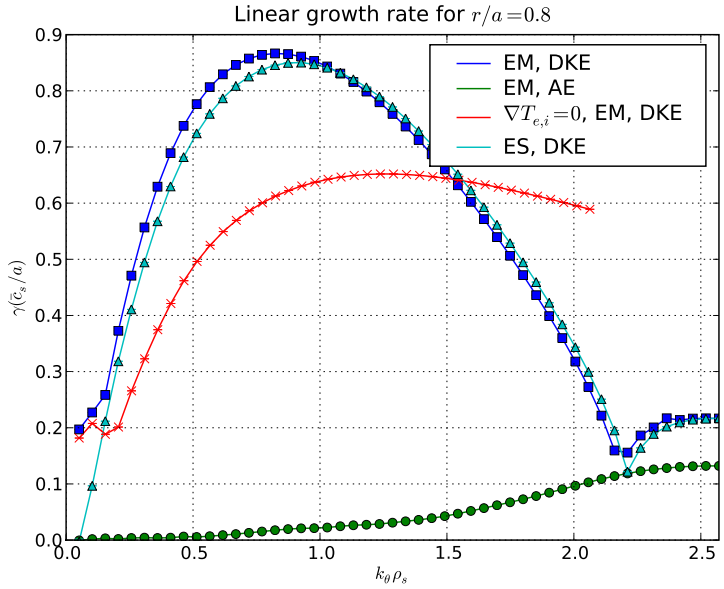

(a)

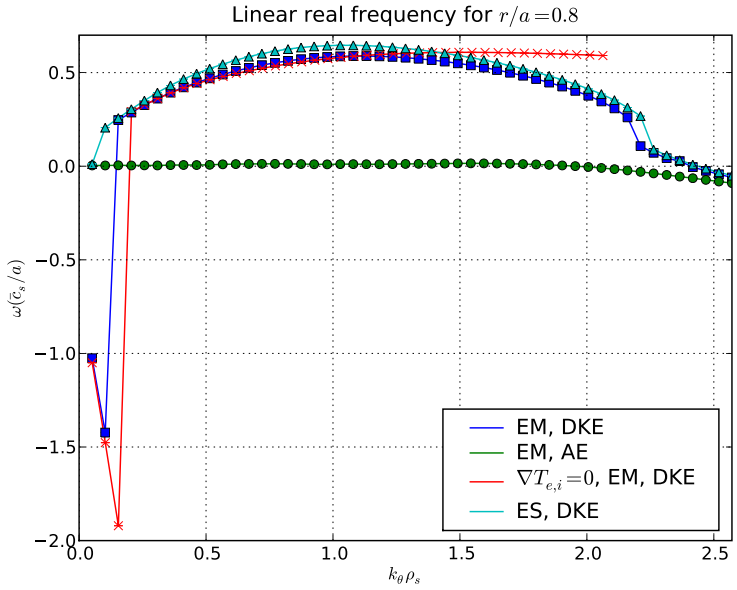

(b)

Figure 3.20: GYRO linear (a) growth rates and (b) real frequencies at $r/a = 0.8$ during gas puffing. The TEM is driven very strongly due to the large density gradient. Note the shift to the ion diamagnetic direction (ITG mode) occurs at higher perpendicular wavenumbers ($k_y\rho_s > 2.2$).

r/a	0.7
R_0/a	1.66
Δ	-0.12
κ	1.32
s_κ	0.038
δ	0.16
s_δ	0.22
q	1.16
s	1.52
ρ_*	0.035
ν_{ei}	0.0007
ν_{ii}	0.0
a/L_n	2.12
a/L_{T_e}	0.47
a/L_{T_i}	0.56
T_i/T_e	0.095
β_e	1.7%

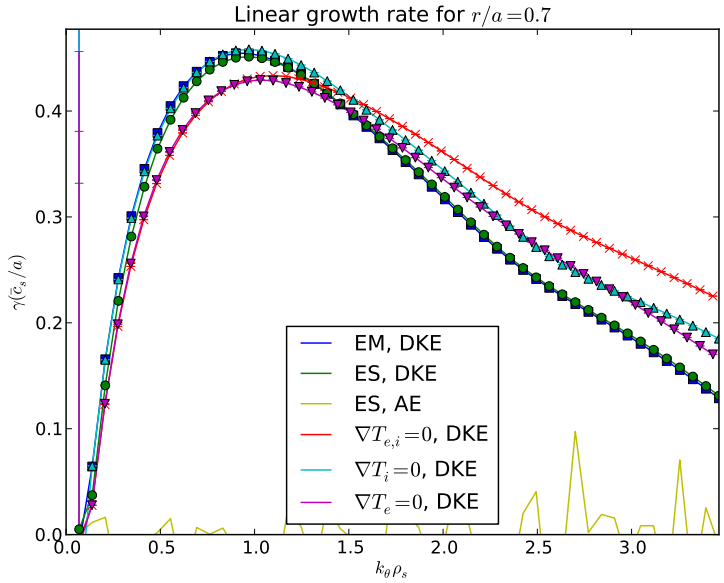

(a)

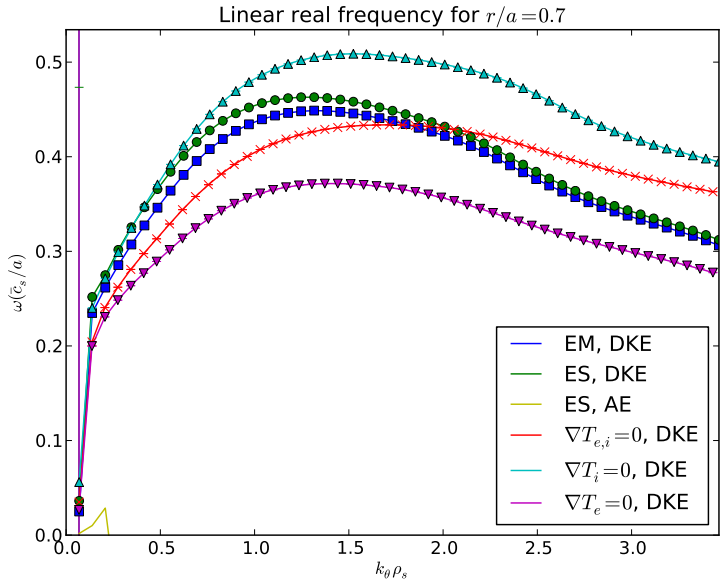

(b)

Figure 3.21: $r/a = 0.7$, GYRO Linear growth-rate spectrum without gas puffing. The ITG mode is stable, but the TEM is still unstable.

3.8 Conclusions

This study explored the features of plasma micro-turbulence for the types of profiles that might be expected with a low-recycling boundary and core fueling. Linear and non-linear flux-tube simulations were performed using GYRO. Several cases were considered:

1. $\nabla T_e = \nabla T_i = 0$ and varying $\nabla P = \nabla n$ in order to examine micro-turbulence driven by only a density gradient.

2. $\nabla T_i = 0$ and varying ∇P and $\eta_e \doteq \nabla T_e / \nabla n$ in order to examine only TEM transport as the free-energy gradient is distributed between density and temperature.

3. $\nabla T_i = \nabla T_e = \nabla T$ and varying ∇P and $\eta \doteq \nabla T / \nabla n$ in order to examine coupled ITG and TEM transport.

What distinguishes this work is the focus on the regime where $\eta \lesssim 1$ and the careful study of how the average energy flux per particle $q/(\Gamma T)$ varies as the free-energy gradient is distributed between density and temperature. This work demonstrates that fully transferring free-energy from the temperature gradient to the density gradient does not necessarily decrease the resulting energy flux. In fact, the purely density-gradient-driven TEM has a substantially lower critical pressure gradient than the ITG mode. Nevertheless, this regime shows several interesting features. The turbulence preferentially causes cold particles to diffuse outward, resulting in a energy flux per particle of less than 3/2, which is usually assumed to be the minimum for convective transport. The transport is also shown to preferentially eject impurity ions. This feature could counteract the neoclassical accumulation of impurities in the core and also help expel helium ash resulting from the fusion reaction.

Next, the linear stability and transport in the case of pure TEM drive ($\nabla T_i = 0$, but scanning ∇P and $\eta_e \doteq \nabla T_e / \nabla n$ was studied. The linear critical pressure gradient was found to be maximized for $\eta_e = 1.0$. Away from marginal stability, for a given pressure gradient, *decreasing* η_e is linearly stabilizing. At η_e=1.0, the energy flux per electron was

found to equal $5T_e/2$, which is the value of convective thermal transport for adiabatic gas expansion. An analytic model for the energy flux per electron was derived, which matched the results of nonlinear simulations surprisingly well. A thermodynamic constraint on the energy flux as a function of η_e was also derived, demonstrating that while surprising, the model prediction and simulation results of q_e as low as $\lesssim 3\Gamma T_e/2$ are thermodynamically permitted. Nonlinear simulations with $\nabla T_i = 0$ showed that the nonlinear critical pressure gradient is much lower than that of the ITG; however, for simulations with moderate drive, the ion thermal transport is substantially less than in the reference ITG case.

Finally, the linear stability and transport for coupled TEM-ITG transport were examined. Linear simulations with $\eta_e = \eta_i = \eta$ find that the linear critical pressure gradient was maximized for $\eta \approx 0.8$. In contrast to the $\eta_i = 0$ case, for fixed ∇P away from marginal stability, *increasing* η is linearly stabilizing. Since most present experiments operate near marginal ITG stability with η substantially greater than one, moving some of the free-energy gradient from temperature to density would have the effect of increasing the linear critical pressure gradient. Nonlinear simulations show substantial thermal transport compared to the ITG case, although due to differences in the geometry and numerical parameters used in the reference ITG simulations, the ITG case might in fact have somewhat higher transport if the same parameters were used. For moderate instability drive, the electron thermal transport is substantially greater for η=0 to 2 compared to the reference ITG case η=3; however, it is important to keep in mind that the transport from electron-scale modes has not been included. These electron-temperature-gradient (ETG) modes are expected to be substantially more unstable in the reference ITG case ($\eta \geq 3$) compared to the others. Nonlinear simulations spanning the full range of $k_y\rho_s$ from ITG-TEM to ETG scales are computationally extremely expensive, but will be required to compare the total transport levels.

Linear and global nonlinear simulations were also performed using predicted profiles from the reference transport model. Linear simulations show the presence of a robust TEM instability, while the ITG also becomes unstable during gas puffing. Therefore, these simulations indicate that a model for density-gradient-driven micro-turbulent transport needs to be included in transport predictions for low-recycling devices. It is important to mention, however, that the potentially stabilizing effect of significant plasma rotation has not been included because no model to predict the rotation profile has been developed. Studies suggest that since low-recycling walls suppress the edge neutral density, the neutral drag is also reduced; therefore, low-recycling devices may have substantially higher rotational velocities than high-recycling devices.

The original motivation for investigating the effects of low-recycling on micro-turbulent transport was because of the high energy confinement measured in CDX-U plasmas (a =0.2 m, R_0 =0.34 m, B_T=1.9 kG, q ~3) during operation with a liquid lithium limiter[90,78]. Although the transport in those discharges could not be analyzed in detail because profile measurements of T_e and T_i were not available, the reference transport model was able to match global measurements in a low-recycling discharge. Typical high-recycling CDX-U discharges had τ_E =0.6 ms, giving a $\chi_{\text{eff}} = a^2/\tau_E$ =70 m^2/s, Spitzer T_e ~100 eV and T_i=35 eV on-axis, corresponding to ν_* ~0.9 ($\nu a/\bar{c_s}$ ~0.9) for electrons at $r/a \sim 0.5$. In contrast, typical low-recycling CDX-U discharges had τ_E =3.2 ms, giving a χ_{eff} =12.5 m^2/s, Spitzer T_e ~300 eV and T_i=70 eV on-axis, corresponding to ν_* ~0.1 ($\nu a/\bar{c_s}$ ~0.1) for electrons at $r/a \sim 0.5$. The simulations in this work use much lower collisionality ($\nu a/\bar{c_s} \sim 0.01$), so the collisionless TEM is likely to have been more stable in the CDX-U discharges than in these simulations, although perhaps a dissipative TEM may have been unstable. Nevertheless, linear simulations using profiles determined by the reference transport model with and without edge gas puffing give qualitative insight into differences between high-recycling and low-recycling discharges. In the absence of edge fueling, the

ITG mode is stable. Although the mixing-length diffusivity is comparable in both cases, the quasilinear energy flux per electron is a factor of three less for the case without edge fueling, suggesting that the nonlinear energy flux may also be substantially reduced. In either case, linear simulations find the profiles are essentially stable for $r/a \lesssim 0.5$, so neoclassical transport may be the only transport mechanism in the inner core. For $r/a \gtrsim 0.5$, drift-waves become increasingly unstable with minor radius, indicating micro-turbulent transport may contribute significantly to transport in this region.

Neoclassical diffusion scales as $T_e^{-1/2}$. In contrast, gyro-Bohm transport from micro-turbulence scales as $T_e^{3/2}$. Transport measurements on low-recycling devices at higher temperature are needed, therefore, to reveal the importance of micro-turbulent transport in the low-recycling regime and to predict the performance of a low-recycling reactor.

In addition to changing the distribution of the free-energy gradient between temperature and density gradients, low-recycling and core fueling are expected to change the equilibrium in other important ways. By raising the edge temperature and flattening the temperature profile, the current profile is expected to flatten as well. This would have the effect of changing the magnetic shear and safety factor, which could be stabilizing or destabilizing. In addition, by reducing the edge neutral density, low-recycling and core fueling might decrease the edge neutral drag on ions, which would alter the rotation profile. This would likely be a stabilizing effect in most regimes of interest. Finally, finite β electromagnetic effects should be considered. For example, although their role in driving electron thermal transport in current high-β experiments is unclear, microtearing modes[146,11] are driven by the electron temperature gradient; as a result, they might be expected to be less unstable in low-recycling experiments with core fueling. Given the complexity of plasma turbulence, this work has only begun to explore the consequences of low-recycling and core fueling on micro-turbulent transport. Computationally expensive, electromagnetic simulations spanning ion and electron transport scales will be needed to fully model core transport.

Chapter 4

Measurements of the dependence of Plasma Parameters on Lithium Wall Condition in High-Performance Discharges

Previous experiments on TFTR, CDX-U, FTU, and NSTX have established a connection between reduced recycling and improved plasma performance. Experiments with solid and liquid lithium PFCs on CDX-U in particular demonstrated low-recycling and dramatic improvement in energy confinement. Since ∼85% of the plasma-facing area on LTX can be covered with lithium coatings, LTX is uniquely suited to explore the limit of low-recycling that can be attained with lithium PFCs. The measurements presented in this chapter build on previous work by exploring in detail the affect of nearly complete low-recycling PFCs on effective particle confinement. In addition, the connection with hydrogen flux from the wall is explicitly established using measurements of Lyman-α emission from VUV diagnostics that were developed as part of this thesis. These measurements are then used to constrain

neutral particle modeling in chapter 5 in order to precisely quantify the recycling. In addition, the suite of visible spectroscopic diagnostics developed as part of this thesis are used to examine the relationship between impurities and discharge performance.

As discussed in section 2.4, discharges on bare stainless-steel are characterized by rapid quenching of the discharge due to hydrogen and impurity influx from the wall. This wall condition, therefore, illustrates the effect of contamination of plasma discharges by adsorbed gases (especially water) on metallic surfaces. Although discharges on fully passivated lithium (sec. 2.5) show improved performance relative to discharges on bare stainless-steel, this wall condition is sufficiently degraded so that hydrogenic recycling and impurities released from the wall dominate the particle fueling into the plasma. These discharges merely demonstrate that recycling and/or impurity desorption/sputtering need to be reduced in order to obtain density control; they cannot inform on the merits of trading wall recycling as a fueling source for external (presumably more efficient) fueling.

Therefore, this work focuses on examining high-performance discharges on fresh or partially passivated solid (cold) lithium surfaces in detail. For the purpose of categorizing discharges performed with different wall preparation methods, but lacking detailed surface characterization measurements, the following operational definitions will be used. Discharges with a fresh lithium surface are characterized as those taken within 1–8 hours following evaporation of about 1 g of lithium from each of the two crucible evaporators onto the shell surfaces, under a helium fill. Following the evaporation, visual inspection of the shell surface found the coatings essentially fully covered the inner shell surface and the coatings appeared frosty white in color. Discharges with partial coatings are defined as those performed within 1–8 hours of evaporating lithium onto the shell surfaces, but whether because of a short in one of the evaporators or other technical issue, a full 1 g of lithium was not evaporated from each crucible. These coatings might appear gray in color. Finally, discharges with a

partially-passivated surface are those which took place one day after lithium was evaporated onto the shells and plasma operations were performed immediately following.

Interferometer measurements show that solid lithium coatings on LTX are able to produce lower effective particle confinement times than were attained on CDX-U with solid or even (for the best cases) liquid lithium in the toroidal tray limiter. Hydrogen Lyman-α emission measurements correlate well with interferometer measurements of effective particle confinement, consistent with the picture that reduced hydrogen recycling (rather than impurity sputtering/desorption or changes in core particle transport) is the primary driver of reduced effective particle confinement. Nevertheless, measurements of line emission from impurities indicate that between fueling pulses during periods of low density, impurity fluxes from the walls may be contributing subtantially to maintain the electron population in the discharge. Langmuir probe measurements show that the electron density in the scrape-off-layer tracks the electron density in the core, dropping substantially as the external fueling is terminated. Probe measurements also show that this reduction in electron density in the SOL is coincident with an increased electron temperature in the SOL for shots with a fresh lithium wall coating. Interestingly, the connection between reduced recycling and plasma performance is somewhat complex. Heavily fueled discharges that produce large plasma currents with fresh lithium walls become over-fueled when the same external fueling is used and the walls are partially passivated. In contrast, moderately-fueled discharges exhibit a different behavior: although the density is substantially higher when operating with partially-passivated walls, the plasma current time evolution is quite similar until near the end of the discharge. Since the Ohmic waveform is identical, this would suggest similar electron temperatures throughout most of the discharge. Only near the end of the discharge do moderately-fueled plasmas on partially-passivated walls achieve lower currents than those on fresh evaporative lithium coatings, despite evidence for substantially increased recycling.

4.1 Dependence of Plasma Electron Density Evolution on Li Wall Condition

4.1.1 Typical Midplane Line-integrated Timeseries of Electron Density

Time-series of of plasma current and near-midplane line-integrated electron density are shown in figure 4.1 for plasma operation within hours of a full lithium operation (blue), a partial lithium evaporation (green), and after allowing the surface to passivate for one day with residual gases (red). All three cases show that the electron density can be controlled by varying the external fueling, indicating $R_{core} < 1$. Nevertheless, despite having very similar fueling, differences between the density traces indicate that the plasma-wall interaction is markedly different. The higher line-integrated density in the red and green traces both during fueling and between the fueling pulses suggests higher recycling for these shots relative to the blue, least-recycling case. The peak densities at the end of fueling pulses are higher for the discharges on 1-day passivated lithium and after only a partial lithium evaporation. This is due to the combined effects of increased recycling of plasma ions that diffuse out from the core, as well as increased recycling of hydrogen from the external gas puff that is ionized or dissociated in the SOL. After the external fueling is terminated, the density plummets in all three cases, with the discharge on a fresh Li coating yielding the minimum density. It is also very interesting that despite having significantly higher density during much of the discharge, the shots after a partial lithium evaporation or on 1-day passivated lithium produce very similar plasma currents to the shot on a fresh lithium surface. This result would suggest that if the plasma Z_{eff} is similar in the three discharges, then the electron temperature is similar as well.

For the shot following a full lithium evaporation, an instability at about 447.0 ms causes a rapid drop in the density and immediate rise in the plasma current.Interestingly, following

this event, the density remains nearly constant for about a millisecond before the gas flow from the second fueling pulse begins to fuel the discharge once again. If recycling is constant during the discharge, then the density should continue to decay. There are four possible explanations as to the fueling source that is maintaining the plasma density: residual flow from the gas puffer, diffusion of prefill gas from the volume between the shells and vessel wall, increased hydrogenic recycling due to ions impacting the walls with higher energy, and increased impurity sputtering. Residual flow from the puffer will be discussed in sec. 4.2.1 and essentially eliminated as a possibility. It is more likely that prefill gas that had diffused into the volume between the shells and the vessel wall is slowly diffusing into the plasma. The decay time of this residual prefill density can be estimated from $\tau \sim \Delta x^2/D$, where Δx is a typical distance the gas must travel, and D is the diffusion coefficient. For 300 K molecular hydrogen (v_{t,H_2} =1.1×10^5 cm/s) and assuming a characteristic distance δx ~5 cm between the outer shell surface and the vessel walls, $D \sim \delta x v_{t,H_2}$ =5.6×10^5cm^2 /s. Taking Δx ~50 cm gives $\Delta\tau \sim \Delta x^2/D$ ~4 ms for the e-folding decay time of prefill gas density between the shells and the vessel. Assuming that the prefill gas becomes evenly distributed throughout the 1.6m^3 vacuum vessel, and the quantity within the 0.68m^3 shell volume is immediately ionized, 58% remains in the shell gaps. For a typical prefill of 2.3×10^{19} H atoms, the gas remaining in the gaps 7–8 ms into the discharge during the low-density time period corresponds to about 3×10^{18} H atoms, with an effective fueling rate into the plasma of 6×10^{17} H atoms/ms. This rate is 8% of the typical fueling rate from GPI.

4.1.2 Cumulative Recycling Measurements

A useful parameter for comparing the cumulative effects of particle confinement and recycling in various discharges is the cumulative recycling (R_{cum}) defined as the ratio of the total electron inventory in the plasma (the electron density integrated over plasma volume) to the

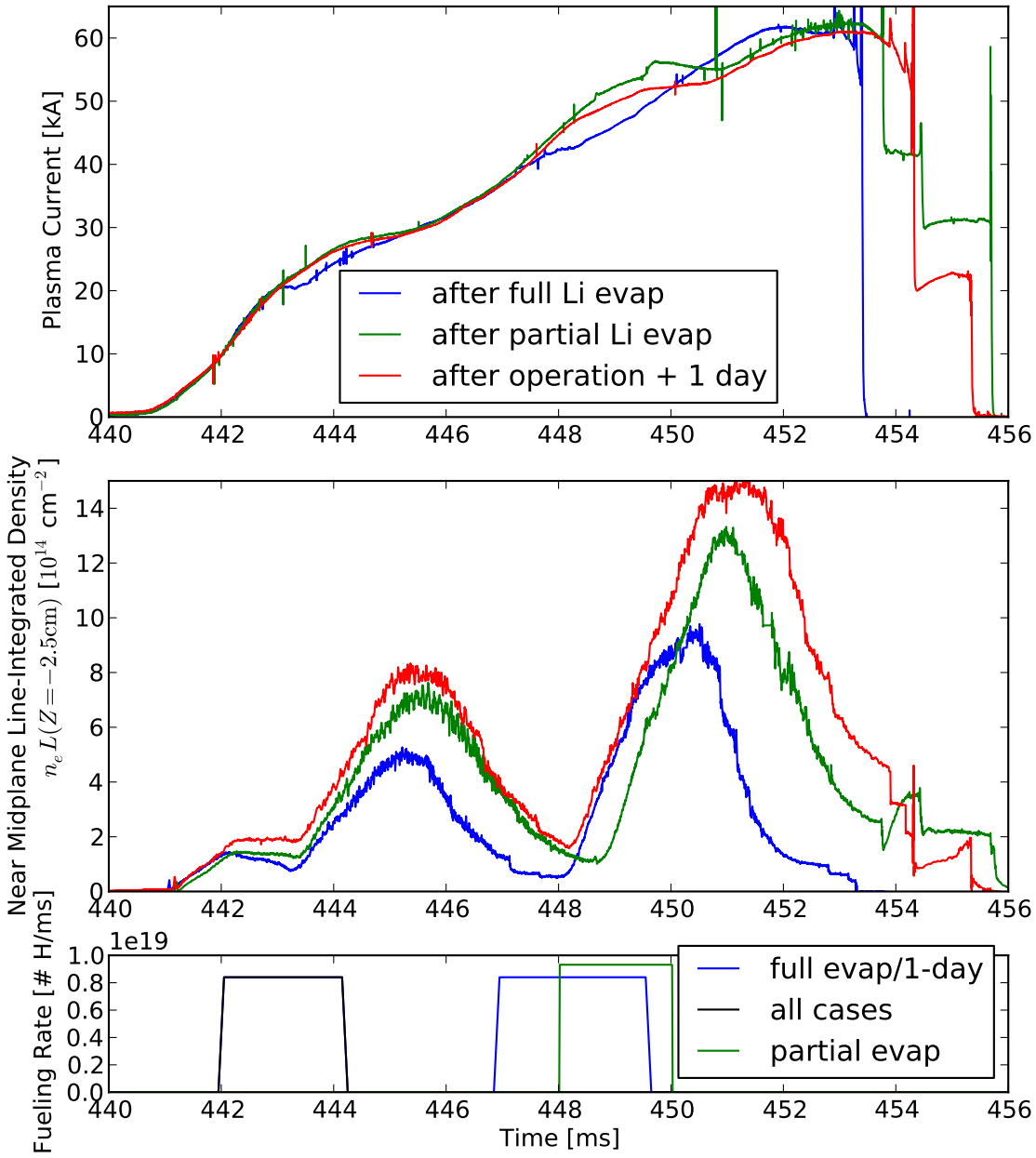

Figure 4.1: Plasma current and near midplane $n_e L$ timeseries for various operating conditions. Blue trace corresponds to a shot within hours after a full evaporation of about 2 g Li from each evaporator (shot 1112201312). The red trace is from a shot taken a day after plasma operation on a fresh lithium surface (shot 1112071141). The green trace is a shot after a partial evaporation (shot 1111301633). The initial fueling pulse is the same for all shots. The blue and red shots have identical external fueling: prefill, GPI triggered from 442–444 ms, and from 447–449.7 ms. The green trace has the same pre-fill and first fueling pulse, but the second pulse is from the warm MCI from 448–450 ms. Note that there is about a 1 ms delay between the trigger for the fueling and when the density begins to respond.

total number of injected hydrogen atoms:

$$R_{\rm cum}(t) \doteq \frac{N_e(t)}{\int_0^t dt' \Gamma_{ext}(t')}. \tag{4.1}$$

Although other authors[147] have used the term "effective global recycling" to describe this quantity, such a label is easily confused with recycling at one point in time integrated over the entire plasma boundary. Therefore, this thesis will use the term cumulative recycling as it represents the cumulative effect of plasma-wall interactions at maintaining the electron inventory of the plasma. If sputtered or desorbed impurity ions contribute a small fraction of the total electron population, and hydrogen plate recycling is below unity, the maximum value of $R_{\rm cum}$ is the fueling efficiency: 0.2–0.24 for GPI fueling. In reality, particle transport and incomplete ionization of the hydrogen gas prefill cause $R_{\rm cum}$ to be less than this amount.

In order to convert the measured line-integrated electron density near the midplane to a total number of electrons in the plasma, the midplane $n_e L$ is multiplied by an "effective area":

$$N_e = \int_0^a dr \frac{dV}{dr} n_e(r) = (n_e L)_{midplane} A_{\rm eff} \tag{4.2}$$

where r is the flux-surface coordinate extending to the midplane minor radius a, and $V(r)$ is the plasma volume contained within flux surface r. Note that the value of $A_{\rm eff}$ includes the factor of 1/2 since $n_e L$ corresponds to a double-pass through the plasma. For all the data points presented in fig. 4.2, a constant $A_{\rm eff} = 5.1 \times 10^3$ cm^2 is used. This value is within 7% of the value of $A_{\rm eff}$ with a parabolic density profile dropping to zero density at the plasma boundary. The random error associated with using a constant $A_{\rm eff}$ is estimated to be about 20% based on Abel-inverted density profiles of a reduced set of discharges. Following an evaporation of ∼4 g Li onto the shells (fig. 4.2a, blue), $R_{\rm cum}$ increases about 60% as the surface is exposed to a cumulative external fueling of 3.5×10^{21} H atoms. At the start of operation after allowing the lithium to passivate for a day and without any

additional evaporation (red), R_{cum} had increased an additional ~60% via passivation of the lithium surface with residual gases. Although the surface was exposed to an additional 2.5×10^{21} H atoms from external fueling, R_{cum} did not increase markedly. Following a partial evaporation (green), R_{cum} began at an intermediate value and quickly increased to a value comparable to the 1-day passivated case. The scatter-plot of R_{cum} at the end of the second GPI fueling pulse versus the peak plasma current at this time (fig. 4.2c) shows a clear trend between increased R_{cum} and lower peak plasma current at the end of the fueling pulse, with discharges on partially-passivated lithium achieving 10–20% lower plasma currents during this time period.

4.1.3 τ_p^* Measurements

The effective particle confinement time τ_p^* (eq. 1.18) is another parameter which characterizes the temporal evolution of the particle inventory in the plasma. This parameter enters directly into the ordinary differential equation for the core particle inventory in a simple, global model (eq. 1.17) and folds together both core particle transport and R_{core}. When all external sources are terminated, the core particle inventory decays with an e-folding time of τ_p^*. Therefore, fitting an exponential to the particle inventory decay after transient external fueling permits measurement of τ_p^*. Exponential fits were performed on the same data-set as shown in fig. 4.2 after the first fueling pulse was terminated. As in the determination of R_{cum}, a constant conversion factor (A_{eff}) from midplane $n_e L$ to N_e is assumed. Note that calculation of τ_p^* is only affected by relative changes in A_{eff} during a particular shot and not its absolute value.

Figure 4.3a (blue) shows that following an evaporation of ~4 g Li onto the shells, τ_p^* values of 0.7–1 ms are obtained with no measurable increase with cumulative external fueling over the course of the run day. Operation on a 1-day passivated lithium surface without any additional evaporation (red) yielded τ_p^* in the range of 1.5–3.0 ms, again with insignificant

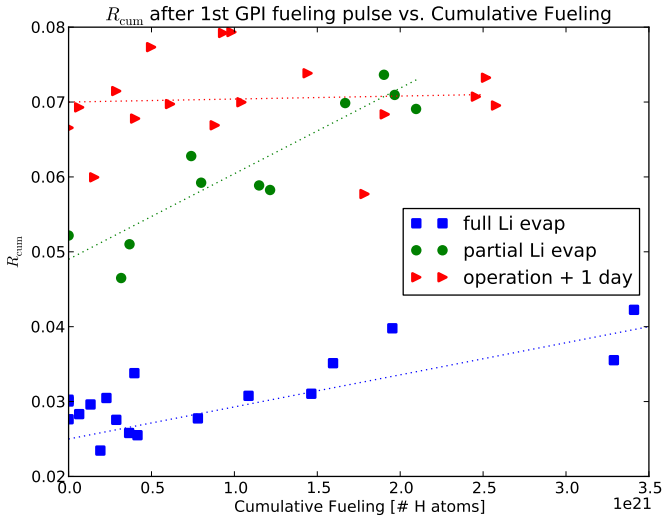

(a)

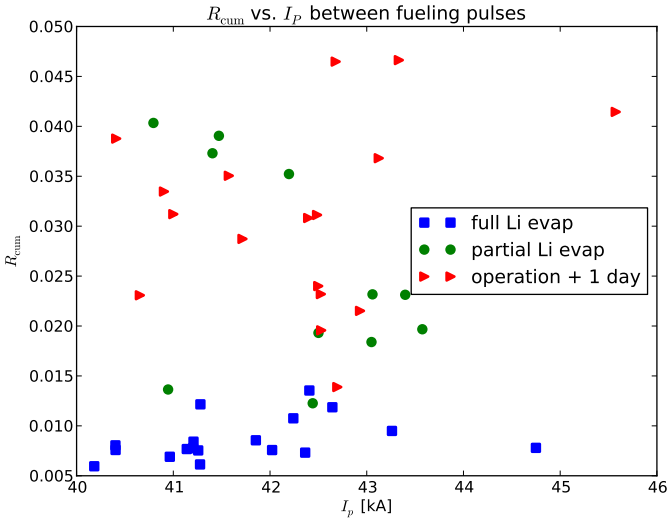

(b)

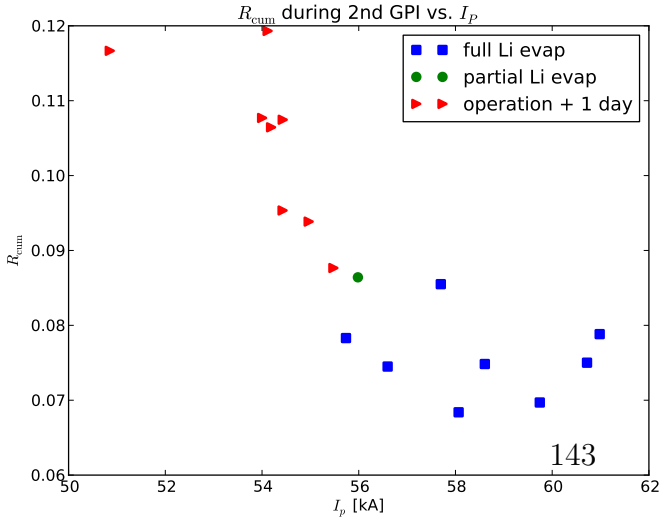

(c)

Figure 4.2: Measurements of Cumulative Recycling vs. Cumulative Fueling and Plasma Current. (a) Scatter-plot of cumulative recycling ($R_{\rm cum}$), versus the total cumulative external fueling during previous shots during that run day. $R_{\rm cum}$ is measured by taking its average value from t =445.75 to 447.25 ms, after the density has decayed substantially following termination of the first external fueling pulse. Dotted lines serve to guide the eye. (b) Scatter-plot of the average $R_{\rm cum}$ vs. the peak plasma current from t=447.25 to 448.0, during which the density is at its minimum. (c) Scatter-plot of $R_{\rm cum}$ vs. the peak plasma current obtained during the second GPI fueling pulse. $R_{\rm cum}$ is measured by taking its average value from t =450.0 to 451.0 ms. The value of I_P plotted is the maximum of the plasma current during this time period.

increase with external fueling. Following a partial evaporation (green), τ_p^* began at an intermediate value for the first discharges, about 1.2 ms, and increased with cumulative fueling up to about 2.5 ms. A scatter-plot of $R_{\rm cum}$ vs. τ_p^* is shown in fig. 4.3b, showing a high degree of correlation between the two quantities, validating the model for exponential decay of density following termination of external fueling. Of the two, $R_{\rm cum}$ is the more sensitive measurement.

Although these are all high-performance discharges with peak plasma currents $\gtrsim$50 kA, τ_p^* varies between them by about a factor of 4, suggesting recycling has been varied substantially. Interestingly, this level of change in recycling does not affect the attainable plasma currents early in the discharge and only very weakly towards the end of the discharge, as shown in fig. 4.2c.

4.2 Dependence of Hydrogen Emission on Wall Condition

While the preceding measurements of τ_p^* and $R_{\rm cum}$ demonstrate changes in effective particle confinement, both of these figures of merit convolve together the core particle transport, edge physics (affecting where recycled hydrogen is ionized), and recycling. Hydrogen line emission, on the other hand, is tied to the neutral hydrogen density and the edge electron density and temperature. If the edge electron density and temperature are known, and are reasonably constant over the neutral penetration length, then line emission can be directly related to the hydrogen ionization rate using ionization-per-photon (S/XB) coefficients[94] pre-computed by ADAS[93]. This approach is applicable whether the source of hydrogen is from recycling or external fueling. The S/XB coefficient for hydrogen Lyman-α emission is minimally dependent on n_e, varying <30% for n_e from 5×10^{10} to 1×10^{13} cm^{-3} (at T_e=20 eV). The dependence on T_e is also relatively weak, varying by less than a factor

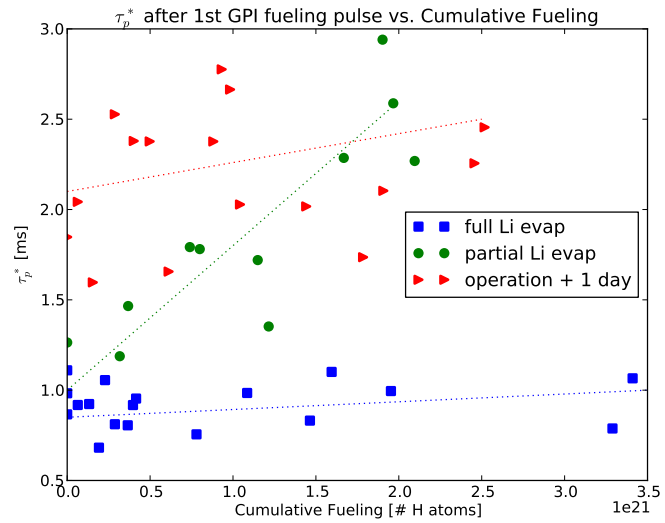

(a)

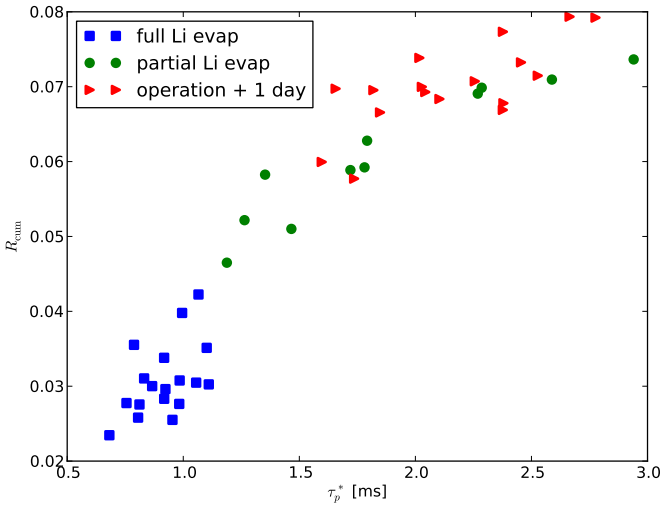

(b)

Figure 4.3: Measurements of τ_p^*. (a) Scatter-plot effective particle confinement time (τ_p^*), versus the total cumulative external fueling during previous shots during that run day. τ_p^* was calculated by fitting an exponential to the midplane density decay timeseries after the first fueling pulse, from t =445.75 to 447.25 ms. Dotted lines serve to guide the eye. As a consistency check a scatter-plot of $R_{\rm cum}$ vs. $\tau_p^*$is shown in (b). The measured values of $R_{\rm cum}$ and τ_p^* are highly correlated indicating both quantities are related to effective particle confinement.

of 2 for T_e from 10 to 100 eV (at n_e=2 $\times$ 10^{12} cm^{-3}). Because of the weak dependence of the hydrogen ionization rate with edge plasma parameters, even if these parameters are not known precisely (but can be assumed to be within this range) changes in the hydrogen ionization rate can be inferred from changes in the Lyman-α emission.

4.2.1 Hydrogen Emission Timeseries

For constant particle flux to the wall, changes in the hydrogen ionization rate can be directly connected to changes in recycling. In addition, during periods fueling from a relatively low-efficiency source (such as a gas puffer on the outboard midplane) hydrogen ionized in the SOL and neutral hydrogen impinging on the wall will recycle at the wall, effectively amplifying the external fueling.

The Lyman-α emission from the three discharges shown in fig. 4.1 are presented in fig. 4.4. Prior to the second fueling pulse, overall emission during the discharge following a full Li evaporation (blue) is significantly less than the other cases. Note that although the emission measured by the outboard array is somewhat higher, the reduced emission on the inboard array dominates. Recall that the second fueling pulse for the discharge following a partial Li evaporation (green trace) is from the MCI. The short vertical extent of emission during the MCI pulse is due to the collimated gas jet produced by the MCI. The lower signal measured by the arrays during MCI fueling is because the MCI is located on the toroidally opposite side of the vessel (see fig. 2.7) from the inboard-viewing array and direct view of the MCI gas jet is obscured by the centerstack.

The discharges discussed above all have very similar plasma current timeseries suggesting comparable electron temperatures. In contrast, more heavily-fueled discharges can produce similar plasma currents on a fresh Li surface, but significantly degraded plasma currents on a partially-passivated surface. Figure 4.5 compares two shots with total gas-puff fueling of 7.6 $\times$ 10^{19} H atoms. The first shot (blue) was taken within a few hours of evaporating

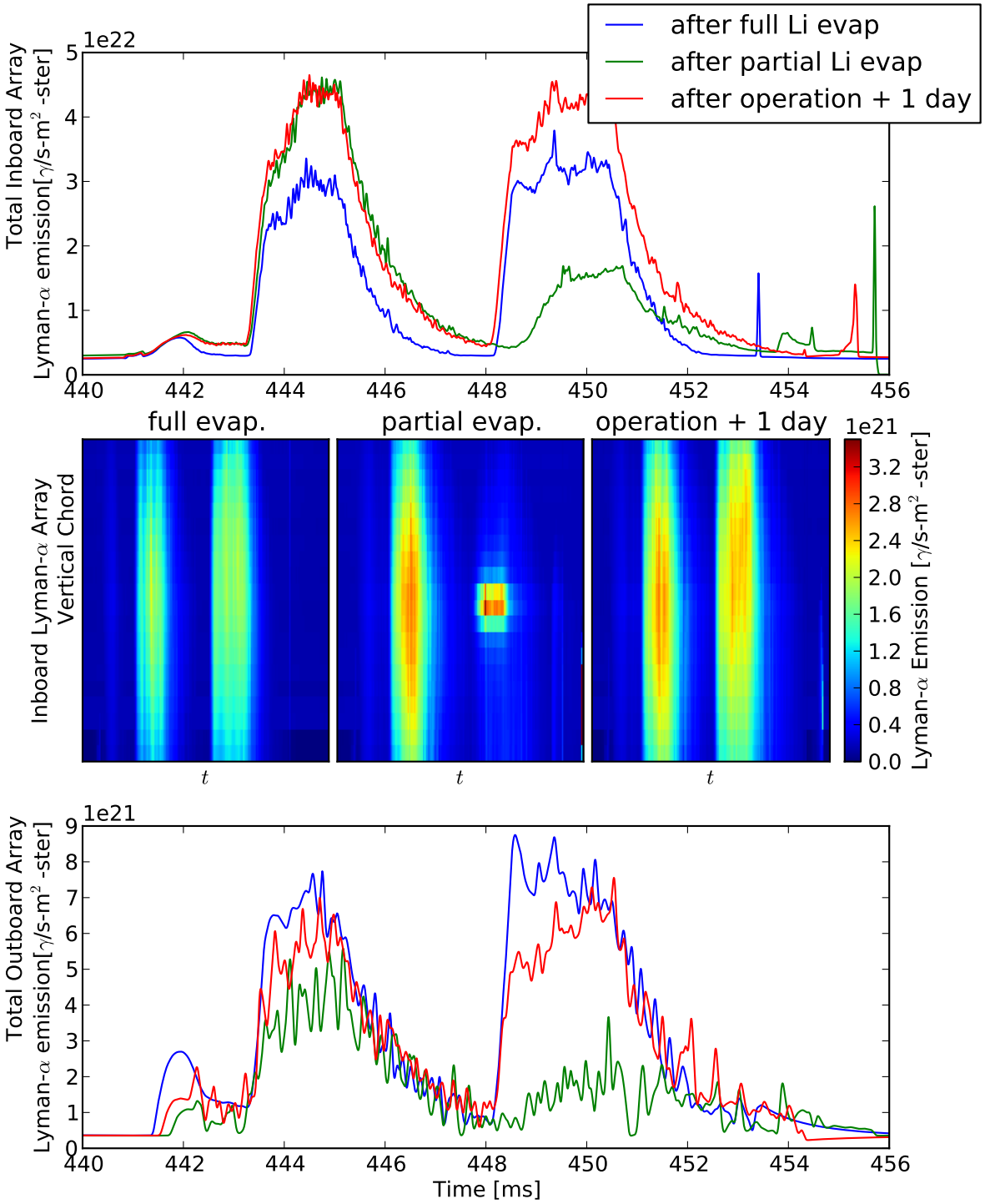

Figure 4.4: Lyman-α emission timeseries for various operating conditions. The same shots are displayed as in fig. 4.1. The vertical axis on the central row corresponds to channels of the inboard array, which view the inboard surface of the shell from $Z = -7.2$ cm to $Z = 7.2$ cm. Recall that the second fueling pulse for the shot following a partial lithium evaporation (green trace) is from the MCI, while GPI is used in the other two cases. Emission during MCI fueling appears is much more localized vertically (middle image in the central row) because of the directed gas flow from the MCI nozzle and vignetting of the view by the shells.

$\sim$2 g of lithium onto the shells, while the second (green) was taken after plasma operation on the fresh surface and 22 hours of allowing the lithium to passivate with residual gases. Prior to the first fueling pulse, the plasma current traces are comparable. The emission level is elevated during the fueling pulse, but remains nearly constant for the shot on a fresh lithium surface (blue trace). In contrast, emission increases linearly with time for the shot on a partially-passivated surface (green trace). This behavior suggests a buildup in the edge neutral density as a result of increased recycling. Hydrogen from external fueling that is not ionized in the core is promptly recycled at the wall; while the external fueling is applied, the edge neutral density increases linearly with time. The result is an amplification of the applied external fueling rate. Note that this effect is expected to be more pronounced with fueling sources that have lower core penetration efficiency since these sources supply more neutrals to the SOL.

A delay of about 1.2 ms is evident between the fueling trigger start times and the increase in emission rate. This identical delay is seen between the fueling trigger start time and an increase in plasma density (see fig. 4.1) and includes both the time for the valve to open and the gas-dynamic time of the gas-puff injector. A similar delay is apparent between the fueling trigger end time and a drop in the emission rate. Interestingly, the discharge on a partially-passivated Li surface shows a sudden drop in the emission at this time. The fact that the emission can change so substantially on such a short ($\lesssim$0.5 ms) timescale suggests that the gas-puff injector on the outboard midplane sources very few molecules into the vessel after $\lesssim$2.0 ms of when the valve is triggered shut. This finding implies that the τ_p^* measurements presented in section 4.1.3 are not subject to systematic error from residual flow out of the gas puff injector.

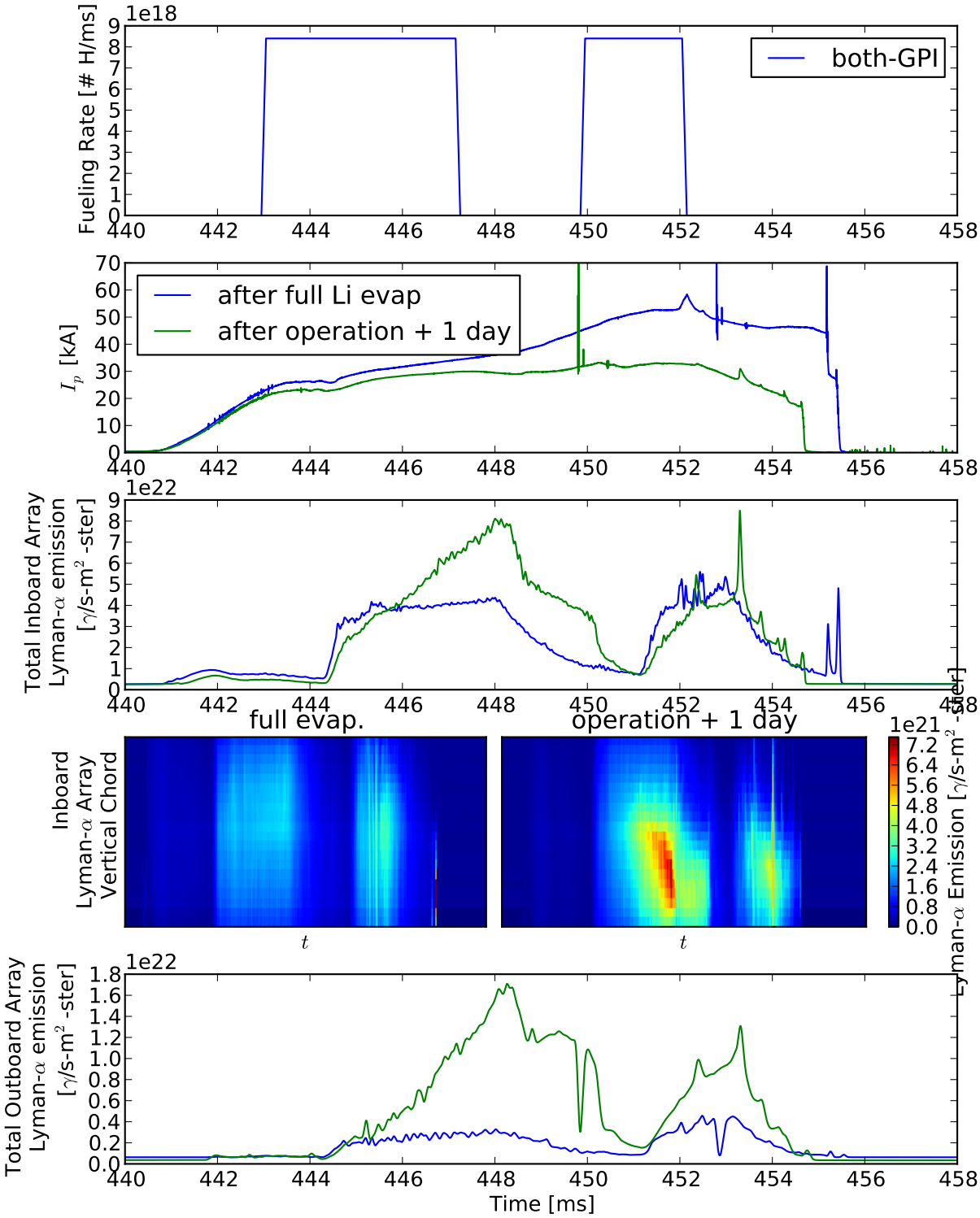

Figure 4.5: A discharge that becomes over-fueled on partially-passivated surface. These shots were taken after a total of ∼6 g of Li was deposited over 3 evaporations, with plasma operations after each. The vertical axis on the fourth row corresponds to channels of the inboard array, which view the inboard surface of the shell from $Z = -7.2$ cm to $Z = 7.2$ cm.The blue shot was taken within hours after the lithium evaporation, while the green shot was taken the following day. Both shots used identical coil programming and side gas puffer fueling of 7.6×10^{19} H atoms.

4.2.2 Emission Trends

The measured emission has been analyzed for a significant number of shots on various wall conditions, but with the same coil programming and fueling. Figure 4.6a is a scatter-plot of the peak emission during a fueling pulse early in the discharge against the total cumulative external fueling for preceding shots on the same run day. The measurement points represents the sum of all the array channels at the time point of maximum emission during the fueling pulse. Lower emission is clearly evident for shots following evaporation of a full lithium coating on the shells, although shots later in the campaign showed consistently higher emission. In either case, the emission intensity increases substantially over a number of discharges as a cumulative 10^{21} H atoms are supplied by external fueling. The increase of emission with cumulative external fueling then appears to slow as an additional 2.5×10^{21} H atoms are supplied. In contrast, discharges on a partially passivated surface show the highest emission during the gas puff, but little trend with increased cumulative fueling. Discharges following evaporation of a partial coating on the shells follow the same trend as those following evaporation of a full coating, only shifted to higher emission. The emission level for these discharges appears to asymptote near the emission level for the discharges on a partially-passivated surface. The dependence of emission intensity with cumulative fueling is qualitatively similar to the dependence of R_{cum} with cumulative fueling shown in fig. 4.2.

The $1/e$ decay time of the total emission measured by the inboard-viewing array following the final fueling pulse is shown in fig. 4.6b. The data are qualitatively consistent with the previous plot: emission increases with cumulative external fueling for discharges following evaporating a full lithium coating onto the shells, while there is no clear trend with cumulative fueling for discharges on a partially-passivated surface. Qualitative agreement between the two plots validates the model that increased recycling results in increased emission during a fueling pulse, by effectively amplifying the external fueling. In addition, by virtue of fueling

the discharge and slowing the density decay (increasing τ_p^*), the recycled particle flux also decays at a slower rate.

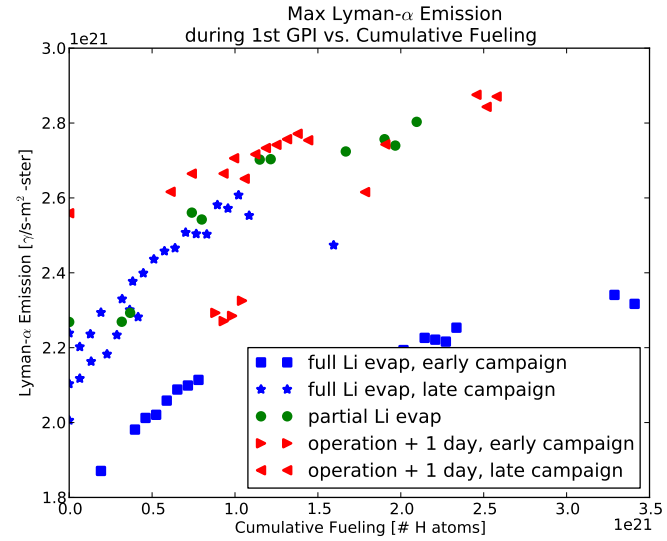

(a)

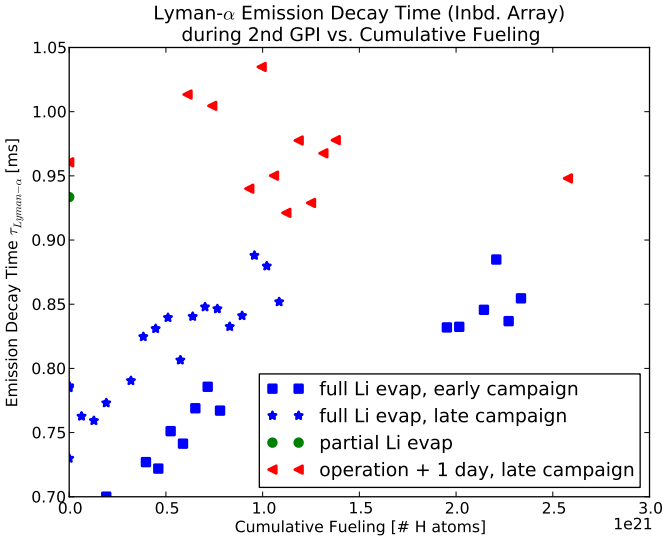

(b)

Figure 4.6: Trends of (a) peak Lyman-α emission and (b) Lyman-α emission decay rate versus cumulative fueling. The peak emission in (a) is calculated by averaging over the emission from all the array channels, then taking the maximum value during the 1st fueling pulse. The emission decay rate in (b) is calculated by fitting an exponential to the emission measured by the inboard array, summed over all channels, following the final fueling pulse. Some of the shots shown in (a) use different fueling later in the discharge; therefore, (b) contains a reduced set of shots using only the same fueling.

As with the plots of R_{cum} against plasma current (fig. 4.2), there is a direct correlation between reduced emission and increased plasma current late in the discharge during the time

period of the second GPI pulse. (See figs. 4.7b and c.). Heavily fueled discharges (such as those in fig. 4.5) with 7.5×10^{19} H atoms or more of external fueling, are not included in these plots. The discharges in these figures were all fueled with about 6.4×10^{19} H atoms from the side gas puffer.

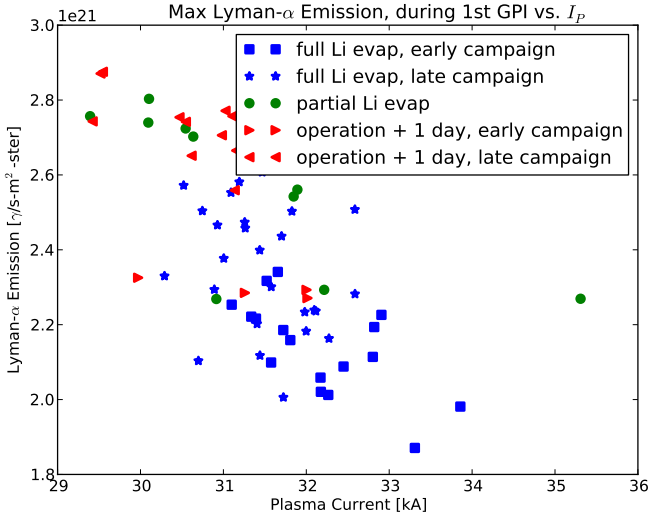

(a)

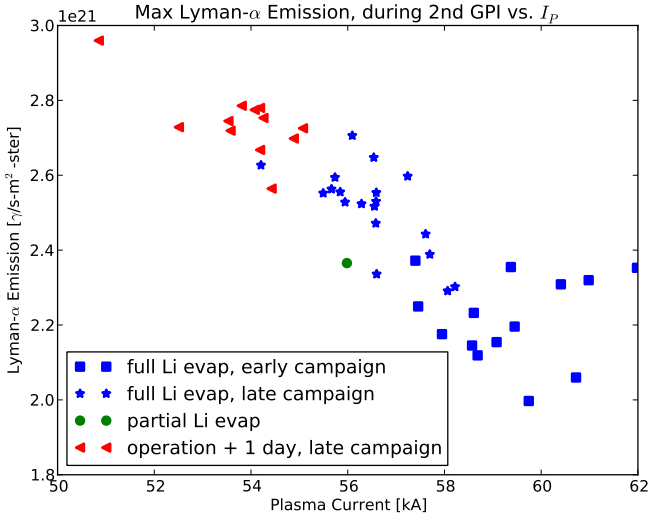

(b)

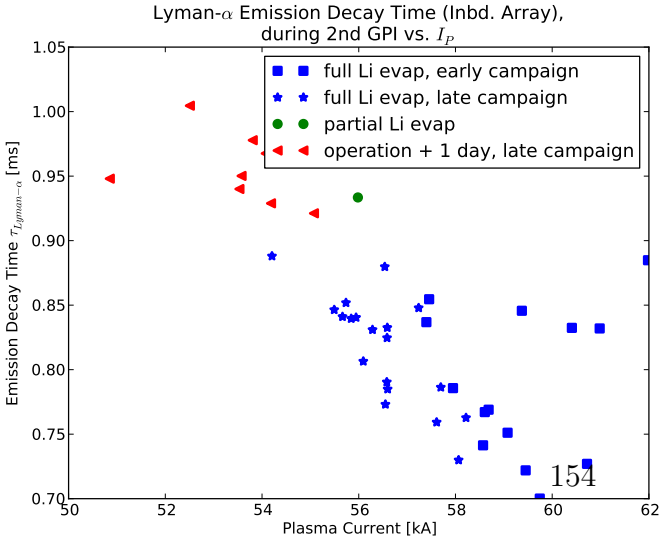

(c)

Figure 4.7: Trend of Lyman-α emission with plasma current. Scatter-plot of the maximum emission averaged over both the inboard-viewing and outboard-viewing array channels during the (a) first and (b) second fueling pulses versus the maximum plasma current during the same time period. (c) A scatter-plot of the $1/e$-folding time for the Lyman-α emission decay rate from the inboard-viewing array following the second fueling pulse.

4.2.3 Langmuir Probe Edge Plasma Measurements

A single-tip swept Langmuir probe (described in sec. 2.2.8) was used to measure the $n_e(t)$ in the $T_e(t)$ SOL. The probe was set to be flush with the inner shell lip on the outboard midplane; therefore the ion flux to the probe served as an estimate of the ion flux to the outboard side of the shells just above and below the midplane. The I-V characteristics were analyzed following the method outlined in sec. 2.2.8. In addition, the ion flux and electron density were calculated as:

$$\Gamma_{SOL-probe} = \frac{I_{sat}}{eA} \tag{4.3}$$

$$n_e = \frac{\Gamma_{SOL-probe}}{0.6 c_s}, \quad c_s \doteq \sqrt{\frac{T_e + \gamma_i T_i}{m_i}} \tag{4.4}$$

where A is the probe area, e the electron charge, c_s the ion sound speed, m_i the ion mass, and T_e and T_i are the electron and ion temperatures, respectively. γ_i may be taken to be 5/3 since the ions are unmagnetized on the scale of the probe. Note that an average charge of $Z = 1$ is assumed. This assumption would tend to over-estimate the flux to the probe and n_e. In addition, for the analysis that follows following, $T_i \to 0$ is assumed for simplicity. Choosing instead $T_i \sim T_e$ would reduce the calculated densities by 30%.

The timeseries presented in figure 4.8 were obtained by analyzing the I-V characteristics for several consecutive shots with identical coil programming and external fueling, then interleaving the calculated $\Gamma_{SOL-probe}$, n_e, and T_e. Higher ion flux and SOL density are evident for the shots on partially-passivated lithium (red), consistent with fueling of the SOL from increased recycling. Despite scatter in the data, measurements indicate the edge T_e increases between the fueling pulses (t=446–448 ms) for the shots on a fresh lithium surface (blue); however, most of the data points on partially-passivated lithium (red) indicate at most a much reduced increase in the edge T_e. Such behavior is consistent with the picture that cooling of the SOL by particles recycled from the wall is markedly reduced for the

discharges on a fresh lithium surface. These timeseries of n_e and T_e in the SOL were used to determine the ionizations-per-photon (S/XB) coefficient, in order to estimate the hydrogen flux from emission measurements.

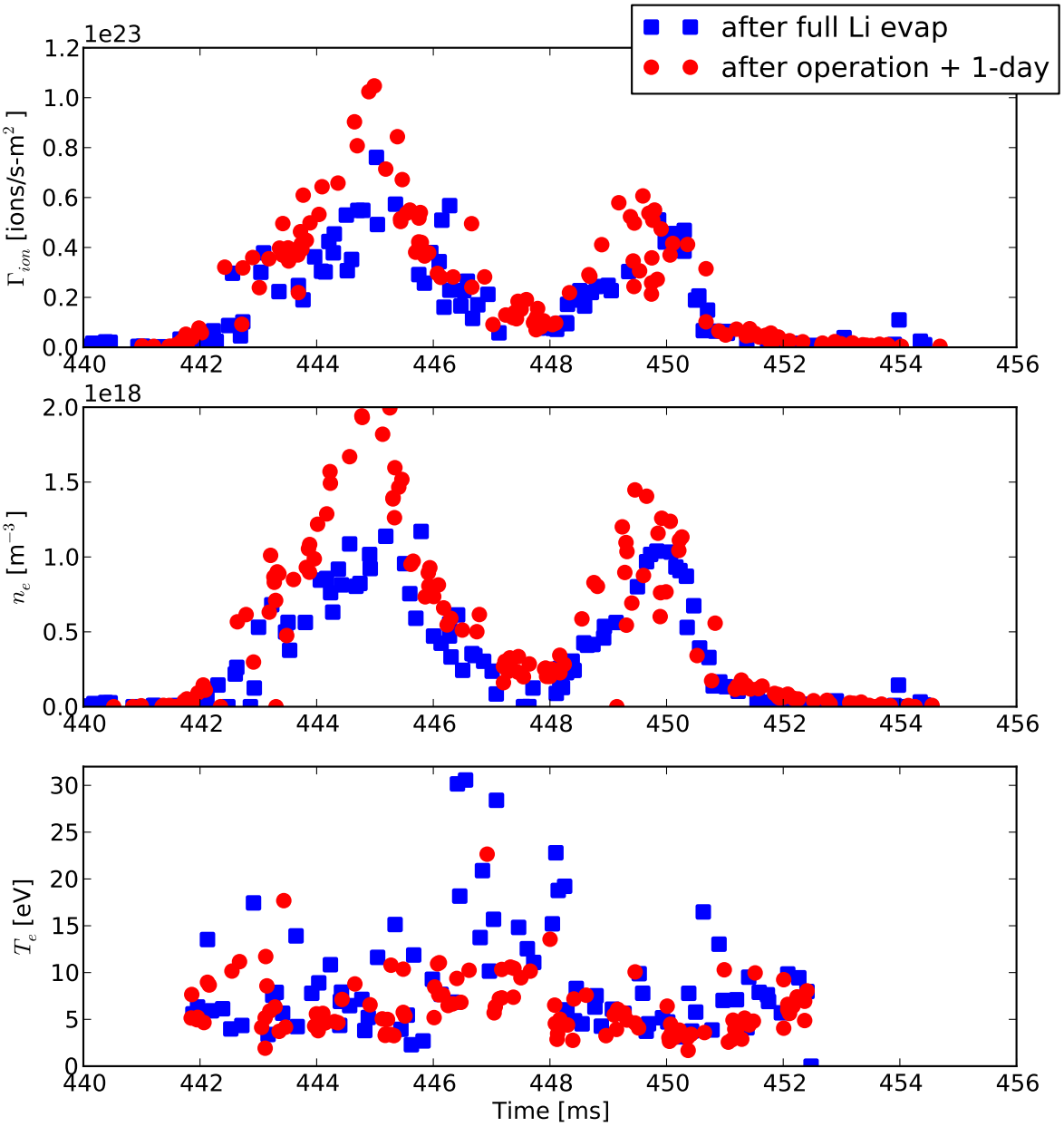

Figure 4.8: Langmuir probe ion flux, n_e, and T_e for various operating conditions. These timeseries were composed by analyzing each of the 1 ms-duration I-V characteristics for a set of consecutive shots with identical fueling and coil programming.

4.3 Simplified Recycling Models

4.3.1 Local Ionized Plate Recycling Estimate

The low SOL electron density in LTX plasmas complicates the inference of $R_{\text{plate}}$from particle flux and emission measurements. In principle only two measurements are required to determine R_{plate} at a particular location: a measure of the particle flux into the PFC ($\Gamma_{SOL-wall}$) and a measure of the particle flux out of the PFC ($\Gamma_{wall-SOL}$). The former can be measured by a Langmuir probe. The latter can be estimated from a measurement of the line emission rate and the S/XB coefficient, which also requires measurement of $n_e(t)$ and $T_e(t)$. These plasma parameters are commonly determined from the probe measurements as well. There are two major issues in this simple use of the S/XB approach to estimating the particle flux from the wall for LTX plasmas.

The first issue is the assumption that the electron density and temperature are reasonably homogeneous over the neutral ionization length. Considering only atomic hydrogen (rather than molecular hydrogen) for simplicity, the neutral ionization length can be estimated from:

$$\lambda = \frac{v_0}{\langle \sigma v_e \rangle \, n_e}, \tag{4.5}$$

where v_0 is the average speed of the atom, and $\langle \sigma v_e \rangle$ is the Maxwell-averaged electron-impact ionization cross-section, which can be found in various references including ADAS[93]. For $T_e > 25$ eV, $\langle \sigma v_e \rangle$ is a very weak function of temperature, varying only from 2–3$\times 10^{-8}$cm^3 /s.

The primary sources of atomic hydrogen are from direct reflection of hydrogen ions or atoms incident on the PFC surface and dissociation of hydrogen molecules or molecular ions either from external fueling or that are desorbed as a result of recycling. Hydrogen atoms from dissociative processes are Franck-Condon neutrals with an energy of 2–3 eV, for an average speed of $v_0 \sim 4 \times 10^6$cm^2 /s. Atoms resulting from direct reflection will retain up to 40% of the energy of the incident ion, so their energy distribution will be on the order of

$E_i/5$, where E_i is the energy of ions incident to the surface:

$$E_i = \frac{1}{2} m_i c_s^2 + \phi_{\text{sheath}} = \frac{1}{2}\gamma T_i + \frac{1}{2}\left[1 + \ln\left(\frac{m_i}{2\pi m_e}\right)\right] \tag{4.6}$$

Taking $\gamma \approx 5/3$, this corresponds to an average speed of $v_0 \sim 9 \times 10^6 \text{cm}^2$ /s using a conservatively low guess that $T_i \ll T_e$ and $T_e \sim 6$ eV.

Recalling fig. 4.8 Langmuir probe measurements with the probe tip flush with the plasma-facing surface of the outboard shell ($R = 66$ cm) measure electron density of 1–2 $\times 10^{12}$ cm^{-3} during GPI fueling, and densities $\lesssim 5 \times 10^{11}$ cm^{-3} between fueling pulses. At such low densities, the SOL plasma is effectively transparent to Franck-Condon atoms ($\lambda > 60$ cm); even using a typical core density ($n_e \sim 1 \times 10^{13}$ cm^{-3}) the neutral ionization length is about half the nominal plasma minor radius ($\lambda \gtrsim 10$ cm). Therefore, the plasma is far from homogeneous over the penetration length for neutral hydrogen atoms. In fact, near the trough in density between the fueling pulses, fig. 4.1 would indicate an average $\bar{n_e} \sim 2 \times 10^{12} \text{cm}^{-3}$ in the core, which would further extend the ionization length of Franck-Condon neutrals. Until now, this discussion has neglected charge exchange which actually has a higher cross-section than electron-impact ionization for the T_e of interest. Although it is non-trivial how to properly capture the full effects of charge-exchange, experiments and modeling typically indicate that charge exchange increases the effective neutral penetration into the plasma[148]. Therefore, the n_e and T_e measured by the probe are not at all indicative of a "spectroscopic average" n_e and T_e to use to calculate the S/XB coefficient. Even though the S/XB coefficient for Lyman-α emission is a weak function of n_e and T_e, such a mean-free-path could have the effect of increasing the calculated $\Gamma_{wall-SOL}$ by 70%. Since atoms from external fueling, direct reflection, and recycling can sample such varied plasma parameters, the S/XB approach does not provide an accurate estimate of $\Gamma_{wall-SOL}$ for LTX.

The second issue with using the S/XB approach to estimate the particle flux from the wall is that the S/XB method actually solves for the ionization rate, not the flux of hydrogen neutrals from the PFC. If the SOL plasma had a high n_e, such as in a high-recycling divertor plasma, it might be reasonable to assume the full ionization of the recycled neutral hydrogen flux. However, since the neutral penetration length in LTX plasmas is long relative to the plasma dimensions, many of the recycled neutrals from the surface are not ionized before striking another surface. This effect could increase the inferred value of $\Gamma_{wall-SOL}$ significantly. In order to address all of these issues, Monte Carlo neutral modeling using the Degas 2 code has been performed, and is presented in chapter 5.

Despite these significant issues, and since the procedure is straightforward, the S/XB approach has been used here to infer the flux of hydrogen ions. Since emission from GPI fueling is well within the field-of-view of both the Lyman-α arrays, the measured emission during GPI fueling (and even during SGI or MCI fueling, in fact) cannot be used to determine the recycled hydrogen flux from the wall. Only the measured emission between fueling pulses can be used to infer the recycled hydrogen flux. The $n_e(t)$ and $T_e(t)$ measurements at a single point in the far-SOL have been used as an estimate of $\Gamma_{SOL-wall}$, and to compute the timeseries of the Lyman-α S/XB coefficient for a number of discharges, from t =445.5 to 446.5. This time region was chosen because the fractional error in the ion saturation current measurement (which is proportional to $\Gamma_{SOL-wall}$) increases as the density decays. The value of the S/XB coefficient is typically 0.5–0.8. This S/XB coefficient is then used to convert the average measured emission from the four central channels of each array into an ionization flux. Note that both the inboard-viewing and outboard-viewing arrays used the same S/XB coefficient and same value of $\Gamma_{SOL-wall}$ from the midplane Langmuir probe. Figure 4.9 shows the result of performing this calculation for several sets of discharges. Just as in fig. 4.8, the probe measurements during several consecutive discharges have been interleaved in to produce each data point. Error bars represent the standard deviation in the measurement

during the time window. Any differences between the discharges on a fresh lithium surface and those on a partially-passivated surface are well within the error in the measurement. Likewise, there does not appear to be a substantial increase in R_{plate} with cumulative fueling. Differences in the true $\Gamma_{SOL-wall}$ to each surface and the ionization efficiency of recycled hydrogen from each surface contribute to the measured disparity between the two views.

4.3.2 Simplified Global Recycling Model

Before embarking on Monte Carlo neutral modeling, however, the highly simplified model for the particle balance in the core and SOL from section 1.3.1 will be explored further. The purpose of this model is to gain qualitative insight into the timeseries of electron density and hydrogen emission. The model solves for the number of electrons in the core and SOL:

$$\frac{dN_{core}}{dt} = \eta_F \Gamma_F(t) - \frac{N_{core}}{\tau_p} + \eta_R \Gamma_R \tag{4.7}$$

$$\frac{dN_{sol}}{dt} = (1-\eta_F)\Gamma_F(t) + \frac{N_{core}}{\tau_p} - \frac{N_{sol}}{\tau_{sol}} + (1-\eta_R)\Gamma_R. \tag{4.8}$$

The parameters entering the model are the external $\Gamma_F(t)$ and recycled ($\Gamma_R \doteq R_{plate} N_{sol}/\tau_{sol}$) fueling rates, the core particle confinement time ($\tau_p \sim a^2/D$), the SOL particle confinement time ($\tau_{sol} \sim qR_0/c_s$), and the external fueling and recycling core fueling efficiencies (η_F and η_R, respectively). Note that with these definitions, in the absence of external fueling:

$$R_{\text{core}} = \frac{\eta_R R_{\text{plate}}}{1-(1-\eta_R)R_{\text{plate}}} \tag{4.9}$$

The key assumptions in the model are that the fueling efficiencies are constant, all the hydrogen from external fueling and recycling is ionized instantaneously in either the core or the SOL, and emission is proportional to total fueling (external + recycling) rates. The assumption of constant fueling efficiency prohibits the model from capturing the effect of

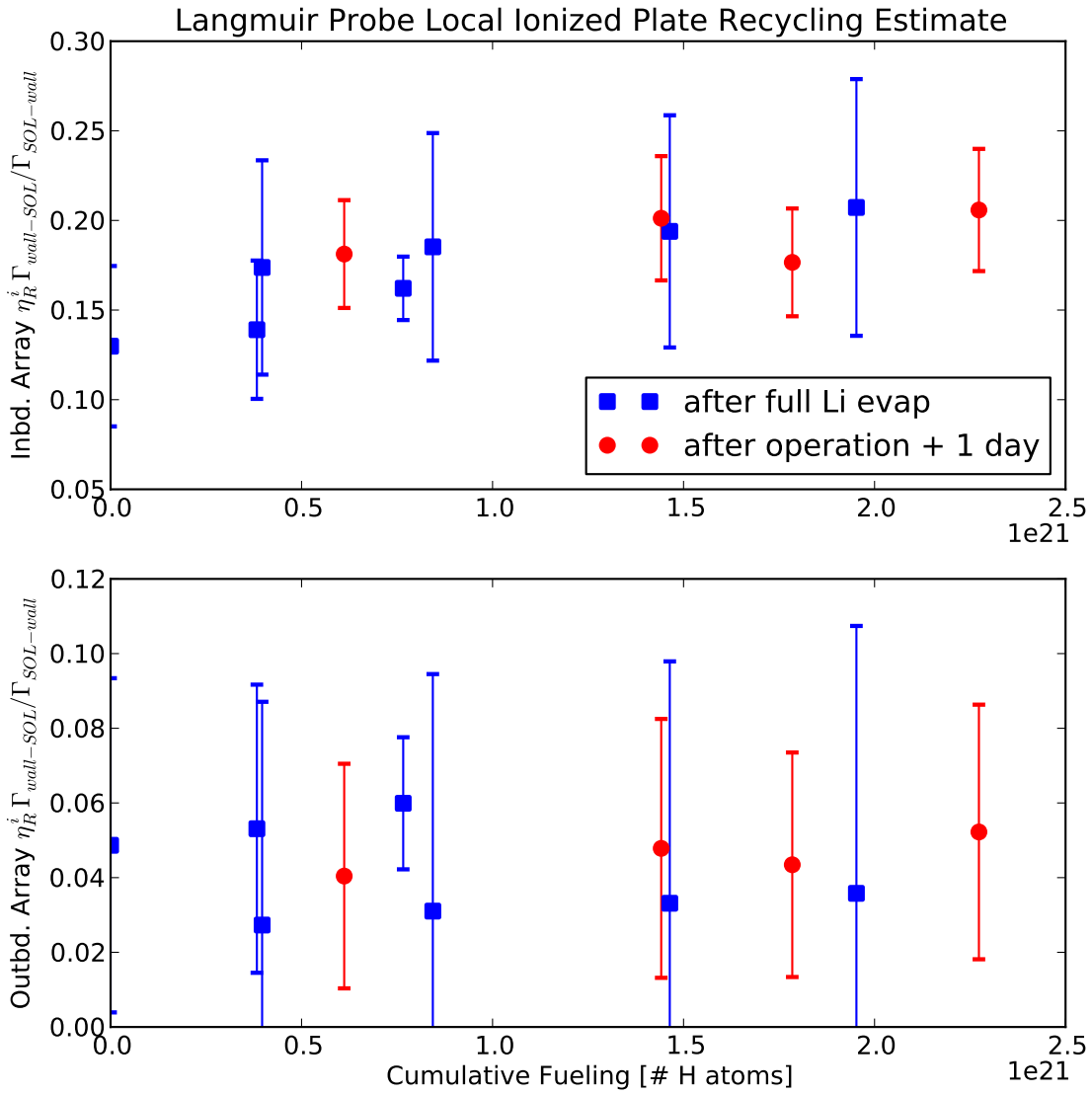

Figure 4.9: Local estimate of the ionized plate recycling ($\eta_R^i R_{plate}$) using Lyman-α emission and Langmuir probe measurements. The ionization efficiency for recycled hydrogen is the fraction of $\Gamma_{wall-SOL}$ that is ionized in the plasma SOL or core.

changes in SOL density affecting core penetration of neutrals from either recycling or external fueling, i.e., "SOL screening" is not captured by the model. Secondly, this model cannot give any insight into the neutral density–it is assumed to be negligible relative to the plasma density.

Figure 4.10 shows the model solution for values of τ_p^* consistent with typical shots on a fresh (blue: τ_p^*=0.95 ms, $R_{\rm core}$=0.47, $R_{\rm plate}$=0.90) or partially-passivated (red: τ_p^*=1.45, $R_{\rm core}$=0.66, $R_{\rm plate}$=0.95) surface. This model qualitatively captures the timeseries of fig. 4.1, showing increased particle inventories and emission with increased recycling. It also produces emission that increases with time during external fueling for higher recycling cases and remains relatively flat for low recycling cases. By using different fueling efficiencies for various fueling sources, the model can also describe relative changes in particle inventories when going from one fueling source to another. Figure 4.10 shows the modeled particle inventories and fluxes, for which emission is a proxy.

4.4 Impurity Emission

In addition to efficiently pumping hydrogen atoms and ions, lithium coatings also serve as a low-Z coating on top of the stainless-steel shells. Since the inner surfaces of the shells are designed to be in close proximity to the plasma, sputtering of metallic impurities could be a concern. Visible survey spectrometers (see sec. 2.2.2, fig. 2.4) do not measure any metallic emission above the noise floor, except perhaps during a disruption at the end of the discharge. Timeseries for visible lithium and oxygen emission from one of the lower shell limiters are shown in fig. 4.11. The H-α emission from the same filterscope view is also shown for reference. Recall that the case following a partial lithium evaporation (green) used MCI rather than GPI fueling during the second fueling pulse, so the H-α emission after t=448 ms cannot be directly compared with the other two cases. The neutral lithium

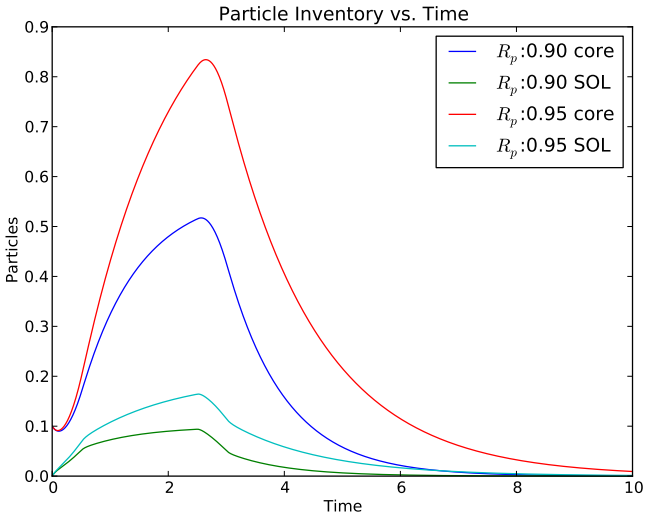

(a)

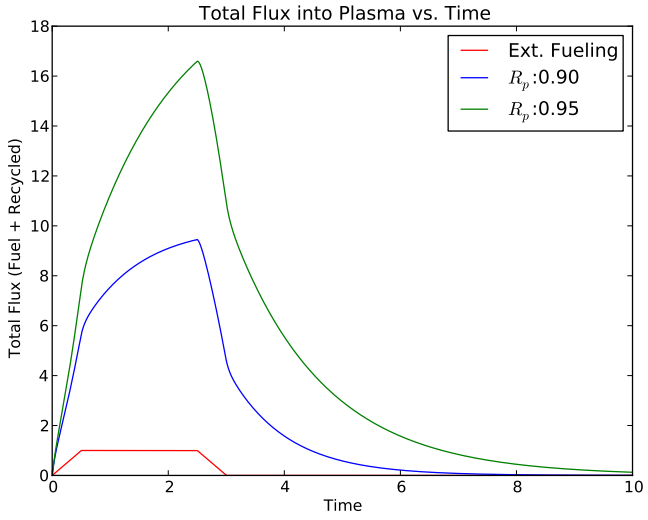

(b)

Figure 4.10: Simple global recycling model captures timeseries behavior. Particle inventories normalized to gas-puff flux in 1 ms (time in ms), τ_p:0.5 ms, τ_{sol}:0.01 ms, η_F:0.24, η_R:0.1. Note that recyling is the dominant source of fueling for $R_{\text{plate}} > 0.5$; $\tau^{total}_{fueling-flux} \propto \tau^*_p$ during the density decay after terminating external fueling.

emission timeseries for the discharge following a full lithium evaporation shows a sharp increase at $t \approx$447 ms, corresponding to the time an instability which caused the sudden drop in density visibile in fig. 4.1. This increase in emission suggests that influx of lithium impurities may be responsible for maintaining the plasma density until the second gas puff is applied.

Values for the S/XB coefficients for H-α, neutral lithium at 610 nm, doubly-ionized lithium at 450 nm, and singly-ionized oxygen at 441 nm are, respectively, 15–30, 1.5–2.7, 0.08–0.5, 20–60, and 15–50. In all cases the SX/B coefficient is much more sensitive to electron temperature than to density. Using these numbers to calculate rough estimates for the discharge-averaged relative source rates of impurities to hydrogen ions gives 0.005–0.1 for the singly-ionized lithium source rate, 5×10^{-4}–0.01 for the doubly-ionized lithium source rate, 0.001–0.03 for the fully-ionized lithium source rate, and 5×10^{-4}–0.04 for the source rate for doubly-ionized oxygen. The purpose of this rough calculation is merely to show that spectral emission measurements indicate that while three plasmas are all fueled predominantly by hydrogen rather than by impurities, they all have significant relative source rates of impurities.

Motivated by the well-known oxygen gettering properties of lithium (see fig. 1.6 for example), fig. 4.12 summarizes changes in oxygen emission with cumulative fueling for various wall conditions. Oxygen emission is about 1.5–4 times higher for the discharges on a partially-passivated surface than for those following deposition of a full lithium coating. The higher emission during the discharges on a partially-passivated surface is consistent with oxygen chemically-bound to the lithium surface being released under plasma bombardment. In both cases, only a very slight trend of increasing emission with cumulative fueling is evident. In contrast, for the discharges following deposition of only a partial lithium coating, oxygen emission increases quickly with cumulative fueling up to an emission intensity consistent with a partially-passivated surface. Although the S/XB coefficient for O II emission at 441 nm is

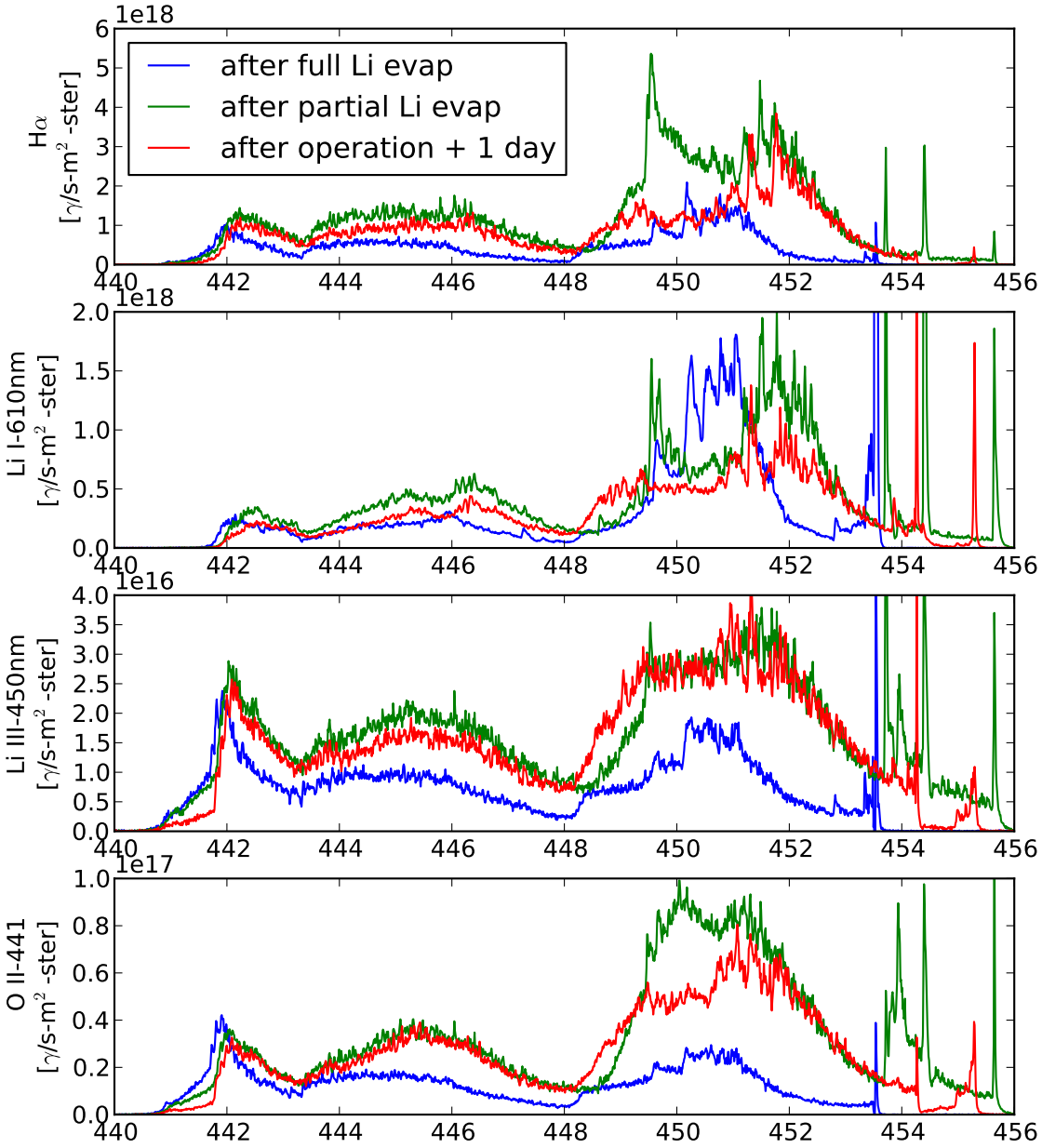

Figure 4.11: Timeseries of lithium and oxygen emission for various wall conditions. The same shots are displayed as in fig. 4.1, with the exception of the shot following a full evaporation (blue). In its place is shown the emission from shot 1112211444. This filterscope views one of the lower shell limiters. The H-α emission from this filterscope view is also shown for reference.

fairly insensitive to density, the increasing density of these discharges, evident in the plot of R_{cum} (fig. 4.2a), and therefore increased particle flux to the surface may account for some of this trend.

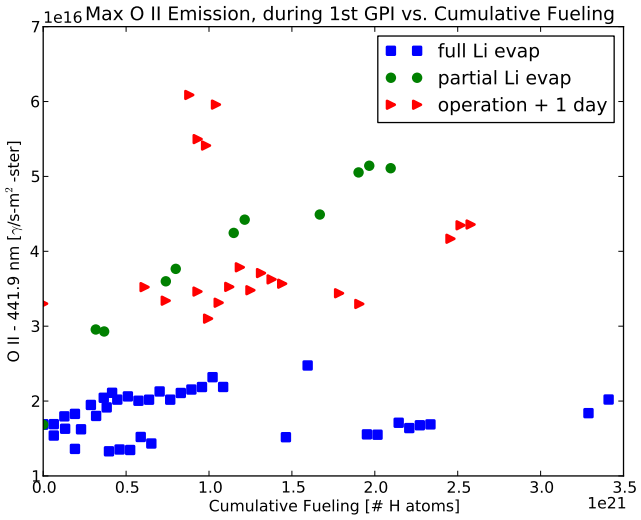

Figure 4.12: Trends of O II emission rate with cumulative fueling. The plotted emission rate is the peak emission during a fueling pulse near the beginning of the discharge.

Returning to the shots from fig. 4.11, an estimate of the impurity density can be derived from the line emission measurements. The emissivity is estimated from the emission rate according to:

$$\epsilon = \frac{4\pi I_{emission}}{L_{sightline}}, \tag{4.10}$$

where $L_{sightline}$ is the length of the sightline through the plasma, about 30 cm. Next, the value of the photon emissivity coefficient (PEC) is estimated from Thomson T_e measurements and the known ionization cross-sections. Finally, the average plasma density is calculated from the midplane line-integrated density:

$$\bar{n_e} = \frac{n_e L}{4a}, \tag{4.11}$$

where the nominal plasma minor radius a=26 cm, and the factor of 4 accounts for a double-pass through both the inboard and outboard halves of the plasma. Figure 4.13 shows the estimated impurity density timeseries, and figure 4.14 shows the impurity densities normalized to the electron density timeseries. Since the photon emissivity is only weakly dependent on electron density, constant values were used. The estimated densities are very likely accurate to within a factor of 3. Uncertainty in the appropriate spectroscopic electron temperature dominates the error in this calculation. The PEC values used in this figure are 6.0×10^{-10} γ-cm^3/s for O^+, 4.25×10^{-9} γ-cm^3/s for Li^{2+}, and 4.0×10^{-12} γ-cm^3/s for Li^{2+}.

These figures illustrate several important findings. First, in all cases, the impurity densities do not decrease between the external fueling pulses, but rather remain constant or increase. Since the electron density is decreasing, the relative impurity density n_I/n_e is increasing. In contrast, during or immediately following periods of external gas fueling, corresponding to periods of high electron density, n_I/n_e are much lower. Second, n_I/n_e increases most for the discharge following evaporation of a full lithium coating onto the shell surfaces. Langmuir probe measurements indicate that for these discharges, T_e in the SOL is elevated during this time period. The sheath and presheath potentials accelerate hydrogen ions diffusing out of the plasma so that they impact the surface with an energy $E_i \sim 3.3 \sim T_e$. Therefore, an elevated T_e in the SOL during the low-density period between fueling pulses would lead to a higher impact energy of ions to the PFCs. Since lithium sputtering yield increases with energy[49], the higher energy ions would sputter more lithium from the surface. In addition, the higher impact energy could liberate other impurity atoms (such as oxygen) that were bound to lithium atoms near the surface. Finally, a significant amount of lithium is becoming doubly-ionized, with $n_{Li^{2+}}/n_e$ reaching up to 10% for the discharge on a fresh lithium surface. Even if this calculation over-estimates the impurity density by a factor of 3, these measurements suggest that impurity fluxes from the wall are contributing to maintain

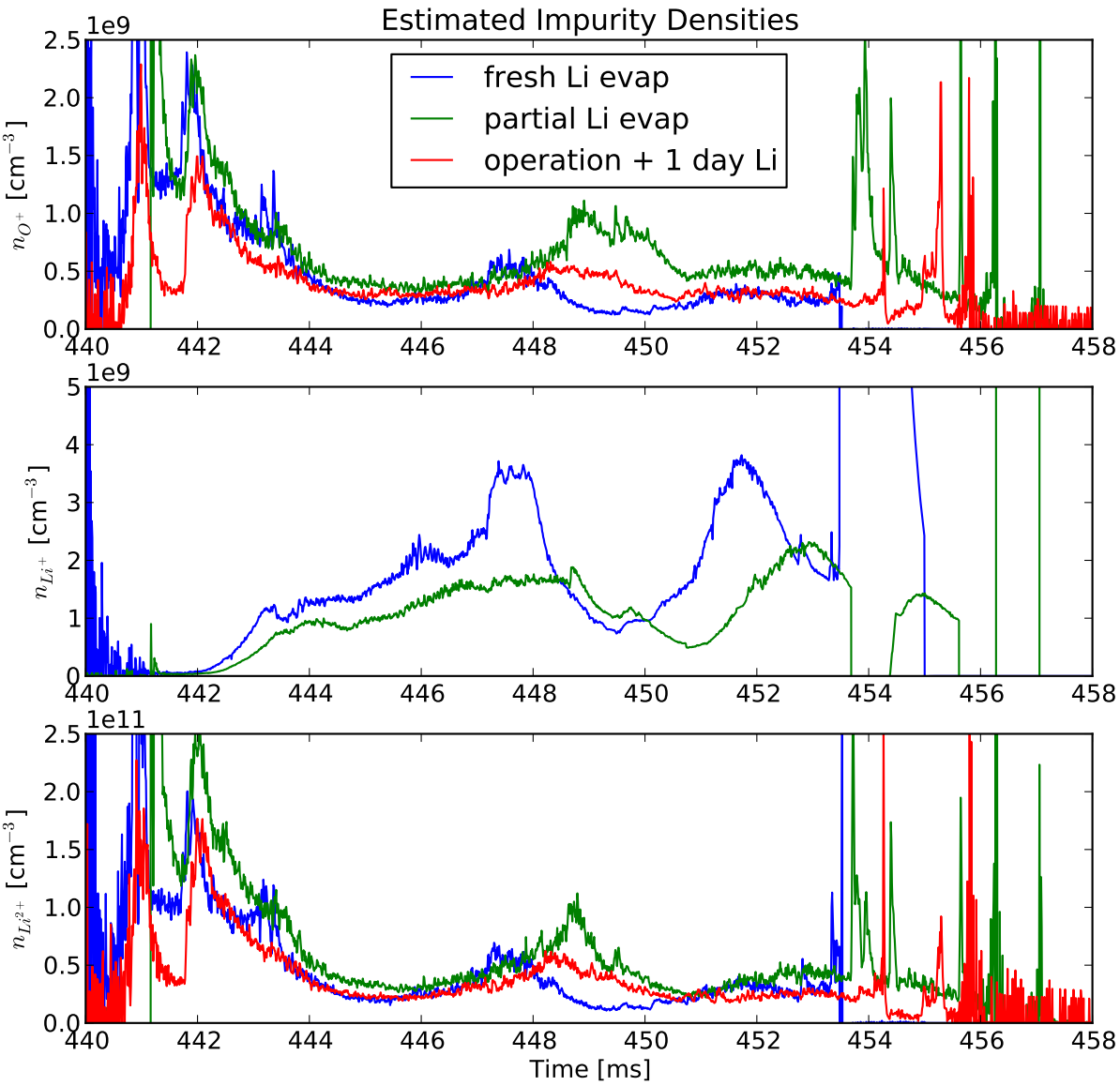

Figure 4.13: Timeseries of lithium and oxygen densities for various wall conditions. The same shots are displayed as in fig. 4.11. The O^+ and Li^{2+} densities are calculated from using emission measurements from a filterscope viewing one of the limiters in the lower shell, while the Li^+ density is calculated from a filterscope viewing the outboard side of the lower shell.

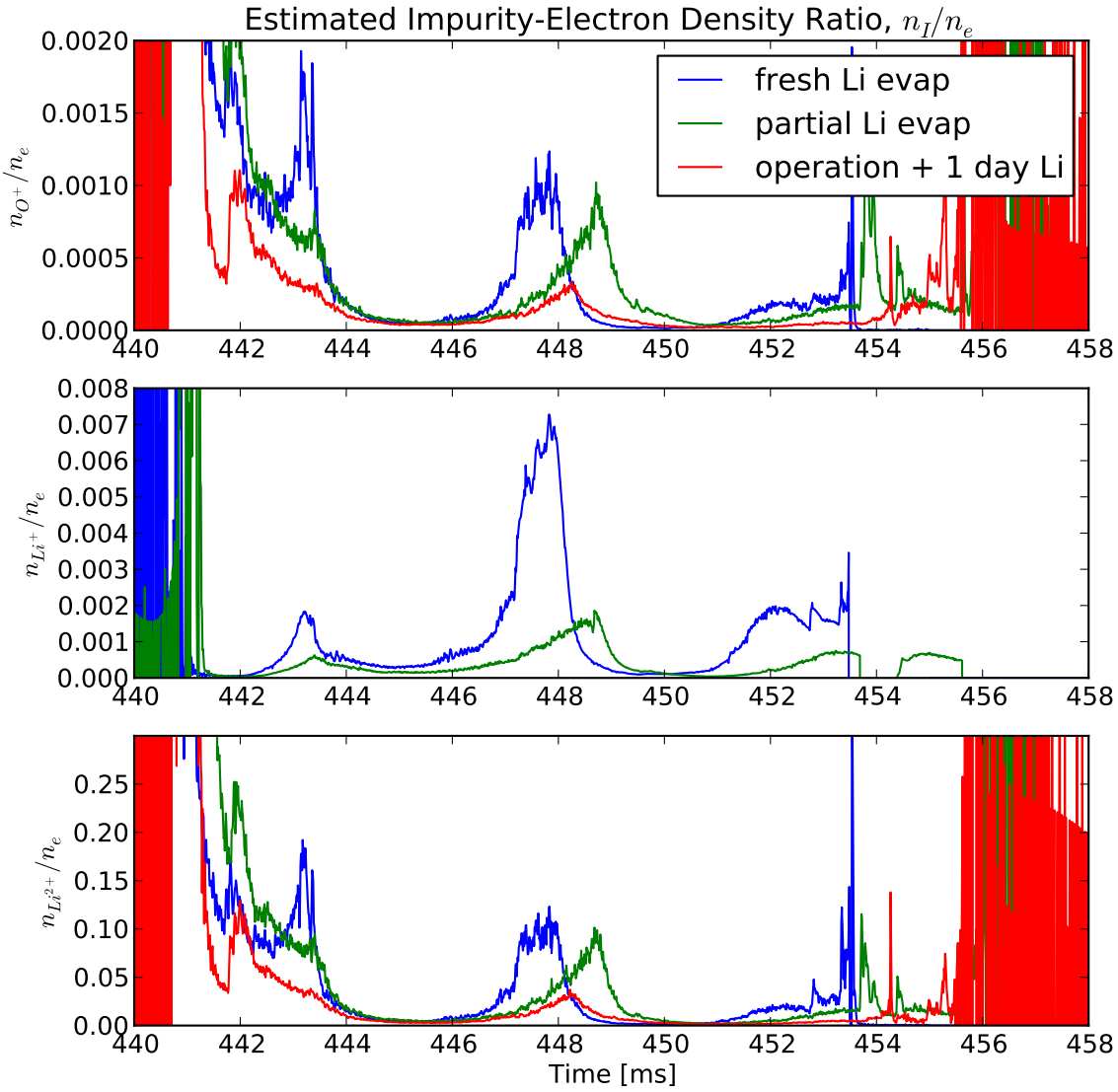

Figure 4.14: Timeseries of lithium and oxygen densities normalized to the electron density for various wall conditions. The same shots are displayed as in fig. 4.11. The O^+ and Li^{2+} densities are calculated from using emission measurements from a filterscope viewing one of the limiters in the lower shell, while the Li^+ density is calculated from a filterscope viewing the outboard side of the lower shell.

the plasma density between the external fueling pulses, especially in the discharges on a fresh lithium surface that exhibit the shortest effective particle confinement times. The C^+ density estimated from C II emission at 658 nm has more noise than the other impurities and is not shown; however, it has a similar temporal trend as the O^+ density, with a maximum of about $n_{C^{2+}}/n_e \approx 2\text{–}4 \times 10^{-3}$.

4.5 Conclusions

This chapter examined high-performance discharges on a variety of wall conditions including full shell coatings of freshly-deposited solid lithium, partial shell coating of solid lithium, and partially-passivated lithium surfaces. Interferometer measurements show that solid lithium coatings on LTX are able to produce values of $\tau_p^* \approx 0.7\text{–}1.1$ ms. These effective particle confinement times are lower than those attained on CDX-U with solid or even liquid lithium in the toroidal tray limiter. Although for discharges following evaporation of a full solid lithium coating onto the shells τ_p^* changes very little with cumulative external fueling up to 3.5×10^{21} H atoms, measurements of R_{cum} do increase with cumulative fueling, suggesting that the surface is indeed changing. In contrast, discharges on a partially-passivated surface show essentially no change in τ_p^* or R_{cum} with cumulative fueling. This is surprising, since these discharges still have relatively short effective particle confinement ($\tau_p^* \approx 1.5\text{–}3$ ms) consistent with strong particle pumping by the lithium surface. Discharges following evaporation of a partial lithium coating onto the shells fall in an intermediate regime. Initially, they are characterized by effective particle confinement times similar to discharges following deposition of a full evaporative coating, with values of $\tau_p^* \sim 1.2$ ms. Unlike discharges following deposition of a full coating, however, both R_{cum} and τ_p^* increase quickly with cumulative fueling, reaching values typical of discharges on a partially-passivated surface after cumulative fueling of $\sim 1.5 \times 10^{21}$ H atoms.

Measurements of hydrogen Lyman-α emission correlate well with the interferometer measurements, consistent with the picture that changes in hydrogen recycling are producing the changes in effective particle confinement. Both measurements of total peak emission during a fueling pulse and emission decay time following a fueling pulse tended to increase with cumulative fueling for discharges following deposition of a full or partial lithium coating. This finding is consistent with $R_{\rm cum}$ measurements and indicate that the surface is indeed evolving with 1–3 $\times$ 10^{21} H atoms of cumulative fueling.

Langmuir probe measurements show that the electron density in the scrape-off-layer tracks the electron density in the core, dropping substantially as the external fueling is terminated. Probe measurements also show that discharges on fresh, full lithium coatings achieve lower densities in the SOL than those on a partially-passivated surface. Measurements also demonstrate that this reduction in electron density in the SOL is coincident with an increased electron temperature in the SOL for shots with a fresh lithium wall coating, but much less so for shots on a partially-passivated surface.

Interestingly, the connection between reduced recycling and plasma current is somewhat complex. Heavily fueled discharges that produce large plasma currents with fresh lithium walls become over-fueled when the same external fueling is used and the walls are partially passivated. In contrast, moderately-fueled discharges exhibit a different behavior: although the density is substantially higher when operating with partially-passivated walls, the plasma current timeseries is quite similar until near the end of the discharge. Since the Ohmic heating current waveform is identical, this would suggest similar electron temperatures. The ratio of impurity density to electron density is seen to rise substantially during the low-density period between fueling pulses. This effect is most pronounced for discharges with the lowest τ_p^*, those on surfaces with fresh lithium coatings. The higher impurity fraction in these discharges during this time would lead to a reduced Spitzer conductivity, which could explain why these discharges actually had lower plasma currents during this time period

than the discharges on less optimal lithium surfaces. Only near the end of the discharge do moderately-fueled plasmas on partially-passivated walls achieve lower currents than those on fresh evaporative lithium coatings, despite evidence for substantially increased recycling. Since line emission measurements indicate the relative concentration of impurities to actually be higher in the discharges on fresh lithium coatings, these discharges must have elevated electron temperature to achieve higher current.

During 1 hour evaporation at 570 °C , about 2.0 g Li is evaporated from each of the two evaporators and deposited on the shells. Given the standard isotopic abundance, the mass of Li is 6.94 g/mol; therefore, about a total of 3.5×10^{23} atoms have been evaporated on each shell. The density of solid Li at room temperature is 0.534 g/cm^{-3}, and the shell surface area is 3.71 m^2; therefore, assuming uniform coverage, the Li coating thickness is 2.0 μm . The Li number density is just the mass density divided by the atomic mass, or 4.63×10^{22} Li atoms/cm^3. Taking the inverse of the cube root, the linear separation between atoms is 2.8 Å. Dividing the coating thickness by this value gives about 7200 monolayers in the coating.

Modeling using the VFTRIM code was performed for NSTX to calculate the implantation depth of D^+ in Li[58]. For divertor temperatures of 30–40 eV, an incident ion energy of ∼200 eV was expected, resulting in a penetration depth of about 10 nm[89]. A 10 nm H^+ penetration depth corresponds to 36 monolayers, for a total of 1.7×10^{21} Li atoms that are accessible for binding with incident H. This would suggest that by the time the cumulative external fueling has reached 2×10^{21} H atoms, the walls should have unity recycling. Langmuir probe measurements on LTX suggest a cooler edge (T_e ≈5–25 eV), and LTX has been operating with H as the fuel species rather than D. Taking into account these differences with the modeling for NSTX would produce an even shorter penetration depth and less accessible lithium for pumping.

In contrast, measurements in this chapter show that after evaporating about 4.0 g Li and cumulative fueling of double that value, $R_{\rm cum}$ increases only about 60% and τ_p^* only about 10%. At the same time, this level of cumulative fueling does seem to produce increased recycling if less lithium is evaporated. One likely explanation for this discrepancy might be that regions of the shells located far from the crucible evaporators are not even covered by ∼40 monolayers unless ∼2 g are evaporated from each crucible. After only a partial evaporation, these regions will quickly reach a sorption equilibrium with unity recycling. This explanation still leaves unresolved why 2×10^{21} H atoms are not sufficient to load a full lithium coating.

One possibility is that finite diffusion of H within the solid lithium might allow incident H to access additional monolayers of the lithium coating. Recent studies in the literature have focused on diffusivity of hydrogen in liquid lithium, and have produced diffusivities varying by orders of magnitude[149,150,151]. Older work examining trapping efficiencies of 18 keV deuterons in solid and liquid lithium[152] found that although measurements of the trapping efficiency were irreproducible and decreased with deuteron dose, high trapping efficiencies were found. Therefore, the possibility of hydrogen diffusion in the solid lithium coating, enabling access to additional monolayers for particle pumping cannot be excluded.

Another possibility is that the lithium surface interacts with the underlying oxide layer and residual gases in the vacuum vessel to form complexes that enhance bonding with incident hydrogen ions. For example, molecular dynamics calculations of the lithium-carbon-oxygen system suggest lithium merely acts as a catalyst to aid bonding of incident hydrogen ions by oxygen[51]. Similar calculations have not been performed for metal substrates however. RGA (residual gas analyzer) measurements on LTX indicate that immediately following evaporating lithium on to the shells, the partial pressures of H_2O and O_2 are (see fig. 2.14) $\sim 2 \times 10^{-8}$ Torr and $\sim 4 \times 10^{-9}$ Torr, respectively. XPS measurements performed on solid Li exposed to residual gases indicate that after 26–32 Torr-s of exposure to H_2O (corresponding

to 1.5 hours for LTX), the top ∼8 nm of the lithium surface are oxidized[153,154]. Since there is typically a 1–2 hour delay between the end of the lithium evaporation and the start of plasma operations, by the time the first discharges are initiated, the surface of the lithium coatings is a mixed material and not a pure lithium surface.

A third possibility, which is partially supported by specroscopic measurements presented in sec. 4.4, is that erosion of lithium during a discharge acts to expose underlying monolayers for binding with indident hydrogen, while lithium re-deposited at other locations also becomes a clean surface for binding with hydrogen. Additional measurements with broad coverage of the PFCs and modeling are necessary to quantify erosion and redeposition during LTX discharges.

In order to quantify the recycling, neutral particle modeling has been performed using the Degas 2 code and is presented in chapter 5.

Chapter 5

Determination of the Recycling Coefficient from Neutral Particle Modeling

Neutral transport modeling is used to simulate where sources of neutral atoms and molecules are ionized in the plasma. By incorporating collision rates and Einstein coefficients from atomic physics calculations, codes commonly used in the fusion community such as DEGAS 2[155,156] and Eirene also model line emission. In this work, the DEGAS 2 code is used to solve an inverse problem: given measurements of hydrogen emission, the code is used to determine the neutral sources that would produce emission matching the measurements. The total neutral sources are then used with other parameters in order to determine both the average plate recycling (R_{plate}) and the core recycling (R_{core}) during a few time points of several discharges. The discharges examined here include both shots with fresh evaporatively-deposited solid lithium PFC coatings, as well as shots with partially passivated solid PFC coatings.

In addition to hydrogen line emission measurements, a plasma model is also required. The LRDFIT[157] code has been used to obtain the position of the magnetic axis and the shapes of the flux surfaces. This model of the magnetic equilibrium is then used to invert the interferometer data in order to determine the density profile. Preliminary data from Thomson scattering is used to estimate the electron temperature profile, and preliminary CHERS data is used to estimate the ion temperature. Finally, a poloidal mesh is generated from the magnetic equilibrium flux-surface shapes. These data sets are sufficient in order to use the DEGAS 2 code to infer a neutral source distribution on the PFCs from hydrogen line emission measurements.

The process used to develop the plasma model will be discussed first, followed by a description of the neutral modeling approach. The process for determining the recycling coefficients is outlined next, followed by results.

5.1 Plasma Model

5.1.1 Centroid and Flux Surfaces

As discussed in section 2.2.9, the LRDFIT code was configured for the LTX magnetic diagnostics, coil set, and conducting structures[81]. Although the code is 2D, a shell model was developed in an attempt to model axissymmetric effects of the shell eddy currents[81,118]. As part of this current thesis, a substantial amount of time was invested in correcting for offsets in the magnetic diagnostics, re-calibrating the magnetic diagnostics, and fixing errors in the LRDFIT model. For the purposes of this present study, only the shapes of the flux surfaces of the magnetic equilibrium are needed. The flux-surface shapes are used to invert the line-integrated density profiles and in the plasma geometry for neutral particle modeling.

With one exception[158], this is the first study to calculate Grad-Shafranov-constrained magnetic equilibria for LTX and and use the results extensively in further modeling. Nev-

ertheless, due to inherent limitations in the 2-D model, equilibrium reconstructions for LTX are to be considered very much a work in progress. All the discharges studied in this chapter used the same coil programming. Examination of several discharges showed similar signals on the magnetic diagnostics; therefore, the same flux-surface shapes have been used for all the discharges. The last closed-flux-surface and magnetic axis for two time-points during a typical discharge are shown in fig. 5.1. To verify the position of the magnetic axis calculated by LRDFIT, the vertical position of the magnetic axis from the equilibrium can be compared to the emission centroid from the Lyman-α and bolometer arrays shown in fig. 5.2a. For the time period t=446–447 ms, the emission centroid for the bolometer is about 4 cm below midplane, while the Lyman-α emission centroid is 1–2 cm below the midplane. These values are in good agreement with the vertical position of the magnetic axis calculated by LRDFIT at t=447 ms. In addition, both the LRDFIT reconstructions and the emission measurements indicate the plasma is shifted inward and limiting on the inboard surface of the shells.

In addition to being used for the plasma geometry and to invert the line-integrated interferometer measurements, the derivative of the flux-surface volume ($dV/d\psi$) is used to calculate the number of electrons in the core and the total in the plasma from the electron density profile:

$$N_{\text{core}} = \int_0^1 d\psi n_e(\psi) \frac{dV}{d\psi} \tag{5.1}$$

$$N_{\text{total}} = \int_0^{\psi_{max}} d\psi n_e(\psi) \frac{dV}{d\psi} \tag{5.2}$$

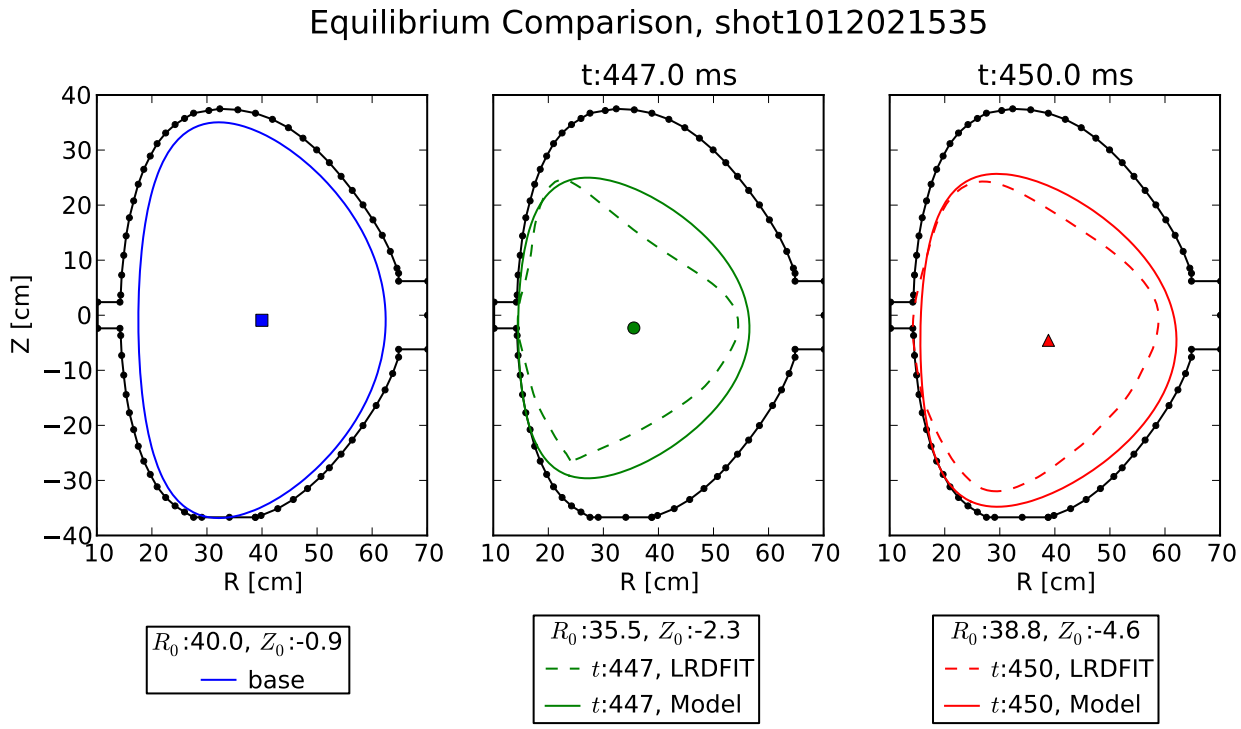

Figure 5.1: Equilibria used in DEGAS 2. The reference equilibrium in the left frame is a model reference equilibrium using the LTX design major radius for the magnetic axis, shifted slightly downward to be more consistent with the emission centroids of the VUV arrays. The dashed lines in the central and right frames are the last closed-flux-surface as determined by LRDFIT. The solid lines correspond to a model equilibrium with the same magnetic axis location, and similar elongation and triangularity.

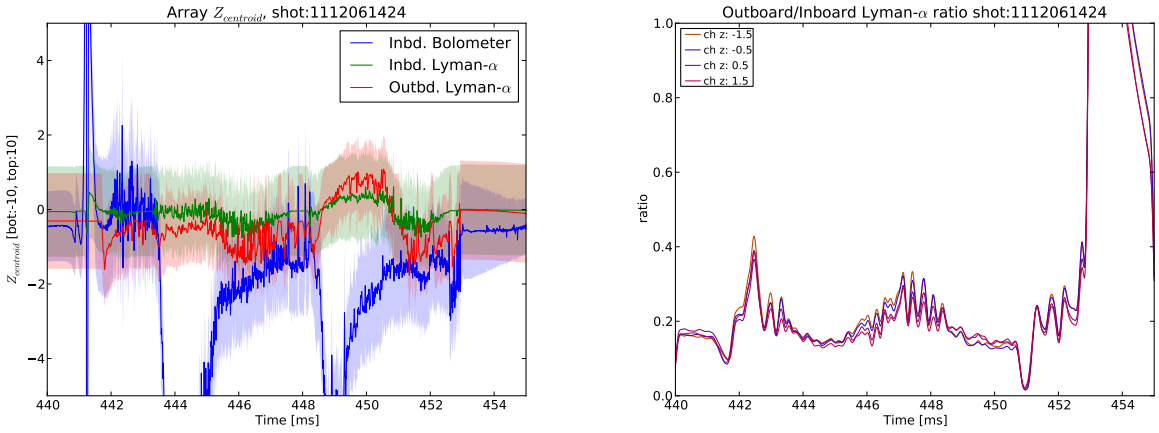

(a) (b)

Figure 5.2: (a) Plasma emission centroid height and (b) outboard/inboard emission ratio from VUV arrays. The Lyman-α contribution has been subtracted from the bolometer emission in order to better localize the core VUV emission, rather than be dominated by emission at the plasma edge. During certain time periods of external fueling, however, (e.g., t =443.5–445 ms and t=448.5–450 ms), edge emission dominates the bolometer signal and therefore this procedure is prone may produce significant error. The emission centroid is calculated by summing the emission from each channel weighted by its angular separation from horizontal. The bands correspond to the weighted standard error if each channel was assumed to be an independent measurement. For t=446 to 447 ms, the emission centroid of the bolometer is about two channels below midplane, while the Lyman-α emission is 0.5-1 channel below midplane. This corresponds to $Z_{centroid} \approx -4$ cm for the bolometer and $Z_{centroid}$ ≈1–2 cm for the Lyman-α emission. (b) Shows the ratio of the measured emission from the four central channels of the outboard and inboard arrays. From t=446 to 447 ms, the ratio of the emission measured by the four central channels of the outboard array to that measured by the corresponding channels of the inboard array is 0.15–0.25, suggesting the plasma is shifted somewhat inward from the nominal R_0=40 cm.

5.1.2 Density Profiles

Poloidal Inversions

In order to determine the density profile, the line-integrated density profile measured by the vertically-scanning 2mm interferometer must be inverted. Experiments typically measure line-integrated density as a function of major radius, allowing a simple Abel inversion on toroidally-symmetric systems. In contrast, the LTX interferometer scan produces a profile time-series at various pelevations below midplane; therefore, the inversion is more complicated and relies on the shapes of the flux surfaces at each time point. A previous study of the efficiency of various fueling methods on LTX assumed a model spherical torus equilibrium[82]. As part of this thesis, a tool was developed to invert the density profiles using an arbitrary equilibrium, including those calculated by LRDFIT. In addition, since the tool developed here does not rely on the density profile following a particular functional form, this tool can be used to invert an arbitrary line-integrated density profile.

The inversion is done in the following steps:

1. Load the $n_e L(t, z)$ time-series and apply smoothing to each chord in order to reduce the sensitivity to fluctuations.

2. Compute the mean of each chord within a time window (typically ± 0.1 ms) around the time of interest, t_i.

3. Use a smoothing spline to interpolate the $n_e L(t_i, z)$ profile and reduce the effect of individual measurement points. It is this smoothed, interpolated profile that is to be inverted.

4. Load the magnetic equilibrium and set-up a bivariate spline interpolation of the poloidal flux.

5. Create "sightline boundaries" midway between consecutive sightlines. Each sightline is assumed to measure the integrated density through its "sightline zone".

6. Determine which sightlines are above the magnetic axis (if any), and which are below. Also find if a sightline zone includes the magnetic axis. If a sightline zone includes the magnetic axis, split up this zone into two: a part above and a part below the magnetic axis using the magnetic axis as an additional sightline zone boundary.

7. Determine the minimum value of ψ intersected by each sightline (ψ_s) and sightline boundary (ψ_{zb}). Note that these ψ are also the flux-surfaces tangent to the sightlines and sightline boundaries. Contours of constant ψ_{zb} effectively split the plasma into flux-surface zones inside which the plasma density is assumed to be constant.

8. Assuming all sightlines are either below (or above) the magnetic axis, starting from the lowest (highest) sightline, calculate the distance along each sightline to the ψ_{zb} for each zone boundary that it intersects. Note that each sightline will intersect each outer zone boundary twice: once radially inside and once radially outside the magnetic axis.

9. For each sightline, compute the distance between each zone boundary intersection point. The length matrix is then formed as the total distance each sightline passes through a particular zone. If all sightlines are below (or above) the magnetic axis, the resulting matrix will be upper-triangular (lower-triangular), and is easily inverted.

10. The density profile is obtained by multiplying the inverted length matrix with the vector of line-integrated densities at that particular time point.

In the event that there are sightlines both above and below the magnetic axis, the inversion proceeds as described above except:

1. The sightline which intersects the outermost ψ is determined. If this sightline is below (or above) the magnetic axis, the length matrix is formed as described above for the

sightlines above the magnetic axis, using only zone boundaries from sightlines above the magnetic axis. In other words, the sightlines below (or above) the magnetic axis are inverted without any knowledge of the sightlines above (or below) the magnetic axis.

2. The sightlines above (or below) the magnetic axis use the zones of the outermost sightlines below (or above) the magnetic axis until the zone boundary for the outermost sightline above (or below) the magnetic axis is reached. From this point, the sightlines above (or below) the magnetic axis only use the zones from sightlines above (or below) the magnetic axis. In other words, sightlines above (below) the magnetic axis assume symmetry in the density profile for the outer zones, but not for the inner zones.

To give a graphical example of this procedure, the inversion sightlines for the reference equilibrium are shown in fig. 5.3. These sightlines correspond to the vertical positions at which the line-integrated interferometer data points are interpolated. Plotting each "sightline zone" in a separate color yields fig. 5.4a. This particular representation was very useful for debugging errors in the algorithm which identified the zone boundary locations. The length matrix is depicted in fig. 5.4b, with each color corresponding to the distance a particular sightline passes through a given zone. This matrix is then inverted. Finally the dot-product is formed between the inverted matrix and the vector of interpolated line-integrated measurements at a given time point. The line-integrated density profiles at several time points during a representative discharge are shown in figure 5.5a. Figure 5.5 shows the resulting density profiles after the inversion. Although not shown, later in the discharge (during the second fueling pulse) density profiles were found to be hollow, consistent with earlier work[82].

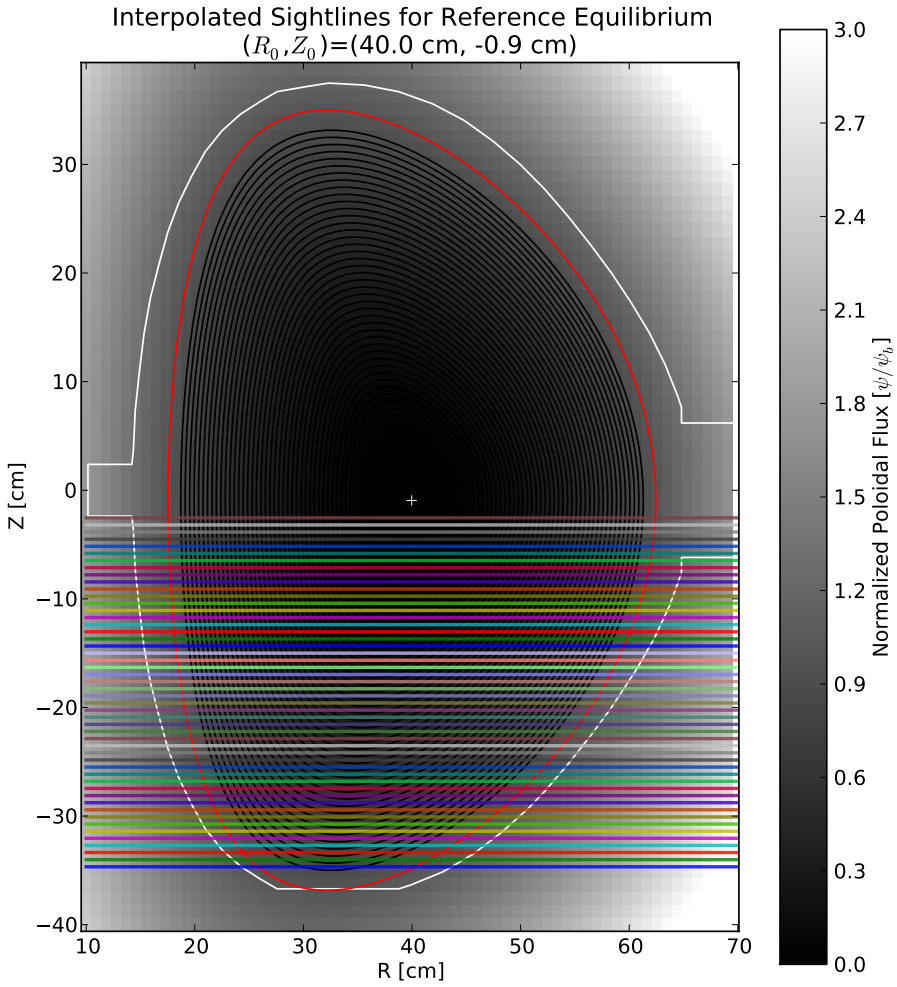

Figure 5.3: Density profile inversion sightlines for the reference equilibrium. The horizontal lines correspond to points at which the spline-interpolation of the line-integrated density profile is evaluated.

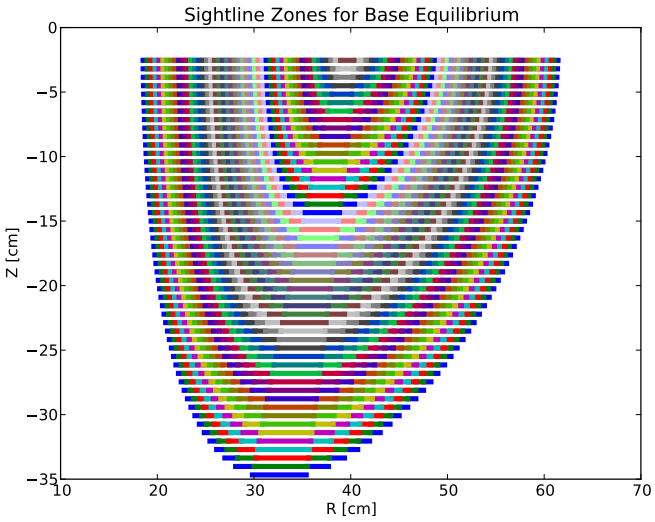

(a)

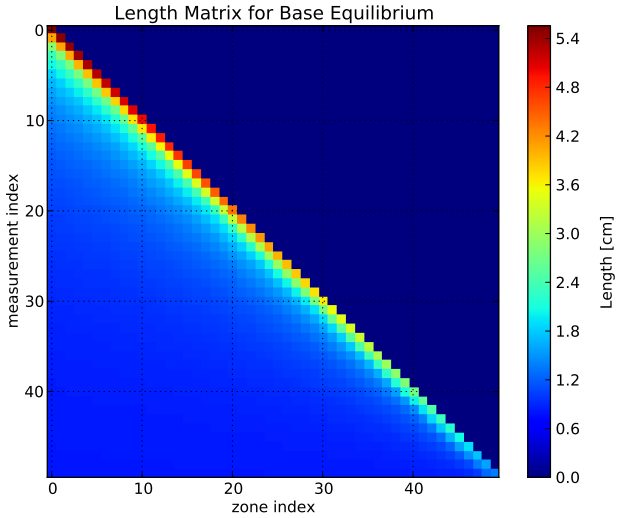

(b)

Figure 5.4: Density profile inversion (a) zones and (b) length matrix for the reference equilibrium. (a) Displaying each zone in a different color verifies that the zone boundaries have been determined correctly by the algorithm and do not overlap. (b) The color of each element of the length matrix corresponds to the distance a particular sightline passes through a given zone. The largest matrix elements correspond to the flux-surfaces tangent to each sightline.

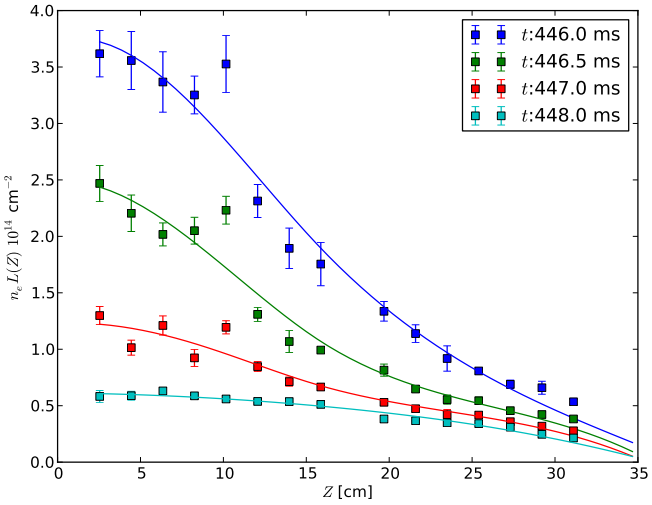

(a)

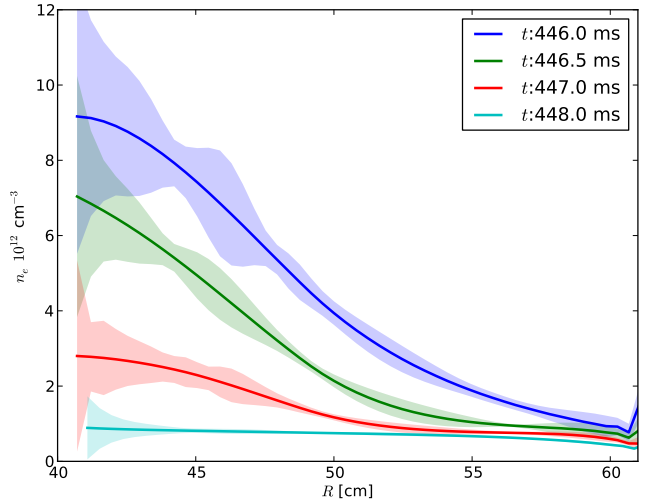

(b)

Figure 5.5: Representative inverted density profiles at several time points during a discharge. This profile is for the gas-puff-only interferometer scan of shots 1112211444–1616. The jump in density at $R \approx 61$ cm in the inverted n_e profiles is a numerical artifact and is removed in the n_e profile used by DEGAS 2.

5.1.3 Temperature Profiles

The electron temperature profile measured by Thomson scattering during a shot with heavy fueling on a fresh lithium surface is used as a reference profile[159]. Thomson scattering measurements during a shot with the more moderate fueling characteristic of the discharges examined here indicated that the electron temperature is substantially higher than this reference temperature profile[159]. Therefore, most simulations have been performed using a scaled temperature profile midway between the two. In addition, to examine the effect of this uncertainty in the temperature profile on the modeling results, sensitivity tests have been performed using both the un-scaled temperature profile for the shot with heavy fueling, and a temperature profile double the scaled value. The T_e profile in the core is then mated to the T_e profile in the SOL, as measured by the Langmuir probe located on the outboard midplane.

Preliminary, line-integrated, passive CHERS measurements of T_i using a lithium charge-exchange line indicate a core temperature of ≈ 35 eV, with little variation across r/a from 0 to 0.5[160]. Therefore, the T_i profile used in this work uses the T_e profile, scaled to 35 eV in the core.

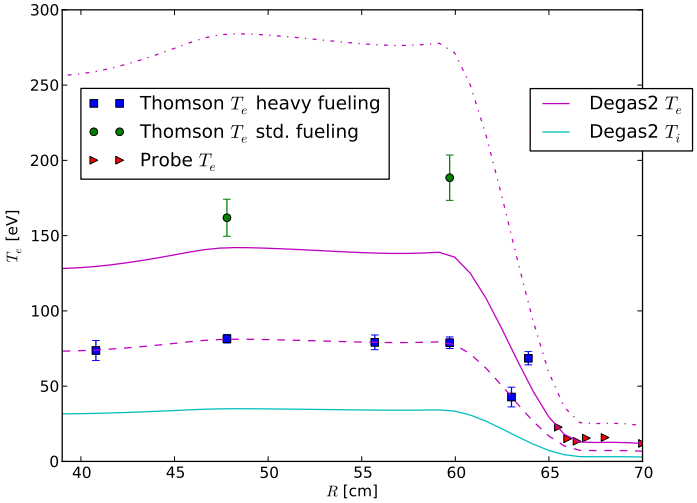

Figure 5.6: Temperature profiles used in DEGAS 2. The case with heavy fueling is shot 1111091353, and is taken at t=448 ms which is at the end of a 4 ms long gas-puff. The case with standard fueling is 1111081759 and is taken at t=447 ms. The temperature profile in the edge is from a radial scan of the Langmuir probe over shots 1201041933–2111. The "reference" T_e profile used in DEGAS 2 is shown in solid magenta, while the dashed and dotted magenta profiles were used in sensitivity tests. The T_i profile (cyan) uses the T_e profile, scaled to match the typical CHERS measurement of line-integrated $T_i \approx 35$ eV for r/a from 0 to 0.5.

5.2 The DEGAS 2 Code

The DEGAS 2 code[155,156] uses a Monte-Carlo approach to solve the kinetic Boltzman equation for neutral atoms and molecules:

$$\frac{\partial f(\mathbf{r},\mathbf{v},t)}{\partial t} + \mathbf{v}\cdot\nabla f = C[f], \tag{5.3}$$

where f is the distribution function of neutral atoms and molecules in three spatial dimensions, three velocity dimensions, and time. The collision operator on the right-hand-side of this expression contains all the physics associated with collisional processes including ionization, excitation, charge-exchange, dissociation, and recombination. In this thesis, the code is used to solve the time-independent version of this equation. The Monte-Carlo approach used in DEGAS 2 randomly samples the distribution function with a finite number of particles, tracking each one as it propagates through the vacuum vessel, experiences collisions with plasma electrons and ions according to probabilities determined by known collision cross-sections, and interacts with material surfaces. The interested reader is encouraged to consult publications describing the DEGAS 2 code[155], the user manual[156], and publications which used the code for interpretive modeling of experimental data[161,162].

Although DEGAS 2 can also iterate the solution to account for neutral-neutral collisions, the effect of these collisions is insignificant for the neutral densities of interest, and is therefore not included in the simulations. The plasma-neutral reactions included in the simulation are listed in table 5.1. Note also that although DEGAS 2 can include the effect of recombination, initial simulations found the effects of recombination to be negligible; therefore, recombination was neglected in subsequent simulations for computational efficiency.

Dissociation:

$$\begin{aligned} e + H_2 &\rightarrow e + 2H \\ e + H_2 &\rightarrow 2e + H^+ + H \\ e + H_2 &\rightarrow e + H^* + H \\ e + H_2^+ &\rightarrow e + H^+ + H \\ e + H_2^+ &\rightarrow 2e + 2H^+ \\ e + H_2^+ &\rightarrow H^* + H \\ e + H_2^+ &\rightarrow e + H^+ + H^* \end{aligned}$$

Ionization:

$$\begin{aligned} e + H &\rightarrow 2e + H^+ \\ e + H_2 &\rightarrow 2e + 2H_2^+ \end{aligned}$$

Charge exchange and Elastic Scattering:

$$\begin{aligned} H + H^+ &\rightarrow H^+ + H \\ H_2 + H^+ &\rightarrow H_2^+ + H \end{aligned}$$

Excitation:

$$e + H \rightarrow e + H^*$$

Recombination:

$$e + H^+ \rightarrow H$$

Table 5.1: Plasma-neutral reactions included in DEGAS 2 neutral modeling

5.2.1 DEGAS 2 Geometry

Although existing mesh generators such as Carre[163] can generate a computational mesh from a magnetic equilibrium, they do not work with limiter geometries. Therefore, a custom mesh generator was developed for use with LTX magnetic equilibria. An initial tool[158] was modified substantially in order to develop a robust generator. The mesh generation for the SOL region is made more difficult by the conformal design of the shells, which causes cells to overlap in some circumstances. Once generated, the mesh is imported into the DG (DivGeo)[164] graphical tool in order to correct mesh errors and connect the mesh boundary with physical surfaces. Plasma parameters (n_e, T_e, and T_i) are interpolated to the center of each mesh element, assuming that they are constant on a flux surface. Finally, polygons are defined in DG (and in the DEGAS 2 geometry definition file) which fill the remaining computational space with either vacuum or solid. Figure 5.7 illustrates the representation of LTX in DEGAS 2 for one of the modeled equilibria.

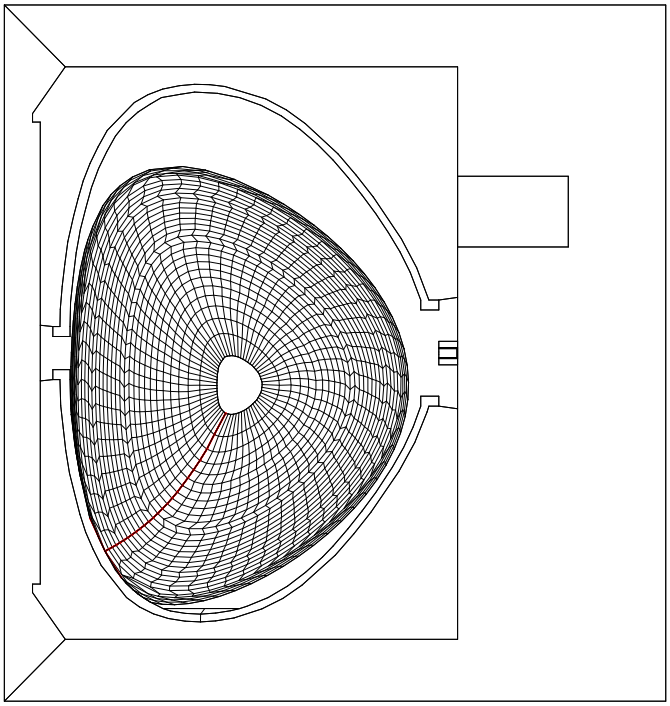

Figure 5.7: LTX representation in DEGAS 2. The computational mesh is a model equilibrium with R_0=38.8 cm, Z_0=-4.6 cm. The red line in the mesh corresponds to a boundary between the first and last poloidal elements. The remaining computational volume is divided into DG polygons, which DEGAS 2 re-interprets as strata.

5.2.2 Plasma-Material Interactions and Simulation Approach

Neutral modeling typically assumes the plasma-material interactions are known. DEGAS 2 uses particle and energy reflection coefficients as a function of incident energy and angle that have been measured or calculated with codes such as TRIM. Plasma-facing materials are typically assumed to be in a "sorption equilibrium", where each atom or molecule incident on a surface that is not reflected will be adsorbed onto the surface and will statistically result in another molecule or atom being desorbed. This is equivalent to an assumption that R_{plate}=1. Evaporatively-deposited solid lithium coatings (and liquid lithium coatings as well) are not in a steady state, however, but are rather dynamically evolving as hydrogen and impurities are adsorbed on the surface. In fact, R_{plate} is one of the quantities to be calculated.

Although lithium reacts with both hydrogen (eqs. 1.24a–c) and impurities (eqs. 1.25a–d for example), due to the short timescale of an LTX plasma (<30 ms) and the typical partial pressures of residual gases ($< 1 \times 10^7$ torr), only the hydrogenic reactions are important. In addition, the reaction of lithium with molecular hydrogen is slow enough to be neglected, so incident H_2 on Li is assumed to be adsorbed and immediately desorbed. Incident hydrogen atoms not reflected from the surface are treated as being immediately adsorbed and retained in the surface.

Of course, the lithium surface is in a mixed state. In order to calculate R_{plate} and determine the fraction of incident particles that are desorbed, the approach used in ref. 52 is adopted. The PFC surfaces are divided into a number of elements. A unit source of hydrogen atoms is placed on each, and DEGAS 2 is used to track the particle as it moves through the vessel volume. Line emission, ionization, particle reflection, and adsorption are all tallied. Figure 5.8 shows the emission calculated by DEGAS 2 for recycling from a handful of isolated recycling sources. Although displayed together, the emission from each source (and those not shown) is tracked independently. A matrix is constructed which maps the emission measured by each diagnostic sightline from each source. Example matrix elements

for the Lyman-α arrays and H-α filterscopes are shown in fig. 5.9. The spikes in the source-emission map (most easily seen for the filterscope rows in fig. 5.9c) is because the simulations are performed with a unit source flux; as a result, source elements with more surface area emit more particles and therefore more emission. In order to ensure non-negativity of the resulting source element weights, a non-negative least-squares approach is used to calculate an approximate solution for the vector of source weights that best matches the experimental measurements. Figure 5.10 shows typical source weights and the resulting match to the experimental measurements. This approach essentially uses a linear superposition of recycling sources to match the measured emission.

Once the source weights are known, other parameters can be calculated from the simulation. In addition to finding the non-negative least-squares solution for the entire matrix, an alternative solution is found by dividing it into a 5×5 block matrix. These blocks correspond to the average emission measured by each of the ten lowest and ten highest channels of the arrays, and the limiter-viewing filterscope (head C) from the outboard lower shell, lower limiter, inboard lower shell, inboard upper shell, and outboard upper shell. The solution flux distribution and emission profile are shown in green in fig. 5.10a and fig. 5.10c. An additional simulation can be performed using these weights to facilitate post-processing. The resulting Lyman-α emission in the poloidal plane is shown in fig. 5.10b.

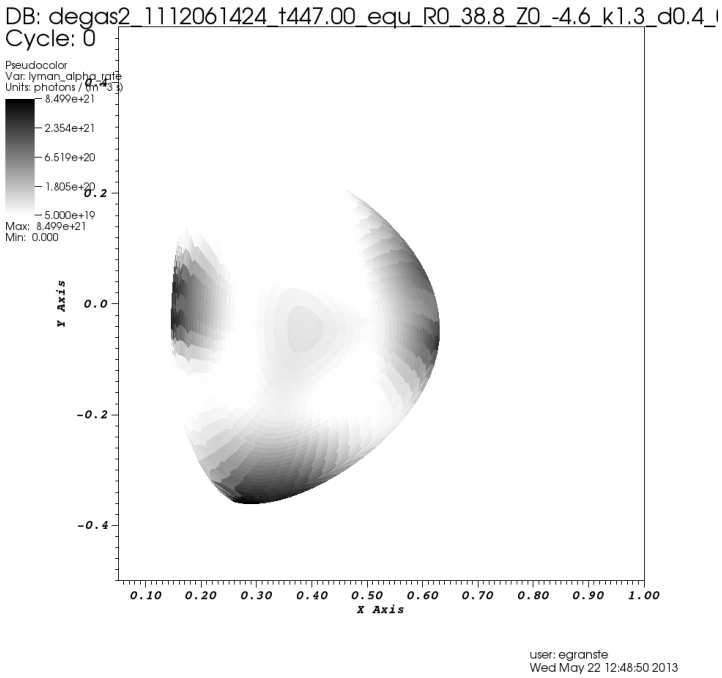

Figure 5.8: Lyman-α emission computed by DEGAS 2 for selected isolated recycling sources located on the inboard and outboard shell edges and the lower limiter. Note the log scale.

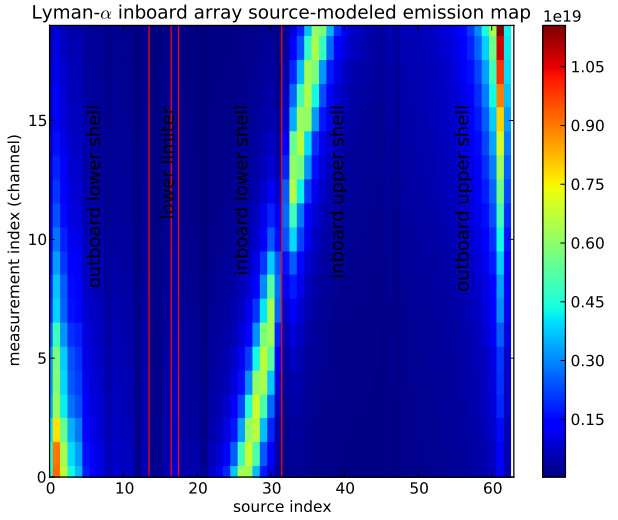

(a)

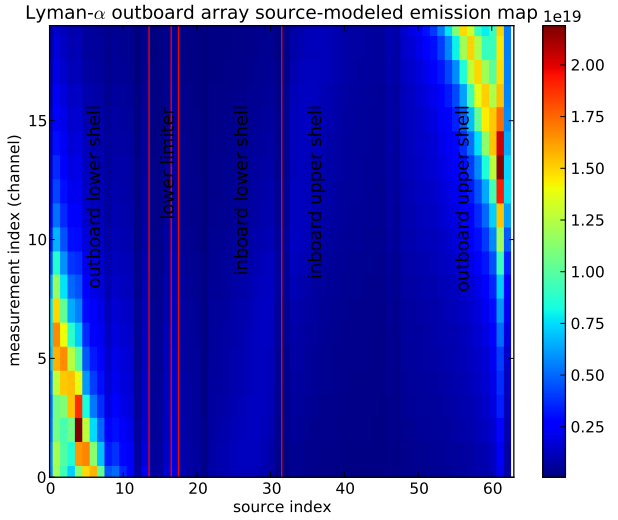

(b)

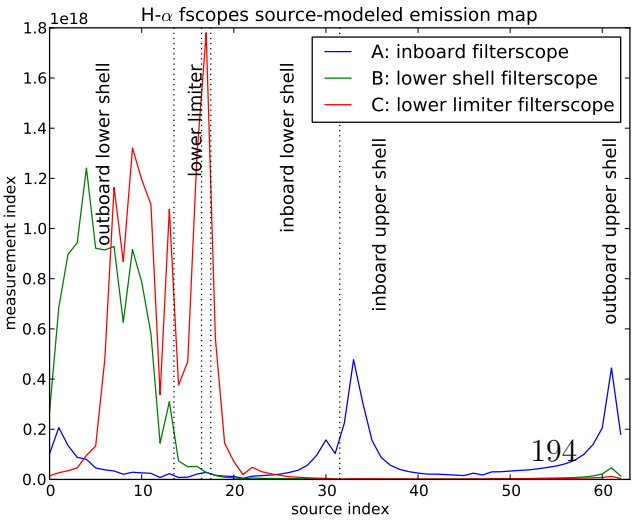

(c)

Figure 5.9: DEGAS 2 source-measurement map matrix for (a) the inboard-viewing Lyman-α array, (b) the outboard-viewing Lyman-α array, and (c) the H-α filterscopes. The solid red lines in (a) and (b) and the dotted black lines in (c) separate regions on the shells. From left to right, the regions correspond to the outboard lower shell, the inner and outer halves of the lower limiter, the inboard lower shell, the inboard upper shell, and the outboard upper shell. The outboard-viewing array (b) detects emission primarily from sources located on the outboard halves of the upper and lower shell. The inboard-viewing array (a) detects some emission from the outboard shell surfaces, but also from the inboard shell surfaces.

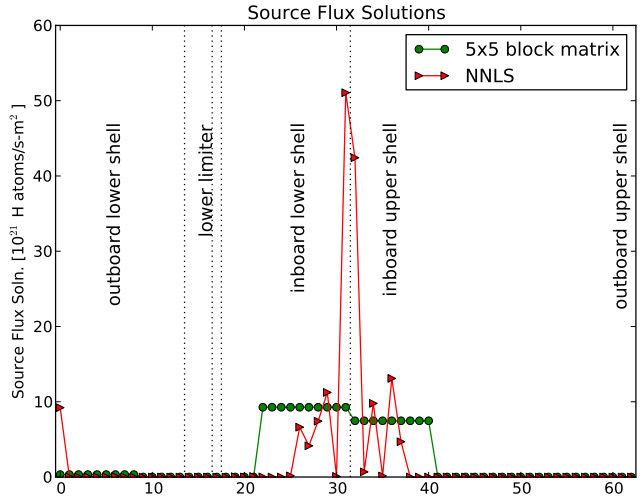

(a)

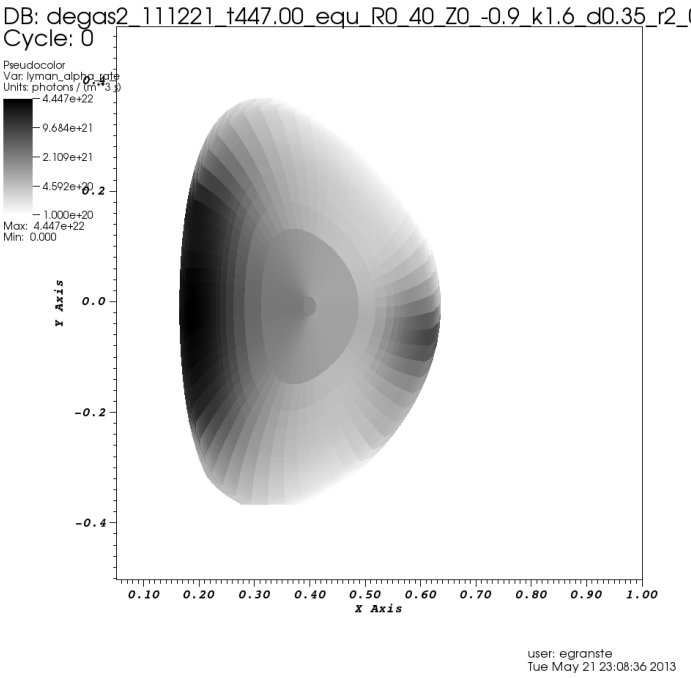

(b)

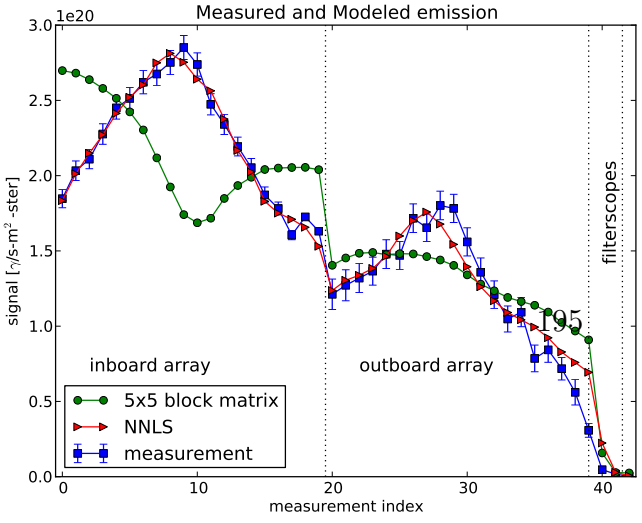

Figure 5.10: Sample solution for the (a) recycling sources, and the resulting emission (b) in the poloidal plane and (c) compared to measurements. The non-negative least-squares solution for the entire source-emission map matrix is shown in red, while the solution to the reduced (averaged) 5×5 block matrix is shown in green. Note the log scale for the polodial Lyman-α emission in (b).

5.3 Results from Recycling Determination with DEGAS 2

Recall that the definitions of the plate recycling coefficient and core recycling coefficient from equations (1.11) and (1.14) are:

$$R_{\text{plate}} \doteq \frac{\Gamma_{wall-SOL}}{\Gamma_{SOL-wall}} \tag{5.4a}$$

$$R_{\text{core}} \doteq \frac{\Gamma^{R}_{SOL-core}}{\Gamma_{core-SOL}}. \tag{5.4b}$$

An important subtlety to consider is how to properly treat particle reflections. The total particle flux coming out of the wall ($\Gamma_{wall-SOL}$) consists of two components: one due to desorption and one due to particle reflection:

$$\Gamma_{wall-SOL} = \Gamma^{\text{desorb}}_{wall-SOL} + \Gamma^{\text{reflect}}_{wall-SOL}. \tag{5.5}$$

The sum of the recycling source elements gives the desorbed $\Gamma^{desorb}_{wall-SOL}$ flux from the PFC. Similarly, the plate recycling can be divided as follows:

$$R_{\text{plate}} = R^{\text{desorb}}_{\text{plate}} + r \tag{5.6}$$

where r is the average particle reflection coefficient and $R^{\text{desorb}}_{\text{plate}}$ is the ratio of the desorbed particle flux from the wall to the particle flux incident on the wall. The average particle reflection coefficient can be calculated from the ratio of the total flux incident on the walls to the reflected particle flux, both of which are tracked by DEGAS 2. The definitions of R_{plate}

and R_{core} in equations (5.7a) and (5.7b) can then be inverted to yield:

$$R_{\text{plate}} = \frac{\Gamma_{wall-SOL}}{\Gamma_{wall-SOL} + \Gamma_g - dN_{\text{total}}/dt} \tag{5.7a}$$

$$R_{\text{core}} = \frac{\eta_R \Gamma_{wall-SOL}}{\eta_R \Gamma_{wall-SOL} + \eta_g \Gamma_g - dN_{\text{core}}/dt} \tag{5.7b}$$

The core fueling efficiency for recycling (η_R) is calculated by summing the ionization rates for the weighted recycling sources over the core plasma mesh elements. The total ionization efficiency for recycling (η_R^i) includes, in addition, the sum of the ionization rates in the SOL elements. The core fueling efficiency for external fueling (η_g) can be determined similarly. The rate of change of the particle inventories in the core dN_{core}/dt and full plasma dN_{total}/dt are determined from the inverted interferometer profiles.

Table 5.2 shows the results of using DEGAS 2 modeling to solve for the recycling sources given measurements of hydrogen line emission. Discharges on both fresh lithium coatings and partially-passivated coatings (labeled "p.p. Li") were modeled. These simulations were all performed during the time between fueling pulses, i.e., from t=446 to 447 ms in the discharge. This time window was chosen for convenience: since there were no localized fueling sources during this time, the only neutral hydrogen sources are from recycling. In these simulations, the emission is assumed to be toroidally symmetric; this assumption neglects the effects of the toroidal shell gaps, but provides a substantial reduction in computational cost by allowing the DEGAS 2 code to be run in assuming toroidal symmetry. The source weights from the non-negative least-squares fit of the full source-emission map matrix are used in the calculation of the remaining parameters.

shot	description	τ_p^* ms	$dN_{\rm core}/dt$ $10^{21}/s$	$dN_{\rm total}/dt$ $10^{21}/s$	$\Gamma_{\rm sources}^{\rm desorb}$ $10^{21}/s$	η_R^i	$\eta_R^{\rm core}$	$R_{\rm plate}$	$R_{\rm plate}^{\rm desorb}$	$R_{\rm core}$
time: 446.0 ms										
1112061424	fresh Li	0.99	-1.26	-1.24	4.99	0.47	0.316	0.82	0.605	0.586
1112061702	fresh Li	0.97	-1.65	-1.65	5.16	0.495	0.353	0.779	0.562	0.554
1112071141	p.p. Li	2.04	-1.21	-1.24	7.86	0.549	0.356	0.876	0.652	0.72
1112071428	p.p. Li	2.44	-1.08	-1.05	8.07	0.547	0.387	0.895	0.672	0.762
time: 446.5 ms										
1112061424	fresh Li	0.97	-0.705	-0.732	3.18	0.414	0.289	0.832	0.623	0.597
1112061702	fresh Li	1.01	-1.06	-1.1	3.48	0.453	0.338	0.782	0.569	0.557
1112071141	p.p. Li	1.12	-1.55	-1.56	5.8	0.508	0.356	0.806	0.587	0.599
1112071428	p.p. Li	1.61	-1.27	-1.29	5.96	0.52	0.391	0.838	0.618	0.672
time: 447.0 ms										
1112061424	fresh Li	1.39	-0.356	-0.376	2.43	0.383	0.29	0.881	0.676	0.694
1112061702	fresh Li	1.65	-0.409	-0.433	2.7	0.406	0.335	0.877	0.671	0.715
1112071141	p.p. Li	1.27	-0.883	-0.895	4.22	0.458	0.352	0.842	0.628	0.656
1112071428	p.p. Li	1.76	-0.847	-0.872	4.29	0.484	0.380	0.847	0.632	0.684
1112211444	fresh Li	1.14	-0.36	-0.358	4.85	0.35	0.292	0.94	0.73	0.820

Table 5.2: DEGAS 2 recycling modeling results. The discharges following evaporation of a full lithium wall coating are labeled "fresh Li", while those after plasma operation and allowing the lithium to passivate for one day with residual gases are labeled "p.p. Li". They all used the model equilibrium with (R_0, Z_0) = (38.8,-4.6) cm.

description	$dN_{\rm core}/dt$ $10^{21}/s$	$dN_{\rm total}/dt$ $10^{21}/s$	$\Gamma_{\rm sources}^{\rm desorb}$ $10^{21}/s$	η_R^i	$\eta_R^{\rm core}$	$R_{\rm plate}$	$R_{\rm plate}^{\rm desorb}$	$R_{\rm core}$
reference	-0.36	-0.36	4.85	0.35	0.292	0.94	0.73	0.820
$n_e\times0.9$	-0.36	-0.36	4.55	0.35	0.286	0.936	0.727	0.807
$n_e\times1.1$	-0.36	-0.36	4.75	0.356	0.292	0.939	0.728	0.817
$T_e\times0.57$	-0.36	-0.36	4.76	0.334	0.281	0.939	0.73	0.812
$T_e\times2.0$	-0.36	-0.36	4.92	0.343	0.284	0.941	0.731	0.818
(R_0, Z_0)=(40,-0.9) cm	-0.57	-0.57	3.69	0.353	0.326	0.881	0.683	0.708

Table 5.3: DEGAS 2 tests of sensitivity to input parameters. The reference case is a shot with fresh Li, 1112211444 at t=447.0, using the model equilibrium with (R_0, Z_0) = (38.8,-4.6) cm, with instantaneous τ_p^*=1.14 ms. Using the alternative equilibrium in the last row, τ_p^*=1.05 ms.

description	dN_{core}/dt $10^{21}/s$	dN_{total}/dt $10^{21}/s$	$\Gamma^{\text{desorb}}_{\text{sources}}$ $10^{21}/s$	η^i_R	η^{core}_R	R_{plate}	$R^{\text{desorb}}_{\text{plate}}$	R_{core}
reference	-0.57	-0.57	3.69	0.353	0.326	0.881	0.683	0.708
1.5× H on Li	-0.57	-0.57	3.54	0.335	0.311	0.886	0.584	0.707
D on Li	-0.57	-0.57	3.37	0.426	0.388	0.870	0.668	0.721

Table 5.4: DEGAS 2 PMI reflection model tests. The reference case is a shot with fresh Li, 1112211444 at t=447.0, using the model equilibrium with (R_0, Z_0) = (40.0,-0.9) cm. The reference case uses the PMI reflection model for H on Li.

5.4 Discussion

At t=446.0 ms, the earliest time-point, R_{core} is found to be 0.55–0.59 for the fresh lithium shots. As might be expected, the shots with a partially passivated lithium surface produce higher values of R_{core}, from 0.72–0.76. In addition, the solution for the total source rate of desorbed hydrogen atoms from the PFCs is 50–60% higher for the shots with a partially passivated lithium surface.

A short time later in the discharges, at t=447.0 ms, the picture has changed somewhat. Although the total source rate of desorbed hydrogen atoms is 56–77% higher for the shots on a partially passivated surface, R_{core} and R_{plate} are actually somewhat lower compared to the first two cases on a fresh lithium surface. Although striking at first, this result is consistent with the analysis of the impurity emission measurements in sec. 4.4. The instantaneous effective particle confinement time is defined as:

$$\tau_p^* = N_e^{core} \left(\frac{dN_e^{core}}{dt} \right)^{-1}. \tag{5.8}$$

For the first shot on a fresh Li surface, τ_p^* is 30% longer at t=447.0 ms than at t=446.0 ms. For the second shot, τ_p^* is 60% longer at t=447.0 ms than at t=446.0 ms. If dN_e/dt was increased to achieve the same τ_p^* as at t=446.0 ms, R_{plate} and R_{core}would be 0.85 and 0.63 respectively for the first shot, and 0.81 and 0.60 for the second. These values would both be slightly lower than R_{core} and R_{plate} for the passivated surface, and quite close to the values calculated at t=446.0 ms. Therefore, the model results are consistent if there is a mechanism that would increase τ_p^* at the later time point, without increasing the hydrogen line emission. The impurity measurements in sec. 4.4 suggest just such a mechanism. The relative density of impurities to fuel ions is increasing, indicating that impurities are becoming a more substantial part of the particle balance. Therefore, the calculated values of R_{core} and R_{plate}at t=447.0 ms shown in table 5.2 for the shots on a fresh lithium surface are inflated

because the electron inventory in the plasma is being maintained by an increased impurity influx from the walls. At t=446.5 the results on a fresh lithium surface are quite close to the results at the earlier time point. This is consistent with the impurity emission measurements which show n_I/n_e does not increase substantially until after t=446.5 ms.

The calculated recycling from the last shot in table 5.2, which is also a shot on a fresh lithium surface, is also surprisingly high. This shot was examined further to explore the sensitivity to input parameters. The results of the sensitivity scan in table 5.3 illustrate that a substantial variation in T_e and n_e used in the plasma model has an insignificant effect on the calculated recycling coefficients. Note, however, that since dN_{core}/dt and dN_{total}/dt appear directly in the expressions used to determine R_{core} and R_{plate}, an error in dN_{core}/dt and dN_{total}/dt carry over directly into an error in R_{core} and R_{plate}. For this particular shot, the measured emission from the inboard-viewing Lyman-α array and H-α filterscope are very similar to the other discharges with fresh lithium surfaces. In contrast, the measured emission from the outboard-viewing Lyman-α array and other H-α filterscopes is a factor of two or more higher. Therefore, an additional modeling run was carried out for this discharge, using an equilibrium with the magnetic axis shifted to R_0=40 cm. The resulting R_{plate} and R_{core} show in the last row of table 5.3 are very similar to the other discharges on fresh lithium surfaces.

The inverse modeling approach used in this chapter solves for R_{plate} by using emission measurements and global particle balance. This allows R_{core} to be calculated for a dynamically-evolving surface without having the result strongly affected by an assumed PMI model. Nevertheless, the PMI model for the surface does enter in the calculation in a subtle way. The PMI model determines the fraction of particles incident to the surface that are reflected, as well as the reflected particle energy distribution. In order to test the sensitivity of the calculated R_{plate} and R_{core} to the PMI model, additional runs were performed, and the results are presented in table 5.4. The first run multiplied the reflection coefficient in

the PMI model for hydrogen incident on lithium by a factor of 1.5. The resulting R_{plate} and R_{core} are essentially unchanged from the reference result. The reason is that to lowest order, the measured emission is simply proportional to the total flux from the PFC, independent of whether the particles are desorbed or reflected. As a result, using a larger particle reflection coefficient merely has the effect of reducing the solution for the total desorbed particle flux. LTX has operated to date with hydrogen rather than deuterium; nevertheless, a run was examined using deuterium atoms as the species desorbed from the walls. Once again, the resulting R_{plate} and R_{core} are very similar to the reference case, indicating a lack of sensitivity to the PMI model. It is worth noting however, that there is more of a difference than with the case that merely multiplied the reflection coefficient for hydrogen on lithium by a fixed factor. The increased ionization and core fueling efficiencies for the deuterium case provide a clue as to the cause. In this PMI modeling approach, particles are assumed to be desorbed with a thermal distribution characterized by a temperature of 300 K. The higher mass of deuterium results in a velocity distribution that is lower by a factor of 30%. As a result, particles entering the plasma are more likely to be ionized. As a result, the total desorbed particle source rate needed to reproduce the measured emission is reduced slightly.

In general, the modeled emission using the solution for the source flux weights matches the measured emission quite well. It is not uncommon however, for some solutions to have difficulty matching the central channels of the inboard-viewing Lyman-α array. Even for solutions with an excellent match, the distribution of source flux weights (as indicated in fig. 5.10a) is not a smooth function. The source-emission map matrix for the inboard-viewing array (fig. 5.9a) suggests a reason for both effects. The two central chords do not intersect the inboard surface of the shells, but rather go through the shell gap and hit the center-stack. The other chords are incident on the shells. The current implementation of the array diagnostic in DEGAS 2 uses a very simple model for the point spread-function for each measurement channel. The model assumes a "top-hat" function which is unity from

the center of the sightline out to the angle half-way to the adjacent sightline. As a result, the source-emission map for the inboard-viewing array indicates that the two central chords (measurement indices 9 and 10 in fig. 5.9a) are much less-sensitive to emission from sources located at the shell edges than the adjacent channels. In reality, the point-spread function for the array channels is a more broad, smooth curve so that these channels are more sensitive to emission from sources on the shell edges than the source-emission map matrix would suggest. As a result, in order to best match the emission measured by these channels, the non-negative least-squares solution over-predicts the weights for the sources located on the inboard shell edges. This has the effect of over-estimating the emission measured by the adjacent channels, so the weights for the adjacent source segments are reduced to near zero. This effect largely explains why the source flux weights are not smooth. It is expected that a more accurate implementation of the point-spread function for the array diagnostics would improve the match with the measured emission for the central channels, and result in a smoother function for the source weight distribution.

In conclusion, neutral particle modeling has been used along with measurements of hydrogen line emission and global particle balance to determine R_{core} and the average R_{plate} for discharges with fresh and partially passivated solid lithium wall coatings. The results are found to be insensitive to errors in the n_e and T_e profiles. A previous study of a low-recycling CDX-U discharge with liquefied lithium in the tray limiter (ref. 52), found R_{core} and R_{plate} were 0.80 and 0.88, respectively. This value of R_{plate} is very close to the value calculated here for discharges with fresh solid Li shell coatings at t=447.0 ms. The difference in R_{core} can be explained by an increased core ionization efficiency for the LTX discharges, perhaps as a result of desorbed particles being partially trapped near the plasma by the shells. This thesis finds substantially lower values of R_{plate} and R_{core} for LTX discharges on fresh lithium wall coatings at time-points with higher electron density compared to the CDX-U case. These lower values are consistent with the lower effective particle confinement times measured in

chapter 4 (0.7–1.2 ms) compared to 1.5–4 ms as measured in the CDX-U study. Finally, the work presented in this chapter uses a relatively large number of measurements, most of which are not susceptible to contamination by light reflections, in order to constrain the determination of the recycling coefficients.

Chapter 6

Conclusions and suggestions for future work

The first goal of this thesis was to explore computationally and theoretically the physics of core particle and thermal transport for profiles that would be expected if core fueling dominates over wall recycling. In this regime, cooling of the edge by recycled neutrals is suppressed, which suggests an elevated edge temperature might be achieved. This in turn, could lead to a flattened temperature profile. Meanwhile, particle pumping at the wall would lead to a stronger density gradient. Although other studies have explored some aspects of TEM particle and thermal transport, this thesis addressed several specific questions for how the transport from micro-turbulence might be different in a device dominated by core fueling rather than recycling.

Linear stability and transport in the extreme case of a pure density-gradient drive (i.e., $\nabla T_e = \nabla T_i \to 0$) were explored. This regime is characterized by a small linear critical gradient, significant particle fluxes, and thermal transport below $3\Gamma T/2$ which is usually assumed to be the minimum heat flux for pure convection. The transport was also shown to preferentially eject impurity ions which could help counteract neoclassical impurity accumulation in the core and expel helium ash from the fusion reaction.

Linear stability and transport in the case of pure TEM drive (i.e., setting $\nabla T_i = 0$, but varying ∇P and $\eta_e \doteq \nabla T_e / \nabla n$) was studied next. An analytic model for the heat flux per electron was derived, which matched the results of nonlinear simulations surprisingly well. The thermodynamic constraint on the heat flux as a function of η_e was also determined, demonstrating that while surprising, the model prediction and simulation results of q_e as low as $\lesssim 3\Gamma T_e/2$ for $\eta_e \to 0$ are thermodynamically permitted. Nonlinear simulations with $\nabla T_i = 0$ showed a nonlinear critical pressure gradient significantly lower than that for the ITG instability; however, for simulations with moderate drive, the ion thermal transport is substantially less than in the reference ITG case.

Linear stability and transport for coupled TEM-ITG transport were also examined. Linear simulations with $\eta_e = \eta_i = \eta$ found that the linear critical gradient was maximized for $\eta \approx 0.8$. Since most present experiments operate near marginal ITG stability with η substantially greater than one, moving some of the free-energy gradient from temperature to density would have the effect of increasing the linear critical gradient. Nonlinear simulations showed substantial thermal transport compared to the reference ITG case, although differences in simulation parameters used in the reference ITG simulations might mitigate the differences in the resulting transport. It is also important to note that electron-scale (ETG) fluctuations were not simulated, which would most likely significantly increase the electron transport in the reference ITG case relative to the cases with stronger density gradients and reduced temperature gradients.

Linear and global nonlinear simulations were also performed using predicted LTX profiles from the reference transport model. A robust TEM instability was found for $r/a > 0.5$, while the ITG was also unstable for a profile during gas puff fueling. Global nonlinear simulations did not saturate unless the profile profiles were substantially flattened. Even so, the transport saturated to a level much higher than the reference transport model prediction.

In addition to changing the distribution of the free-energy gradient between temperature and density gradients, low-recycling and core fueling are expected to change the equilibrium in other important ways. By raising the edge temperature and flattening the temperature profile, the current profile is expected to flatten as well. This would have the effect of changing the magnetic shear and safety factor, which could be stabilizing or destabilizing. Also, by reducing the edge neutral density, low-recycling and core fueling might decrease the edge neutral drag on ions, which would alter the rotation profile. This would likely be a stabilizing effect in most regimes of interest. Finally, finite β electromagnetic effects should also be considered. For example, although their role in driving electron thermal transport in current high-β experiments is unclear, microtearing modes[146,11] are driven by the electron temperature gradient; as a result, they might be expected to be less unstable in low-recycling experiments with core fueling. Given the complexity of plasma turbulence, this work has only begun to explore the consequences of low-recycling and core fueling on micro-turbulent transport. Computationally expensive, electromagnetic simulations spanning ion- and electron-scale fluctuations will be needed to fully examine how core transport is affected by changes in recycling.

Since the combination of low-recycling and core fueling strongly affect the edge plasma, future work will need to examine the transport in this region in order to establish the proper boundary condition for the core. Plasma physics processes, atomic physics processes, and plasma-material interactions are all coupled together in the edge plasma, making this region difficult to model. In addition, large fluctuation amplitudes and sharp gradients add numerical difficulties to simulating this region. Nevertheless, recently released and upcoming gyrokinetic edge transport codes coupled to neutral and impurity transport codes and plasma-material interaction models will be needed in order to understand the boundary condition imposed on the core by the edge plasma and the changes that take place as a consequence of reduced recycling.

In summary, the simulation results presented in this thesis support the result that reduced recycling and the resulting higher edge temperature can significantly improve performance; at the same time, they also indicate that there may be limits on how large the improvement can be due to increased turbulence if the density gradient gets too strong. A detailed quantitative assessment of the degree of improvement will require a better understanding of stabilizing effects of sheared flows and transport barriers and the interaction with the edge boundary conditions, and thus will need the development of comprehensive edge simulations.

The second goal of this thesis was to assess the impact of recycling on discharge behavior, and measure the limit of low-recycling that can be achieved in a small tokamak using evaporatively-deposited solid lithium coatings. An extensive developmental effort was undertaken to design and deploy a suite of VUV and visible spectroscopic diagnostics to measure line emission from hydrogen and impurities. These instruments were described in chapter 2. These instruments were used in chapter 4 to examine high-performance discharges with a variety of wall conditions including full shell coatings of freshly-deposited solid lithium, partial shell coating of solid lithium, and partially-passivated lithium surfaces.

Measurements of effective particle confinement time found that solid lithium coatings on LTX are able to produce values of $\tau_p^* \approx 0.7$–1.1 ms. These effective particle confinement times are lower than those attained on CDX-U with solid or even liquid lithium in the toroidal tray limiter. Although τ_p^* changes little with cumulative fueling up to 3.5×10^{21} H atoms, measurements of R_{cum} are more sensitive and do increase, indicating that the surface is indeed evolving. Measurements of hydrogen Lyman-α emission correlate well with the interferometer measurements, consistent with the picture that changes in hydrogen recycling are producing the changes in effective particle confinement. Both measurements of peak emission during a fueling pulse and emission decay time following a fueling pulse tended to increase with cumulative fueling for discharges following deposition of a full or partial lithium coating.

Interestingly, an estimate of the total number of lithium atoms accessible for binding with incident hydrogen if the shell surfaces are fully coated would suggest that the surface should become fully saturated by a cumulative external fueling of about 2×10^{21} H atoms. Instead, these measurements find that R_{cum} increases only about 60% and τ_p^* only about 10% for a cumulative external fueling up to 3.5×10^{21} H atoms. In contrast, if a reduced quantity of lithium is evaporated onto the shell surfaces, τ_p^* is found to increase significantly with cumulative fueling. This result is consistent with experiments on the National Spherical Torus Experiment (NSTX) which found a continuous reduction in divertor D-α emission, considered indicative of reduced recycling, with increasing thickness of solid lithium coatings[89,165]. In both NSTX and LTX, a mechanism is needed to account for access to lithium binding sites beyond the $\lesssim$10 nm penetration length of plasma ions. For the NSTX case, non-uniform lithium coverage and lithium intercalation in the complex graphite surface morphology[46] have been proposed as explanations. Since the LTX shell surface is stainless-steel, the surfaces can likely be treated as flat to good approximation; therefore surface morphology is not a probable explanation. Although lithium evaporation in LTX was performed with helium background gas in order to distribute the lithium more evenly over the shell surface, measurements of coating thicknesses have not been performed to assess the non-uniformity in the deposited coatings. It is possible that regions of the shells far from the evaporators are only sufficiently coated if about $\sim$2 g are evaporated from each crucible. Installation of one or more quartz deposition monitors planned for the next run campaign will aid in quantifying non-uniformity in the lithium coatings.

It is important to emphasize that while non-uniformity in the evaporated coatings could explain the increase in τ_p^* with cumulative fueling following a partial evaporation, it does not account for strong pumping of hydrogen following evaporation of a full lithium coating, even after almost double the cumulative fueling is applied that should saturate the lithium coating up to the penetration depth of hydrogen ions. Possible mechanisms that might provide access

to additional binding sites for pumping of hydrogen include finite diffusion of hydrogen in the solid lithium coatings, chemical reactions between lithium and residual gases which result in complexes that more efficiently bind hydrogen, and erosion of the lithium coatings by the plasma which result in co-deposition and burial of hydrogen-containing lithium monolayers. Spectroscopic measurements indicate lithium erosion occurs during discharges, but more extensive measurements and modeling are needed to quantify erosion and re-deposition rates.

Discharges on a partially-passivated surface show essentially no systematic trend in τ_p^* or $R_{\rm cum}$ with cumulative fueling. This is surprising, since these discharges still have relatively short effective particle confinement (τ_p^*≈1.5–3 ms) consistent with strong particle pumping by the lithium surface. Planned experiments with dedicated sample-analysis probes and surface characterization instruments should inform on the hydrogen retention capability of both solid and liquid lithium coatings in a fusion environment.

Langmuir probe measurements show that the electron density in the scrape-off-layer tracks the electron density in the core, dropping substantially as the external fueling is terminated. Probe measurements also show that discharges on fresh, full lithium coatings achieve lower densities in the SOL and higher electron temperatures during the period between fueling pulses than those on a partially-passivated surface, consistent with the model of reduced edge cooling from recycled particles. Additional three-tip Langmuir probes at multiple locations surrounding the plasma would provide more spatial information for constraining edge models, and provide increased time resolution to better capture fast temporal behavior during the relatively short LTX discharges.

Interestingly, the connection between reduced recycling and plasma current is somewhat complex. Although heavily-fueled discharges that produce large plasma currents with fresh lithium walls become over-fueled when the same external fueling is used with partially-passivated walls, moderately-fueled discharges have comparable plasma current during most of the discharge. During the low-density period between fueling pulses, discharges with lower

τ_p^* actually have less plasma current. The extensive visible spectroscopic diagnostics fielded in this thesis work were used to show that during this time period, the ratio of impurity density to electron density is seen to rise substantially, and more so for discharges with the lowest τ_p^*. Therefore, during this low-density period, low τ_p^* discharges have higher Z_{eff}, resulting in reduced Spitzer conductivity, and explaining the reduced plasma current relative to discharges with higher τ_p^*. In contrast, near the end of the discharge, moderately-fueled plasmas with partially-passivated walls have systematically lower plasma currents than those with fresh evaporative lithium coatings. At this time, plasma current is inversely correlated with τ_p^*, suggesting that the discharges with fresh evaporative lithium coatings achieve higher electron temperature in the core.

Chapter 5 applied a neutral transport modeling code in order to quantify the recycling for a subset of high-performance discharges on solid lithium wall coatings. A novel approach was developed to the inverse problem of finding the distribution of hydrogen recycling fluxes from PFC surfaces given a large number of emission measurements. Moreover, because of the significant diagnostic development effort undertaken in this thesis to field VUV arrays measuring Lyman-α emission, most of the emission measurements used to constrain the recycling coefficient are not susceptible to contamination by optical reflections, increasing the fidelity of the resulting solutions. Modeling revealed that depending on wall preparation, discharges were found to have a range of recycling coefficients. In particular, extremely low levels of recycling has been achieved with thin coatings of solid lithium evaporatively deposited on the in-vessel shells. For shots following evaporation of a full solid lithium coating onto the shell surfaces, values of R_{core} as low as 0.55–0.59 and R_{plate} as low as 0.78–0.82 are found. This level of recycling is even less than what was calculated for a CDX-U discharge during operation with liquefied lithium in the tray limiter[52]. The lower R_{core} (and R_{plate}) are consistent with the lower effective particle confinement times measured in LTX plasmas (0.7–1.2 ms) compared to 1.5–4 ms in the CDX-U study. Finally, the results of neutral modeling

are consistent with the impurity emission measurements. They suggest that during periods of particularly low electron density in the discharges with the lowest levels of recycling, influx of impurities from the walls rather than merely hydrogenic recycling contributes substantially to the global particle balance.

In addition to developing and fielding multiple diagnostics as part of this thesis, a useful framework has been developed to integrate data sets from a wide variety of instruments and also magnetic equilibria. In addition, tools have been developed to perform poloidal inversions of arbitrary line-integrated measurements and generate a computational mesh for LTX magnetic equilibria for use in subsequent modeling. These object-oriented tools have been written in Python, and use the open-source numerical packages Numpy, SciPy, and matplotlib. Web documentation for these tools has been generated using the open-source Doxygen package. Future studies of neutral and impurity transport in LTX can leverage these existing diagnostics and hardware.

Given the importance of impurities in affecting the performance of LTX discharges established in this thesis, one avenue of future work would be to assess the source rates of impurities into the plasma and their accumulation in the core. Despite the engineering complexity of shuttered re-entrant windows, such techniques will most likely be needed to obtain views with adequate coverage for high-resolution measurements of visible light emission using filtered high-speed cameras. These measurements could then be used to constrain impurity transport modeling, and be compared with CHERS measurements of fully-ionized lithium in the plasma core.

Finally, the Lyman-α and bolometer arrays are currently limited in their views because their apertures sit immediately behind a gate valve. Their angular coverage is then determined by the distance from the gate valve to the shell and the vertical extent of the shell midplane gap. However, the recent availability of very high pin-density electrical connectors on small flanges allows for the development of re-entrant array diagnostics. For example, a

tangential, multi-energy soft X-ray instrument could be incorporated on a re-entrant flange along with the outboard-viewing Lyman-α array. This would enable direct identification of the magnetic axis major radius, full inversion of the emission profile, and potentially time-resolved estimates of electron temperature.

Improvements to the existing profile diagnostics will allow realistic interpretive modeling of particle and thermal transport. In the future, it would be interesting to consider a follow-up to the gyrokinetic simulations presented in this work, using actual LTX profiles and magnetic equilibria. For example, linear studies can elucidate if temperature-gradient-driven modes are indeed stable in the absence of edge gas fueling, and if $\mathbf{E} \times \mathbf{B}$ shear combined with finite plasma β is sufficient to reduce or even stabilize the linear growth rate of trapped-electron modes. Despite the technical difficulties with global gyrokinetic simulations for a small device, continued improvements in codes such as GYRO and GENE may enable this type of work. It would be also be very informative to examine if the thermal transport is dominated by convection, as predicted for profiles with $\eta \lesssim 1$. Density fluctuation measurements using microwave reflectometry, beam-emission-spectroscopy, or phase contrast imaging would then permit further comparison between the experiment and theory.

Appendix A

Technical Details for Visible Spectroscopic Diagnostics

A.1 General Calibration Procedure

The signal measured from an illumination source with spectral radiance I (units of W/s-m^2-ster-nm), filter transmission η_f, and system responsivity (including transmission and detection) R, each of which can have wavelength dependence, can be written as:

$$V = \int_0^\infty \eta_f(\lambda) R(\lambda) I(\lambda) d\lambda. \tag{A.1}$$

For an atomic emission line centered at λ_0 with minimal line broadening relative to the filter transmission bandwidth, the source spectral radiance can be written as:

$$I(\lambda) \approx I_{\lambda_0}^{line} \delta(\lambda - \lambda_0). \tag{A.2}$$

Therefore:

$$V^{line} \approx \eta_f(\lambda_0) R(\lambda_0) I_{\lambda_0}^{line}. \tag{A.3}$$

In contrast, for a broad-band illumination source such as the Labsphere or Optronics sources used for calibration, the illumination spectral radiance is approximately uniform across the filter bandwidth. Therefore, for a filter centered around wavelength λ_c, we can write:

$$\eta_f(\lambda) \approx \eta_{\lambda_c}\delta(\lambda - \lambda_c)w. \tag{A.4}$$

In the above expression, w is a parameter that characterizes the filter width:

$$w \doteq \frac{1}{\eta_f(\lambda_c)} \int_0^\infty \eta_f(\lambda)d\lambda. \tag{A.5}$$

For a filter with a Gaussian transmission profile:

$$w = \frac{\text{FWHM}}{2}\sqrt{\frac{\pi}{\ln 2}} \approx 1.06\text{FWHM}. \tag{A.6}$$

Therefore, the measured signal from a calibration light-source is:

$$V^{cal} \approx w\eta_f(\lambda_c)R(\lambda_c)I^{cal}(\lambda_c). \tag{A.7}$$

Assuming either that the atomic emission line center is the interference filter central wavelength ($\lambda_c = \lambda_0$) or that the responsivity of the system (lenses, fibers, and detectors) is virtually equal at λ_c and λ_0, we can write $R(\lambda_0) = R(\lambda_c)$. Then equations A.3 and A.7 can be combined to yield:

$$I^{line}_{\lambda_0} = C_{\lambda_0}V^{line}, \tag{A.8}$$

where the calibration coefficient is:

$$C_{\lambda_0} \doteq w\frac{\eta_f(\lambda_c)}{\eta_f(\lambda_0)}\frac{I^{cal}(\lambda_c)}{V^{cal}}. \tag{A.9}$$

If the filter is centered exactly at the wavelength of the atomic line, expression A.9 above reduces to:

$$C_{\lambda_0} = w\frac{I^{cal}(\lambda_0)}{V^{cal}}. \tag{A.10}$$

Equation A.9 gives small corrections that can be used, for example, to account for a filter wavelength centered at the D_α (656.1 nm), while the measurement is of H_α (656.3 mn) emission.

A.2 Filterscopes

A.2.1 Hardware Details

The filterscope hardware is described in detail in ref. 92; however, several modifications were made for better integration with the LTX data acquisition system. Since the PMT gain control voltages were changed occasionally, they were digitized along with the signal voltages. Unfortunately, the relatively low input impedance (20 kΩ) of the digitizer (D-tacq ACQ196CPCI-96-200), would cause the unbuffered control voltages to droop. To eliminate this issue, buffer pre-amplifiers were installed in each filterscope module. These pre-amplifiers have a 5× voltage gain to more fully utilize the dynamic range of the digitizer. Therefore, the control voltage recorded by the digitizer is 5× the contorol voltage at the PMT.

A.2.2 Calibration Procedure and Results

The calibration method for the filterscopes is essentially as described in A.1 with minor modification. The high-voltage power supply in each photomultiplier tube (PMT) module is determined by a reference voltage, with the responsivity of the PMT being approximately

exponential with the reference voltage. Therefore, equations A.8 and A.9 are modified:

$$I_{\lambda_0}^{line} = C_{\lambda_0}(V_{ctrl})V^{line} \tag{A.11}$$

$$C_{\lambda_0}(V_{ctrl}) \doteq w\frac{\eta_f(\lambda_c)}{\eta_f(\lambda_0)}\frac{I^{cal}(\lambda_c)}{V^{cal}(V_{ctrl})}. \tag{A.12}$$

Since LTX discharges vary considerably (depending on the condition of the wall and other factors), the emission intensities of atomic transition lines can also span a considerable range. As a result, the PMT control voltages need to be changed on occassion. Therefore, in addition to digitizing and storing the signal voltages, the control voltages are also stored in the LTX data system. A photometric calibration for each filterscope channel is obtained by separately illuminating each filterscope head, and taking data "shots" while varying the illumination spectral radiance and PMT control voltages. A linear fit is used to find the calibration constant at each control voltage, then an exponential fit with 5-term polynomial is used to find the calibration constant as a function of control voltage:

$$C_{\lambda_0}(V_{ctrl}) = C_{spectral}\exp\left(a_0 + a_1V_{ctrl} + a_2V_{ctrl}^2 + a_3V_{ctrl}^3 + a_4V_{ctrl}^4\right). \tag{A.13}$$

The spectral coefficient converts the lightsource luminance (specified in units of foot-lamberts) to the spectral radiance at a particular wavelenth and has units of [W/m^2-ster-nm-ft-lam]. This calibration was performed using a Labsphere URS-600 Uniform Source Standard. Connections for the filterscope channels in their current (since May 2012) configuration are shown in table A.1. An example of the resulting calibration is shown in fig. A.1. Connections information and calibration constants are all stored in the "ltxcal" MDSplus tree.

Filterscope PMT Module and Channel	Filterscope Head and Fiber	Filter Unique Name	Filter Wavelength [nm]	Filter FWHM [nm]
1.1	A–1.1	Dbeta–1	486.0	1.5
1.2	A–1.2	Dalpha–1	656.1	1.5
1.3	A–4.0	CII–658–2	658.5	1.5
1.4	A–1.3	Dgamma–1	433.9	1.5
1.5	A–5.0	Vbrem–1	527.0	4.5
2.4	A–2.2	LiI–610–3	610.4	1.0
2.1	B–1.0	Dalpha–2	656.1	1.0
2.2	B–2.1	LiI–670–1	670.8	1.5
2.3	B–2.2	LiI–610–1	610.0	1.5
2.5	B–4.0	LiII–2	548.6	1.5
3.1	B–2.3	LiI–460–1	460.3	1.0
3.2	C–2.3	LiI–497–1	497.2	1.5
3.3	C–6.0	LiIII–1	450.0	1.5
3.4	C–7.0	CII–658–1	658.5	1.5
4.1	C–1.0	Dalpha–3	656.1	1.0
4.2	C–2.1	LiI–610–2	610.4	1.0
4.3	C–2.2	LiI–670–2	670.8	1.5
4.4	C–5.0	OII–441–1	441.6	1.5

Table A.1: The current configuration of the filterscopes. Non-integer numbers for the fiber show the connections to a fiber splitter (ex. A–1.2 corresponds to fiber 2 output from a fiber splitter connected to fiber 1 of head A. From 2011–2013, Head A viewed the inboard edge of the upper shell, head B viewed the lower shell, and head C viewed one of the limiters in the lower shell next to the shell gap near the Thomson scattering laser entrance port.

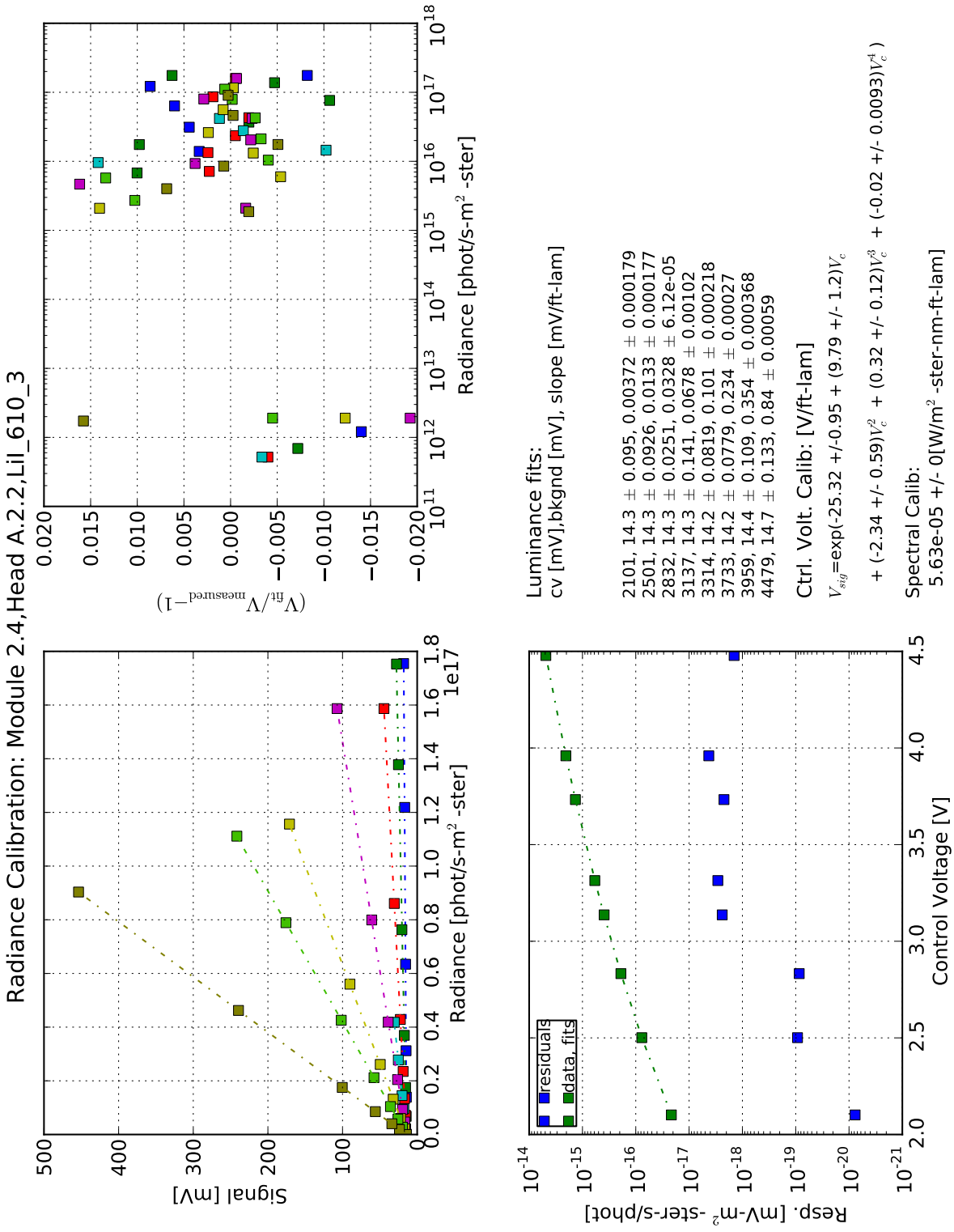

Figure A.1: Filterscope calibration example

A.3 Cameras

A.3.1 Calibration Procedure and Results

Photometric calibration was performed using a Labsphere URS-600 Uniform Source Standard. Since only part of the detector was illuminated by the light-source at a given instant, the camera was rotated relative to the light-source while recording frames at high-speed in order to expose the entire detector. Photometric calibration results are shown in fig. A.2 for the Phantom camera with 2" H-α filter. The non-uniformity in the responsivity is due primarily to vignetting of the camera view by the filter and holder.

A.4 Mini-Spectrometers

A.4.1 Calibration Procedure and Results

Wavelength calibration of each spectrometer was performed by connecting an Ocean Optics HG-1 Mercury Argon Calibration Source to the fiber input of the spectrometer. Relevant mercury and argon emission lines are shown in table A.3. The peaks of the emission lines are fit to a third-order polynomial for the pixel number (x):

$$\lambda(x) = c_0 + c_1 x + c_2 x^2 + c_3 x^3. \tag{A.14}$$

Photometric calibration is performed by following the procedure described in A.1. Results of the wavelength and photometric calibration follow.

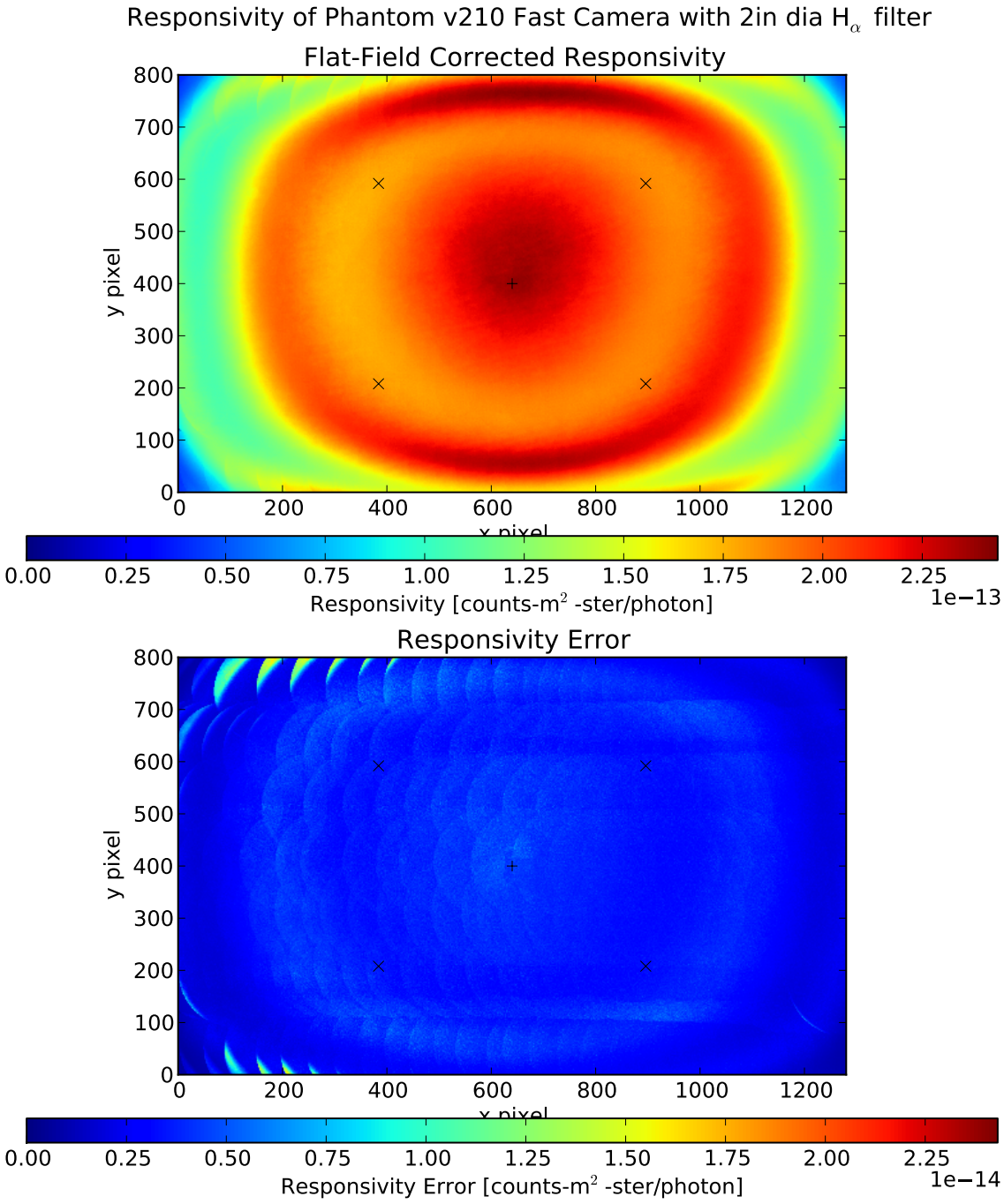

Figure A.2: Phantom high-speed camera photometric calibration. The black cross is the image center, while the black × marks correspond to the corners of the 512×384 pixel frame typically used during experiments.

Mercury wavelength (nm)	Rel. Intensity	Argon wavelength (nm)	Rel. Intensity
404.6565	12000	415.859	400
407.7837	1000	419.0713	100
434.74945	150	419.8317	200
435.8335	12000	420.0674	400
496.01	100	425.9362	200
535.4034	130	426.6286	100
546.075	6000	427.2169	150
567.581	600	430.0101	100
576.961	1000	433.3561	100
579.067	900	451.0733	100
580.3782	400		
585.9254	130		

Table A.2: Listing of mercury and argon emission lines used in the wavelength calibration of the visible survey spectrometers. Wavelengths and relative intensities taken from the NIST Atomic Spectra Database.

Spectrometer Name	Spectrometer S/N	Filterscope head and fiber	c_0 [nm]	c_1 [nm/px]	c_2 [nm/px^2]	c_3 [nm/px^3]
OO–01	HR+C1783	A3	377.728	0.111743	-4.25416e-06	-9.93028e-11
OO–02	HR+C1275	C6	376.681	0.115274	-4.83039e-06	1.24165e-11
OO–03	HR+C1274	C8	377.227	0.113193	-3.99409e-06	-1.76587e-10

Table A.3: Calibration coefficients to convert pixel number to wavelength and filterscope connections.

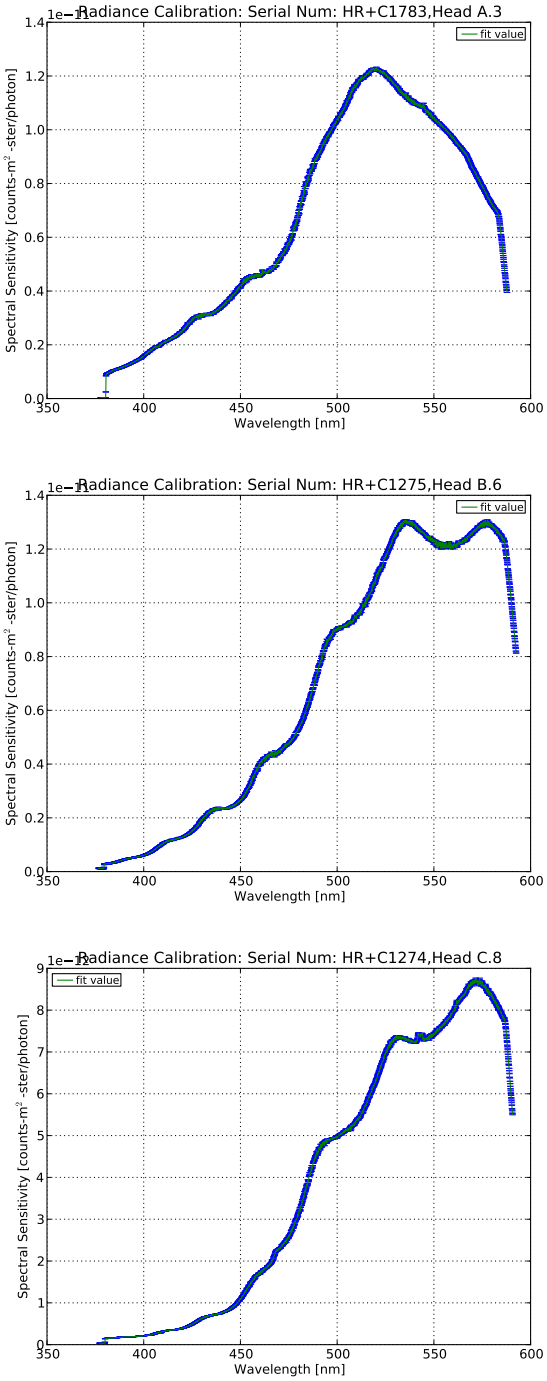

Figure A.3: Results of the photometric calibration for each spectrometer.

A.5 Ionizations per Photon (SX/B) Coefficients

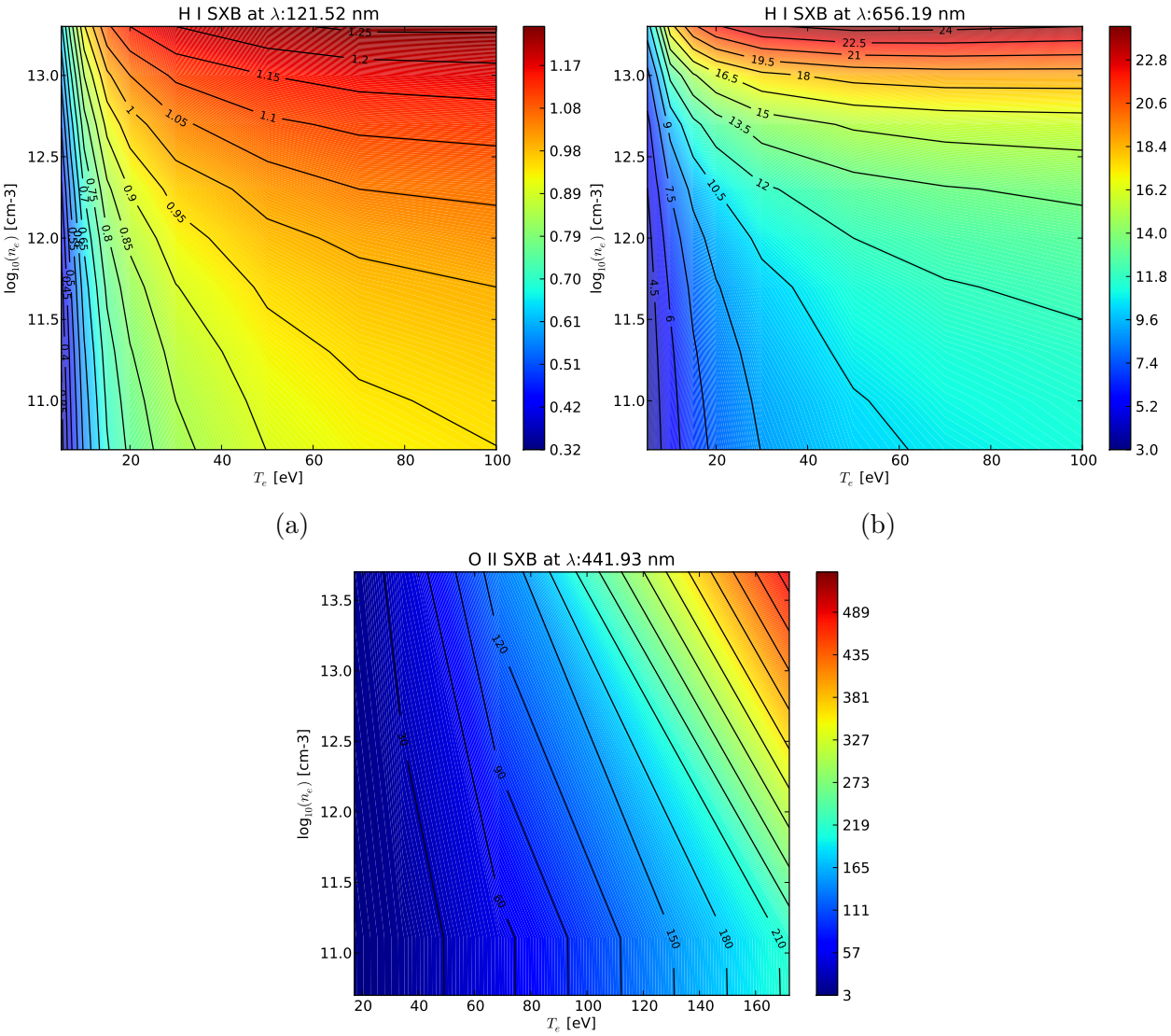

(a) (b) (c)

Figure A.4: S/XB coefficients for (a) hydrogen Lyman-α, (b) hydrogen Balmer-α (aka. H-α), and (c) O^{1+} at 441 nm. Units of the S/XB coefficients are ionizations per photon emitted into 4π steradians.

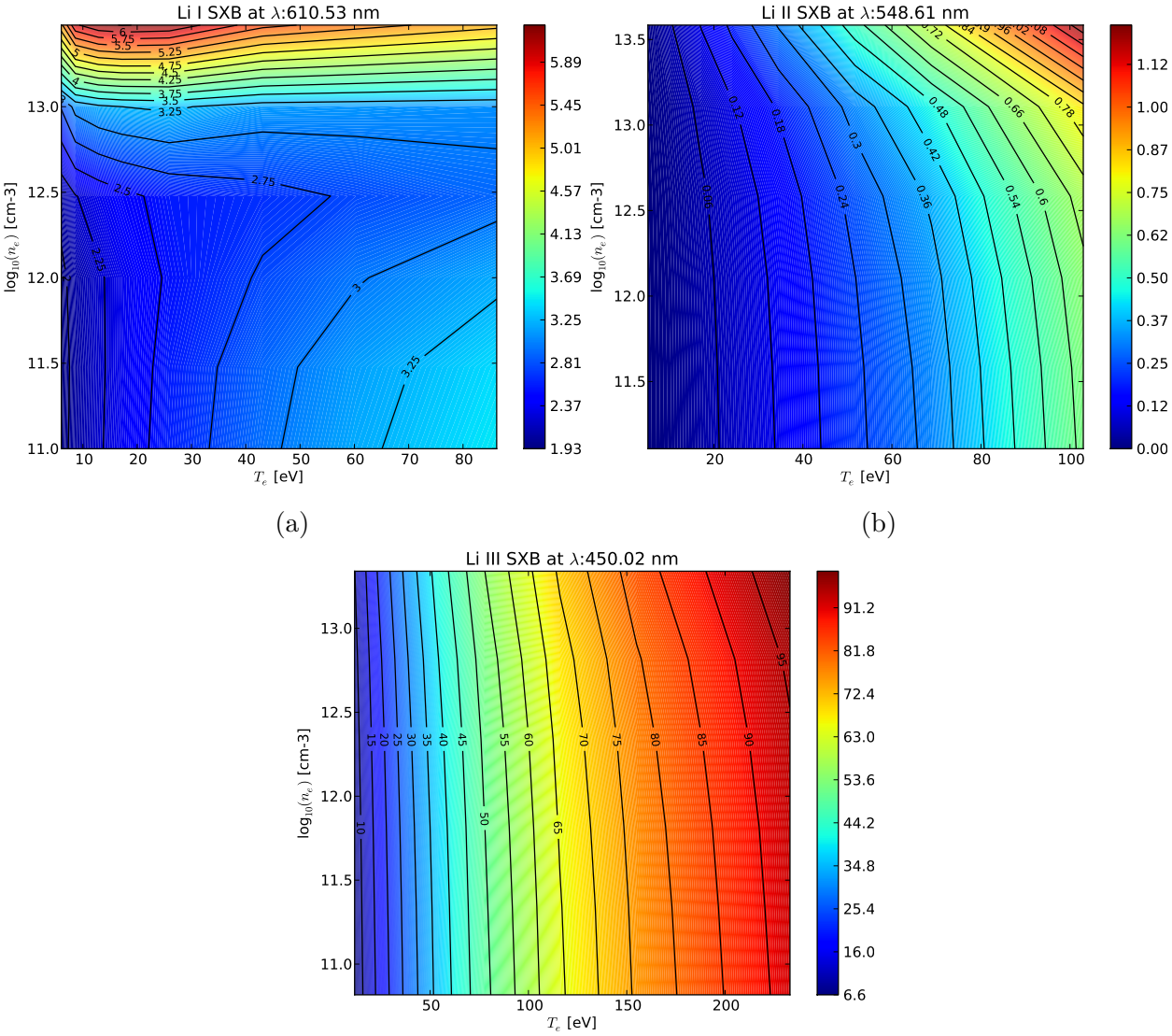

(a) (b) (c)

Figure A.5: S/XB coefficients for (a) Li^{0+} at 610 nm, (b) Li^{1+} at 548 nm, and (c) Li^{2+} at 450 nm. Units of the S/XB coefficients are ionizations per photon emitted into 4π steradians.

A.6 Photon Emissivity (PEC) Coefficients

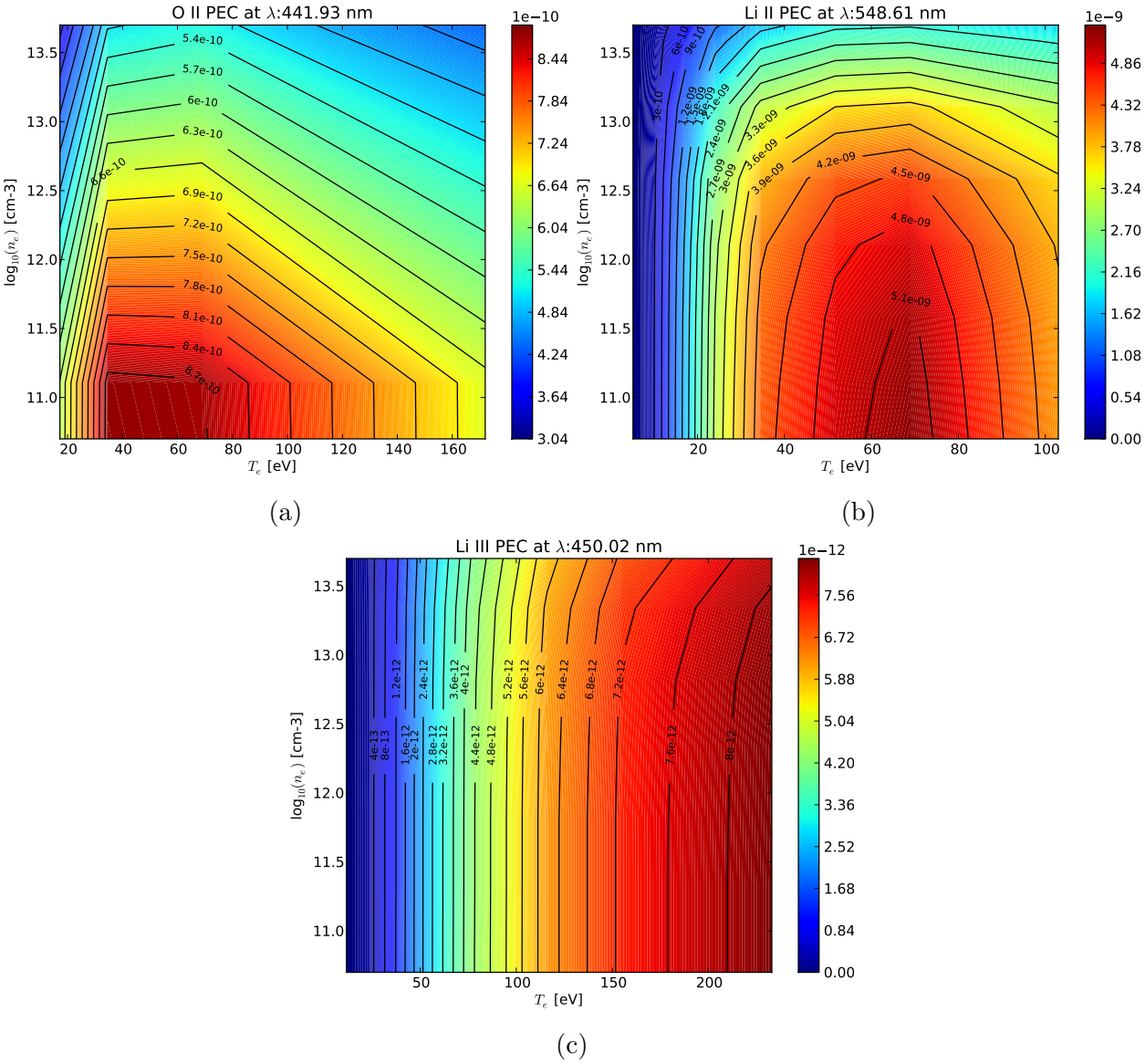

Figure A.6: Photon Emissivity (PEC) Coefficients for (a) O^{1+} at 441 nm, (b) Li^{1+} at 548 nm, and (c) Li^{2+} at 450 nm. Units of the PEC coefficients are photons-cm^3/s.

Appendix B

Technical Details for Vacuum Ultra-Violet (VUV) Diagnostics

B.1 Inboard-Viewing and Outboard-Viewing Arrays

B.1.1 Pre-Amplifier Calibration Procedure

Transimpedance pre-amplifiers were calibrated with respect to an SRS current pre-amplifier. A light-tight calibration box consisting of an IRD AXUV-SP2 detector diode and visible LED was constructed. The LED was biased with a sawtooth wave (typically 10-1000 Hz), and the voltage waveforms from the SRS current pre-amplifier and instrument pre-amplifiers were recorded. This calibration method did not work with the four highest gain settings of the arrays, due to the relatively large capacitance of the AXUV-SP2 diode (even with reverse-biasing). Therefore, a second calibration method was employed as well. The aperture and filter of each array were removed, and the remaining assembly was attached to light-tight calibration chamber. Inside the calibration chamber was an array of eight LEDs to illuminate the AXUV20ELM detector array. Electrical connections were made to the LED array through a vacuum electrical feedthrough. Once again, a sawtooth waveform was

applied to the LEDs. Data "shots" were taken with the instrument pre-amplifiers attached the air-side electrical feedthrough of each array. Next, voltage waveforms using the SRS current pre-amplifier were recorded for each channel individually. It was found that despite > 150 MΩof resistance between each AXUV20ELM cathode channel, nearest-neighbor channels needed to be grounded in order to prevent the SRS current pre-amplifier from detecting current from more than one channel at a time.

The pre-amplifiers used in the array diagnostics consist of two stages: a MaZeT MTI04 pin-programmable transimpedance amplifier and a cascade of two inverting voltage amplifiers. The first inverting voltage amplifier has a voltage adjustment connected to the non-inverting input. Since the voltage output from the transimpedance amplifier is ≥ 0, by adjusting the offset of the second stage, to be negative, the ± 10 V input range of the digitizers can be more fully used. This must be done with caution, however, because of the relatively low input impedance of the inverting amplifier coupled with the low maximum output current of the MaZeT transimpedance amplifier. To account for non-ideal effects, a 5-degree polynomial was used to fit the current measured by the SRS current pre-amplifier to the voltage measured at each gain setting for the instrument pre-amplifiers:

$$I(V) = a_{g,0} + a_{g,1}V + a_{g,2}V^2 + a_{g,3}V^3 + a_{g,4}V^4 \tag{B.1}$$

B.1.2 Etendue Calculation

To first order, the etendue of each detector is simply:

$$A\Omega = \frac{A_{\text{det}} A_{\text{ap}}}{r^2}, \tag{B.2}$$

where A_{det} is the area of the detector, A_{ap} is the area of the aperture, and r is the normal distance between the aperture and detector. This simple formula was used to determine the

etendue of the single-channel instruments. Although the formula is very accurate for the central channels of the array instruments, it does not capture the reduced etendue of the detector channels located off-axis. To account for this effect, a correction factor for each detector channel i was calculated via numerical integration of the rays through the aperture over the area of that detector:

$$C_i \doteq \frac{r^2}{A_{\rm det}} \int_{U_-}^{U_+} du \int_{V_-}^{V_+} dv \frac{C_{{\rm ang},x}(u) C_{{\rm ang},y}(v, y_i)}{\left(1 + u^2 + v^2\right)^2} \tag{B.3}$$

$$C_{{\rm ang},x} \doteq \left[1 - \frac{1}{2}\left(\theta_{-x}(u) + \theta_{+x}(u)\right)\left(1 - \frac{\Delta x_d}{\Delta x_a}\right) + \frac{ur}{\Delta x_a}\left(\theta_{-x}(u) - \theta_{+x}(u)\right)\right] \tag{B.4}$$

$$C_{{\rm ang},y} \doteq \left[1 - \frac{1}{2}\left(\theta_{-y}(v, y_i) + \theta_{+y}(v, y_i)\right)\left(1 - \frac{\Delta y_d}{\Delta y_a}\right) + \frac{vr + y_i}{\Delta y_a}\left(\theta_{-y}(v, y_i) - \theta_{+y}(v, y_i)\right)\right] \tag{B.5}$$

$$\theta_{\pm x}(u) \doteq \theta(\Delta x_a - \Delta x_d \pm 2ru) \tag{B.6}$$

$$\theta_{\pm y}(v, y_i) \doteq \theta(\Delta y_a - \Delta y_d \pm 2y_i \pm 2rv) \tag{B.7}$$

$$U_\pm \doteq \pm\frac{\Delta x_d + \Delta x_a}{2r} \tag{B.8}$$

$$V_\pm \doteq \pm\frac{\Delta y_d + \Delta y_a \mp 2y_i}{2r}. \tag{B.9}$$

In the above equations, Δx_a (Δy_a) is the half-width of the aperture in the horizontal (vertical) direction, Δx_d (Δy_d) is the half-width of the detector channel in the x (y) direction, and y_i is the distance from the aperture center-line to the center of detector channel i. $\theta(x)$ is the Heaviside function:

$$\theta(x) \doteq \begin{cases} 0 & \text{if } x < 0, \\ 1 & \text{if } x >= 0. \end{cases} \tag{B.10}$$

This factor resulted in a 15% correction for the outermost channels of the inboard-viewing array and a 5% correction for the outermost channels of the outboard-viewing array. The actual etendue parameters for each instrument are stored in the "ltxcal" MDSplus tree.

B.1.3 Array Hardware

Mechanical drawings for the inboard array aperture assembly and mount are stored in the LTX CAD database as drawing number ELTXS-157 and are not reproduced here. The mechanical drawings of the outboard array mount is likewise stored in LTX CAD database as drawing number CLTXS-153. A schematic of the array-preamplifier circuit is shown in fig. B.1. The circuit was developed by K. Tritz (Johns Hopkins University) and VORG Electronics (317 Blacksmith Arch., Yorktown, VA 23693; 757-865-6442). The first-stage mounts directly to the 25-pin Dsub electrical feedthrough, while the second-stage output is a 68-pin micro-D (SCSI-III) connector. Nominal gain settings for the amplifiers are given in table B.1. Detailed information on the MaZeT MTI04 pin-programmable transimpedance amplifiers can be found in the product datasheet. An adapter board mates the 3× 68-pin cables from the array pre-amplifiers (one from each array) to 2× 68-pin cables which connect to the D-tacq digitizer. The drawing and parts list for this board is stored in the LTX CAD database as drawing number BLTXS-163.

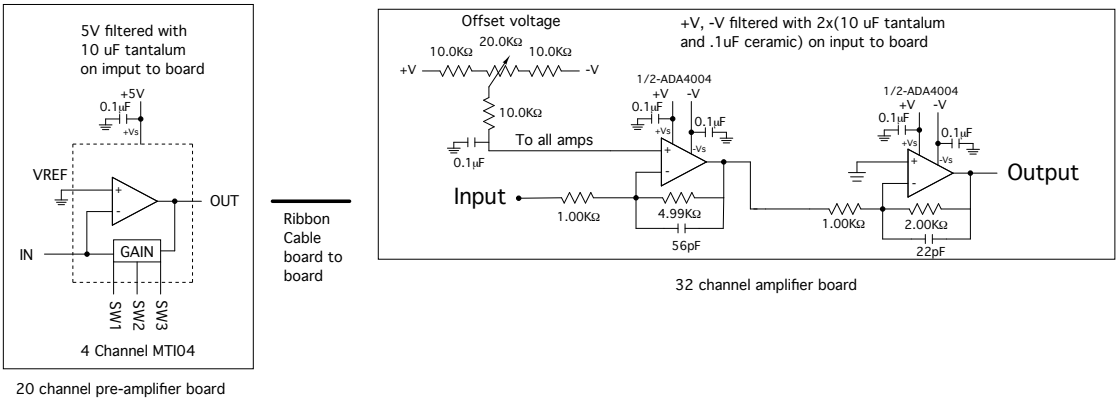

Figure B.1: Array pre-amplifier circuit diagram.

The AXUV20ELM detector arrays mount to an in-vacuum PCB that adapts the DIP-22 footprint of the detector array to the 25-pin Dsub electrical feedthrough. The PCB material is either Rogers 4003 (glass-reinforced hydrocarbon/ceramic laminate, preferred) or Rogers

Displayed/Stored Gain Setting	MTI04 gain-control pin settings SW3, SW2, SW1	MTI04 (first-stage) Gain	Total Inboard Lyman-α and Bolometer Array Gain	Total Outboard Lyman-α Array Gain
0	0, 0, 0	25kΩ	250kΩ	125kΩ
3	0, 1, 1	100kΩ	1MΩ	500kΩ
1	0, 0, 1	500kΩ	5MΩ	2.5MΩ
4	1, 0, 0	1MΩ	10MΩ	5MΩ
5	1, 0, 1	2MΩ	20MΩ	10MΩ
2	0, 1, 0	5MΩ	50MΩ	25MkΩ
6	1, 1, 0	10MΩ	100MΩ	50MΩ
7	1, 1, 1	20MΩ	200MΩ	100MΩ

Table B.1: Nominal gain settings for the arrays. The actual (calibrated) values are stored in the "ltxcal" MDSplus tree.

3003 (ceramic-filled PTFE composite) with gold contacts deposited electrolytically or via gold immersion. The adapter board PCB layout and parts list is drawing number BLTXS-165 in the LTX CAD database. Tin/silver (lead-free) solder, was used to mount the pins to the PCB and the boards were ultrasonically cleaned for vacuum.

B.2 Single-Channel Lyman-α Instruments

These instruments used an IRD AXUV100 diode detector with a directly-deposited Lyman-α filter (IRD P/N AXUV100GLA). The quantum efficiency for this detector (including the attenuation of the filter) is shown in fig. B.2. These instruments used custom-designed pre-amplifiers consisting of an in-vacuum transimpedance amplifier and a voltage pre-amplifier on the air-side. The diode mounts directly into the in-vacuum amplifier, which in turn mounts onto a 9-pin subminiature-C electrical feedthrough. The air-side voltage pre-amplifier gain can be controlled with small "DIP-style" switches. The mechanical drawing for the aperture assembly is stored in the LTX CAD database as drawing number ELTXS-167. The drawings and parts list for the first and second stage pre-amplifiers are drawing numbers BLTXS-156 and BLTX-139, respectively. The pre-amplifiers for these instruments were calibrated

according to the procedure described in sec. B.1.1, but use only a linear equation for the gain. The etendue for these instruments were calculated according to eq. B.2 without accounting for off-axis effects.

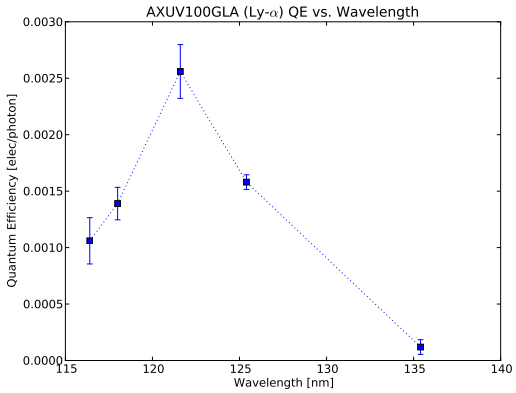

Figure B.2: AXUV100GLA Quantum Efficiency vs. Wavelength

Bibliography

[1] J. Wesson and D. J. Campbell. *Tokamaks*. 3rd ed edition. Clarendon Press, Oxford (2004).

[2] J. C. Adam, W. M. Tang, and P. H. Rutherford. Physics of Fluids **19**, 561–566 (1976).

[3] D. W. Ross, W. M. Tang, and J. C. Adam. Physics of Fluids **20**, 613–618 (1977).

[4] W. Tang. Nuclear Fusion **18**, 1089 (1978).

[5] J. Horton, D. Choi, and W. M. Tang. Physics of Fluids **24**, 1077–1085 (1981).

[6] M. Kotschenreuther, W. Dorland, M. A. Beer, et al. Physics of Plasmas **2**, 2381–2389 (1995).

[7] R. E. Waltz, G. M. Staebler, W. Dorland, et al. Physics of Plasmas **4**, 2482–2496 (1997).

[8] F. Wagner, G. Becker, K. Behringer, et al. Physical Review Letters **49**, 1408 (1982).

[9] H. Biglari, P. H. Diamond, and P. W. Terry. Physics of Fluids B: Plasma Physics **2**, 1–4 (1990).

[10] J. A. Boedo, P. W. Terry, D. Gray, et al. Phys. Rev. Lett. **84**, 2630–2633 (2000).

[11] S. Kaye, F. Levinton, D. Stutman, et al. Nuclear Fusion **47**, 499–509 (2007).

[12] S. M. Kaye, R. E. Bell, D. Gates, et al. Physical Review Letters **98**, 175002–4 (2007).

[13] G. M. Staebler and H. E. S. John. Nuclear Fusion **46**, L6 (2006).

[14] R. V. Budny. Nuclear Fusion **49**, 085008 (2009).

[15] W. Dorland, F. Jenko, M. Kotschenreuther, et al. Physical Review Letters **85**, 5579 (2000).

[16] J. Y. Kim and M. Wakatani. Physics of Plasmas **2**, 1012–1014 (1995).

[17] C. Kessel, J. Manickam, G. Rewoldt, et al. Physical Review Letters **72**, 1212 (1994).

[18] F. M. Levinton, M. C. Zarnstorff, S. H. Batha, et al. Physical Review Letters **75**, 4417 (1995).

[19] M. Bell, R. Bell, D. Gates, et al. Nuclear Fusion **46**, S565–S572 (2006).

[20] M. A. Beer, G. W. Hammett, G. Rewoldt, et al. In *The 38th annual meeting of the Division of Plasma Physics (DPP) of the American Physical Society*, volume 4, 1792–1799. AIP, Denver, Colorado (USA) (1997).

[21] G. Federici, C. Skinner, J. Brooks, et al. Nuclear Fusion **41**, 1967–2137 (2001).

[22] D. Naujoks and S. Benkadda. In *Plasma Material Interaction in Controlled Fusion Devices: 3rd ITER International Summer School*, 3–17 (2010).

[23] R. Majeski and S. Benkadda. In *Plasma Material Interaction in Controlled Fusion Devices: 3rd ITER International Summer School*, 122–137 (2010).

[24] R. P. Doerner. Journal of Vacuum Science & Technology A: Vacuum, Surfaces, and Films **23**, 1545–1547 (2005).

[25] e. a. Wright, G.M. In *Plasma-Surface Interactions Conference* (2012).

[26] e. a. Wright, G.M. In *APS-Division of Plasma Physics Conference* (2012).

[27] J. D. Strachan, M. Bitter, A. T. Ramsey, et al. Physical Review Letters **58**, 1004 (1987).

[28] J. Strachan, M. Bell, A. Janos, et al. Journal of Nuclear Materials **196-198**, 28 – 34 (1992).

[29] D. K. Mansfield, K. W. Hill, J. D. Strachan, et al. Physics of Plasmas **3**, 1892–1897 (1996).

[30] C. E. Bush and the TFTR team. In *Edward Bouchet international conference on physics and technology*. Legon, Ghana (1990).

[31] S. I. Krasheninnikov, L. E. Zakharov, and G. V. Pereverzev. Physics of Plasmas **10**, 1678–1682 (2003).

[32] L. Zakharov, W. Blanchard, R. Kaita, et al. Journal of Nuclear Materials **363365**, 453–457 (2007).

[33] L. Zakharov, N. Gorelenkov, R. White, et al. FUSION ENGINEERING AND DESIGN **72**, 149–168 (2004).

[34] A. Y. Dnestrovskij, S. I. Krasheninnikov, and P. N. Yushmanov. Nuclear Fusion **31**, 647 (1991).

[35] H. W. Kugel, M. G. Bell, J.-W. Ahn, et al. Physics of Plasmas **15**, 056118–056118–13 (2008).

[36] E. Reis, C. Baxi, and A. Bozek. In *Fusion Engineering, 1999. 18th Symposium on*, 519–522 (1999).

[37] J. T. Hogan, R. Maingi, P. K. Mioduszewski, et al. Journal of Nuclear Materials **241-243**, 612–617 (1997).

[38] L. E. Zakharov. Physical Review Letters **90**, 045001 (2003).

[39] D. Whyte, T. Evans, C. Wong, et al. Fusion Engineering and Design **72**, 133–147 (2004).

[40] S. V. Mirnov, E. A. Azizov, V. A. Evtikhin, et al. Plasma Physics and Controlled Fusion **48**, 821 (2006).

[41] R. Kaita, R. Majeski, T. Gray, et al. Physics of Plasmas **14**, 056111 (2007).

[42] R. Kaita, R. Majeski, R. Doerner, et al. Journal of Nuclear Materials **363-365**, 1231–1235 (2007).

[43] M. A. Jaworski, T. K. Gray, M. Antonelli, et al. Physical Review Letters **104**, 094503 (2010).

[44] M. Baldwin, R. Doerner, S. Luckhardt, et al. Nuclear Fusion **42**, 1318–1323 (2002).

[45] H. Sugai, M. Ohori, and H. Toyoda. Vacuum **47**, 981–984 (1996).

[46] J. P. Allain and C. N. Taylor. Physics of Plasmas **19**, 056126–056126–9 (2012).

[47] R. Bastasz and J. Whaley. Fusion Engineering and Design **72**, 111–119 (2004).

[48] E. Thomas, R. Janev, and J. Smith. Nuclear Instruments and Methods in Physics Research Section B: Beam Interactions with Materials and Atoms **69**, 427–436 (1992).

[49] J. Allain and D. Ruzic. Nuclear Fusion **42**, 202–210 (2002).

[50] D. Jeppson, J. Ballif, W. Yuan, et al. Lithium Literature Review: Lithium's Properties and Interactions. Technical report, Hanford Engineering Development Laboratory (1978).

[51] P. S. Krstic, J. P. Allain, C. N. Taylor, et al. Physical Review Letters **110**, 105001 (2013).

[52] T. G. Gray. *Demonstration of low recycling on a spherical torus with lithium plasma facing components*. Ph.D. thesis, Princeton University (2008).

[53] M. Jaworski, T. Abrams, J. Allain, et al. Nuclear Fusion **submitted** (2012).

[54] J. Allain, M. Nieto, M. Coventry, et al. Fusion Engineering and Design **72**, 93–110 (2004).

[55] R. Doerner, M. Baldwin, S. Krasheninnikov, et al. Journal of Nuclear Materials **313316**, 383–387 (2003).

[56] J. Allain, M. Coventry, and D. Ruzic. Journal of Nuclear Materials **313-316**, 641–645 (2003).

[57] J. Allain, D. Ruzic, D. Alman, et al. Nuclear Instruments and Methods in Physics Research Section B: Beam Interactions with Materials and Atoms **239**, 347–355 (2005).

[58] J. Brooks, J. Allain, T. Rognlien, et al. Journal of Nuclear Materials **337-339**, 1053–1057 (2005).

[59] M. G. Bell, H. W. Kugel, R. Kaita, et al. Plasma Physics and Controlled Fusion **51**, 124054 (2009).

[60] R. Majeski, M. Bell, R. Bell, et al. In *Radio Frequency Power in Plasmas, 12th Topical Conference*, volume 403 of *AIP Conference Proceedings*, 73–76. AIP, Savannah, GA (1997).

[61] E. Thomas. Particle-Impact Induced Electron Ejection from Surfaces. Technical Report INDC(NDS)-322, IAEA International Nuclear Data Committee (1995).

[62] R. A. Baragiola, E. V. Alonso, and A. O. Florio. Physical Review B **19**, 121–129 (1979).

[63] H. Bruining and J. De Boer. Physica **5**, 17–30 (1938).

[64] A. Dekker. *Solid State Physics, Advances in Research and Applications*, volume 6, chapter Secondary Electron Emission, 251–311. Academic Press, New York (1958).

[65] N. W. Ashcroft and N. D. Mermin. *Solid state physics*. Saunders College (1976).

[66] L. M. Kishinevsky. Radiation Effects **19**, 23–27 (1973).

[67] W. H. Souder. Physical Review **8**, 310–319 (1916).

[68] P. J. Catto and R. D. Hazeltine. Physics of Plasmas **13**, 122508–10 (2006).

[69] D. R. Ernst, P. T. Bonoli, P. J. Catto, et al. Physics of Plasmas **11**, 2637–2648 (2004).

[70] K. Zhurovich, C. Fiore, D. Ernst, et al. Nuclear Fusion **47**, 1220–1231 (2007).

[71] A. M. Dimits, G. Bateman, M. A. Beer, et al. Physics of Plasmas **7**, 969–983 (2000).

[72] D. Ernst, N. Basse, W. Dorland, et al. In *Proceedings of the 21st IAEA Fusion Energy Conference (Chengdu, China)*, TH/1–3. IAEA, Vienna (2006).

[73] D. R. Ernst, J. Lang, W. M. Nevins, et al. Physics of Plasmas **16**, 055906–7 (2009).

[74] T. Dannert and F. Jenko. Physics of Plasmas **12**, 072309–8 (2005).

[75] J. Lang, Y. Chen, and S. E. Parker. Physics of Plasmas **14**, 082315–12 (2007).

[76] M. Hoffman and D. Ernst. Bulletin of the American Physical Society **52**, JP8.35 (2007).

[77] B. Kadomtsev and O. Pogutse. *Reviews of Plasma Physics*, volume 5, chapter Turbulence in Toroidal Systems, 249–400. Consultants Bureau (1970).

[78] R. Majeski, L. Berzak, T. Gray, et al. Nuclear Fusion **49**, 055014 (2009).

[79] R. Majeski, H. Kugel, R. Kaita, et al. Fusion Engineering and Design **85**, 1283–1289 (2010).

[80] R. Kaita, L. Berzak, D. Boyle, et al. Fusion Engineering and Design **85**, 874–881 (2010).

[81] L. F. Berzak. *Plasma start-up in a spherical tokamak with close-fitting conducting walls*. Ph.D., Princeton University, United States – New Jersey (2010).

[82] D. Lundberg. *Fueling Studies on the Lithium Tokamak Experiment*. Ph.D. thesis, Princeton University (2012).

[83] R. Budny, D. Coster, D. Stotler, et al. Journal of Nuclear Materials **196198**, 462–465 (1992).

[84] S. Scott, D. McCune, M. Bell, et al. In *19th European Conference on Controlled Fusion and Plasma Physics*. EPS, Innsbruck, Austria (1992).

[85] M. C. Zarnstorff, V. Arunasalam, C. W. Barnes, et al. In *Plasma Physics and Controlled Nuclear Fusion Research*, volume 1 of *Proceedings of the 12th International Conference*, 183. International Atomic Energy Agency, Vienna, 1989, Nice, France (1988).

[86] M. W. Kissick, P. C. Efthimion, D. K. Mansfield, et al. Physics of Fluids B: Plasma Physics **5**, 3618–3621 (1993).

[87] J. Strachan, H. Alder, C. Barnes, et al. In *21st EPS Meeting of Plasma Physics Division*. Montpellier, France (1994).

[88] M. Apicella, G. Mazzitelli, V. Pericoli Ridolfini, et al. Journal of Nuclear Materials **363365**, 1346–1351 (2007).

[89] R. Maingi, S. M. Kaye, C. H. Skinner, et al. Physical Review Letters **107**, 145004 (2011).

[90] R. Majeski, R. Doerner, T. Gray, et al. Physical Review Letters **97**, 075002 (2006).

[91] G. Pereverzev and P. Yushmanov. ASTRA—Automated System for Transport Analysis in a Tokamak. Report, IPP Garching (2002).

[92] R. J. Colchin, D. L. Hillis, R. Maingi, et al. Review of Scientific Instruments **74**, 2068 (2003).

[93] H. Summers. *The ADAS User Manual*. http://adas.phys.strath.ac.uk, 2.6 edition (2004).

[94] K. Behringer. Journal of Nuclear Materials **145-147**, 145–153 (1987).

[95] R. Soskind and A. McLean. In *53rd Annual Meeting of the APS Division of Plasma Physics*, volume 56 of *Bulletin of the American Physical Society*, JP9.27. Salt Lake City, Utah (2011).

[96] E. M. Hollmann, A. Y. Pigarov, and R. P. Doerner. Review of Scientific Instruments **74**, 3984 (2003).

[97] K.-D. Zastrow, S. R. Keatings, L. Marot, et al. Review of Scientific Instruments **79**, 10F527–10F527–4 (2008).

[98] W. Haynes, ed. *CRC Handbook of Chemistry and Physics*. 93 edition. CRC Press, Cleveland, Ohio (2012–2013).

[99] E. D. Palik. *Handbook of Optical Constants of Solids II*. Academic Press, Boston (1991).

[100] D. L. Greenway, G. Harbeke, F. Bassani, et al. Physical Review **178**, 1340 (1969).

[101] R. L. Boivin, J. A. Goetz, E. S. Marmar, et al. Review of Scientific Instruments **70**, 260–264 (1999).

[102] I. Furno, H. Weisen, J. Mlynar, et al. Review of Scientific Instruments **70**, 4552–4556 (1999).

[103] D. Stutman, M. Finkenthal, V. Soukhanovskii, et al. Review of Scientific Instruments **70**, 572–576 (1999).

[104] V. A. Soukhanovskii, D. Stutman, M. Iovea, et al. Review of Scientific Instruments **72**, 737–741 (2001).

[105] R. L. Boivin, J. W. Hughes, B. LaBombard, et al. Review of Scientific Instruments **72**, 961–964 (2001).

[106] D. S. Gray, S. C. Luckhardt, L. Chousal, et al. Review of Scientific Instruments **75**, 376 (2004).

[107] C. Suzuki, B. J. Peterson, and K. Ida. Review of Scientific Instruments **75**, 4142–4144 (2004).

[108] A. W. Degeling, H. Weisen, A. Zabolotsky, et al. Review of Scientific Instruments **75**, 4139 (2004).

[109] M. L. Reinke and I. H. Hutchinson. Review of Scientific Instruments **79**, 10F306–10F306–4 (2008).

[110] V. A. Soukhanovskii, A. L. Roquemore, R. E. Bell, et al. Review of Scientific Instruments **81**, 10D723–10D723–5 (2010).

[111] K. Tritz, D. J. Clayton, D. Stutman, et al. Review of Scientific Instruments **83**, 10E109–10E109–3 (2012).

[112] I. Hutchinson. *Principles of plasma diagnostics*. Second edition. Cambridge University Press, New York (2002).

[113] C. B. Forest, G. Greene, and M. Ono. Eighth topical conference on hightemperature plasma diagnostics **61**, 2888–2890 (1990).

[114] Y. Jiang, D. L. Brower, L. Zeng, et al. Review of Scientific Instruments **68**, 902–905 (1997).

[115] L. Berzak, R. Kaita, T. Kozub, et al. In *PROCEEDINGS OF THE 17TH TOPICAL CONFERENCE ON HIGH-TEMPERATURE PLASMA DIAGNOSTICS*, volume 79, 10F116–3. AIP, Albuquerque, New Mexico (USA) (2008).

[116] L. Berzak, A. D. Jones, R. Kaita, et al. Review of Scientific Instruments **81**, 10E114–10E114–7 (2010).

[117] J. Menard, R. Bell, E. Fredrickson, et al. Nuclear Fusion **45**, 539–556 (2005).

[118] L. Berzak Hopkins, J. Menard, R. Majeski, et al. Nuclear Fusion **52**, 063025 (2012).

[119] T. Strickler, R. Majeski, R. Kaita, et al. In *Rev. Sci. Instrum.*, volume 79, 10E738–5. AIP (2008).

[120] B. P. LeBlanc, R. E. Bell, D. W. Johnson, et al. Review of Scientific Instruments **74**, 1659–1662 (2003).

[121] T. Gray, R. Kaita, R. Majeski, et al. Review of Scientific Instruments **77**, 10E901–10E901–3 (2006).

[122] V. A. Soukhanovskii, H. W. Kugel, R. Kaita, et al. Review of Scientific Instruments **75**, 4320 (2004).

[123] T. Abrams, D. Stotler, and R. Majeski. In *53rd Annual Meeting of the APS Division of Plasma Physics*, volume 56 of *Bulletin of the American Physical Society*, PP9.00017. Salt Lake City, Utah (2011).

[124] E. A. Frieman and L. Chen. Physics of Fluids **25**, 502–508 (1982).

[125] D. H. E. Dubin, J. A. Krommes, C. Oberman, et al. Physics of Fluids **26**, 3524–3535 (1983).

[126] W. W. Lee. Physics of Fluids **26**, 556–562 (1983).

[127] T. S. Hahm. Physics of Fluids **31**, 2670 (1988).

[128] M. Beer. *Gyrofluid Model of Turbulent Transport in Tokamaks*. Ph.D. thesis, Princeton University (1994).

[129] H. Sugama and W. Horton. Physics of Plasmas **4**, 405–418 (1997).

[130] H. Sugama and W. Horton. Physics of Plasmas **5**, 2560–2573 (1998).

[131] H. Sugama. Physics of Plasmas **7**, 466–480 (2000).

[132] H. Qin, W. M. Tang, G. Rewoldt, et al. Physics of Plasmas **7**, 991–1000 (2000).

[133] A. J. Brizard and T. S. Hahm. Reviews of Modern Physics **79**, 421–468 (2007).

[134] J. A. Krommes. Annual Review of Fluid Mechanics **44**, 175–201 (2012).

[135] W. Tang, C. Liu, M. Rosenbluth, et al. Nuclear Fusion **16**, 191–202 (1976).

[136] W. M. Tang, G. Rewoldt, and L. Chen. Physics of Fluids **29**, 3715–3718 (1986).

[137] J. Candy and R. Waltz. Journal of Computational Physics **186**, 545–581 (2003).

[138] J. Candy and R. E. Waltz. Physical Review Letters **91**, 045001 (2003).

[139] J. Candy and E. Belli. GYRO Technical Guide. Technical report, General Atomics, P.O. Box 85608, San Diego, CA 92186-5608, USA (2013).

[140] A. Arakawa. Journal of Computational Physics **1**, 119–143 (1966).

[141] R. E. Waltz and R. L. Miller. Physics of Plasmas **6**, 4265–4271 (1999).

[142] D. Ernst, N. Basse, P. Bonoli, et al. In *20th IAEA Fusion Energy Conference (Villamoura, Portugal)*, TH/4–1. IAEA, Vienna (2004).

[143] K. M. Zeller. *Gyrokinetic simulations of the nonlinear upshift of the critical density gradient for TEM turbulence in tokamak fusion plasmas.* Senior thesis, Massachusetts Institute of Technology (2006).

[144] J. Kinsey. The GYRO Nonlinear Gyrokinetic Simulation Database. Technical report, General Atomics, San Diego, CA (2007).

[145] F. Jenko, W. Dorland, and G. W. Hammett. Physics of Plasmas **8**, 4096–4104 (2001).

[146] J. F. Drake, N. T. Gladd, C. S. Liu, et al. Physical Review Letters **44**, 994 (1980).

[147] D. Bettella, L. Carraro, M. Puiatti, et al. *Hydrogen Recycling at Plasma Facing Materials*, chapter Hydrogen Recycling in the RFX Reversed Field Pinch, 17–23. Kluwer Academic Publishers (1999).

[148] P. C. Stangeby. *The plasma boundary of magnetic fusion devices.* Plasma physics series. Institute of Physics Pub, Bristol ; Philadelphia (2000).

[149] S. Fukada, M. Kinoshita, K. Kuroki, et al. Journal of Nuclear Materials **346**, 293–297 (2005).

[150] R. M. Alire. The Journal of Chemical Physics **65**, 1134–1137 (1976).

[151] N. M. Blagoveshchenskii, N. I. Loginov, V. A. Morozov, et al. Journal of Physics: Conference Series **98**, 022014 (2008).

[152] S. K. Erents, G. M. McCracken, and P. Goldsmith. Journal of Physics D: Applied Physics **4**, 672 (1971).

[153] R. Sullenberger. *Uptake and Retention of Residual Vacuum Gases in Lithium and Lithium Films*. Master's thesis, Princeton University (2012).

[154] C. Skinner, R. Sullenberger, B. Koel, et al. Journal of Nuclear Materials (2013).

[155] D. Stotler and C. Karney. Contributions to Plasma Physics **34**, 392–397 (1994).

[156] D. Stotler, C. Karney, R. Kanzleiter, et al. The DEGAS 2 User's Manual. Technical report, Princeton Plasma Physics Laboratory (2013).

[157] J. E. Menard, R. E. Bell, D. A. Gates, et al. Physical Review Letters **97**, 095002 (2006).

[158] J. Squire, E. Granstedt, C. Jacobson, et al. In *53rd Annual Meeting of the APS Division of Plasma Physics*, volume 56 of *Bulletin of the American Physical Society*. Salt Lake City, Utah (2011).

[159] C. Jacobson. private communication (2013).

[160] D. Boyle. private communication (2013).

[161] D. Stotler, C. Skinner, W. Blanchard, et al. Journal of Nuclear Materials **415**, S1058–S1061 (2011).

[162] D. A. Russell, J. R. Myra, D. A. DIppolito, et al. Physics of Plasmas **18**, 022306–022306–12 (2011).

[163] R. Marchand and M. Dumberry. Computer Physics Communications **96**, 232–246 (1996).

[164] H.-J. Klingshirn, D. Coster, and X. Bonnin. Journal of Nuclear Materials (2013).

[165] R. Maingi, D. P. Boyle, J. M. Canik, et al. Nuclear Fusion **52**, 083001 (2012).